Using measurements and modelling of carbon isotopes for evaluating methane emissions and sources in the UK

Eric Saboya

Department of Physics

Imperial College London

London SW7 2AX

July 2022

A thesis submitted in fulfilment of the requirements for the degree of Doctor of Philosophy.

Abstract

Atmospheric methane is an important greenhouse gas that is emitted from a diverse range of anthropogenic and natural sources. Quantifying and attributing methane emissions can provide information on the sources that are driving the increases in atmospheric methane concentrations and be used to guide mitigation policies. In this thesis, I use, assess, develop and compare different approaches for attributing specific sources and quantifying emissions of methane in the UK. The work in this thesis uses carbon isotopes of methane and satellite observations of total methane columns (XCH_4) from the TROPOSpheric Monitoring Instrument (TROPOMI) between 2018-2020.

Urban areas are hotspots of anthropogenic methane emissions, which are emitted from a number of different sources. I use in situ atmospheric methane and $\delta^{13}CH_4$ measurements made in central London to demonstrate that continuous measurements from a Picarro isotopic analyser can be used for methane source attribution of large pollution events. These measurements indicated a predominance of fossil methane in central London which was found to be underreported in the UK national emissions inventory. The utility of additional isotopic measurements of atmospheric $\Delta^{14}CH_4$ is explored for the UK by developing a joint CH_4-$\delta^{13}CH_4$-$\Delta^{14}CH_4$ isotopic framework and using pseudo-data simulations. Pseudo-data indicate additional isotopic measurements of $\Delta^{14}CH_4$ could improve the UK's methane source apportionment. A first analysis of TROPOMI methane measurements for the UK is also conducted. I conclude that TROPOMI XCH_4 retrievals from 2018-2020 are not useful for informing on UK methane emissions and spatial variations due, in part, to the low data availability for the UK over this period.

My findings indicate that ground-based atmospheric measurements are more useful for constraining sector specific methane emissions and informing on regional differences than TROPOMI measurements for the UK. Whilst $\delta^{13}CH_4$ measurements are found to be valuable for source attribution, additional measurements of atmospheric $\Delta^{14}CH_4$ could be used to improve the methane source constraint for the UK.

Declaration of Originality

The work presented in this thesis is my own work, except where referenced. The results presented here have been published or submitted for publication in the following:

Saboya, E., Zazzeri, G., Graven, H., Manning, A. J., Englund Michel, S. (2022): "Continuous CH_4 and $\delta^{13}CH_4$ measurements in London demonstrate under-reported natural gas leakage". *Atmospheric Chemistry and Physics.* 22.5, pp. 3595-3613. ISSN: 1680-7324. DOI 10.5194/acp-22-3595-2022.

Signed: _____

Date: _____

Copyright

The copyright of this thesis rests with the author. Unless otherwise indicated, its contents are licensed under a Creative Commons Attribution-Non Commercial 4.0 International Licence (CC BY-NC).

Under this licence, you may copy and redistribute the material in any medium or format. You may also create and distribute modified versions of the work. This is on the condition that: you credit the author and do not use it, or any derivative works, for a commercial purpose.

When reusing or sharing this work, ensure you make the licence terms clear to others by naming the licence and linking to the licence text. Where a work has been adapted, you should indicate that the work has been changed and describe those changes.

Please seek permission from the copyright holder for uses of this work that are not included in this licence or permitted under UK Copyright Law.

"I took month-long vacations in the stratosphere,

And you know it's really hard to hold your breath."

Bruce Springsteen

Growin' Up

This thesis was typeset using the LaTeX typesetting system originally developed by Leslie Lamport, based on TeX created by Donald Knuth. The results and figures presented herein were produced in Python3.

Contents

Abstract 3

Declaration of Originality 5

Copyright 7

List of Figures 19

List of Tables 22

List of Abbreviations 23

Acknowledgements 27

1 Introduction 29

1.1 Rationale . . . 29

1.2 Aims and objectives . . . 30

1.3 Outline of the thesis . . . 30

2 Background 31

2.1 The role of methane as a greenhouse gas . . . 31

2.2 Quantifying methane emissions: top-down vs. bottom-up . . . 32

2.3 Atmospheric methane sources . . . 33

2.4 Atmospheric methane sinks . . . 35

2.5 Atmospheric methane trends in the UK . . . 36

2.6 Isotopic tracer approaches for attributing sources of CH_4 emissions . . . 43

2.6.1 Overview of carbon-13 isotopic notation . . . 43

2.6.2 Using $\delta^{13}CH_4$ to understand sources of CH_4 . . . 44

2.6.3 Overview of atmospheric carbon-14 and carbon-14 isotopic notation 50
2.6.4 Using $\Delta^{14}CH_4$ to understand contemporary CH_4 sources 55
2.7 Using methane satellite measurements to constrain CH_4 emissions 58
2.7.1 Satellite instruments for measuring atmospheric methane 59
2.7.2 GOSAT methane measurements 60
2.7.3 TROPOMI methane measurements 62
2.8 Summary 67
2.8.1 Isotopic approaches 67
2.8.2 Satellite approaches 68

3 Data, observations and models **71**
3.1 In situ measurements at Imperial College London 71
3.1.1 Laboratory setup 74
3.1.2 Calibration procedure and uncertainties 74
3.1.3 Water correction 78
3.2 Bottom-up emissions data 78
3.2.1 Anthropogenic emissions: EDGAR 79
3.2.2 Anthropogenic emissions: UK NAEI 83
3.2.3 Wetland emissions: WetCHARTs 85
3.2.4 Biomass burning emissions: GFED 87
3.2.5 Processing emissions data 88
3.3 Atmospheric model 89
3.3.1 Overview of NAME 90
3.3.2 Back-trajectories from NAME 91
3.3.3 Estimating model uncertainty in NAME 93
3.3.4 Simulating CH_4 94
3.4 Remote sensing measurements from TROPOMI 97
3.4.1 Overview of TROPOMI 97
3.4.2 Overview of TROPOMI's retrieval algorithm 98
3.4.3 Data products and quality 99
3.4.4 Data validation 100
3.4.5 Data processing 102

3.5 CAMS XCH_4 analysis and forecast products . . . 103
3.5.1 CAMS EGG4 greenhouse gas reanalysis data product . . . 103
3.5.2 CAMS atmospheric composition forecast data product . . . 104
3.5.3 CAMS data processing . . . 105
3.5.4 CAMS data setup . . . 106

4 Measurements and modelling of CH_4 concentrations and $\delta^{13}CH_4$ in central London 107
4.1 Introduction . . . 108
4.2 Methods . . . 110
4.2.1 Keeling plot analysis . . . 110
4.2.2 Atmospheric simulations . . . 112
4.3 Results . . . 114
4.3.1 Measurements . . . 114
4.3.2 Keeling plot analyses . . . 120
4.3.3 Simulations of methane: simulated CH_4 mole fractions . . . 123
4.3.4 Simulations of methane: simulated $\delta^{13}CH_4$ values . . . 127
4.3.5 Sectoral source apportionment in the simulations . . . 128
4.4 Discussion . . . 130
4.5 Conclusion . . . 136

5 Developing a framework for regional source attribution using atmospheric measurements of CH_4 concentrations, $\delta^{13}CH_4$ and $\Delta^{14}CH_4$ 137
5.1 Introduction . . . 138
5.2 Methods . . . 143
5.2.1 Joint CH_4-$\delta^{13}CH_4$-$\Delta^{14}CH_4$ regional framework . . . 143
5.2.2 Deviations in atmospheric $\delta^{13}CH_4$ and $\Delta^{14}CH_4$ from the background . . . 147
5.2.3 Pseudo-data across the UK measurement network . . . 149
5.2.3.1 Contemporary CH_4 simulations . . . 150
5.2.3.2 Projected SSP CH_4 simulations for 2030 . . . 152
5.2.4 Simulating nuclear power plant $^{14}CH_4$ emissions . . . 154
5.3 Results . . . 156
5.3.1 Contemporary simulations for 2018 using EDGAR and NAEI emissions . . . 156
5.3.2 Nuclear power plant $\Delta^{14}CH_4$ influences across the UK . . . 159

5.3.3 Future simulations for 2030 using CMIP6 SSP emissions . . . 165
5.3.3.1 Changes between 2015 and 2030 in emissions across the UK . . . 165
5.3.3.2 Future changes in CH_4, $\delta^{13}CH_4$ and $\Delta^{14}CH_4$ across the UK . . . 166
5.4 Discussion . . . 169
5.5 Conclusion . . . 172

6 Assessing the utility of TROPOMI XCH_4 retrievals for the UK **173**
6.1 Introduction . . . 174
6.2 Data products and methods . . . 176
6.2.1 Overview of TROPOMI XCH_4 data products and processing . . . 176
6.2.2 Overview of CAMS XCH_4 data products and processing . . . 180
6.2.3 Comparing CAMS and TROPOMI XCH_4 . . . 181
6.2.4 Cross-sectional flux method . . . 181
6.3 Results . . . 182
6.3.1 TROPOMI measurements across the UK . . . 182
6.3.2 CAMS-TROPOMI XCH_4 comparison over the UK . . . 191
6.3.3 Using TROPOMI measurements to quantify CH_4 emissions from Drax power station 204
6.4 Discussion . . . 206
6.5 Conclusion . . . 208

7 Conclusions **209**
7.1 Summary of key findings . . . 209
7.2 Future work . . . 210

Bibliography **213**

Appendices **233**

A Derivation of Chapter 5 CH_4-$\delta^{13}CH_4$-$\Delta^{14}CH_4$ equations **235**

B Calculating uncertainties of $\Delta^{14}CH_4$-$\delta^{13}CH_4$ slopes **239**

List of Figures

2.1 Global methane budget for the 2008–2017 decade. . . . 34
2.2 Methane global emissions for five categories for 2008-2019. . . . 35
2.3 NAEI methane emission trends . . . 37
2.4 Inversion posterior methane emissions from UK studies . . . 38
2.5 Greenhouse gas measurement sites in the UK . . . 41
2.6 Methane UK bottom-up top-down estimates time-series . . . 42
2.7 Discrete $\delta^{13}CH_4$ isotope measurements . . . 44
2.8 Atmospheric methane and $\delta^{13}CH_4$ at Earth's surface in the remote marine troposphere. . . . 45
2.9 Normalised probability density distributions for the $\delta^{13}CH_4$ of microbial, fossil and biomass burning sources of methane. . . . 46
2.10 Emissions and $\delta^{13}CH_4$ isotopic map for London based on 2013 NAEI methane inventories. . . 48
2.11 $\delta^{13}CH_4$ and δD source signatures. . . . 50
2.12 Compiled historical dataset for $\Delta^{14}C$. . . . 52
2.13 A simulated $\Delta^{14}C$ history in atmospheric methane. . . . 54
2.14 Observed $\Delta^{14}CO_2$ for 1940-2015 and simulated $\Delta^{14}CO_2$ for 2015-2100 for the six SSP-based CMIP6 scenarios. . . . 55
2.15 ^{14}C activity in atmospheric methane at Heidelberg. . . . 57
2.16 Diagram showing the expected change in CH_4 concentration and change in $\Delta^{14}CH_4$ from background values. . . . 58
2.17 Annual anthropogenic methane emissions for 2019 for five major source regions from Qu et al. (2021). . . . 64
2.18 Scatter plot of NO_2 vs. methane mixing ratios from Gouw et al. (2020). . . . 65
2.19 Urban CH_4 emissions generated with the observed 2019 $\Delta CH_4/\Delta CO$ ratios by Plant et al. (2022) 66

3.1 Imperial College London measurement site. . . . 72
3.2 NAEI CH_4 emissions in the Imperial College London area with locations of large CH_4 sources. 73
3.3 Allan deviation of Imperial College London measurements. . . . 75
3.4 Water correction setup used for Imperial College London measurements. . . . 77
3.5 Imperial College London water correction experiment data. . . . 77
3.6 EDGAR methane emissions over the UK 81
3.7 NAEI methane emissions over the UK 83
3.8 WetCHARTs 2015 extended ensemble mean CH_4 emissions 86
3.9 GFED biomass burning CH_4 emissions over the UK 87
3.10 Regridding emissions data 89
3.11 NAME footprint domains with EDGAR v4.3.2. emissions superimposed. . . . 92
3.12 Atmospheric optical depths of major trace gases (1.5-2.5μm) 97
3.13 TROPOMI measuring principle 100
3.14 Ratio of XCH_4 measurements by TCCON and TROPOMI as a function of surface albedo and aerosol optical depth. . . . 101
3.15 Latitudinal distribution of XCH_4 measured by TROPOMI and GOSAT 102

4.1 Isotopic source values for ideal pollution events with different isotopic signatures and peak strengths. . . . 112
4.2 Standard deviations of the recovered isotopic source values for different peak strengths. . . . 114
4.3 London CH_4 emissions from EDGAR v4.3.2 (2012) and NAEI (2017). . . . 115
4.4 The 20-minute averaged measured mole fractions and $\delta^{13}CH_4$ values at ICL. . . . 118
4.5 Detrended seasonal cycles of CH_4 and $\delta^{13}CH_4$ measurements at ICL and Mace Head 119
4.6 Detrended weekly CH_4 and $\delta^{13}CH_4$ measurements at ICL. . . . 120
4.7 Distributions of the isotopic source values from Keeling plot analysis. . . . 121
4.8 Time-series and correlation plots of isotopic source values and wind direction. . . . 122
4.9 Excess simulated and observed 13:00-17:00 mole fractions for 2020. . . . 124
4.10 Excess simulated and observed 13:00-17:00 mole fractions for 2019. . . . 125
4.11 Excess simulated and observed 13:00-17:00 mole fractions for 2018. . . . 125
4.12 Simulation-observation comparisons of excess mole fractions using linear regressions and distributions of the simulation-observation differences. . . . 126
4.13 Simulated and measured $\delta^{13}CH_4$ values for 2020 using 13:00-17:00 data. . . . 128

4.14 Simulated and measured $\delta^{13}CH_4$ values for 2019 using 13:00-17:00 data. 129
4.15 Simulation-observation comparisons of $\delta^{13}CH_4$ using point-by-point comparisons and distributions of the differences. 130
4.16 Recalculated NAEI-25km and NAEI-2km $\delta^{13}CH_4$ values. 131
4.17 London EDGAR and NAEI waste CH_4 emissions. 132
4.18 London EDGAR and NAEI natural gas CH_4 emissions. 133

5.1 The expected changes in CH_4 concentrations and $\Delta^{14}CH_4$, and $\delta^{13}CH_4$ and $\Delta^{14}CH_4$. 140
5.2 Schematic to show the deviations in isotopic values from the background for various added CH_4 concentrations of different fossil-fraction values. 149
5.3 UK measurement network of sites (black circles) along with nearby PWR nuclear power plants (red squares). 150
5.4 Anthropogenic CH_4 emissions from EDGAR v5.0 (2015), NAEI (2017) and emissions from WetCHARTs. 151
5.5 Boxplot distributions of added concentrations, $\Delta\delta^{13}CH_4/\Delta CH_4$ and $\Delta\Delta^{14}CH_4/\Delta CH_4$ for EDGAR5 and NAEI-EDGAR4 simulations. 156
5.6 Two-dimensional histograms of $\Delta\Delta^{14}CH_4$-ΔCH_4 and $\Delta\Delta^{14}CH_4$-$\Delta\delta^{13}CH_4$. 158
5.7 Histograms of modelled NPP $\Delta^{14}CH_4$ influences at each of the measurement sites. 160
5.8 Boxplot distributions of $\Delta\Delta^{14}CH_4$ at each of the sites with (cyan) and without (red) NPP influences for EDGAR5 and NAEI-EDGAR4 simulations. 162
5.9 Two-dimensional histograms of $\Delta\Delta^{14}CH_4$-ΔCH_4 and $\Delta\Delta^{14}CH_4$-$\Delta\delta^{13}CH_4$ with NPP $\Delta^{14}CH_4$ influences. 163
5.10 Distributions of simulated NPP $\Delta^{14}CH_4$ influences at the measurement sites under upwind and downwind conditions with two-dimensional histograms. 164
5.11 Relative differences between 2015 and 2030 SSP1-1.9 and SSP5-8.5 methane emissions over the UK. 167
5.12 Boxplot distributions of added concentrations,$\Delta\delta^{13}CH_4$ and $\Delta\Delta^{14}CH_4$ for EDGAR5, NAEI-EDGAR4, SSP1-1.9, SSP5-8.5 simulations. 168
5.13 Two-dimensional histograms of simulated $\Delta\Delta^{14}CH_4$-ΔCH_4 and $\Delta\Delta^{14}CH_4$-$\Delta\delta^{13}CH_4$ for HFD, ICL and TAC under SSP1-1.9 and SSP5-8.5 emission scenarios. 169

6.1 2017 UK NAEI points sources. 177
6.2 UK 2018-2020 averaged TROPOMI XCH_4 products. 178

6.3 UK mean 2018-2020 TROPOMI CH_4 subtracted from the corresponding bias-corrected TROPOMI XCH_4, filtered for AOT<0.10, values. 179
6.4 Difference between XCH_4 bias-corrected product with and without filtering for aerosol optical thickness. 180
6.5 Example of the cross-sectional flux method. 182
6.6 Comparison of TROPOMI averaged XCH_4 with 2017 NAEI emissions. 183
6.7 UK 2018-2020 averaged TROPOMI surface albedo, AOT and pixel numbers. 184
6.8 TROPOMI UK 2018-2020 averaged XCH_4-albedo and XCH_4-AOT two-dimensional histograms. 185
6.9 TROPOMI XCH_4, surface albedo, AOT data products for 15 February 2019. 186
6.10 TROPOMI XCH_4, surface albedo, AOT data products for 26 February 2019. 186
6.11 TROPOMI XCH_4, surface albedo, AOT data products for 27 June 2019. 186
6.12 TROPOMI XCH_4, surface albedo, AOT data products for 20 April 2020. 187
6.13 TROPOMI XCH_4, surface albedo, AOT data products for 21 April 2020. 187
6.14 TROPOMI XCH_4, surface albedo, AOT data products for 6 May 2020. 187
6.15 TROPOMI XCH_4, surface albedo, AOT data products for 17 September 2020. 188
6.16 TROPOMI XCH_4, surface albedo, AOT data products for 21 September 2020. 188
6.17 Two-dimensional histograms of TROPOMI XCH_4-surface albedo for individual days with clear-sky scenes over the UK. 189
6.18 Two-dimensional histograms of TROPOMI XCH_4-AOT for individual days with clear-sky scenes over the UK. 190
6.19 CAMS-TROPOMI differences for 15 February 2019. 192
6.20 CAMS-TROPOMI differences for 26 February 2019. 193
6.21 CAMS-TROPOMI differences for 27 June 2019. 194
6.22 CAMS-TROPOMI differences for 20 April 2020. 195
6.23 CAMS-TROPOMI differences for 21 April 2020. 196
6.24 CAMS-TROPOMI differences for 6 May 2020. 197
6.25 CAMS-TROPOMI differences for 17 September 2020. 198
6.26 CAMS-TROPOMI differences for 21 September 2020. 199
6.27 Averaged TROPOMI, CAMS reanalysis and CAMS forecast XCH_4 data for the eight days with good UK coverage. 202
6.28 Eight-day averaged TROPOMI XCH_4 subtracted from averaged CAMS reanalysis XCH_4 and from CAMS forecast XCH_4 203

6.29 Two-dimensional histograms of UK CAMS-TROPOMI XCH_4 differences against surface albedo and aerosol optical thickness. 204
6.30 TROPOMI XCH_4 retrievals in the vicinity of Drax power station with ERA5 wind data and plume transects. 205

List of Tables

2.1 Summary of UK methane inversion studies (2000-2019). 39

2.2 $\delta^{13}CH_4$ signatures of UK methane sources. 47

2.3 Compiled mean isotopic composition values of methane with 1 standard deviation. With $\Delta^{14}CH_4$ data from Quay et al. (1999), Wahlen et al. (1989), and Graven et al. (2017) and $\delta^{13}CH_4$ data from Zazzeri et al. (2017) and Fisher et al. (2017) 56

2.4 Satellite instruments that measure CH_4 in the SWIR 60

2.5 2009-2011 methane emissions reported by Turner et al. (2015). 61

2.6 Global methane budget for 2019 reproduced from Qu et al. (2021). 63

3.1 UK EDGAR v4.3.2 and v5.0 CH_4 emissions by sector 82

3.2 UK NAEI CH_4 emissions 84

3.3 UK GFED biomass burning CH_4 emissions 88

3.4 NAME footprint parameters 91

3.5 Source sector $\delta^{13}CH_4$ and $\Delta^{14}CH_4$ isotopic signatures for NAEI emission source sectors. . . 96

4.1 Keeling plot pseudo-data peak strength mean and 1σ. 113

4.2 Imperial College London isotopic source values summary for different peak strengths and window sizes. 116

4.3 Summary of atmospheric CH_4 simulations at ICL. 116

4.4 EDGAR and NAEI emissions and $\delta^{13}CH_4$ for the UK and London. 117

4.5 Simulation-observation 13:00-17:00 RMSE values, scaling factors and correlation coefficients. 124

4.6 Mean simulated source apportionment for excess CH_4 at Imperial College London and in the CH_4 emissions for London. 134

5.1 $\Delta^{14}CH_4$-CH_4 slope values for different methane fossil-fractions. 145

5.2 $\Delta^{14}CH_4$-$\delta^{13}CH_4$ slope values for different sources of methane. 148
5.3 Locations and sampling heights of UK and Republic of Ireland measurement sites used in the simulations. 152
5.4 Contemporary and projected methane emission inventory values for the UK. 153
5.5 $^{14}CH_4$ emissions and locations of the nearest PWRs to the UK. 155
5.6 $\Delta\Delta^{14}CH_4$-ΔCH_4 and $\Delta\Delta^{14}CH_4$-$\Delta\delta^{13}CH_4$ pseudo-data slope values for each of the measurement sites calculated using a least-squares fit. 159
5.7 NPP $\Delta^{14}CH_4$ influence statistics for each of the measurement sites. 161
5.8 Mean increases in $\Delta^{14}CH_4$ from each of the seven individual NPPs near the measurement sites. Values in ‰. 165

6.1 TROPOMI mean XCH_4, surface albedo and AOT for eight individual dates in 2018-2020 with UK-wide clear-sky scenes. 191
6.2 CAMS reanalysis and forecast XCH_4 median values for the UK. 200
6.3 CAMS reanalysis - TROPOMI and CAMS forecast - TROPOMI XCH_4 median differences for the UK. 201
6.4 CAMS reanalysis and forecast XCH_4 median differences with TROPOMI for London. 201

Abbreviations

AGRs advanced gas-cooled reactors.

AOT aerosol optical thickness.

BSD Bilsdale.

CAMS Copernicus Atmosphere Monitoring Service.

CASA Carnegie-Ames-Stanford approach.

CMIP6 Coupled Model Intercomparison Project.

CRDS Cavity Ring-Down Spectroscopy.

CSF cross-sectional flux.

DARE-UK Detection and Attribution of Regional greenhouse gas Emissions in the UK.

DECC Deriving Emissions to Climate Change.

EDGAR Emissions Database for Global Atmospheric Research.

GAUGE Greenhouse Gas UK and Global Emissions.

GAW Global Atmospheric Watch.

GFED Global Fire Emissions Database.

GHG greenhouse gas.

GRA Gravelines.

HFD Heathfield.

IAEA International Atomic Energy Agency.

ICL Imperial College London.

ICOS Integrated Carbon Observation System.

IFS Integrated Forecasting System.

INSTAAR the Institute of Arctic and Alpine Research.

InTEM Inversion Technique for Emission Modelling.

MHD Mace Head.

MPI-BGC Max Planck Institute for Biogeochemistry.

NAEI National Atmospheric Emissions Inventory.

NAME Numerical Atmospheric dispersion Modelling Environment.

NDACC Network for the Detection of Atmospheric Composition Change.

NIR near-infrared.

NIST National Institute of Standards and Technology.

NPPs nuclear power plants.

PBL planetary boundary layer.

PWRs pressurised water reactors.

RADD Radioactive Discharges Database.

RGL Ridge Hill.

S-5P Sentinel-5 Precursor.

SCIAMACHY Scanning Imaging Absorption Spectrometer for Atmospheric Cartography.

SSP Shared Socioeconomic Pathways.

SWB Sizewell B.

SWIR shortwave infrared.

TAC Tacolneston.

TCCON Total Carbon Column Observing Network.

TROPOMI TROPOspheric Monitoring Instrument.

TTA Angus.

UM Unified Model.

WAO Weybourne Atmospheric Observatory.

WMO World Meteorological Organisation.

Acknowledgements

This is not a short list of thanks, but no one achieves anything alone.

I am extremely grateful to my supervisor, Heather Graven for first giving me the opportunity to undertake this research and then for her invaluable support, guidance, encouragement, mentoring and seemingly endless patience over the last four years. I have learnt so much from you, especially about what it means to be a scientist. It's been a privilege to be your student.

Many thanks also to my supervisor, Tim Arnold whose insights into atmospheric modelling, atmospheric measurements and his support have been invaluable throughout my PhD. Tim, thank you for always making the time to chat and making me feel welcome at NPL.

Giulia and Ryo, thank you so much for all your help and encouragement. I am incredibly lucky to have worked with both of you and grateful for all you've taught me. Thank you for also being such great travelling companions. Without you both, I'd be many good memories and stories poorer from our trip to California.

I've been very fortunate to have had shared an office with such excellent people over the last four years. You've all made Huxley 709 an enjoyable place to work. Pietro, Philipp, Jo, Robbie, Shuai, Goody, and Hamish thank you for all the dinner parties, the support and helping me through the tough times. I'm also very glad to have shared much of the Grantham SSCP DTP experience with Carl, Laura, Marie and Sadie.

Massive thanks to Alistair Manning and Ed Chung for answering my many emails about atmospheric modelling and for always providing such clear answers. Ed, thank you for also making me feel so welcome at NPL and getting me involved in the Stanton Trophy - despite my shoddy table tennis skills.

Matt and Joe, thank you for being such great friends and flatmates. You've probably heard more about my PhD and research than you'd like, but you never complained too much. You have no idea how grateful I am for your support and friendship over the last eight years.

To some memorable scientists and educators; my sixth form physics teacher, Mr. James Rouse whose enthusiasm for science sent me down this path. To Mark Sullivan at the University of Southampton who seven years ago showed me the joys of academic research and encouraged me to take this journey.

Finally, thank you to my Mum and my sister, Julia, for their endless encouragement these last few months. Being at home has made the writing easier, even if at times it's seemed like a chaotic process. I will never be able to find the words to say how thankful and grateful I am for all that you've done for me.

Without all of you, none of this would've been possible.

Chapter 1

Introduction

"Everything starts somewhere, although many physicists disagree."

— Terry Pratchett, *Hogfather*

1.1 Rationale

Methane emissions have significantly contributed to the increase in global air and ocean temperature over the last century (IPCC 2014a). Compared to other greenhouse gases, methane is emitted from a diverse range of anthropogenic and natural sources. Attributing and constraining methane emissions from different sources is a major challenge but paramount to understanding the key sources driving the rise in atmospheric methane concentrations.

The UK reports its spatially resolved methane emissions in the UK national emissions inventory each year (Ricardo Energy & Environment 2019). The UK's most recent methane emission estimates for the year 2019 are reported at 2176 kt CH_4 (Ricardo Energy & Environment 2019), which comprise ~ 0.6% of global methane emissions (Saunois et al. 2020). Whilst UK atmospheric methane measurements are often used to verify the magnitude of reported emissions (e.g. Lunt et al. 2021a; Ganesan et al. 2015), there are few studies that have evaluated the UK inventory source apportionment outside of London - and usually only target specific places or sources (e.g. Zazzeri et al. 2015; Riddick et al. 2018). Questions therefore remain on the accuracy of the distribution and attribution of emissions of UK methane sources reported in the inventories. With the signing of the Global Methane Pledge (Arora and Mishra 2021) to reduce methane emissions by 30% relative to 2020 levels by 2030, it is vital that UK methane emissions and their sources are well-constrained to ensure effective mitigation. To do this, we must use existing measurement-modelling techniques and develop

new methodologies to ensure we are on track.

1.2 Aims and objectives

In this thesis, I aim to develop and use different measurement and modelling approaches to assess which methods are more suitable for regional methane source attribution and emissions quantification in the UK. As there are a suite of methodologies available I focus on using carbon isotopes and satellite measurements. To achieve this aim, the following research questions are addressed in my thesis:

1. Can continuous ^{13}C methane measurements constrain sector specific methane emissions in London?
2. To what extent can ^{14}C isotopic measurements of methane be theoretically used to enhance ^{13}C constraints of sectoral methane emissions in the UK?
3. How do satellite methane measurements compare with ground-based measurements for constraining methane emissions in the UK?

1.3 Outline of the thesis

The structure of this thesis is as follows: In Chapter 2, a review of previous research relating to carbon isotopic measurements and satellite measurements of methane, with an emphasis on UK studies, is presented. In Chapter 3, I describe the methane measurements, emissions data and modelling methodologies that are used in my thesis. Chapter 4 presents the findings of the London methane measurement and modelling campaign. In which, ^{13}C measurements were used to evaluate the London methane source apportionment reported in global and national emission inventories. In Chapter 5, I investigated the utility of joint ^{13}C-^{14}C isotopic measurements for methane source attribution in the UK. I test this combined isotopic approach by using UK pseudo-data generated for the year 2018 and pseudo-data using projections of UK methane emissions for the year 2030 under different future emission scenarios. In Chapter 6, I evaluate the utility of TROPOMI methane satellite measurements for the UK by first assessing the data coverage and then comparing regional spatial gradients to modelled data that use emission inventory estimates. In Chapter 7, I conclude by summarising the findings of this thesis and I also suggest further work that could be carried out in the future.

Chapter 2

Background

"My mistake was in ever opening the books."

— Jack London, *The Sea Wolf*

2.1 The role of methane as a greenhouse gas

The Industrial Revolution marks the point in time when anthropogenic greenhouse gas (GHG) emissions began to noticeably alter the chemical composition of our atmosphere. In the last two hundred years, or thereabouts, anthropogenic GHG emissions have continued to increase at an alarming rate. As our atmosphere becomes more burdened with carbon dioxide (CO_2), methane (CH_4) and other greenhouse gases the impact on our climate, ecology and lives becomes more devastating.

Atmospheric methane is the most important anthropogenic GHG after carbon dioxide. The relatively high atmospheric abundance of CH_4 (1891 ppb as of April 2021; Dlugokencky 2022) and a twenty-year global warming potential 84 times larger than CO_2 (IPCC 2014a) leads to CH_4 having one of the largest impacts on our climate. The methane in the atmosphere contributes to about half the radiative forcing (0.48 W m^{-2}; IPCC 2014a) of methane emissions. The production of ozone, stratospheric water vapour and CO_2 from methane emissions gives an overall effective radiative forcing of 0.97 (0.74-1.20) W m^{-2} (IPCC 2014b), which is almost two-thirds the 1.68 (1.33-2.03) W m^{-2} effective radiative forcing of CO_2.

Whilst CO_2 has an atmospheric lifetime of 5-200 years* (IPCC 2014b), CH_4 has a total atmospheric lifetime

*A smaller lifetime range cannot be constrained for CO_2 as different removal processes have different rates of uptake.

of 9.1 ± 0.9(1σ) yr as reported in the Sixth IPCC report (Masson-Delmotte et al. 2021) and a tropospheric lifetime of 9.7 ± 1.1(1σ) yr (Masson-Delmotte et al. 2021). Therefore an effective way for mitigating some of the short-term impacts of climate change would be to drastically reduce methane emissions on a global scale (Ganesan et al. 2019; Nisbet et al. 2020). A significant reduction in CH_4 emissions has the potential of keeping us on a path where the global temperature change does not rise above 2^oC by 2100 (Nisbet et al. 2020). However, we do not have a complete understanding of the global methane budget (Lan et al. 2021; Saunois et al. 2016; Saunois et al. 2020; Kirschke et al. 2013). Trends in the atmospheric concentrations of the hydroxyl radical (OH) - the primary sink of atmospheric CH_4 - which oxidises CH_4 in the troposphere and stratosphere, are indirectly determined using measurements of CH_3CCl_3 (methyl chloroform) (e.g. Prather et al. 2012; giving an observational tropospheric methane lifetime of 12 ± 1 years) or from chemical transport models (e.g. Voulgarakis et al. 2013; finding a total atmospheric CH_4 lifetime of 8.2 (6.4-9.2) yr and tropospheric CH_4 lifetime of 9.8 ± 1.6 yr for the year 2000). The constraint on the atmospheric methane lifetime introduces a large uncertainty into the global methane budget. Similarly, CH_4 emissions from wetlands are observed to be highly-varied with reported emissions ranging 80 Tg CH_4 yr^{-1} (Saunois et al. 2020). This also contributes to large uncertainties in the global CH_4 budget, especially when wetland emissions are upscaled (Lan et al. 2021). Most importantly, however, is that there are parts of the world (the Tropics, South America, Africa) that are lacking high-quality CH_4 measurements. Atmospheric measurements in these places are needed to reduce the uncertainty in global and regional scale methane emission budgets (Nisbet et al. 2020).

2.2 Quantifying methane emissions: top-down vs. bottom-up

Approaches for quantifying CH_4 emissions follow either a "top-down" or a "bottom-up" methodology. A top-down approach makes use of atmospheric measurements and has the advantage of capturing seasonal changes, unexpected pollution events and integrating multiple sources from across a region of interest (Nisbet and Weiss 2010) but is limited in distinguishing between different sources (Nisbet and Weiss 2010; Townsend-Small et al. 2012). Advances in laser-spectroscopy instruments (Rigby et al. 2012; Röckmann et al. 2016; Rennick et al. 2021), the expansion of atmospheric measurement networks (Lunt et al. 2021a) and use of isotopic measurements to characterise sources of CH_4 (Zazzeri et al. 2017) have contributed to improving the top-down CH_4 emissions constraint.

A bottom-up approach uses emission rates of different CH_4 sources and statistical activity data to estimate CH_4 emissions across a region of interest (Crippa et al. 2018). Emission rates (or factors) are usually calculated

from measurements that are assumed to be representative of CH_4 emissions from different sources across a certain region. Activity statistics that provide spatial data on, for example, population density or vehicle density, are used to upscale CH_4 emissions across a region of interest (Ricardo Energy & Environment 2019). Some emission inventories provide spatially resolved emissions data at national and global scales for different source sectors (e.g. waste, transport). Compared to a top-down approach, the spatial distribution of emissions in a bottom-up inventory are typically more accurate but the magnitude of emissions is less precise (Nisbet and Weiss 2010). Emission uncertainties in bottom-up estimates are typically statistical in nature and attempt to capture the extent emission rates are representative of a particular region and the accuracy of the data extrapolation across a region of interest (Solazzo et al. 2021).

Discrepancies between top-down and bottom-up CH_4 emissions exist on both a global and regional scale. Global CH_4 emissions between 2000-2009 in the first global CH_4 budget (Saunois et al. 2016) had mean top-down bottom-up differences of 167 (48-295) Tg CH_4 yr^{-1}. This discrepancy was reduced to 156 (42-282) Tg CH_4 yr^{-1} in the second global CH_4 budget 2000-2009 estimate (Saunois et al. 2020), which reported average anthropogenic top-down bottom-up emission differences of $\sim 2(9-11)$ Tg CH_4 yr^{-1}. Reconciling top-down bottom-up differences is an ongoing challenge and integrating these two approaches is a primary objective within the atmospheric science community (Saunois et al. 2016; Kirschke et al. 2013).

2.3 Atmospheric methane sources

Methane is emitted by a range of anthropogenic and natural sources (Fig. 2.1). Waste emissions and agricultural emissions, including those from ruminant livestock, manure management and rice cultivation, are globally the largest source of anthropogenic emissions comprising $28\% - 38\%$ of total emissions (Saunois et al. 2020). Fossil fuel CH_4 emissions account for approximately $17\% - 20\%$ of anthropogenic emissions (Saunois et al. 2020, Fig. 2.1) and includes emissions from the oil and gas industry, coal mining and transport sector. Wetlands are regarded as the largest natural source of CH_4 emissions accounting for $20\% - 31\%$ of total emissions (Saunois et al. 2020). Other natural sources of methane include emissions from freshwaters, wild animals, termites, permafrost soils and geological seeping of fossil methane, which generally form a smaller proportion of CH_4 emissions but have large ranges reported in the literature (Saunois et al. 2020).

Sources of methane emissions are also categorised as being biogenic, thermogenic or pyrogenic in origin (Saunois et al. 2016; Kirschke et al. 2013). Methane emissions from wetlands, rice cultivation, ruminant

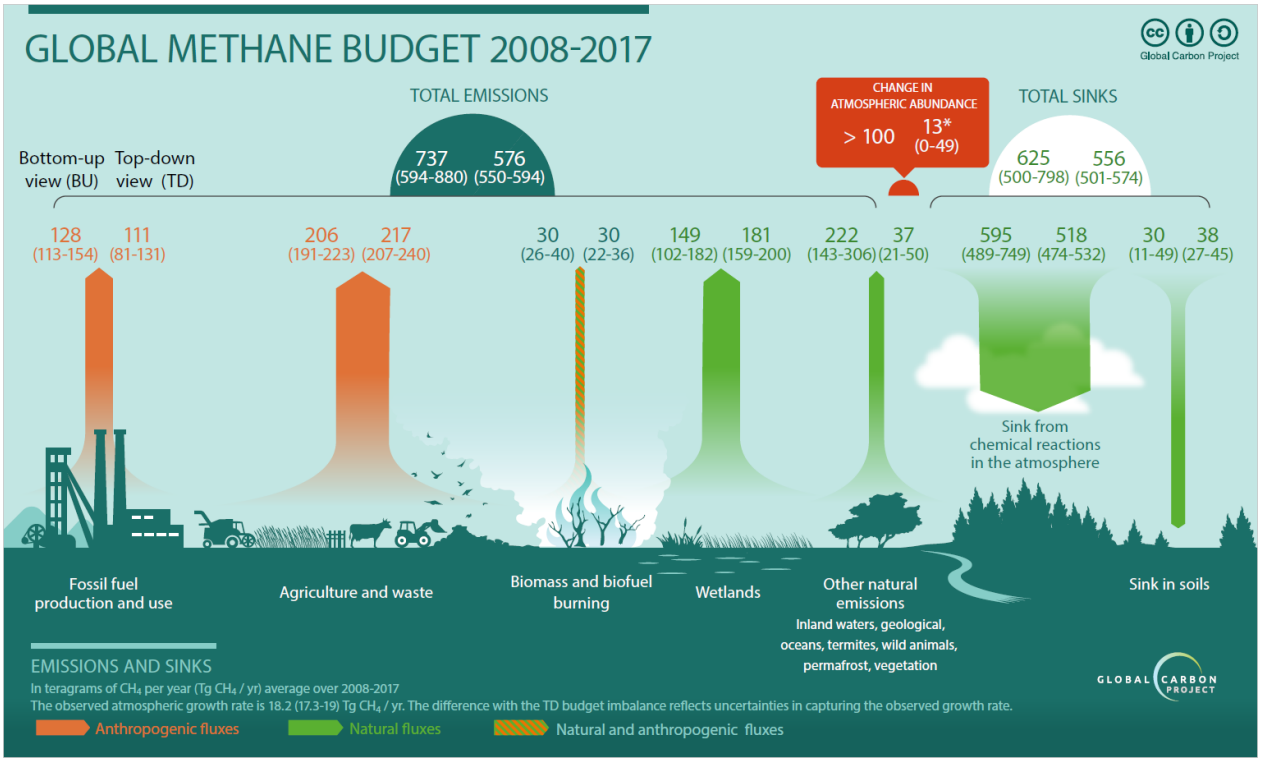


Figure 2.1: Global methane budget for the 2008–2017 decade. Both bottom-up (left) and top-down (right) estimates (Tg CH_4 yr^{-1}) are provided for each emission and sink category, as well as for total emissions and total sinks. Biomass and biofuel burning emissions are depicted here as both natural and anthropogenic emissions while they are fully included in anthropogenic emissions in the budget tables. Figure and caption from Saunois et al. (2020).

animals and landfills are all considered biogenic sources. Fossil fuel methane sources are spread between thermogenic (e.g. coal mining activity) and pyrogenic sources. Pyrogenic sources emit methane as a result of the incomplete combustion of biomass material, biofuels and fossil fuels (Sherwood et al. 2017; Saunois et al. 2020).

Methane emissions from different source sectors are estimated through a range of top-down and bottom-up methodologies. Large uncertainties are reported in global emission estimates aggregated for five different CH_4 source sectors (Fig. 2.2; Saunois et al. 2016). Anthropogenic fossil fuel and agriculture-waste sources have large reported emission ranges with mean bottom-up top-down values differing by 17 Tg CH_4 yr^{-1} and 11 Tg CH_4 yr^{-1}, respectively (Fig. 2.1; Saunois et al. 2020). In contrast, top-down bottom-up estimates of biomass burning CH_4 are in good agreement having the same mean values and similar reported ranges (Fig. 2.1, 2.2)

Aquatic CH_4 emissions from non-wetland sources contribute to the large range of reported emissions for "other

natural" sources (Fig. 2.2) and are poorly constrained leading to the largest differences between top-down bottom-up CH_4 emissions estimates (Saunois et al. 2020; Rosentreter et al. 2021).

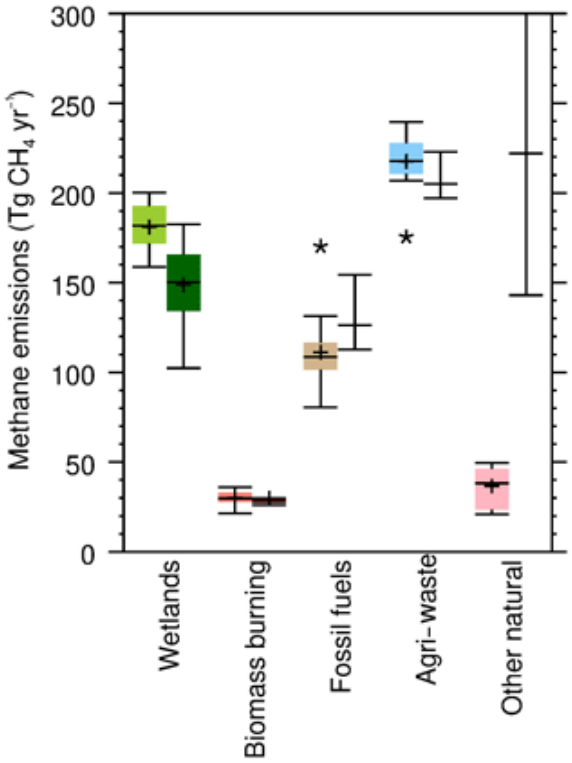


Figure 2.2: Methane global emissions from the five broad categories for the 2008–2017 decade for top-down inversion models (left light coloured box plots, Tg CH_4 yr^{-1}) and for bottom-up models and inventories (right dark coloured box plots). Median value and first and third quartiles are presented in the boxes. The whiskers represent the minimum and maximum values when suspected outliers are removed. Suspected outliers are marked with stars when they exist. Bottom-up quartiles are not available for bottom-up estimates, except for wetland emissions. Mean values are represented with "+" symbols. Figure and caption (adapted) from Saunois et al. (2020).

2.4 Atmospheric methane sinks

Any process that removes atmospheric CH_4 is considered a CH_4 sink. The primary CH_4 sink is oxidation with hydroxyl radicals (OH) in the troposphere and stratosphere, which each year removes an amount equivalent to $\sim$ 90% of CH_4 emissions (Ciais et al. 2013). Methane's reaction with OH produces methyl radicals and water vapour, which can lead to a net production of ozone under one dominant chemical pathway (e.g. Holloway and Wayne 2010). The tropospheric lifetime of CH_4 is $9.7 \pm 1.1 (1\sigma)$ yr (Masson-Delmotte et al. 2021). Chemical

transport models suggest a range of magnitudes and variability of OH concentrations in the atmosphere (Voulgarakis et al. 2013; Rigby et al. 2017) but concentrations are difficult to constrain with atmospheric measurements as the OH lifetime is short (Dalsøren and Isaksen 2006). Observations of methyl chloroform (CH_3CCl_3), which also reacts with tropospheric OH, have been used to indirectly constrain atmospheric concentrations of OH (Lovelock 1977; Prinn et al. 2001; Prinn et al. 2005; Prather et al. 2012).

Minor sinks of CH_4 include uptake by soils (e.g. by methanotrophic bacteria) which removes between 9 Tg CH_4 yr^{-1} to 47 Tg CH_4 yr^{-1} giving CH_4 an average lifetime of 160 years; photochemical destruction in the stratosphere (e.g. chlorine radicals and O(1D); Shallcross et al. 2007) gives methane an average lifetime of 120 years; and oxidation by chlorine radicals in the marine boundary layer giving an average lifetime of 150-years (Rigby et al. 2017). Methane lifetimes are added in parallel resulting in a total atmospheric CH_4 lifetime of $9.1 \pm 0.9(1\sigma)$ yr (assuming a static* tropospheric lifetime of 9.6 years). Carbon capture technologies for CH_4 are significantly underdeveloped in comparison to CO_2 making it unlikely for an anthropogenic sink to contribute to the removal of atmospheric CH_4 in the near-future (Abernethy et al. 2021; Jackson et al. 2021).

2.5 Atmospheric methane trends in the UK

Since 1990, annual bottom-up anthropogenic CH_4 emissions have been reported in the UK National Atmospheric Emissions Inventory (NAEI) (Fig. 2.3; Ricardo Energy & Environment 2019). Agricultural and waste emissions have consistently been reported as the largest sources of CH_4 emissions in the UK, comprising $\sim$ 47% and $\sim$ 32% in the 2019 (most recent) NAEI, respectively (Ricardo Energy & Environment 2019). Methane emissions from the energy sector ($\sim$ 13%) and anthropogenic land-use, land use change and forestry sector ($\sim$ 8%) make up the rest of the NAEI methane budget (Fig. 2.3). Natural sources of methane emissions in the UK are much smaller than UK anthropogenic emissions (Ganesan et al. 2015) and are not reported in NAEI. Specific natural CH_4 emissions for the UK can be estimated from other bottom-up emission inventories (e.g. wetland CH_4 emissions are captured in the global WetCHARTs inventory, Bloom et al. 2017).

Figure 2.3 shows a steady decline in anthropogenic CH_4 emissions from 1990 to c.2015 after which UK CH_4 emissions plateau. Large reductions in the waste and fugitive fossil CH_4 emissions are shown to be the main drivers of these decreases (Fig. 2.3), whereas agricultural methane emissions have remained approximately constant since 1990. The 2008 UK Climate Change Act legally committed the UK to reducing its greenhouse

*Not accounting for chemical relaxation times (Palmer et al. 2021).

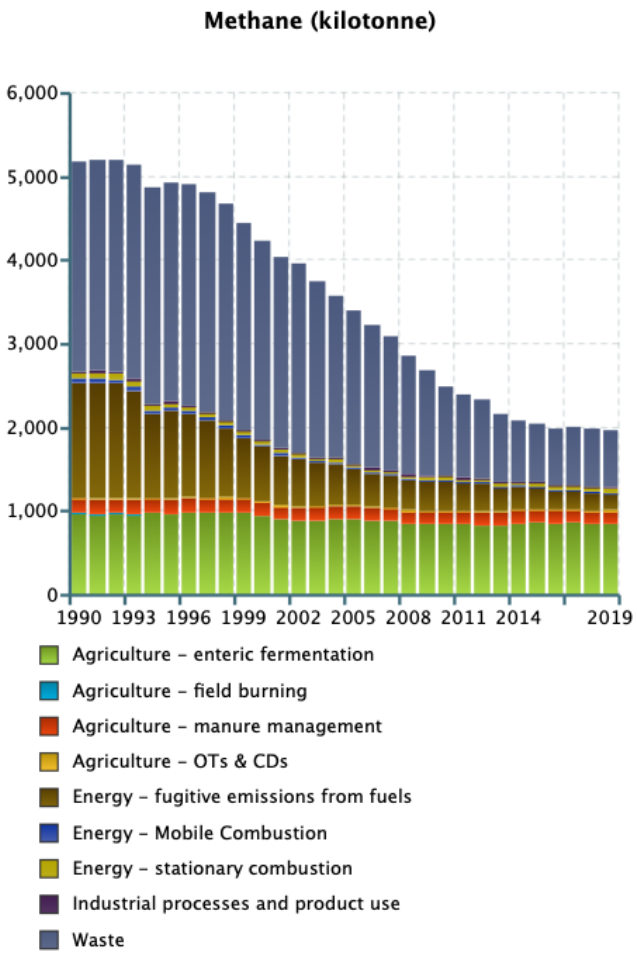


Figure 2.3: Trends in UK methane emissions by source type as reported in the NAEI. Figure from Ricardo Energy & Environment (2019).

gas emissions by at least 80% below 1990 levels by 2050, with an interim target of 34% below 1990 levels by 2020 (UK Government 2008; Shepheard 2020). Emissions of 2176 kt CH_4 are reported for 2019, which is $\sim$ 60% below 1990 emissions of 5376 kt CH_4. However, methane emissions are only $\sim$ 11% of the UK's CO_2 equivalent emissions with CO_2 emissions accounting for $\sim$ 81% and the remaining 8% are from N_2O and fluorinated gases (Palmer et al. 2018). For completeness, CO_2 emissions for 2019 are 40% below 1990 levels (Ricardo Energy & Environment 2019) suggesting the UK has exceeded its 2020 interim target. But how confident are we that the bottom-up NAEI CH_4 emissions for the UK are accurate and that UK emission reduction targets have been met and are on track?

Atmospheric CH_4 measurements have be used to independently verify bottom-up emissions and provide addi-

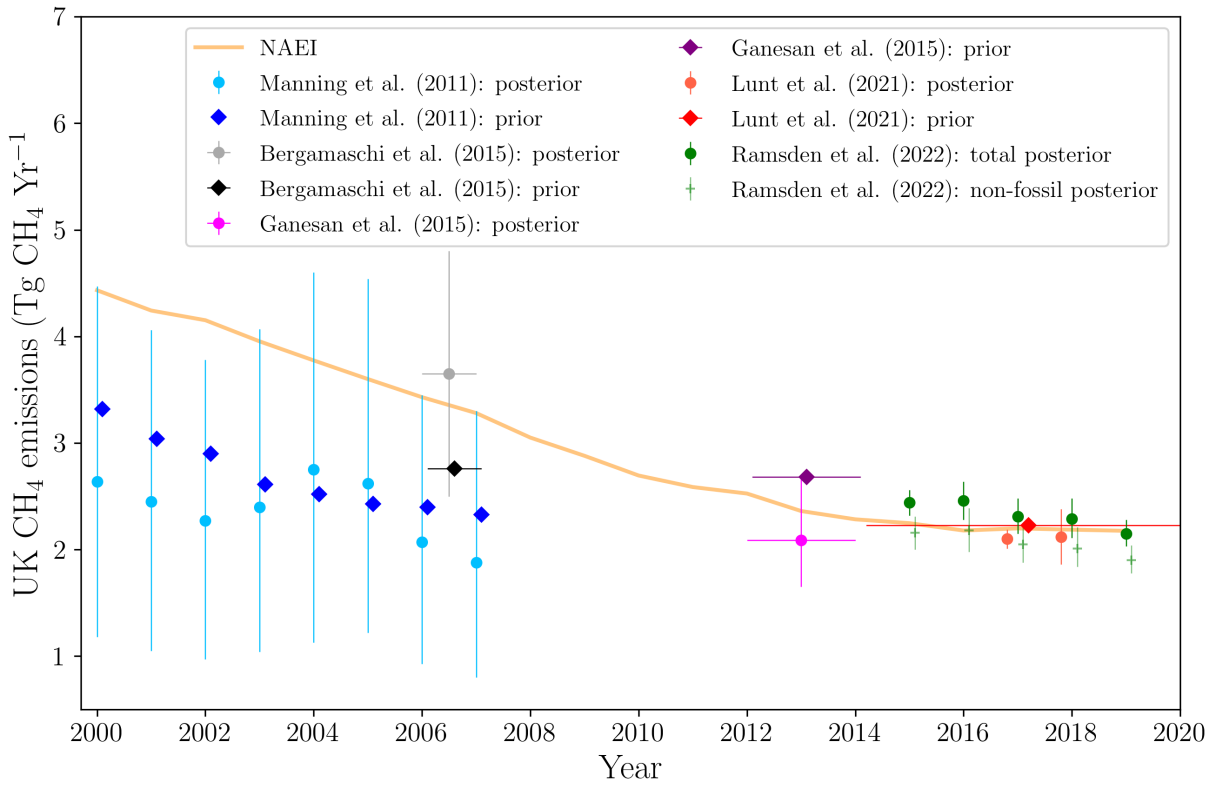


Figure 2.4: Time-series of UK prior and posterior CH_4 emissions reported in the literature. Error bars represent 5th-95th percentile range and markers denote median values except for Lunt et al. (2021a) where the mean and 1σ standard deviation are shown and Bergamaschi et al. (2015) which shows the range of posterior estimates. Prior emissions are denoted by diamonds and posterior emissions by circles. Prior emissions were not reported in Ramsden et al. (2022). Horizontal error bars denote the period for which the reported value is averaged over. Annual NAEI CH_4 emissions are shown by the orange line.

tional constraints on the spatial and sectoral distributions of CH_4 emissions in the UK. Since 1991, flask-based measurements of atmospheric methane concentrations have been made at the Mace Head (MHD) atmospheric station on the west coast of Ireland. Methane in the air arriving at MHD from over the Atlantic Ocean (that is also not influenced by local sources) is considered representative of the Northern Hemispheric time-varying background as regional emissions are not yet fully-mixed on the hemisphere scale (i.e. above background enhancements or perturbations). Atmospheric methane measurements from MHD have contributed to a range of global and regional studies (e.g. Bergamaschi et al. 2005; Lu et al. 2021; Stavert et al. 2022; Palmer et al. 2018) including some focused on the UK.

Table 2.1: Summary of UK methane inversion studies (2000-2019). Posterior emission values in brackets denote the 5th and 95th quartile values, except for Lunt et al. (2016) which shows the 1σ value.

Year(s)	Posterior emissions (Tg CH_4 yr^{-1})	Prior emissions (Tg CH_4 yr^{-1})	Posterior-Prior (Tg CH_4 yr^{-1})	Inversion method	Number of stations	Prior emission source	Reference
2000	2.64 (1.18-4.47)	3.32	-0.68	InTEM	1	2009 submitted UNFCCC emissions	Manning et al. 2011
2001	2.45 (1.03-4.06)	3.04	-0.59	InTEM	1	2009 submitted UNFCCC emissions	Manning et al. 2011
2002	2.27 (0.97-3.78)	2.90	-0.63	InTEM	1	2009 submitted UNFCCC emissions	Manning et al. 2011
2003	2.40 (1.04-4.07)	2.61	-0.21	InTEM	1	2009 submitted UNFCCC emissions	Manning et al. 2011
2004	2.75 (1.13-4.60)	2.52	+0.23	InTEM	1	2009 submitted UNFCCC emissions	Manning et al. 2011
2005	2.62 (1.22-4.54)	2.43	+0.19	InTEM	1	2009 submitted UNFCCC emissions	Manning et al. 2011
2006	2.07 (0.93-3.45)	2.40	-0.33	InTEM	1	2009 submitted UNFCCC emissions	Manning et al. 2011
2007	1.88 (0.80-3.30)	2.33	-0.45	InTEM	1	2009 submitted UNFCCC emissions	Manning et al. 2011
2006-2007	2.50-4.80	2.76	-2.6 to +2.0	4 Inverse models	10 (1 in UK)	UNFCCC inventory	Bergamaschi et al. 2015
2012-2014	2.09 (1.65-2.67)	2.68	-0.59	Bayesian hierarchical	4	NAEI scaled to UNFCCC values	Ganesan et al. 2015
Mar. 2014	2.28 (2.04-2.52)	2.8	-0.52	MCMC[a]	4	EDGAR	Lunt et al. 2016
2015	2.44 (2.32-2.56)	-[b]	-	Ethane tracer Bayesian hierarchical	5	2015 UK GHG model; Levy 2020	Ramsden et al. 2022
2016	2.46 (2.28-2.64)	-[b]	-	Ethane tracer Bayesian hierarchical	5	2015 UK GHG model; Levy 2020	Ramsden et al. 2022
2017	2.31 (2.16-2.47)	-[b]	-	Ethane tracer Bayesian hierarchical	5	2015 UK GHG model; Levy 2020	Ramsden et al. 2022
2018	2.29 (2.11-2.48)	-[b]	-	Ethane tracer Bayesian hierarchical	5	2015 UK GHG model; Levy 2020	Ramsden et al. 2022
2019	2.15 (2.03-2.28)	-[b]	-	Ethane tracer Bayesian hierarchical	5	2015 UK GHG model; Levy 2020	Ramsden et al. 2022

[a] Reversible-jump Markov chain monte carlo.
[b] Prior values not reported in Ramsden et al. (2022).

Manning et al. (2011) used CH_4 mole fraction observations from MHD in the UK Met Office Bayesian inversion model: Inversion Technique for Emission Modelling (InTEM) to verify UK emissions reported to the UNFCCC from 1990-2007 by calculating yearly posterior CH_4 emissions for this period. Posterior and prior UK methane emissions for 2000-2007 are shown in Fig. 2.4 and Table 2.1. The 5th-95th percentile range (shown by the error bars) is large for the posterior emissions, which could be a result of using one measurement station (MHD) in the inversion. Manning et al. (2011) find an average posterior-prior difference of -0.31 Tg CH_4 yr^{-1} for 2000-2007, with posterior-prior differences largest for the year 2000 and smallest for the year 2005 (Table 2.1).

In a similar approach, Bergamaschi et al. (2015) used methane measurements from 10 atmospheric measurement stations across Europe in four different inversion modelling schemes that used different atmospheric transport models. Posterior methane emissions of 2.5 Tg CH_4 yr^{-1} to 4.8 Tg CH_4 yr^{-1} were calculated for the UK and Republic of Ireland between 2006-2007 (Bergamaschi et al. 2015; Table 2.1). The average UK and Republic of Ireland posterior CH_4 emission from the different inversion models used by Bergamaschi et al. (2015) is denoted by the marker on Fig. 2.4 and the ends of the vertical error bar represent the range of posterior emission values. Posterior methane emissions that used the same atmospheric transport model as Manning et al. (2011) in the inversion were $\sim$ 0.5 Tg CH_4 yr^{-1} smaller than the other posterior emissions calculated for the UK and Republic of Ireland by Bergamaschi et al. (2015).

In 2012, three tall-tower atmospheric measurement stations in the UK became operational (Fig. 2.5). Together, Angus (TTA), Tacolneston (TAC), Ridge Hill (RGL) and MHD stations formed the UK Deriving Emissions to Climate Change (DECC) network. In situ measurements of atmospheric CO_2, CH_4, N_2O and other trace gases being made at these sites provide better measurement coverage for the UK. The network was briefly expanded to include the Bilsdale (BSD) tall-tower site, which would later replace TTA from September 2015. Alongside the onset of these atmospheric measurements was the establishment of the Greenhouse Gas UK and Global Emissions (GAUGE) project designed to use atmospheric data to estimate the magnitude, distribution and uncertainties of UK GHGs (Palmer et al. 2018; Rigby et al. 2018). With a measurement network now established in the UK, atmospheric measurements from these additional sites improved the top-down constraint of UK methane emission estimates, which could be used to better evaluate the NAEI bottom-up methodology through independent assessment. From 2012 onwards top-down bottom-up discrepancies of CH_4 emissions in the UK are much smaller (Fig. 2.6).

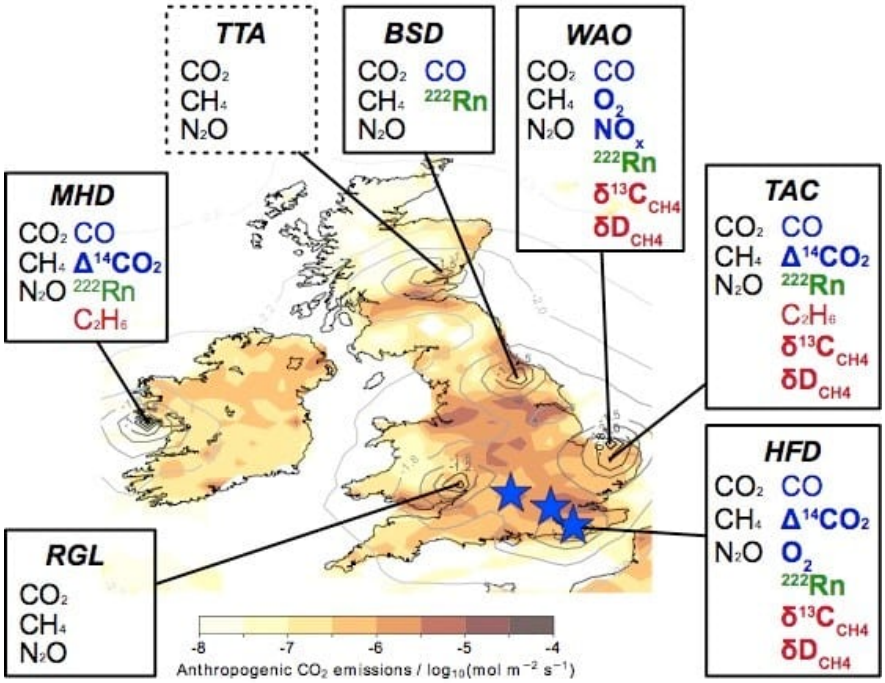


Figure 2.5: Greenhouse gas measurement sites in the UK and Republic of Ireland along with the primary atmospheric gases and isotopes being measured. Figure courtesy of DARE-UK (dareuk.blogs.bristol.ac.uk).

Ganesan et al. (2015) were the first to use atmospheric CH_4 mole fraction measurements from the UK-DECC network to evaluate the NAEI CH_4 emissions. Measurements from TTA, TAC, RGL, and MHD were used in a hierarchical Bayesian inverse framework that calculated monthly UK CH_4 posterior emission estimates from August 2012 to August 2014. A median posterior of 2.09 (1.65-2.67) Tg CH_4 yr^{-1} is reported for this period which is smaller than the prior NAEI CH_4 emissions estimate (Table 2.1, Fig. 2.4). Ganesan et al. (2015) hypothesised that agricultural CH_4 emissions were overestimated in parts of the UK in NAEI.

In a recent study, Lunt et al. (2021a) used two different inversion modelling frameworks with methane mole fraction measurements from the extended UK DECC network (UK DECC + observations from the Heathfield (HFD) station south of London; Fig. 2.5), aircraft and ships to compute the posterior total and sectoral CH_4 emissions for 2013-2020 over the UK. There is good agreement between the mean posterior emissions ($2.10 \pm 0.09 (1\sigma)$ Tg CH_4 yr^{-1} and $2.12 \pm 0.26 (1\sigma)$ Tg CH_4 yr^{-1}; Fig. 2.4) and the UK NAEI emissions for this period (2.23 Tg CH_4 yr^{-1}; Fig. 2.4). A negative trend of 2% – 3% is captured in the posterior emissions,

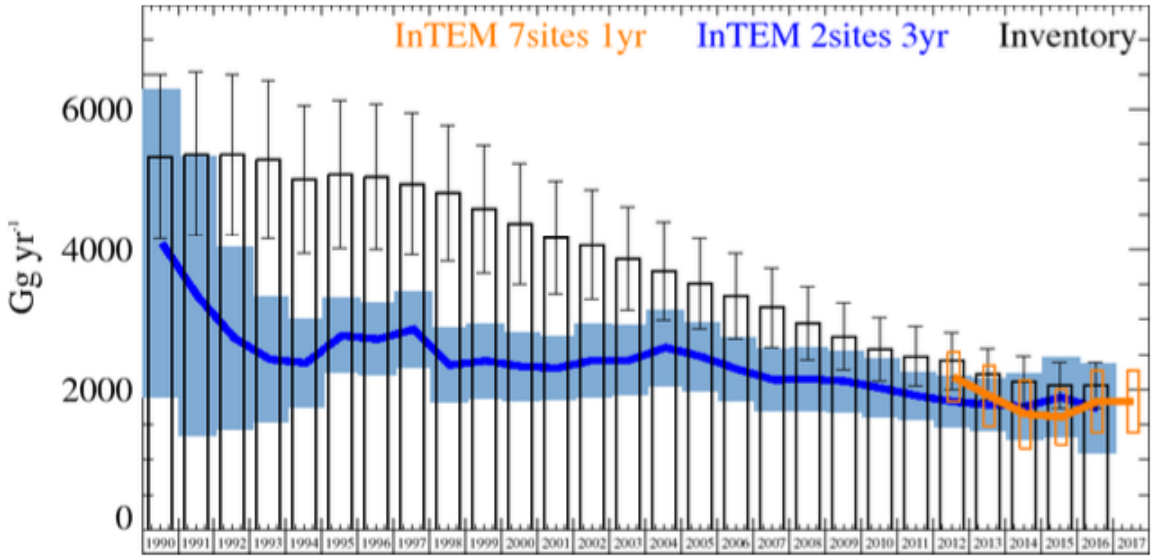


Figure 2.6: Methane UK emission estimates from the UNFCCC inventory (black) and InTEM (inverion model estimates) with global meteorology: 3-year Mace Head station and Cabauw station emissions (blue) and 12-month UK network + Cabauw station (orange). Uncertainty bars represent 1 standard deviation. Figure and caption (adapted) from Rigby et al. (2018).

which is comparable to the ~ 1% decrease in NAEI CH_4 emissions over the same period. Larger posterior emission uncertainties are also obtained when two measurement sites are used in the inversion compared to when the full UK DECC network is used. This could partially explain the larger uncertainty of posterior emissions in early inversion studies of UK CH_4 (Fig. 2.6) and highlights the benefit of having a network of measurement sites in the UK (Lunt et al. 2021a).

Posterior emissions were also calculated for different CH_4 source sectors in Lunt et al. (2021a) where the relative source apportionment of CH_4 emissions is assumed correct in the prior (NAEI) and that it is only the emission magnitudes that need adjusting. Although Lunt et al. (2021a) find waste sector emissions are driving this negative trend the underlying assumption that the methane emission apportionment is accurate is potentially problematic for several reasons. Firstly, the posterior source apportionment is entirely based on the bottom-up inventory emissions source apportionment. The observations used do not add information on the emissions from specific sources. Secondly, diffuse emissions such as those from the agricultural sector could have spatial distributions that differ from what is reported in the bottom-up emission inventory. Thirdly, for sources that are co-located emissions for specific sources could be misattributed or underreported in the inventory. For example, atmospheric methane measurements in urban environments often find natural gas

emissions from leaks in the distribution pipes are underestimated in the inventories (Brandt et al. 2014; Plant et al. 2022; McKain et al. 2015; Sargent et al. 2021).

To constrain the CH_4 emissions of specific sources additional tracer measurements are needed, which could also be incorporated into a methane inversion or other modelling framework. Although there are in situ atmospheric measurements of ^{13}C in methane (that can be used to characterise sources of CH_4) at HFD and TAC these data have yet to be reported in the literature. Non-isotopic tracers of CH_4 emissions have also been used to identify emissions from specific source sectors. For example, atmospheric ethane measurements have been used as a tracer of fossil CH_4 emissions as ethane is often co-emitted during the extraction of coal, oil and natural gas and during the transport/distribution of natural gas (Helmig et al. 2016; Hausmann et al. 2016; Assan et al. 2018). Specific ratios of ethane-to-methane have been observed for different fossil CH_4 sources around the globe. At a regional scale, changes in the ethane:methane ratio during large enhancements of CH_4 concentrations can provide additional information about the source of those elevated concentrations (e.g. Helmig et al. 2016). Atmospheric ethane measurements were recently incorporated in a methane inversion framework to estimate posterior CH_4 emissions for fossil and non-fossil CH_4 sources in the UK (Ramsden et al. 2022).

Using a joint methane-ethane hierarchical Bayesian inversion framework Ramsden et al. (2022) quantified posterior CH_4 emissions for fossil and non-fossil sources in the UK for 2015-2019 (Table 2.1, Fig. 2.4). Total emissions are in good agreement with the posterior emissions from Lunt et al. (2021a) for this period (Fig. 2.4) and around 11% – 13% of posterior emissions in the methane-ethane inversion are attributed to fossil CH_4. Concurrent atmospheric ethane-methane measurements are better suited for environments where the proportion of fossil fuel CH_4 (i.e. the fossil-fraction) is higher. Atmospheric ethane measurements cannot be used to distinguish between different biogenic sources, such as waste and agriculture CH_4, which are the largest sources of methane emissions in the UK. Therefore to distinguish between different biogenic methane sources other non-isotopic or isotopic tracer measurements are needed.

2.6 Isotopic tracer approaches for attributing sources of CH_4 emissions

2.6.1 Overview of carbon-13 isotopic notation

^{12}C makes up 98.89% of the carbon budget, with most of the remaining 1.11% in the form of ^{13}C (Valley and Cole 2019). On a global scale, these relative abundances remain unchanged. However, different physicochemical and biological reactions can lead to preferential partitioning of carbon isotopes thus changing

the carbon isotope ratios in different carbon pools but only by a few thousandths (i.e a few ‰) (Roy-Barman and Jeandel 2016). Variations in isotopic abundances are generally reported as the relative deviation (δ) of the isotopic ratio in a sample (R_{sample}) with respect to a standard value (R_{standard}), where for $^{13}C/^{12}C$ in methane

$$\delta^{13}\text{CH}_{4,\text{sample}} = \frac{R_{\text{sample}}}{R_{\text{standard}}} - 1 = \frac{(^{13}C/^{12}C)_{\text{sample}}}{(^{13}C/^{12}C)_{\text{standard}}} - 1. \tag{2.1}$$

δ is usually expressed in ‰ and the Vienna Pee Dee belemnite (VPBD) fossil is used as the universal $^{13}C/^{12}C$ standard, which has a value of $^{13}C/^{12}C$=0.0112372 (Umezawa et al. 2017).

2.6.2 Using $\delta^{13}\text{CH}_4$ to understand sources of CH_4

Isotopic fractionation results in different sources of methane have different $^{13}C/^{12}C$ ratios. Fossil fuel sources of CH_4 are more ^{13}C-enriched and isotopically heavier than biogenic CH_4 sources, which are ^{13}C-depleted. In this way methane sources can be characterised by their different $\delta^{13}CH_4$ signatures. The global average $\delta^{13}CH_4$ signature for: fossil fuel CH_4 is around -45‰, around -60‰ for biogenic CH_4 and around -25‰ for biomass burning CH_4 (Sherwood et al. 2017).

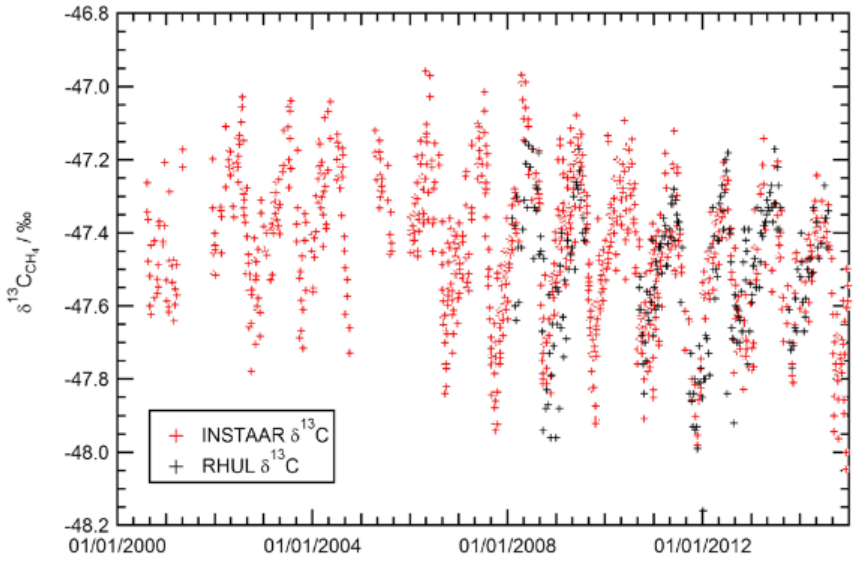


Figure 2.7: $\delta^{13}CH_4$ isotope measurements in discrete samples collected from Alert, Canada. Isotopic measurements from NOAA-INSTAR and Royal Holloway, University of London (RHUL). Figure and caption (adapted) from Nisbet et al. (2016).

The global $\delta^{13}CH_4$ background value is currently close to -47.5‰ and exhibits clear seasonal cycles (Dlugokencky 2022). Seasonal cycling of methane mole fractions are driven by the production of OH in the

troposphere, which is larger during the summer months and leads to seasonal lows of CH_4 concentrations. Kinetic fractionation means $^{12}CH_4$ is preferentially oxidised by OH over $^{13}CH_4$ (Valley and Cole 2019). This changes the isotopic $^{13}C/^{12}C$ ratio in the atmosphere, shifting $\delta^{13}CH_4$ towards more ^{13}C-enriched values (i.e. peaks) during the summer and towards less ^{13}C-enriched values (i.e. lows) during the winter (e.g. Fig. 2.7).

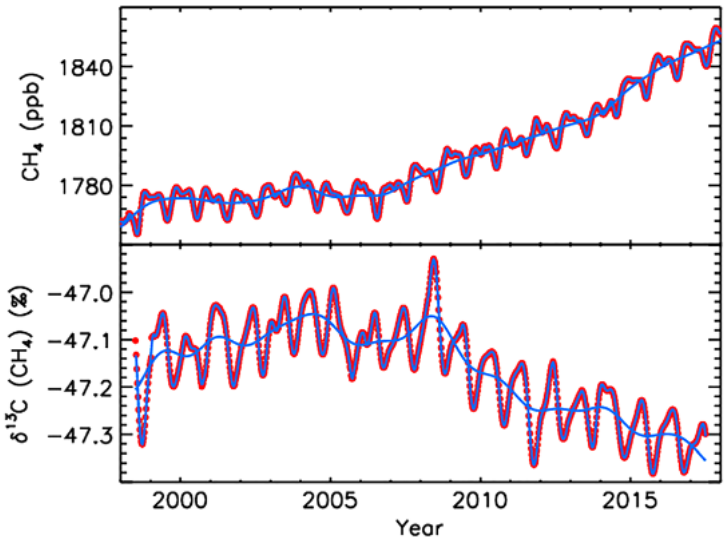


Figure 2.8: Atmospheric methane at Earth's surface in the remote marine troposphere. Upper panel shows globally averaged surface atmospheric CH_4 at weekly resolution (red and blue) and deseasonalised trend (blue), 2000-2017. Lower panel as above, but for globally averaged surface atmospheric $\delta^{13}CH_4$. Data from NOAA. The x-axis tick marks denote the 1st of January of the year indicated. Figure and caption (adapted) from Nisbet et al. (2019).

Changes in the proportion of fossil, biogenic and biomass burning methane emitted over time has resulted in gradual changes in the global atmospheric $\delta^{13}CH_4$ trend. Shifts in $\delta^{13}CH_4$ towards more negative values over time are suggestive of a larger proportion of biogenic emissions and shifts towards less negative values are suggestive of fossil and biomass burning emissions of CH_4, assuming there are not large changes in the $\delta^{13}CH_4$ source signatures (Nisbet et al. 2019). Changes in global $\delta^{13}CH_4$ towards more negative values could also indicate a decline in atmospheric OH (Rigby et al. 2017; Turner et al. 2017), which is one explanation that has been suggested for the large global increase in CH_4 concentrations since 2007 and the continuing negative trend of global atmospheric $\delta^{13}CH_4$ (Fig. 2.8; Nisbet et al. 2016; Nisbet et al. 2019). Other explanations for the large global increase in CH_4 concentrations and concurrent decline in $\delta^{13}CH_4$ include an increase in biogenic emissions with very negative $\delta^{13}CH_4$ signatures (Nisbet et al. 2016); or a rise in CH_4 emissions from

oil and natural gas with $\delta^{13}CH_4$ their signatures larger than -47‰ accompanied with a concurrent decline in biomass burning CH_4 emissions (Hausmann et al. 2016).

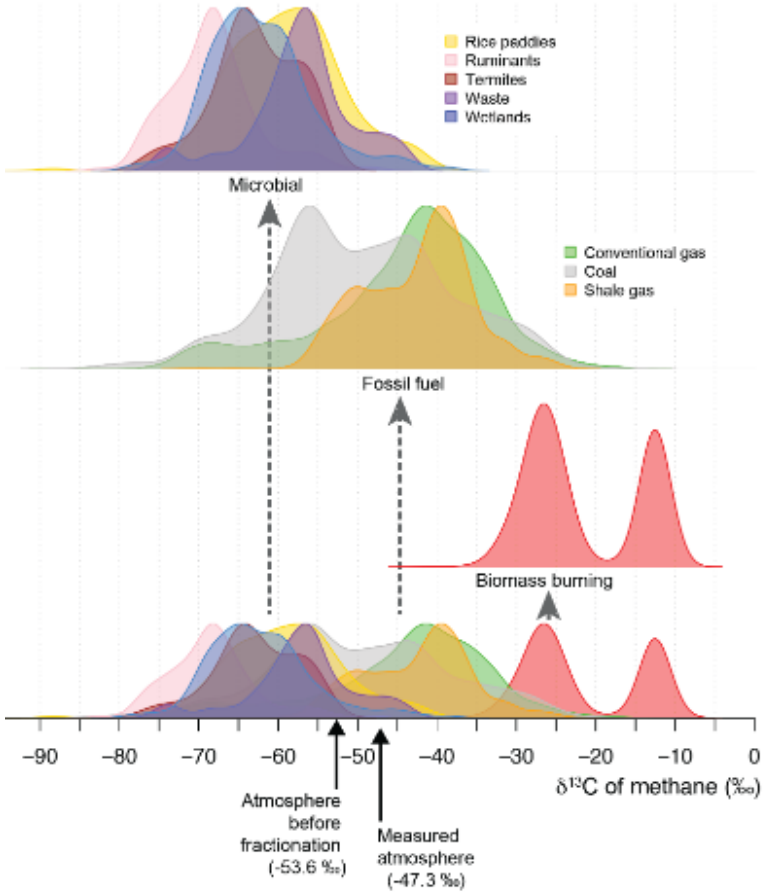


Figure 2.9: Normalised probability density distributions for the $\delta^{13}CH_4$ of microbial, fossil and biomass burning sources of methane. The flux-weighted average of all sources produces a mean atmospheric $\delta^{13}CH_4$ of −53.6‰, as inferred from measured atmospheric $\delta^{13}CH_4$ and isotopic fractionation associated with photochemical methane destruction. Figure and caption from Sherwood et al. (2017).

It is clear that interpreting global isotopic observations is complex, especially as it takes several decades for isotopic equilibrium to be reached (Tans 1997). Although $\delta^{13}CH_4$ signatures can guide our understanding of global and regional sources some $\delta^{13}CH_4$ signatures are reported with large ranges that can overlap with the $\delta^{13}CH_4$ signatures of other methane sources (Fig. 2.9). Some of these large reported ranges could be due to spatiotemporal variations in $\delta^{13}CH_4$ signatures (Feinberg et al. 2018). For example, the $\delta^{13}CH_4$ signature of ruminant CH_4 emissions varies depending on the proportion of C_3 and C_4 plants in their diet, which varies

depending on where livestock are in the world (Crutzen et al. 1986). As a result, ruminant animals have reported $\delta^{13}CH_4$ signatures between -50‰ and -74‰ (Sherwood et al. 2017). It is therefore preferable to use regional $\delta^{13}CH_4$ signatures, if available, for analysing $\delta^{13}CH_4$ measurements from regional scale campaigns (Feinberg et al. 2018). Recent estimates for $\delta^{13}CH_4$ signatures for CH_4 sources in the UK have been made by Zazzeri et al. (2015) and Zazzeri et al. (2017) (Table 2.2). These are further described and used in Chapter 4.

Table 2.2: $\delta^{13}CH_4$ signatures of UK methane sources based on measured values and literature review. 2013 NAEI emission inventories are provided without errors. Offshore refers to emissions from fossil fuels. Errors of measured isotopic values are within ±3‰. Table (reproduced) and caption from Zazzeri et al. (2017).

UK methane sources	2013 emissions kilotonne	Sector	Typical $\delta^{13}CH_4$ (‰)
Enteric fermentation	945	Agriculture	-66[a]
Landfills	696	Waste	-58[a]
Gas transmission and distribution	218	Offshore	-36[a]
Manure management	139	Agriculture	-58
Wastewater	134	Waste	-53[a]
Coal mining	64	Offshore	-45[a]
Industrial and domestic combustion	44	Combustion in energy production and transfer	-25
Road transport	2	Road transport	-20
Biomass burning	1	Agricultural burning	-28
UK total	2243		-58

[a]Indicates values that have been revised by Zazzeri et al. (2015).

Atmospheric measurements of $\delta^{13}CH_4$ and CH_4 mole fractions have been used for understanding sources of methane emissions at city-wide and regional scales (e.g. France et al. 2016; Warwick et al. 2016; Zazzeri et al. 2015; Townsend-Small et al. 2012). Observed enhancements of CH_4 mole fractions and concurrent $\delta^{13}CH_4$ data can be analysed using a Keeling plot (Keeling 1961) or Miller-Tans (Miller and Tans 2003) approach to infer the $\delta^{13}CH_4$ signature associated with the CH_4 enhancement event. Both methods assume mass balance of $^{12}CH_4$ and $^{13}CH_4$. For regional scale studies with timescales much less than the atmospheric CH_4 lifetime the atmospheric sink can be neglected (Graven et al. 2019).

In the Keeling plot approach, constant CH_4 and $\delta^{13}CH_4$ backgrounds are assumed and the $\delta^{13}CH_4$ signature due to CH_4 enhancements is inferred from the y-intercept of a linear regression of atmospheric $\delta^{13}CH_4$ against the inverse of CH_4 mole fractions (Pataki et al. 2003), which follows a linear relationship in the mass balance approach:

$$\begin{aligned} \delta_a &= C_{bg}(\delta_{bg} - \delta_s) \times \frac{1}{C_a} + \delta_s, \\ y &= m\,x + b, \end{aligned} \tag{2.2}$$

where δ_a are atmospheric $\delta^{13}CH_4$ values, C_a are atmospheric CH_4 mole fractions and δ_{bg} and δ_s are the atmospheric background and source signature $\delta^{13}CH_4$ values, respectively.

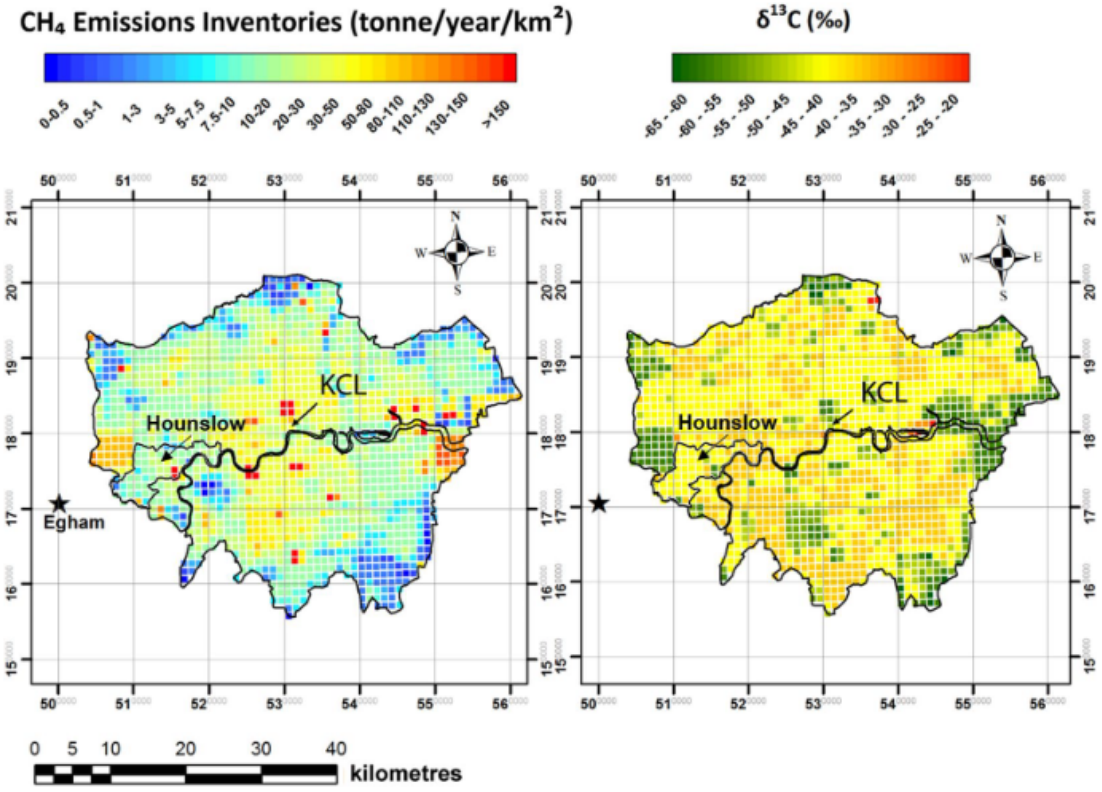


Figure 2.10: Emissions (a) and isotopic (b) map for London based on 2013 NAEI methane inventories. Emissions are provided in t CH_4 km^{-2} yr^{-1}. The star indicates Egham, where the Royal Holloway University of London is located. Most of the hotspots are associated with ^{13}C-depleted areas. The large area affected by high emissions on the east side of the London region includes biogenic methane sources, such as landfill sites and waste-water treatment plants. Figure and caption from Zazzeri et al. (2017).

When changes in the background are small in comparison to the span of the measurements the Keeling Plot

approach is suitable (Miller and Tans 2003). If this is not the case then the Miller-Tans approach (Miller and Tans 2003), which takes into account a varying background, should be used. The Miller-Tans approach infers the $\delta^{13}CH_4$ signature due to CH_4 enhancements from the gradient of a linear regression of $\delta_a C_a - \delta_{bg} C_{bg}$ (i.e. $^{13}CH_4$ enhancements) and $C_a - C_{bg}$ (i.e. $^{12}CH_4$ enhancements), which also follows a linear relationship:

$$\begin{aligned} \delta_a C_a - \delta_{bg} C_{bg} &= \delta_s (C_a - C_{bg}), \\ y &= m\, x (+b). \end{aligned} \tag{2.3}$$

The Miller-Tans approach, however, relies on having measurements of both CH_4 concentrations and $\delta^{13}CH_4$ that are representative of background/upwind values.

Multiple sources can contribute to observed CH_4 enhancements; particularly in areas where there are a range of sources that are co-located. The $\delta^{13}CH_4$ signatures of these CH_4 enhancements will reflect a weighted-average of those sources. For example, Zazzeri et al. (2017) found an average $\delta^{13}CH_4$ of -45.7±0.5(1σ)‰ for London. This is slightly more ^{13}C-enriched than the current $\delta^{13}CH_4$ global background but not ^{13}C-enriched enough to correspond to a purely fossil $\delta^{13}CH_4$ signature implying there is a mixture of biogenic, thermogenic and pyrogenic CH_4 sources present in London, most likely waste and natural gas CH_4. The mean London isotopic values measured by Zazzeri et al. (2017) was 2‰ higher than the $\delta^{13}CH_4$ value calculated using bottom-up NAEI emission estimates (Fig. 2.10) suggesting the methane source apportionment in the NAEI methane emission inventory needed revising for London (Zazzeri et al. 2017).

Previous $\delta^{13}CH_4$ measurements made in the UK have either been used to characterise $\delta^{13}CH_4$ signatures of specific sources (e.g. Zazzeri et al. 2015) or to analyse methane sources in short measurement campaigns targeted at places like London (e.g. Lowry et al. 2001; Zazzeri et al. 2017).

Atmospheric CH_4 observations from the Cabauw measurement station in the Netherlands have been previously used in inversion modelling studies to quantify CH_4 emissions (e.g. Bergamaschi et al. 2015). Hourly atmospheric $\delta^{13}CH_4$ measurements from November 2014 to January 2015 at Cabauw were made using laser spectrometer systems and were used to quantify regional sources of methane (Röckmann et al. 2016). Most of the $\delta^{13}CH_4$ signatures of CH_4 enhancements corresponded to ruminant emissions with a few events attributed to natural gas and landfill emissions. Röckmann et al. (2016) were able to demonstrate that hourly in situ measurements were effective for regional methane source attribution and monitoring. There is potential that the in situ, laser spectroscopy $\delta^{13}CH_4$ measurements being made at the Heathfield and Tacolneston tall-tower sites in the UK could be used to improve the constraint of UK CH_4 emissions from specific source sectors and

evaluate the source apportionment in emission inventories.

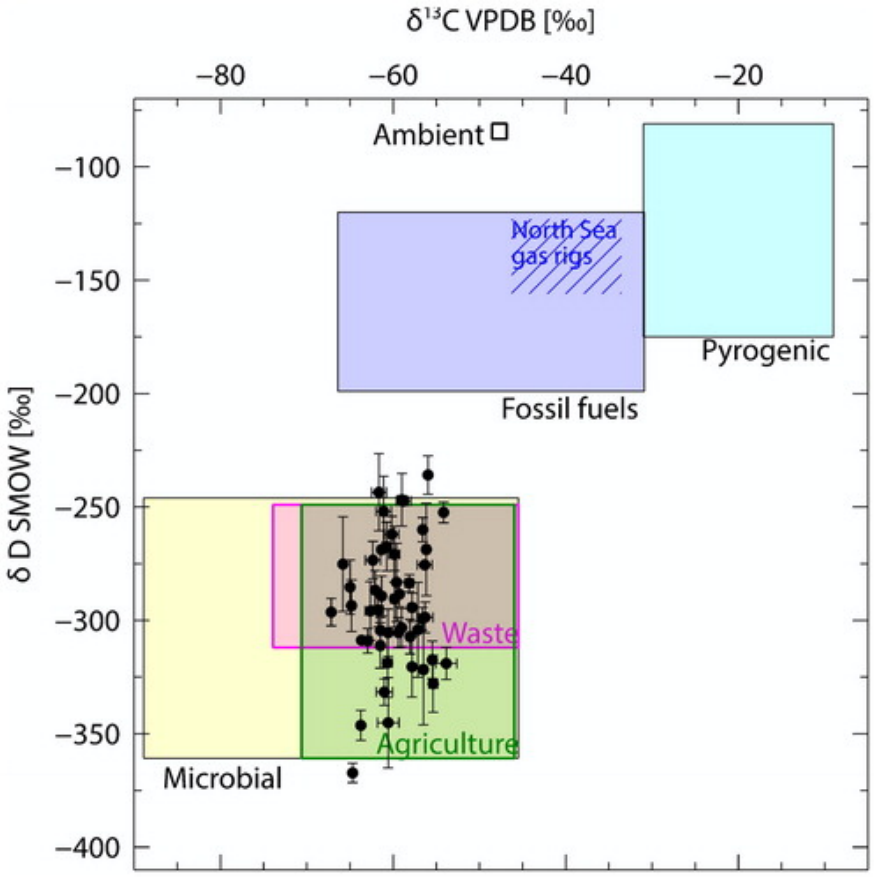


Figure 2.11: $\delta^{13}CH_4$ and δD source signatures derived with the Keeling plot approach (black dots). Coloured areas indicate typical isotopic signatures for CH_4. Figure and caption (adapted) from Menoud et al. (2020).

Additional gaseous or isotopic tracer measurements could improve the top-down constraint of different sources of methane emissions. Deuterated methane measurements (δD) have also been used for inferring CH_4 sources (e.g. Townsend-Small et al. 2012) and are becoming more common in lab setups (e.g. Rennick et al. 2021; Menoud et al. 2020; Röckmann et al. 2016) but similar to $\delta^{13}CH_4$ δD isotopic signatures have large uncertainties and overlapping signatures (Fig. 2.11; Menoud et al. 2020). Measurements of ^{14}C in methane, however, provide the primary constraint on fossil CH_4 emissions as fossil fuel sources are devoid of ^{14}C.

2.6.3 Overview of atmospheric carbon-14 and carbon-14 isotopic notation

Radiocarbon (^{14}C) is the only naturally occurring radioactive isotope of carbon and makes up around one part in a trillion of carbon atoms on Earth (Schuur et al. 2016). The interaction of cosmic rays with

atmospheric nitrogen in the stratosphere and upper troposphere produces ^{14}C atoms, which react to form $^{14}CO_2$ in the troposphere (Key 2001). Photosynthesis, respiration and physical processes (e.g. dissolution, transport, particulate deposition etc.) distributes $^{14}CO_2$ through different carbon pools in the Earth (Key 2001). Radiocarbon undergoes β^- decay with a half-life of 5700 ± 30 years (Roberts and Southon 2007), giving enough time for ^{14}C atoms to move through different parts of the global carbon cycle. The distribution of radiocarbon provides information on how long carbon resides in different carbon pools (Schuur et al. 2016).

The amount of radiocarbon in atmospheric methane can be determined in two ways. Firstly, by measuring the activity of the sample with a Geiger counter, or similar device. This requires a very large sample size (~ 1000 m^3; Levin et al. 1992) to obtain a ^{14}C signal above the background noise. The other approach uses accelerator mass spectrometry, where much smaller sample sizes are needed (~ $1-2$ m^3; Levin et al. 1992)and the amount of ^{14}C in a sample can be obtained much faster (Schuur et al. 2016). This approach is more commonly used in contemporary radiocarbon analyses. Whilst there are in situ laser spectrometers that can measure stable CO_2 and CH_4 isotopologues such instruments are not precise enough for atmospheric $^{14}CO_2$ or $^{14}CH_4$ measurements.

Radiocarbon notation

Similar to ^{13}C measurements, radiocarbon is reported as the ratio of $^{14}C/C$ with respect to a standard. To remove the fractionation effect, which is assumed to be twice that of ^{13}C, the sample is normalised to have a $\delta^{13}CH_4$ value of -25‰, which in terms of isotopic ratios:

$$\left.\frac{^{14}C}{C}\right|_{\text{sample,-25}} = \left.\frac{^{14}C}{C}\right|_{\text{sample}} \left(\frac{0.975}{1+\delta^{13}C/1000}\right)^2. \tag{2.4}$$

The term in parentheses corrects for fractionation. Atmospheric radiocarbon data is usually reported using $\Delta^{14}C$ notation (Stuiver and Polach 1977),

$$\Delta^{14}C = \left(\frac{\left.\frac{^{14}C}{C}\right|_{\text{sample,-25}}}{0.95\left.\frac{^{14}C}{C}\right|_{\text{OX-I}} \exp\left((y-1950)/8267\right)} - 1\right), \tag{2.5}$$

which is expressed in ‰. The ^{14}C standard is National Institute of Standards and Technology (NIST) Oxalic Acid I (OX-I) (Stuiver 1983) and the absolute (or modern) ^{14}C standard is 95% of OX-I activity for the year 1950 (i.e. decay corrected), which is equal to 1.18×10^{-12} $^{14}C/C$ (Roberts and Southon 2007).

In some atmospheric radiocarbon studies, radiocarbon values are reported using percent Modern (pM) notation,

which is related to Δ^{14}C by:

$$\text{pM} = 100 \times \left(\frac{\Delta^{14}C}{1000} + 1 \right) \times \exp\left((y - 1950)/8267 \right), \tag{2.6}$$

for measurements made in year y.

Radiocarbon in the atmosphere

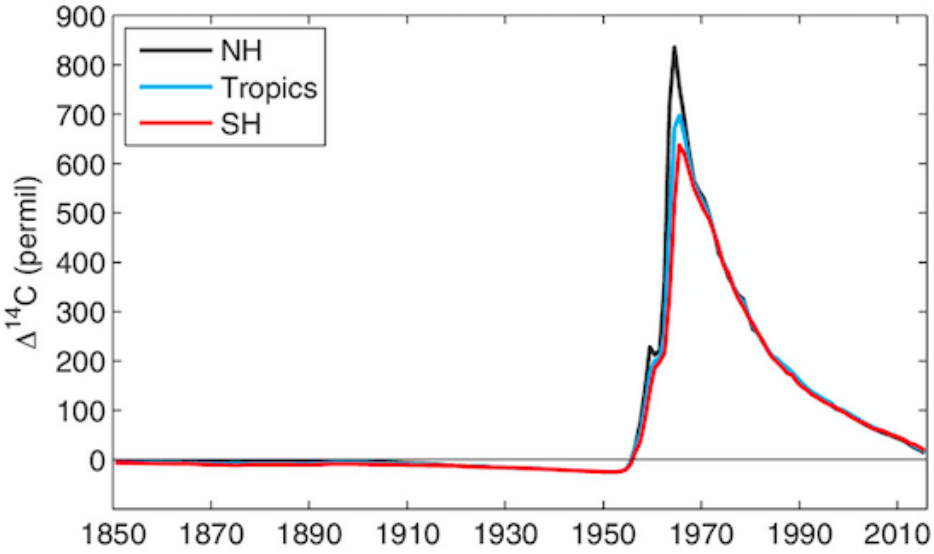


Figure 2.12: Compiled historical dataset for Δ^{14}C. Annual mean values are provided for three zonal bands representing the Northern Hemisphere (30^o-90^{o}N), the Tropics (30^{o}S-30^{o}N), and the Southern Hemisphere (30^o-90^{o}S). Figure and caption (adapted) from Graven et al. (2020).

Changes in the solar wind and Earth's geomagnetic field result in relatively small changes in the production of atmospheric ^{14}C (Key 2001; Schuur et al. 2016; Stuiver and Quay 1981). Since the start of the Industrial Revolution the ratio of ^{14}C/C in the atmosphere has been significantly perturbed by human activities. The combustion of fossil fuels, which are ^{14}C-free, caused an increase in the atmospheric carbon burden and a decrease in the ratio of atmospheric ^{14}C/C. The diluting of atmospheric ^{14}C by fossil fuel emissions is known as the "Suess effect" (Suess 1955) and can be seen in Fig. 2.12 up to c.1950.

Atmospheric Δ^{14}C would have continued to decline if it were not for the above-ground testing of nuclear weapons in the late 1950's and early 1960's. Neutrons produced from these tests reacted with nitrogen in the stratosphere resulting in a rapid increase in atmospheric Δ^{14}C that nearly doubled the amount of radiocarbon in the atmosphere (Schuur et al. 2016). This huge increase in atmospheric Δ^{14}C can be clearly seen in Fig. 2.12. The peak of "bomb" Δ^{14}C occurred in the mid-1960's, shortly after the Partial Test-Ban Treaty was

signed in 1963. This was followed by a decline in atmospheric $\Delta^{14}C$ as it got distributed to different carbon pools through photosynthesis and ocean dissolution (Graven et al. 2012) and ongoing fossil fuel emissions continued to decrease the atmospheric $^{14}C/C$ ratio.

The rise of nuclear power in the early 1970's brought with it a new source of anthropogenic radiocarbon emissions. Radiocarbon is produced by neutron activation of oxides in the nuclear fuel, coolant and moderators of nuclear power plants (NPPs) by the $^{17}O(n,\alpha)^{14}C$ reaction, and by the $^{14}N(n,p)^{14}C$ reaction for impurities in the coolant, fuel and moderator (Davis 1977). Radiocarbon produced in the coolant is released to the atmosphere via NPP stacks (Kunz 1985; Graven and Gruber 2011). Around 70% of radiocarbon effluents from NPPs that use pressurised water reactors (PWRs) is in the form of $^{14}CH_4$ (Kunz 1985). Whilst the flux of $^{14}CH_4$ is very small, it significantly increases the atmospheric $^{14}CH_4/CH_4$ ratio affecting the methane source apportionment and fossil-fraction inferred from $\Delta^{14}CH_4$ measurements if NPP emissions are not accounted for (Kunz 1985; Zazzeri et al. 2018). Figure 2.13 shows an increase in atmospheric $\Delta^{14}CH_4$ from ice-core and atmospheric measurements in the 1980's-1990's, which can only be due to NPP $^{14}CH_4$ emissions.

At some NPPs, radiocarbon emissions are measured onsite (Van der Stricht and Janssens 2005) or estimated using information about the reactor (EPRI 2010). In Europe, the European Commission reports annual measurements of radioactive airborne and liquid releases from NPPs in the European Commission Radioactive Discharges Database (RADD) (RADD 2017; Zazzeri et al. 2018). Radiocarbon emissions from NPPs are also estimated using a nuclear power factor, ϕ, that relates the NPP electrical power output to the ^{14}C source strength (Lassey et al. 2007b). However, only annual emissions are reported in RADD and times when venting occurs or when there are large releases of $^{14}CH_4$ are not reported in RADD. NPP emissions form the largest uncertainty when using radiocarbon measurements to infer methane fossil fractions (Lassey et al. 2007b; Zazzeri et al. 2018).

Future radiocarbon changes

Atmospheric $\Delta^{14}CO_2$ simulations from Graven et al. (2020) show projected $\Delta^{14}CO_2$ values from a range of future warming scenarios drop below 0‰ in the next few years (Fig. 2.14). Future $\Delta^{14}CH_4$ for biospheric methane sources will likely follow a similar trajectory to atmospheric $\Delta^{14}CO_2$ (with a turnover time) for the different emission scenarios. At present, there have not been any published projections of $\Delta^{14}CH_4$ under different scenarios. Simulations of future atmospheric changes show that some applications of $\Delta^{14}C$ will be less effective in the future and predicted changes will impact the way $\Delta^{14}C$ can be used in carbon cycle research (Graven et al. 2020).

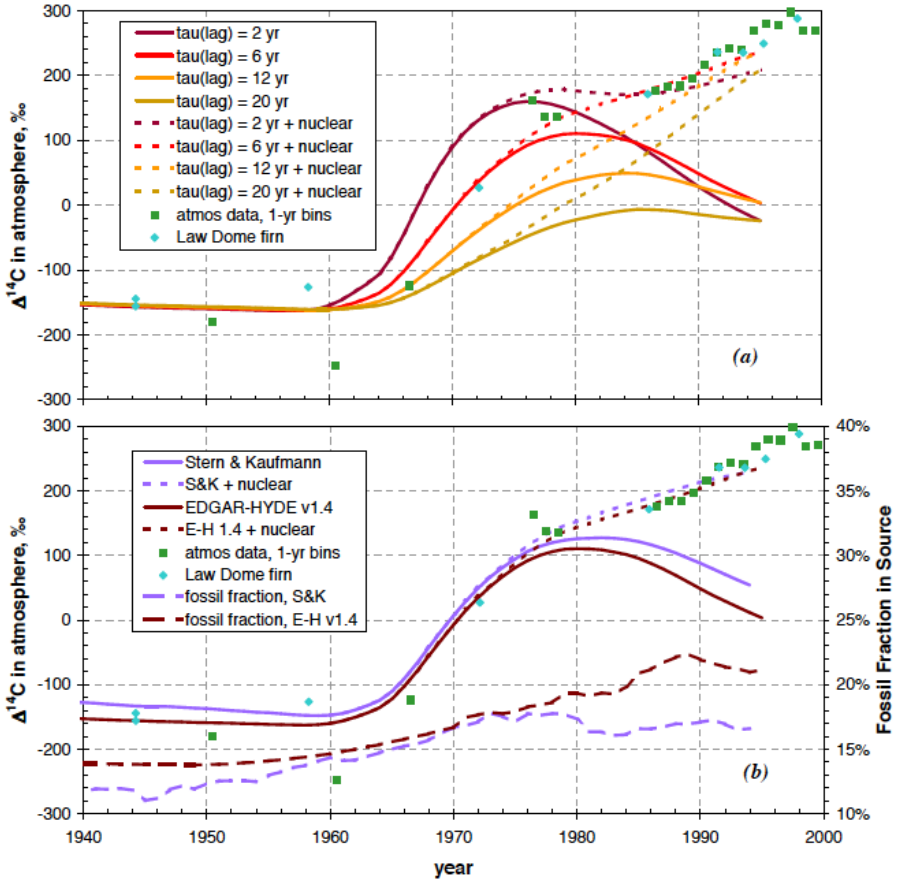


Figure 2.13: A simulated $\Delta^{14}C$ history in atmospheric methane. Solid lines show the biospheric $^{14}CH_4$ (BR) only, and the dashed lines show the augmentation from nuclear power $^{14}CH_4$ (NPR) using a value for the nuclear power factor, ϕ, selected to optimise the fit to data for a mean biospheric turnover time of 6 years. Two observational records are reported. (a) Simulations for EDGAR-HYDE v1.4 for a range of biospheric turnover values. (b) Simulations for Stern and Kaufmann and EDGAR-HYDE v1.4 are contrasted. Also shown is the fossil-fraction in each source construction. Figure and caption (adapted) from Lassey et al. (2007b).

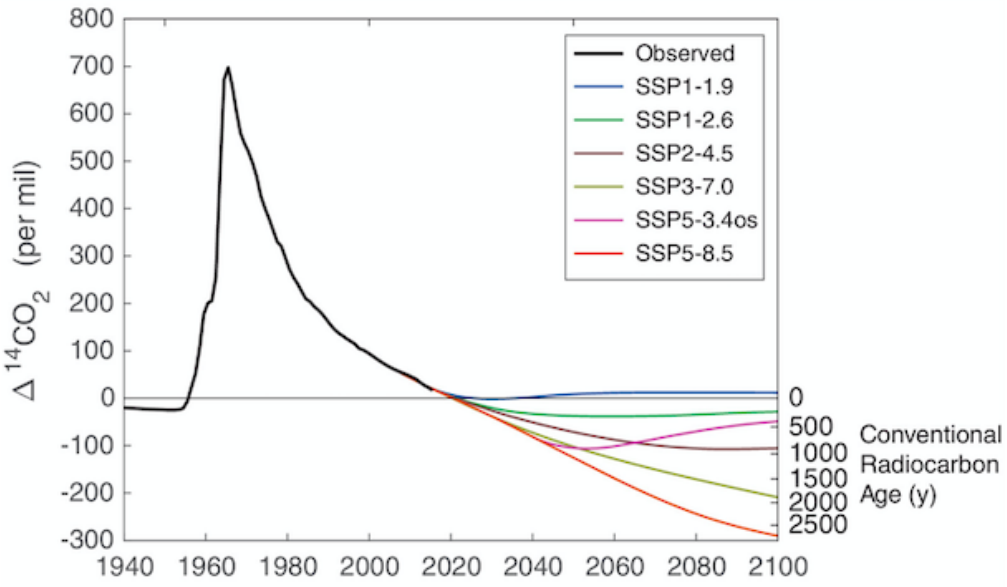


Figure 2.14: Observed $\Delta^{14}CO_2$ for 1940-2015 and simulated $\Delta^{14}CO_2$ for 2015-2100 for the six SSP-based CMIP6 scenarios. Colored lines show the midrange values across the 32 sets of parameters used in the simulations. The right axis shows the conventional radiocarbon age of a carbon-containing specimen with the same radiocarbon content. Figure and caption (adapted) from Graven et al. (2020).

2.6.4 Using $\Delta^{14}CH_4$ to understand contemporary CH_4 sources

Values of $\Delta^{14}CH_4$>0‰ are indicative of a sample having more radiocarbon than the preindustrial atmosphere i.e. the presence of bomb or NPP ^{14}C. Whereas $\Delta^{14}CH_4$<0‰ indicates that radiocarbon in the sample has been isolated from atmospheric exchange long enough for significant radioactive decay to occur (Schuur et al. 2016). By definition fossil fuel sources of CH_4 have $\Delta^{14}CH_4$ values of -1000‰, reflecting the ^{14}C-free nature of these sources, which can be easily shown with Eq. 2.5.

Biospheric methane contains ^{14}C that is characteristic of atmospheric $^{14}CO_2$ at the time it was photosynthesised. The time between when carbon is photosynthesised and released as methane is known as the biospheric turnover time. $\Delta^{14}CH_4$ values of biospheric methane are therefore the atmospheric $\Delta^{14}CO_2$ value adjusted for the biospheric turnover time and the decay of radiocarbon (Lassey et al. 2007b). Biospheric turnover times have been estimated from 0 yr (Wahlen et al. 1989) to 45 yr (Quay et al. 1991). To improve the biospheric turnover constraint, Lassey et al. (2007b) and Lassey et al. (2007a) developed a mathematical framework (Fig. 2.13) using $\Delta^{14}CH_4$ measurements from 1940 to 2000 and found a mean value of 6 yr for the biospheric turnover time best represented observations from this period. However, there is a single data point for 1972

which is shown to have significant leverage on the estimate of the biospheric turnover time (Fig. 2.13).

Table 2.3: Compiled mean isotopic composition values of methane with 1 standard deviation. With $\Delta^{14}CH_4$ data from Quay et al. (1999), Wahlen et al. (1989), and Graven et al. (2017) and $\delta^{13}CH_4$ data from Zazzeri et al. (2017) and Fisher et al. (2017)

Source type	$\delta^{13}CH_4$ (‰)	$^{14}CH_4$ (pM)	$^{14}CO_2$ (pM)	Year of measurement	Implied turnover time
Wetlands	-71 ± 1	116 ± 5	117-119	1986-88	5 years
Ruminants	-60 ± 5	120 ± 5	117-119	1986-88	0 years
Rice cultivation	-63 ± 5	112 ± 5	118	1987	5 years
Landfills	-50 ± 2	120 ± 5	-	year not given	-
Natural gas	-43 ± 7	0	-	-	-
Coal mining	-36 ± 7	0	-	-	-
Biomass burning	-24 ± 3	130 ± 5	118	1987	13 years

Measurements of pM $^{14}CH_4$ signatures were made for some CH_4 sources in the late 1980's and early 1990's (Wahlen et al. 1989; Quay et al. 1999). Quay et al. (1999) summarised these values (Table 2.3) finding similar pM values for wetland, ruminant, rice cultivation and landfill CH_4, but slightly larger pM values for biomass burning CH_4. However, the ^{14}C level in biomass burning CH_4 is dependent on the age of the biomass material. The pM of cows is the same as atmospheric $^{14}CO_2$ in 1986-87, which is expected as cattle feed on forage from the same year or the previous year (Wahlen et al. 1989). Although a turnover time is not given for landfills if the bulk of landfill CH_4 is assumed to be produced from recently derived organic waste it will have a ^{14}C content close to atmospheric $\Delta^{14}CO_2$ (Quay et al. 1991).

Historical atmospheric $\Delta^{14}CH_4$ measurements from Baring Head, New Zealand and from air trapped in Antarctic firn at Law Dome are also shown in Fig. 2.13. The shape of the bomb pulse suggests that the increase in global $\Delta^{14}CH_4$ from the mid 1980's is related to NPP $^{14}CH_4$ emissions showing NPP ^{14}C needs to be accounted for in global studies using atmospheric $\Delta^{14}CH_4$.

Lassey et al. (2007b) and Lassey et al. (2007a) calculated a methane fossil-fraction of $30 \pm 2.3\%$ for 1986-2000 using $\Delta^{14}CH_4$ measurements from Baring Head. Global fossil-fraction estimates from other studies found values closer to 20% (Wahlen et al. 1989; Quay et al. 1999), which is not dissimilar to the fossil-fraction from Lassey et al. (2007b) and Lassey et al. (2007a).

Atmospheric $^{14}CH_4$ measurements made at Heidelberg, Germany in the late 1980's to early 1990's by Levin et al. (1992) are shown in Fig. 2.15. The influences of nearby NPPs Biblis (35 km northwest of the site) and Philippsburg (25 km southwest of the site) are evident in Fig. 2.15 where $^{14}CH_4$ measurements peak at values nearly 6 times the maritime $^{14}CH_4$ value (Levin et al. 1992). Clearly PWRs have a significant impact on $\Delta^{14}CH_4$ and NPP emissions are highly variable, which is likely due to a range of operating procedures being used (Zazzeri et al. 2018). Identifying fossil methane sources with atmospheric measurements of $^{14}CH_4$, even in an industrial region like Heidelberg, is found to produce ambiguous results because of NPP $^{14}CH_4$ contributions (Levin et al. 1992).

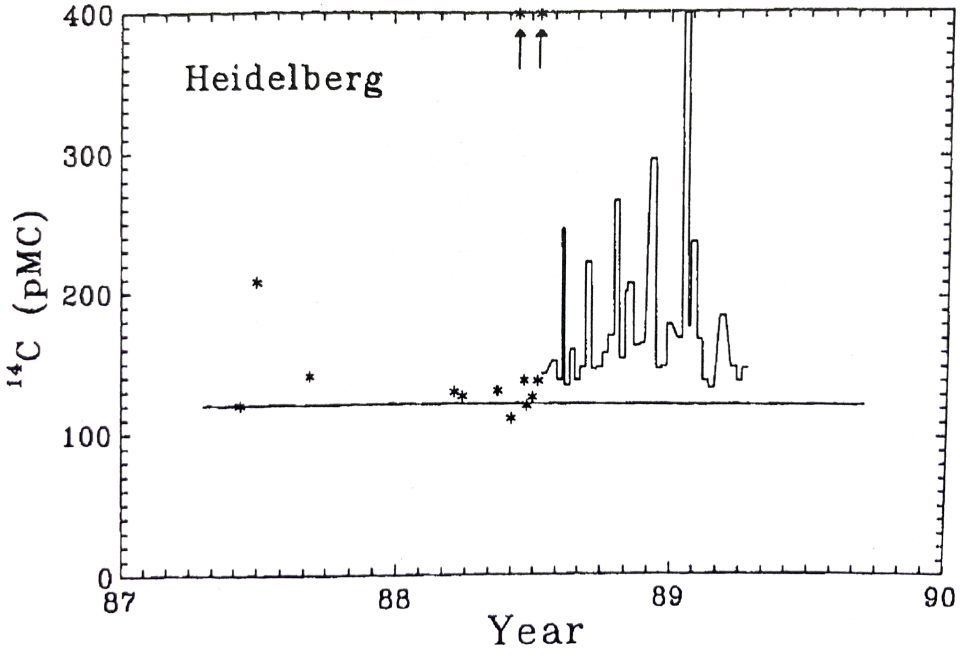


Figure 2.15: ^{14}C activity in atmospheric methane at Heidelberg. $^{14}CH_4$ peaks up to 600 pMC were identified as direct contamination from nearby nuclear power plants. Figure and caption from Levin et al. (1992).

Whilst atmospheric measurements of $\Delta^{14}CO_2$ have been made at one measurement station in the UK (Wenger et al. 2019), there have been even fewer atmospheric $\Delta^{14}CH_4$ measurements made in Europe since the late 1990's. Recently, Zazzeri et al. (2021) developed a new measurement system for atmospheric $\Delta^{14}CH_4$, which was tested at Imperial College London (ICL). Measurements from 7 and 18 March 2020 had $\Delta^{14}CH_4$ values of 330.7 ± 6.9‰ and 302.2 ± 4.1‰ and concurrent CH_4 mole fractions had averages of 1960 ppb and 1992 ppb, respectively. Model trajectories of air arriving at ICL on these days originated from over the Atlantic Ocean suggesting atmospheric $\Delta^{14}CH_4$ measurements are unlikely affected by PWRs on these days.

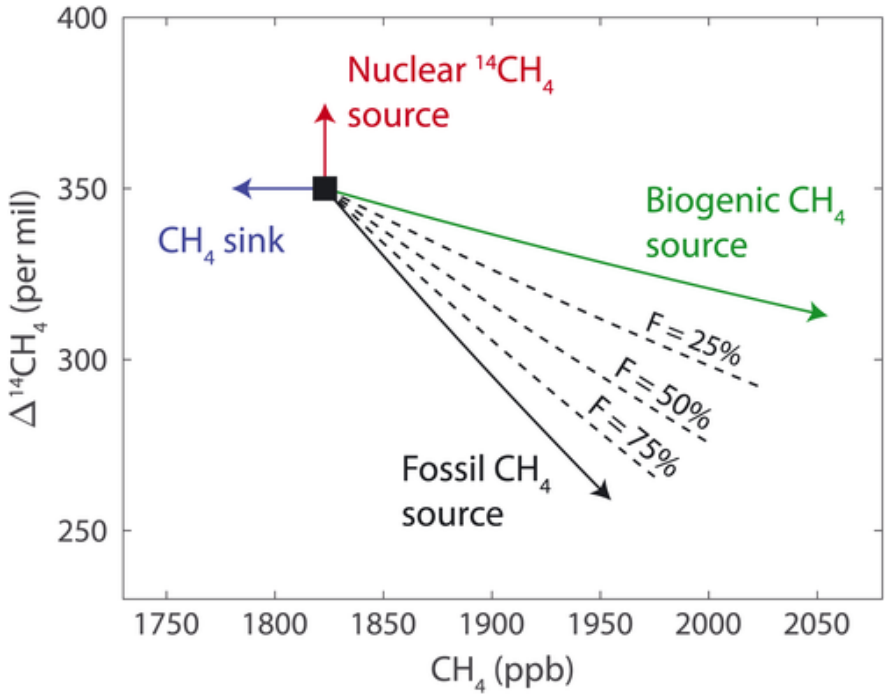


Figure 2.16: Diagram showing the expected change in CH_4 concentration and change in $\Delta^{14}CH_4$ from background values for different processes in 2014. Estimated global mean background composition in 2014 is shown with the black square. The dashed lines show the changes expected from mixed biogenic and fossil CH_4 sources, with F denoting the fossil-fraction of emissions. Figure and caption from Graven et al. (2019)

Changes in atmospheric $\Delta^{14}CH_4$ for concurrent changes in CH_4 concentrations can theoretically be used to estimate methane fossil-fractions (Fig. 2.16; Graven et al. 2019). For a fossil-fraction of 100% (indicating a purely fossil CH_4 source) $\Delta^{14}CH_4$ decreases by -7.1‰ per 10 ppb of CH_4, whereas for a purely biogenic methane source (fossil-fraction of 0%) $\Delta^{14}CH_4$ decreases by -1.7‰ per 10 ppb of CH_4 for the year 2014 (Fig. 2.16; Graven et al. 2019). Assuming the same background and PWR conditions for the two days measured by Zazzeri et al. (2021) and assuming NPP influences are negligible, there is a change in $\Delta^{14}CH_4$ between the two samples of around -9‰ per 10 ppb of CH_4. This indicates methane sources with high fossil-fractions were observed in London.

2.7 Using methane satellite measurements to constrain CH_4 emissions

Satellite measurements of atmospheric methane columns have been used for inferring CH_4 emissions at a range of scales (Jacob et al. 2016; Streets et al. 2013; Kort and Frankenberg 2014; Turner et al. 2018; Varon

et al. 2019). Spatially dense and timely global observations make satellite measurements well-suited for inverse analyses (Qu et al. 2021; Ganesan et al. 2017), monitoring of emission trends (Turner et al. 2016) and detecting emission hotspots (Kort and Frankenberg 2014). Compared to ground-based observations, satellite measurements cover large areas in single overpasses, measure atmospheric CH_4 in areas inaccessible to ground-based measurements and can detect large emission events that are potentially not captured by ground-based measurements. However, to ensure data is accurate satellite measurements require careful calibration with ground-based instruments, such as the upwards facing spectrometers used in the Total Carbon Column Observing Network (TCCON) (Wunch et al. 2011; Jacob et al. 2016). Whilst satellite observations of methane have been made in the near-infrared, thermal-infrared and in the shortwave infrared (SWIR) spectral bands, only SWIR satellite measurements of CH_4 are considered in this chapter. Compared to other spectral bands, satellite instruments measuring CH_4 in the SWIR are more sensitive to the lower troposphere but they are also sensitive to cloud cover (Palmer et al. 2021) meaning measurements are sparse in regions with high cloud coverage.

2.7.1 Satellite instruments for measuring atmospheric methane

Satellite SWIR measurements of total methane columns (XCH_4) have been made since the Scanning Imaging Absorption Spectrometer for Atmospheric Cartography (SCIAMACHY) was launched in 2002 (Frankenberg et al. 2006), where XCH_4 measurements were retrieved from a sun-synchronous orbit in the 1.66-1.67 μm band. SCIAMACHY observations achieved near global coverage every 6 days with a 30×60 km^2 pixel spatial resolution (Wecht et al. 2014; Table 2.4). However, towards the end of 2005 pixels in the detector had started to degrade making SCIAMACHY measurements less reliable (Frankenberg et al. 2011).

Launched in 2009, Greenhouse Gases Observing Satellite (GOSAT) was the first spaceborne mission dedicated to measuring greenhouse gases (Kuze et al. 2009). GOSAT total column CH_4 measurements, made at the same wavelength as SCIAMACHY, have a 10.5×10.5 km^2 spatial resolution and global coverage is obtained approximately every 3 days (Palmer et al. 2021; Table 2.4). GOSAT measurements have led to improvements in regional CH_4 budgets worldwide (Lunt et al. 2019; Lunt et al. 2021b; Feng et al. 2017; Fraser et al. 2013; Ganesan et al. 2017; Jacob et al. 2016; Miller et al. 2019; Pandey et al. 2016; Turner et al. 2015), the results from some of these studies are presented in the next section.

Launched in 2017, the TROPOSpheric Monitoring Instrument (TROPOMI) onboard the Sentinel-5 Precursor satellite measures atmospheric CH_4 in the SWIR at 2.3 μm. Whilst measurements at 2.3 μm make it possible

for concurrent measurements of CO, atmospheric measurements of CO_2 cannot be made at this wavelength. Near-daily global coverage is achieved by TROPOMI and retrievals are currently made with a pixel spatial resolution of 5.5×7 km^2 (Hu et al. 2018a; Table 2.4). TROPOMI XCH_4 measurements have been shown to be in relatively good agreement with GOSAT and TCCON measurements (Hu et al. 2018a; Hasecamp et al. 2019). A mean bias of $13.6 \pm 19.6(1\sigma)$ ppb is found between TROPOMI and GOSAT XCH_4 (Hu et al. 2018a). The bias between TROPOMI and TCCON measurements depends on the surface albedo values where for low albedo values (<0.15) TROPOMI underestimates TCCON and for high albedo values (>0.25) TROPOMI overestimates TCCON XCH_4 (Hasecamp et al. 2019). To account for this albedo dependence a bias-correction is applied to TROPOMI XCH_4 data by using GOSAT retrievals (Hasecamp et al. 2019). The bias-corrected TROPOMI XCH_4 data are included in the operational TROPOMI product.

Table 2.4: Satellite instruments (that are in sun-synchronous (SS) orbit) have measured atmospheric CH_4 in the SWIR. LECT refers to the local equatorial crossing time and coverage refers to the time required for full global coverage.

SWIR instrument	Data availability	Orbit, LECT	Coverage	Spatial resolution	Instrument precision
SCIAMACHY	2002-2012	SS, 10:00	6 d	30×60 km^2	1.5%
GOSAT	2009-	SS, 13:00	3 d	10.5×10.5 km^2	0.7%
TROPOMI	2018-	SS, 13:30	1 d	5.5×7 km^{2,a}	0.6%
GHGSat-D	2016-	512 km, 09:30	-^{b}	0.05×0.05 km^2	$1-5$%

[a] Before August 2019 the spatial resolution was 5.5×7 km^2.
[b] GHGSat-D measures over 12×12 km^2 domain.

2.7.2 GOSAT methane measurements

Atmospheric methane measurements from GOSAT have been used in a range of different inversion modelling studies to infer global and national CH_4 emissions, where countries with historically large CH_4 emissions were usually targeted. GOSAT measurements from 2009-2011 used in a Bayesian inversion framework calculated a global posterior emissions estimate that differed by 2 Tg CH_4 yr^{-1} from the prior global inventory (EDGAR - Emissions Database for Global Atmospheric Research - v4.2) of CH_4 emissions (Turner et al. 2015). The posterior coal and rice cultivation methane emissions indicated large adjustments to these emission sectors are needed in the EDGAR inventory (Table 2.5). In particular, coal emissions for

China were found to be largely overestimated in EDGAR compared to GOSAT observations (Turner et al. 2015).

Table 2.5: 2009-2011 methane emissions reported by Turner et al. (2015).

Source type	Global prior (Tg CH_4 yr^{-1})	Global posterior (Tg CH_4 yr^{-1})
Total	537	539
Wetlands	164	169
Livestock	111	116
Oil/gas	69	67
Waste	60	65
Coal	47	30
Rice	38	45
Open fires	17	16
Other[a]	31	32

[a]Including wetlands, open fires, termites, soil absorption

Ganesan et al. (2017) used a combination of GOSAT measurements, aircraft measurements and ground-based measurements from 2010-2015 in an inverse modelling framework to quantify methane emissions from India and China finding emissions from both countries are overestimated in the EDGAR v4.2 inventory. Similar to Turner et al. (2015), fossil fuel emissions in China and ruminant and waste emissions in India were overestimated in EDGAR (Ganesan et al. 2017). Maasakkers et al. (2019) reached a similar conclusion, where 2010-2015 GOSAT measurements used in an inversion framework suggested coal-related CH_4 emissions from China and Middle East oil and gas CH_4 emissions were still being overestimated in EDGAR v4.3.2 - an updated version of the global inventory.

The spatial resolution and instrument precision of GOSAT has made it challenging to use these XCH_4 measurements for quantifying methane emissions from smaller, more cloudy regions such as the UK. However, the higher spatial resolution and daily coverage of TROPOMI measurements makes it more probable to quantify regional emissions. TROPOMI's higher pixel resolution potentially means some pixels may escape cloud coverage and an XCH_4 value could be observed. Near-daily retrievals increase the likelihood of more cloud-free scenes being observed (Jacob et al. 2016; Hu et al. 2018b).

2.7.3 TROPOMI methane measurements

In a recent study, Qu et al. (2021) used XCH_4 measurements from GOSAT and TROPOMI in a $2^o \times 2.5^o$ global inversion of methane sources for the year 2019 using three inversion setups (Table 2.6). The joint TROPOMI-GOSAT inversion posterior produced the largest CH_4 emission estimate (570 Tg CH_4 yr^{-1}) whereas the smallest posterior emission (556 Tg CH_4 yr^{-1}) was obtained when using just TROPOMI measurements in the inversion (Table 2.6). Posterior emissions suggest overall CH_4 emissions are overestimated in the EDGAR v4.3.2 inventory for the year 2012 (used as the prior estimate; Table 2.6). Whilst oil and gas emissions are inferred to be overestimated in the 2012 EDGAR v4.3.2 inventory, compared to the posterior emissions, livestock emissions were found to be underestimated in the prior by 10 Tg CH_4 yr^{-1} to 23 Tg CH_4 yr^{-1} (Qu et al. 2021). GOSAT retrievals were found to be better suited for resolving CH_4 from over wetlands than TROPOMI, as an error weighting had to be applied to the TROPOMI measurements in the inversion to avoid unrealistic wetland emissions in the posterior (Qu et al. 2021). Adjustments are therefore needed in TROPOMI retrievals for resolving wetland measurements.

TROPOMI posterior emissions (26 Tg CH_4 yr^{-1}), GOSAT posterior emissions (33 Tg CH_4 yr^{-1}) and the TROPOMI-GOSAT joint posterior (29 Tg CH_4 yr^{-1}) are all smaller than the 37 Tg CH_4 yr^{-1} EDGAR v4.3.2 methane emissions for Europe (Fig. 2.17; Qu et al. 2021). Posterior emissions suggest there have been large reductions from fossil fuel methane emissions that are not captured in the EDGAR emissions over Europe (Qu et al. 2021). Qu et al. (2021) provide, to the best of the author's knowledge at the time of writing, the only study to use both GOSAT and TROPOMI observations to infer methane emissions from Europe.

Although optimised for quantifying emissions from area sources, TROPOMI measurements have been used to quantify point source emissions from plumes observed in the XCH_4 retrievals. In a study using TROPOMI XCH_4, Pandey et al. (2019) detected a large CH_4 gas well blowout* in Ohio during February 2018 to March 2019. Methane emissions were reported at 120 ± 32 t CH_4 h^{-1}, twice that of the Aliso Canyon methane leak in California 2015 which at that time was the largest methane leak from an underground storage facility in the USA (Thompson et al. 2016; Pandey et al. 2019).

Varon et al. (2019) used TROPOMI measurements (along with GHGSat-D* measurements) to quantify emis-

*A "gas well blowout" is an uncontrolled release of natural gas from a gas well after pressure control systems have failed.

*GHGSat-D is a satellite instrument that measures atmospheric CH_4 columns in the SWIR with a 50×50 m^2 resolution over 12×12 km^2 scenes.

Table 2.6: Global methane budget for 2019 reproduced from Qu et al. (2021).

	Prior estimate (Tg CH_4 yr^{-1})	Posterior estimates (Tg CH_4 yr^{-1})		
		TROPOMI	GOSAT	Joint
Total sources	**542**	**556**	**562**	**570**
Anthropogenic	341	336	371	363
Livestock	116	126	143	139
Oil and gas	66	53	54	56
Rice	38	NR[a]	43	NR[a]
Wastewater	37	44	48	44
Coal	31	NR[a]	26	NR[a]
Landfills	30	27	30	31
Other anthropogenic	23	26	27	26
Natural	201	220	191	207
Wetlands	168	195	163	183
Termites	12	12	13	12
Open fires	19	11	13	10
Seeps	2	2	2	2
Total sinks	**563**	**543**	**543**	**533**

[a]Not reported (NR) because of potential for bias in the sectoral attribution of TROPOMI inversion results for China, which is a major source of emissions from rice and coal.

sions from a previously undetected large plume coming from a gas compressor station in western Turkmenistan. Between December 2017 and January 2019, emissions of 10-43 t CH_4 h^{-1} were quantified (Varon et al. 2019). More recently, TROPOMI measurements from 2018-2019 were used to quantify CH_4 emissions from six coal mines in Queensland, Australia. The collective emissions from these coal mines (570 ± 98 Gg CH_4 yr^{-1}) were more than seven times larger than the 2018 Australian methane emission inventory estimate (Sadavarte et al. 2021). The cross-sectional flux method (White et al. 1976) was used in these three studies (Pandey et al. 2019; Varon et al. 2019; Sadavarte et al. 2021) to quantify CH_4 emissions from point sources. This method does not use an atmospheric transport model and instead uses wind speed data and TROPOMI measurements to quantify an emission rate for a point source. The cross-sectional flux method is further described in Chapter 6.

TROPOMI measurements of other atmospheric trace gases have been used to explore regional scale correlations with atmospheric CH_4 enhancements as a way to infer the sources of CH_4 emissions. Correlations of CH_4

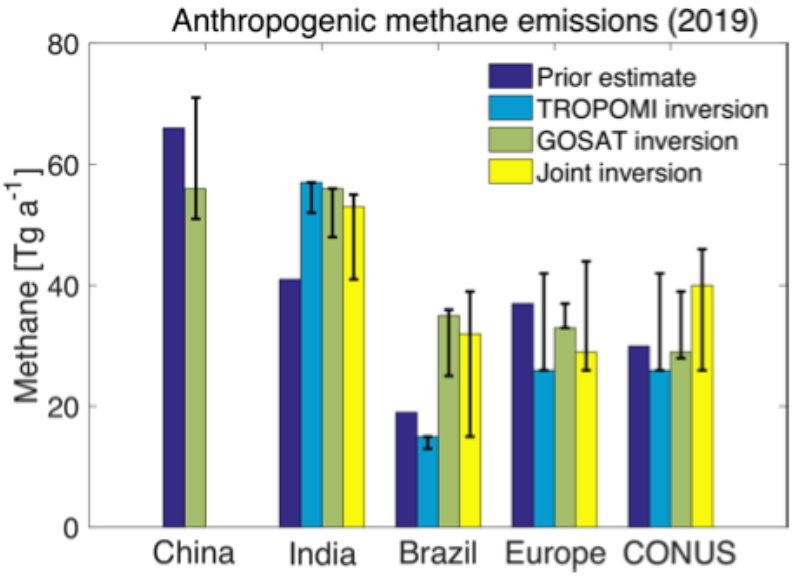


Figure 2.17: Annual anthropogenic methane emissions for 2019 for five major source regions, accounting for 56% of global anthropogenic emissions in the inversion of GOSAT data. The vertical bars represent the range of posterior emissions from the ensemble of inversions. Europe is defined as west of 37^{o}E. The CONUS is the Contiguous United States. Figure and caption (adapted) from Qu et al. (2021).

and nitrogen dioxide (NO_2) enhancements over the Permian Basin had correlation coefficients larger than 0.4 for 45 out of 55 days of clear-sky TROPOMI observations (Gouw et al. 2020). Whilst Gouw et al. (2020) demonstrated a positive correlation between TROPOMI XCH_4 and XNO_2 columns a large amount of scatter is exhibited, even on days with larger correlation coefficients (Fig. 2.18). This approach was not used to quantify methane emissions from the Permian Basin, but only to demonstrate that large XCH_4 values observed in TROPOMI retrievals can be attributed to oil and gas emissions based on concurrent XNO_2 retrievals.

Similarly, ratios of concurrent TROPOMI CH_4 and CO column enhancements from 2018-2019 were used to infer methane emissions from 8 cities in the USA (Fig. 2.19; Plant et al. 2022). Ratios of TROPOMI XCH_4/XCO enhancements were scaled using EDGAR v5.0 CO estimates to infer CH_4 emissions for each of these cities (Fig. 2.19; Plant et al. 2022). Pseudo-data were used to test this approach and found a direct relationship between surface emissions and urban column enhancements of CH_4 and CO (Plant et al. 2022). Methane emissions for the 8 US cities are collectively estimated at 1.47 Tg CH_4 yr^{-1} from TROPOMI which is much larger than the US Environmental Protection Agency estimate of 0.52 Tg CH_4 yr^{-1} (Plant et al. 2022). Missing emissions are attributed to natural gas emissions from leaks in the distribution network (Fig. 2.19).

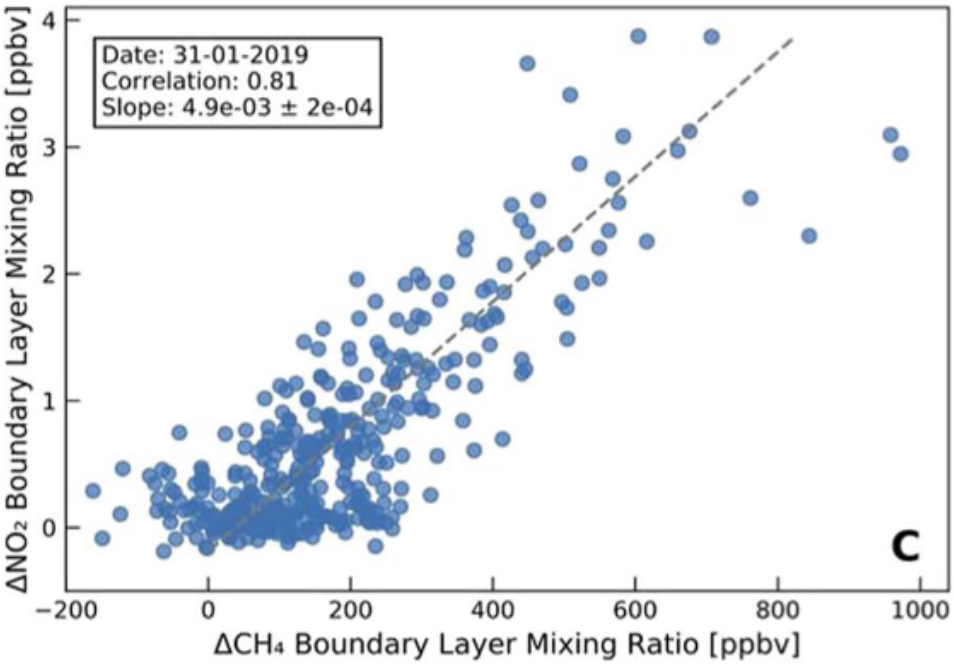


Figure 2.18: Scatter plot of NO_2 vs. methane boundary layer mixing ratios calculated from the TROPOMI columns in the Permian Basin. Figure and caption (adapted) from Gouw et al. (2020).

The Environmental Protection Agency inventory scaled to include missing natural gas emissions were found to be in better agreement with the TROPOMI CH_4:CO emission estimate (Fig. 2.19). However, there are large uncertainties associated with the methane emission estimates for each of the cities which overlap with some of the prior CH_4 emission values (Fig. 2.19).

Barré et al. (2021) developed a novel approach for global systematic detection of methane point sources. Using 2019 TROPOMI CH_4 measurements and modelled atmospheric CH_4 forecasts produced by the Copernicus Atmosphere Monitoring Service (CAMS) - these data are further described in the following chapter - to search for regions with large TROPOMI-CAMS differences. After filtering to remove synoptic scale biases in the CAMS forecasts and TROPOMI measurements, a simple classification scheme was used to search for point source anomalies and plumes missing in the CAMS forecast data. This approach was developed as a way to retain the high-resolution TROPOMI retrievals whilst simultaneously working on a global scale that would otherwise be too computationally expensive in an inversion framework.

Methane emissions are underestimated over the Permian Basin and at the gas compressor station in western Turkmenistan in the TROPOMI-CAMS departures approach which supports the findings of Gouw et al. (2020)

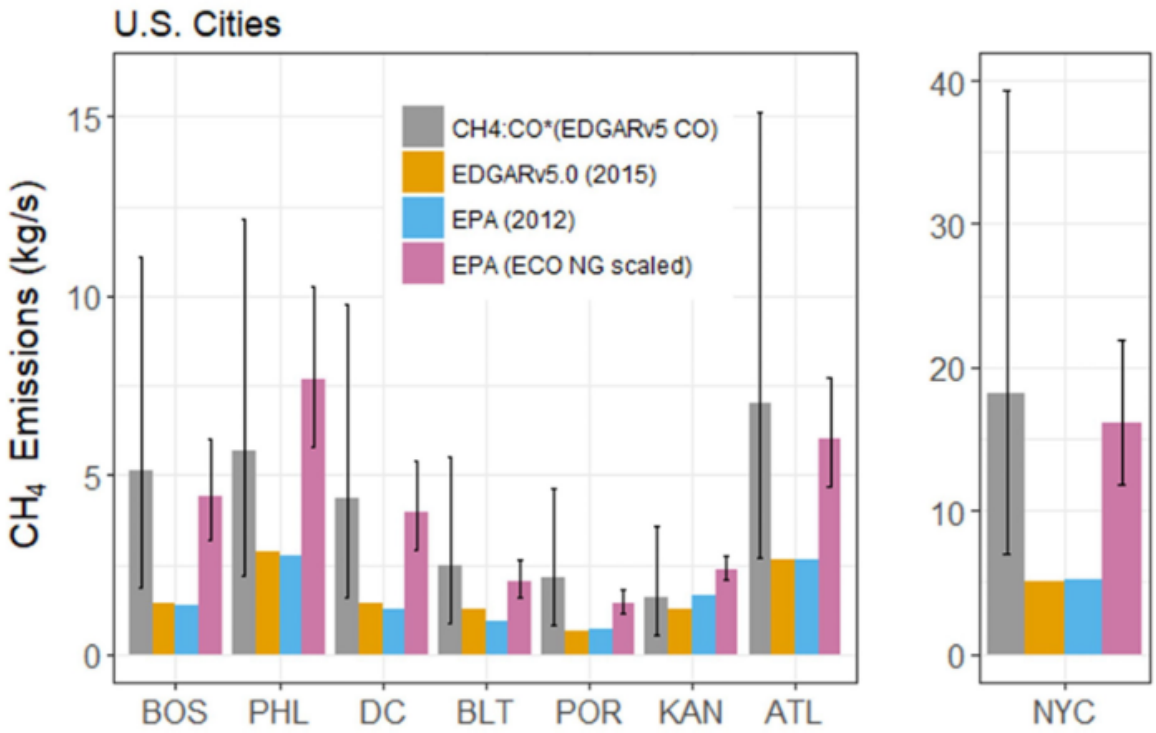


Figure 2.19: Urban CH_4 emissions generated with the observed 2019 $\Delta CH_4/\Delta CO$ ratios and inventoried CO from EDGAR v5.0 (gray), compared to CH_4 inventory estimates from EDGAR v5.0 (yellow), Gridded EPA (blue), and ECO-scaled Gridded EPA (pink). NYC - New York City, BOS - Boston, PHL - Philadelphia, DC - District of Columbia, BLT - Baltimore, POR - Portland, KAN - Kansas city, ATL - Atlanta. Figure and caption (adapted) from Plant et al. (2022).

and Varon et al. (2019), respectively. Large discrepancies are also found near Baja, California and south Nevada but the cause of these discrepancies have yet to be investigated (Barré et al. 2021). There are also places where large point source CH_4 emissions are observed in the forecasts but not in TROPOMI. For example, the CH_4 emissions used in CAMS seem to overpredict CH_4 over San Bernardino and Palmdale in Los Angeles.

Whilst this method has the potential to detect missing sources and evaluate point sources in emission inventories it assumes that synoptic biases in the TROPOMI and forecasts can be filtered. Barré et al. (2021) do not attempt to explain the cause of the synoptic biases but underscore that these large scale differences are not yet fully understood and that understanding these biases is crucial for improving the quality of TROPOMI XCH_4 retrievals and CAMS CH_4 forecasts.

2.8 Summary

2.8.1 Isotopic approaches

Measurements of carbon isotopes in atmospheric methane are an established and useful approach for characterising CH_4 sources. Measurements of atmospheric $\delta^{13}CH_4$ have been frequently used in measurement campaigns and global studies to better understand the attribution of CH_4 sources (Townsend-Small et al. 2012; Zazzeri et al. 2017; France et al. 2016; Fischer et al. 2017) and the underlying causes of atmospheric mole fraction trends (Nisbet et al. 2019).

Whilst $\delta^{13}CH_4$ signatures are well-characterised globally (Sherwood et al. 2017) and regionally (Zazzeri et al. 2017; Menoud et al. 2020) values for some sources (e.g. ruminants, natural gas) can change with time and location for socioeconomic reasons (e.g. livestock diet, where natural gas is extracted or supplied). This introduces some uncertainty into the $\delta^{13}CH_4$ signatures used for quantifying sources, which can overlap for different sources (Sherwood et al. 2017). The recent increase in global CH_4 mole fractions and concurrent $\delta^{13}CH_4$ decrease has yet to be conclusively explained despite a number of possible explanations that have been proposed in the literature (Nisbet et al. 2019; Nisbet et al. 2016). Additional methane tracer measurements could be used to improve our understanding of global and regional trends on longer timescales and to improve source attribution on shorter timescales, particularly in areas where there are co-located CH_4 sources.

Atmospheric measurements of radiocarbon in methane form the primary fossil CH_4 constraint. However, measurements require larger samples of air, are expensive and labour intensive, which is possibly why there are few atmospheric $^{14}CH_4$ measurements compared to $\delta^{13}CH_4$. Emissions of $^{14}CH_4$ from PWRs need to be accounted for when using radiocarbon for source attribution as $\Delta^{14}CH_4$ can be shifted to unrealistically large values as a result of nearby NPPs. Whilst radiocarbon emissions from PWRs in Europe are well-documented in RADD, specific operating details are not reported (e.g. times when $^{14}CH_4$ is released into the atmosphere). PWR emissions introduce a large uncertainty when using radiocarbon for source attribution (Zazzeri et al. 2018; Graven et al. 2019).

There have been few measurements of $\Delta^{14}CH_4$ used to characterise the $\Delta^{14}CH_4$ signatures of biospheric methane sources (Quay et al. 1999). The biospheric $\Delta^{14}CH_4$ signatures that have been measured mostly have similar values and turnover times (Table 2.3). The $\Delta^{14}CH_4$ value for biomass burning CH_4 is the most challenging to constrain as it will vary depending on the age of the organic material. Assuming a

turnover time of 0 years for landfill CH_4 (Quay et al. 1991) then 90% of biogenic methane emissions in the UK (based on values reported in the 2017 NAEI) will have a turnover time of 0 years. The remaining 10% of biogenic CH_4 in the UK is from waste water (where a turnover time has not been constrained) and biomass burning emissions. Global changes of less than 10‰ yr^{-1} in atmospheric $\Delta^{14}CO_2$ since 1992 (Graven et al. 2020) mean that biospheric $\Delta^{14}CH_4$ will have more similar values (assuming a range of turnover times of 0-15 years; Quay et al. 1999; Wahlen et al. 1989; Lassey et al. 2007a) than other periods, such as the 1980's where global changes of up to 30‰ yr^{-1} in atmospheric $\Delta^{14}CO_2$ are observed (Graven et al. 2020). Therefore using one $\Delta^{14}CH_4$ signature for biospheric sources, derived from contemporary atmospheric $\Delta^{14}CO_2$ values is a valid approximation for UK studies using $\Delta^{14}CH_4$ today. However, it would be useful to have a better understanding of spatiotemporal variations of the biospheric $\Delta^{14}CH_4$ and if there are other factors, such as air or water temperature, that could affect the biospheric turnover times of different sources.

There are few studies that have used both $\delta^{13}CH_4$ and $\Delta^{14}CH_4$ measurements for analysing methane sources (Quay et al. 1999; Townsend-Small et al. 2012; Zazzeri et al. 2021; Gonzalez Moguel et al. 2022). Analysis is usually done on a case-by-case basis and as highlighted in Graven et al. (2020): "There is a lack of shared atmospheric modelling tools for isotopic simulations and existing observations are not being fully used". A coherent framework incorporating both $\delta^{13}CH_4$ and $\Delta^{14}CH_4$ measurement is therefore needed for fully exploiting these isotopic measurements.

Whilst a focus of this chapter has been on carbon isotopic tracers of methane there are other isotopic tracers (δD, $\Delta^{13}CH_3D$, $\Delta^{12}CH_2D_2$) and gaseous tracers (ethane) that have been used for methane source attribution (e.g. Assan et al. 2018; Townsend-Small et al. 2012; Rennick et al. 2021; Chung and Arnold 2021; Ramsden et al. 2022).

2.8.2 Satellite approaches

Satellite measurements of atmospheric CH_4 over the UK have, to date, not been used nor reported in the literature. Palmer et al. (2018) highlighted the measurement capabilities of SCIAMACHY and GOSAT were not suitable for the UK and could only provide sparse and uneven sampling because of the UK's geographical size and cloud coverage. TROPOMI could provide sufficient satellite data coverage for the UK and be used as an additional resource for methane emissions monitoring, quantification and analysis.

In this chapter, an overview of four measurement approaches for quantifying CH_4 emissions using satellite

data was presented. These are:

1. Inversion modelling (Qu et al. 2021).

2. Point source quantification using the CSF approach (Varon et al. 2019; Pandey et al. 2019; Sadavarte et al. 2021).

3. Tracer gas approaches for CH_4 emissions quantification using additional TROPOMI measurements of CO (Plant et al. 2022) and NO_2 (Gouw et al. 2020).

4. Point source quantification using TROPOMI-CAMS differences (Barré et al. 2021).

An emphasis was placed on techniques that have been previously applied to TROPOMI retrievals that could potentially be used for quantifying regional scale methane emissions in the UK.

The inversion approach used by Qu et al. (2021) for quantifying global emissions aggregated TROPOMI retrievals to a coarse spatial resolution. Whilst this likely improved the computational efficiency of the inversion, many of the finer scale spatial variations that are captured by TROPOMI are not exploited in the inversions. Inversion modelling applied to a regional scale would be able to fully exploit the high-resolution XCH_4 TROPOMI data and could potentially be used to evaluate spatial differences between the prior and posterior estimates. The size of the UK makes it suitable for high-resolution inverse modelling using TROPOMI retrievals, but high levels of cloud coverage in the UK potentially mean a longer period of observations would be needed to obtain a sufficient number observations of UK CH_4 emissions. Even then, there remains the question of whether XCH_4 retrievals from cloud-free days are representative of UK CH_4 emissions. However, since TROPOMI's XCH_4 UK data coverage has not been assessed it is difficult to say whether it would be possible to use these data to improve the UK methane emission constraint.

Tracer approaches for quantifying CH_4 emissions using TROPOMI CO and NO_2 measurements were also examined. Ratios of TROPOMI CH_4/NO_2 enhancements are reasonably correlated on individual overpasses (as CH_4 and NO_2 are co-emitted from the extraction, production and flaring of natural gas) but exhibit a lot of scatter (Gouw et al. 2020) in measurements over the Permian Basin. The large number of sources in the region (including emissions from livestock) could lead to the scatter observed in correlations of CH_4-NO_2 enhancements. Ratios of TROPOMI CH_4/CO enhancements assume that CO and CH_4 emissions are co-located (but not co-emitted) when there is "sufficient mixing" (Plant et al. 2022), in which case a strong correlation is expected to be observed. This approach for quantifying CH_4 emissions does not seem accurate since it also

relies on accurate bottom-up CO emission estimates for inferring CH_4 emissions. This tracer approach could be further tested by comparing estimates in regions where ground-based measurements have been used to evaluate emission inventories (e.g. London; Saboya et al. 2022) or by comparing methane emissions quantified using different inventory CO estimates.

TROPOMI measurements have been used to successfully quantify emissions from large fossil fuel super emitters (> 1 t CH_4 h^{-1}) in various locations (Varon et al. 2019; Sadavarte et al. 2021; Pandey et al. 2019; Lauvaux et al. 2021). In the UK, emissions from the largest CH_4 point source are less than 4000 t CH_4 yr^{-1} (or 0.45 t CH_4 h^{-1}; assuming uniform, constant emissions) (NAEI 2017), which is much smaller than emissions reported for Australian coal mines (~ 65.1 t CH_4 h^{-1}; Sadavarte et al. 2021), or the gas compressor in western Turkmenistan (4-32 t CH_4 h^{-1}; Varon et al. 2019). The instrument precision of TROPOMI makes it difficult to detect low-emitting point sources, which are likely missed in the TROPOMI CH_4 retrievals (Lauvaux et al. 2021). Using TROPOMI to search for plumes from high-emitting UK point sources in single overpasses will be challenging, but could give a clearer picture of the extent to which TROPOMI methane measurements could be used for detecting and quantifying UK CH_4 emissions.

The approach by Barré et al. (2021) used CAMS XCH_4 forecasts and TROPOMI XCH_4 measurements to detect point sources has potential for quantifying global sources that are missed or overestimated in the CAMS emissions inventory whilst retaining the high-resolution TROPOMI data. An understanding of the large scale biases in the forecasts is, however, needed to improve the accuracy of the emission differences between TROPOMI XCH_4 and the CAMS XCH_4 forecasts. This approach could be used as a precursor to quantifying emissions in an inversion modelling framework as it is able to highlight regions that should be targeted and studied in-depth.

Whilst TROPOMI XCH_4 measurements have been used for quantifying different methane point sources and emissions from cities, regional-scale spatial patterns and changes in rural area sources (e.g. agricultural emissions) have not been reported in the literature. Since TROPOMI is optimised for detecting methane area sources there is potentially more information to be extracted from TROPOMI XCH_4 measurements than what is currently presented in the literature.

Chapter 3

Data, observations and models

"My enthusiasm to study atmospheric CO_2 never slackened; it depended, however, on acquiring data that truly reflected nature."

— Charles Keeling, *Rewards and penalties of monitoring the Earth*

In the following chapter the CH_4 measurement laboratory setup at Imperial College London (ICL), the sources of other observation and model data, and their data products that are used in this thesis are described. The first half of this chapter outlines the atmospheric measurements, emissions data, and atmospheric model used in Chapter 4 and Chapter 5, in which ground-based isotopic tracer approaches are used to evaluate sources and emissions of methane. In the second half of this chapter I describe the data products and data processing of methane retrievals from the TROPOspheric Monitoring Instrument (TROPOMI) onboard the Sentinel-5P satellite used to establish a high-quality dataset that is later used in Chapter 6. Data products from the Copernicus Atmosphere Monitoring Service (CAMS) atmospheric composition forecast and reanalysis models are also presented and I describe the data processing of the CAMS data products for comparison with TROPOMI methane retrievals.

3.1 In situ measurements at Imperial College London

Atmospheric methane mole fractions and $\delta^{13}CH_4$ measurements have been made at Imperial College London using a Picarro G2201-i isotopic analyser since early 2018. Ambient air is sampled from an air inlet ~ 26 magl. The air inlet is mounted on a 2 m mast on the southeast corner of the Huxley building roof (51.4999^{o}N, 0.1749^{o}W; Fig. 3.1) and is approximately level with the surrounding rooftops. The Picarro isotopic analyser uses Cavity Ring-Down Spectroscopy (CRDS). This technique is based on measuring the optical extinction of



Figure 3.1: Measurement site at Imperial College London. (a) View of mounted air-inlet and weather station on the rooftop of the Huxley Building. (b) Location of the Huxley building (red arrow) in reference to the area surrounding the site. (c) Location of air-sampling from the Huxley building (red star) in reference to the South-Kensington area.

gaseous samples that scatter and absorb light*. As atmospheric trace gases, such as CO_2 and CH_4, absorb light at specific wavelengths their mole fractions from an air sample can be calculated using CRDS. Within the Picarro instrument a laser beam is emitted into a small optical cavity containing mirrors to increase the path length and light intensity (through constructive interference) to some specified, threshold intensity. Once this intensity is reached the laser is switched off and the beam exponentially decays through the cavity. When a gaseous, absorbing sample is placed in the cavity the decay time will decrease. Different absorbing gases have different light intensity decay rates. Through measuring the time taken for the light to reach $1/e$ of the threshold intensity the mole fraction of the absorbing substance in the gas sample can be calculated.

The Picarro G2201-i atmospheric measurements are averaged into 1-, 5-, 20-, and 60-minute intervals by GCWerks software (http://www.gcwerks.com), which is used for automating the monitoring and recording of observations. There are gaps in the measurement data from times when the Picarro instrument was being used for laboratory tests. A weather station (ClimeMet) is also mounted to the mast and measures 5-minute averaged wind speed and direction as well as atmospheric pressure and temperature.

*"light" referring to any electromagnetic radiation.

There are several large potential sources of CH_4 in the vicinity of ICL that may influence atmospheric CH_4 and $\delta^{13}CH_4$ measurements. The locations of some of these sources are shown in Fig. 3.2 with the UK NAEI CH_4 1 km^2 resolution emissions superimposed. There are ~ 20 small sewage pumping stations and a waste facility south of the site in the Battersea area. The precise locations of the sewage pumping stations are unknown and there are potentially more in the Battersea area that have not been reported to Thames Water, who now manage all sewage pumping stations in London (Thames Water, *personal communication, 14 October 2020*).

There is an on-campus natural gas-fired power station located in the basement of the Electrical and Electronic Engineering building (~ 200 m east of the inlet) with the stack emitting at ~ 52 magl. (Sparks and Toumi 2010). Eddy-covariance measurements of CO_2 previously conducted from the top of the adjacent building frequently detected emissions from the power station and found a mean CO_2 flux of 18.6 μmol CO_2 m^{-2} s^{-1} from the power station (Sparks and Toumi 2010). This was ~ 70% smaller than the UK CO_2 NAEI estimates

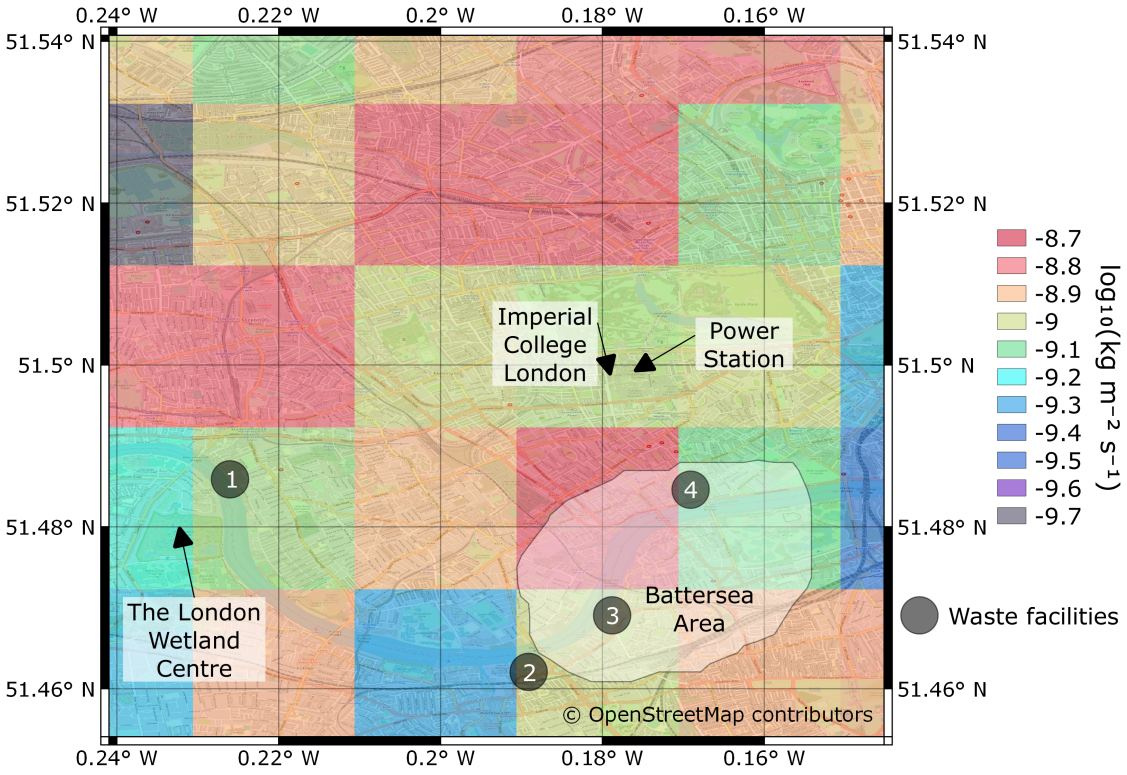


Figure 3.2: Map of the surrounding area of Imperial College London with the UK CH_4 1 km^2 NAEI estimates for the year 2017 overlaid. The locations of large CH_4 sources are indicated. ©OpenStreetMap contributors 2019. Distributed under the Open Data Commons Open Database License (ODbL) v1.0.

of the power station emissions at the time. The UK NAEI inventory currently estimates CH_4 emissions of 3.47×10^3 kg CH_4 yr^{-1} from the power station (NAEI 2017).

3.1.1 Laboratory setup

Ambient air is drawn into the ICL lab system through a 3/8″ Synflex tube using a 30 L min^{-1} KNF LABOPORT pump. Air is dried to water levels of 0.01% using a Nafion Perma Pure gas dryer (PD-50-24) in the split sample configuration with a 5 L min^{-1} diaphragm pump for counterflow. As the Nafion dryer was installed in August 2019, sample air between March 2018 and August 2019 needed a water "correction" to account for the higher water levels in these measurements. A Picarro 16-port manifold is used to switch valves and direct either outside air or air from the standard tank (used for calibration) into the Picarro. A pressure controller is used between the manifold and Picarro inlet to keep the inlet pressure constant at ~ 14 psia (96.5 kPa).

An Allan precision (Allan 1966) was calculated to measure the noise and drift response of the instrumentation across different averaging times. Two air tanks with ambient CH_4 mole fractions and $\delta^{13}CH_4$, referred to as the "low" standard (1900 ppb, -48.0‰) and the "high" standard (2000 ppb, -47.0‰), have each been measured continuously for 24 h. An averaging time of four minutes gives Allan precisions of 0.3‰ for the low standard tank and 0.2‰ for the high standard tank $\delta^{13}CH_4$ values (Fig. 3.3). These values are consistent with previous tests performed using Picarro G2201-i instruments (Rella et al. 2015; Miles et al. 2018). As Allan precisions are less than 0.1‰ for averaging times of 20 minutes, 20-minute GCWerks averaged atmospheric measurements are used.

3.1.2 Calibration procedure and uncertainties

Different calibration procedures were tested using one air tank as a working standard to correct for instrument drift and another air tank as a target tank to assess the standard deviation of the measurements. It is assumed the response of the instrument was linear within the observed range (-50‰ to -42‰, 1900 ppb to 4000 ppb) (Rella et al. 2015) and the working standard is stable. A one-point calibration is applied by measuring the working standard once per day for an hour. The "bracketing technique" was used to correct for instrumental drift; i.e. the measurements were calibrated against the time-interpolated value of two adjacent standard tank measurements. There was an average daily drift of 0.25 ppb for CH_4 and 0.7‰ for $\delta^{13}CH_4$. Both air tanks were calibrated against two primary standards that were prepared at the Max Planck Institute for Biogeochemistry (MPI-BGC). Specific guidelines for calibration procedures of $\delta^{13}CH_4$ were not reported in the latest Global Atmospheric Watch (GAW) (20th World Meteorological Organisation (WMO)/International Atomic Energy

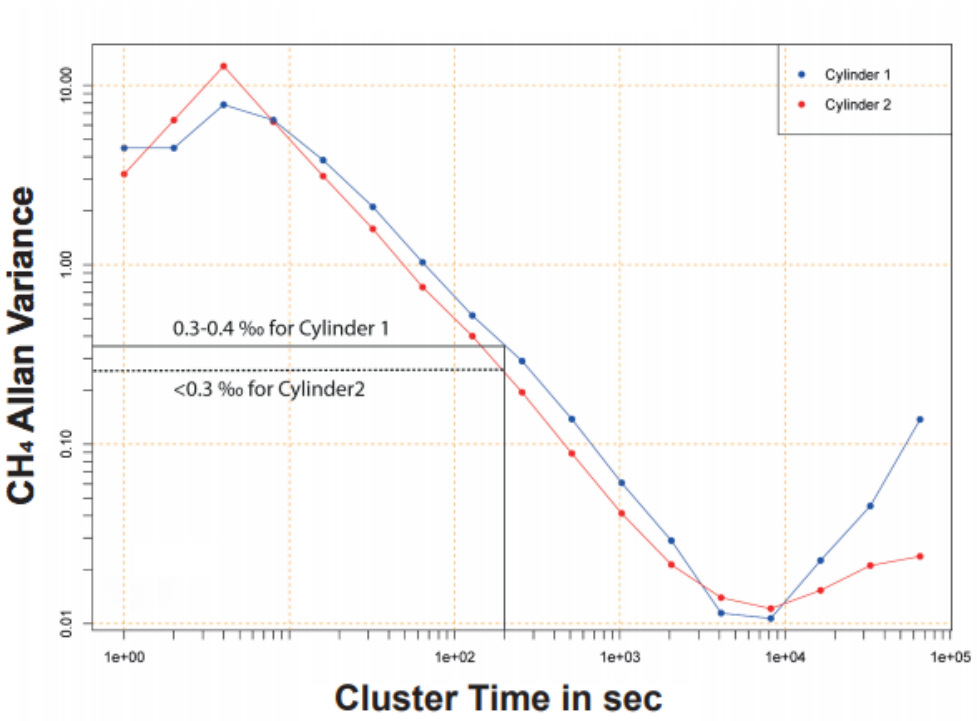


Figure 3.3: Allan variance of $\delta^{13}CH_4$ values for two working standards. Cylinders 1 and 2 are the low and high standard tanks, respectively. The vertical line denotes four minutes. (Figure courtesy of Giulia Zazzeri).

Agency (IAEA) Meeting on Carbon Dioxide, Other Greenhouse Gases and Related Measurement Techniques (GGMT-2019)), so each laboratory has to develop a customised calibration routine.

Primary standards had a $\delta^{13}CH_4$ uncertainty of 0.20‰ (JRAS-M16 scale) but an uncertainty for CH_4 mole fractions was not provided. The working standards had uncertainties of 0.2 ppb for CH_4 and 0.18‰ for $\delta^{13}CH_4$, which are based on the standard deviation of the measurements calibrated against the primary standards. Propagating the error of the primary standard gives a $\delta^{13}CH_4$ uncertainty of 0.27‰ for the working standard.

Calibrations based on the *ratio* or the *offset correction* between the measured value of the standard and the assigned calibrated value were tested. Ratio-based calibration adjusts the slope, thus the correction varies with the measured value, whereas offset correction-based calibration adjusts the intercept and the correction does not vary across the measured value. Some studies recommend calibration of individual isotopologues (Griffith 2018), while others use $\delta^{13}CH_4$ (Rella et al. 2015). The following calibration procedures for $\delta^{13}CH_4$ were tested:

1. The $^{13}CH_4$ and $^{12}CH_4$ mole fractions were calibrated independently based on the *ratio* and then a

calibrated $\delta^{13}CH_4$ was computed.

2. The $^{13}CH_4$ and $^{12}CH_4$ mole fractions were calibrated independently based on the *offset correction* and then a calibrated $\delta^{13}CH_4$ was computed.

3. The $\delta^{13}CH_4$ values were calibrated directly based on the *ratio*.

4. The $\delta^{13}CH_4$ values were calibrated directly based on the *offset correction*.

The different calibration procedures were applied to the 20-minute averaged measurements of the target tank from May 2019 to November 2019. All the calibration procedures performed comparably and reduced the standard deviation of the target tank $\delta^{13}CH_4$ values from 1.1‰ to 0.2‰. A one-point calibration based on the ratio between the measured standard tank value and the assigned $\delta^{13}CH_4$ values is applied, which is also the default calibration procedure used by GCWerks software. Rella et al. (2015) also applied calibration constants on the $\delta^{13}CH_4$ values rather than on the $^{13}CH_4$ values. Whilst a two-point calibration yields a smaller uncertainty it could not be performed as the $\delta^{13}CH_4$ values of the two standard tanks (where one is used as the target tank) are too similar, differing by 0.3‰, and it is assumed the working standard tank is stable over time. The total CH_4 mole fraction was calculated using calibrated $^{12}CH_4$ and $\delta^{13}CH_4$ values, where $^{12}CH_4$ was also calibrated using a one-point calibration based on the ratio of the measured and assigned values. The standard deviation of calibrated CH_4 mole fractions and $\delta^{13}CH_4$ in the target tank is regarded to be the best indicator of the ICL measurement uncertainty, at 0.28 ppb and 0.2‰ for 20-minute averages after May 2019 and 1.8 ppb and 0.6‰ before May 2019. The mean of the standard deviations of each standard tank is 0.18 ppb and 0.5‰ before May 2019 and 0.16 ppb and 0.4‰ after May 2019, for CH_4 and $\delta^{13}CH_4$ respectively. The larger uncertainty before May 2019 is likely related to unexplained larger variations in the measurements of one of the reference tanks.

A correlation between atmospheric pressure and $\delta^{13}CH_4$ is found in the raw measurements, which has been observed for CO in other Picarro analysers (Yver Kwok et al. 2015). The daily working tank calibrations removed the effect of atmospheric pressure variations over more than one day. For some days when atmospheric pressure changed rapidly within one day, artefacts appeared in $\delta^{13}CH_4$. The $\delta^{13}CH_4$ measurements were inspected for periods of high variability in atmospheric pressure and manually flagged to remove these artefacts.

Here, atmospheric measurements at ICL were compared to the $\delta^{13}CH_4$ observations at the Mace Head Observatory carried out by the Institute of Arctic and Alpine Research (INSTAAR) of the University of Colorado. Therefore, a value of +0.28‰ is applied to correct for the laboratory offset between INSTAAR and MPI-BGC measurements (Umezawa et al. 2017).

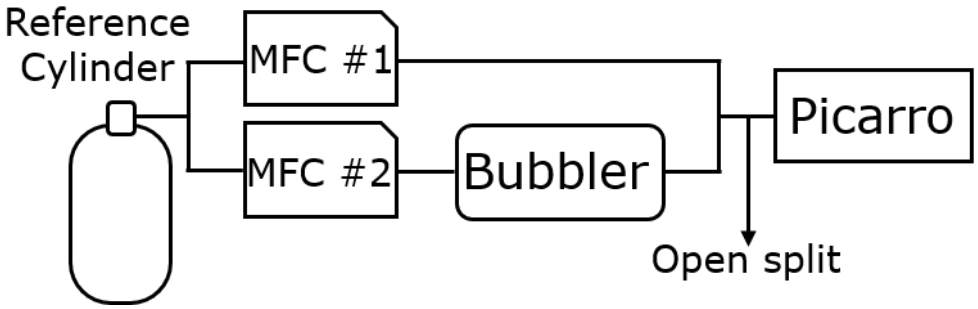


Figure 3.4: Experimental setup used for the water correction. The bubbler is a 1 L stainless steel vessel filled with 0.3 L of distilled water. The mass flow controller (MFC) is a red-y smart series meter (red-y GSC-B flow rate 0-1000 sccm).

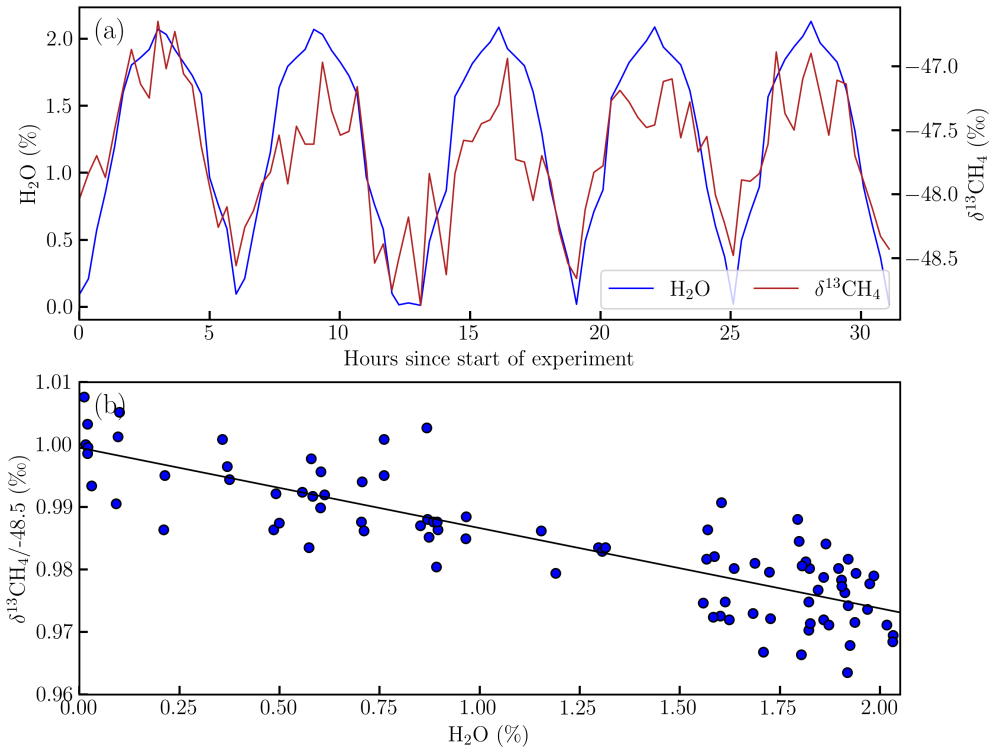


Figure 3.5: Imperial College London water correction experiment data. Panel (a) $\delta^{13}CH_4$ values measured during the experiment to correct isotopic data for water vapour along with water concentration values. Panel (b) regression line of the ratio of wet-to-dry $\delta^{13}CH_4$ values against the water correction.

3.1.3 Water correction

A cross interference from water has been observed on the $\delta^{13}CH_4$ values during the period March 2018 to August 2019 when sample air was not dried. Rella et al. (2015) state the gas stream should be dried to < 0.1‰ water vapour content to increase measurement accuracy. Data measured before applying the Nafion dryer were corrected for the water vapour influence. To determine the correction coefficients, the water vapour concentration of a working standard with a $\delta^{13}CH_4$ value of -48.5‰ was varied using the setup in Fig. 3.4. Two mass flow controllers were used to adjust the flow rates through the bubbler (Fig. 3.4) enabling the water correction values to be calculated for water vapour content between 0‰ to 2.2‰. Five measurement cycles (each lasting ~ 6 h) with $\delta^{13}CH_4$ values increasing with water vapour concentration are shown in Fig. 3.5a. The correction coefficients were determined by applying a least squares regression on the ratio of wet-to-dry $\delta^{13}CH_4$ values against water vapour concentration (Fig. 3.5b). Using the calibrated working standard $\delta^{13}CH_4$ value of -48.5‰ as the dry value, the following equation to correct for the water dependency was calculated:

$$\text{dry data} = \text{observed data} \times (-0.0109\ X_{H2O} + 1.0023)^{-1}. \tag{3.1}$$

The errors of the linear regression parameters from the water vapour correction experiment were ~ 10^{-3}‰ suggesting there is no additional uncertainty resulting from the water vapour correction. No water interference on the CH_4 mole fraction measurements was found.

3.2 Bottom-up emissions data

Methane emissions can be calculated through a bottom-up approach. Emission rates of CH_4 sources and their activity data are used to model the emissions of specific CH_4 sources for some geographical region. Some CH_4 emission datasets use satellite measurements of the atmospheric composition as additional constraints, but most of the bottom-up emissions datasets used in this thesis do not include measurements of the well-mixed atmosphere in their emission estimates.

Spatially resolved, disaggregated CH_4 emissions are available from the different emission datasets that are used in this thesis. There are, however, differences in their spatiotemporal resolutions, the sources of data used to construct the emissions data, and how CH_4 emissions from different sources are aggregated.

3.2.1 Anthropogenic emissions: EDGAR

Global anthropogenic greenhouse gas emissions are captured in the Emissions Database for Global Atmospheric Research (EDGAR) inventories that provide modelled emissions for 26 anthropogenic source sectors as specified by the IPCC (IPCC 2006). Methane emissions are available for 19 of the anthropogenic source sectors in EDGAR (Table 3.1).

EDGAR uses a large set of activity data, that covers a range of anthropogenic activities, to estimate CH_4 emissions (Solazzo et al. 2021) in a consistent and "IPCC-compliant" approach (Crippa et al. 2018; Janssens-Maenhout et al. 2019). Activity data is compiled from "international statistics" (Janssens-Maenhout et al. 2012) and is combined with emission factors (from the IPCC; IPCC 2006) to calculate sectoral emissions for each country. Some emissions, such as combustion sources, are calculated by simply multiplying the activity data with their emission factor. Whereas other sources, such as emissions from the waste sector, require more complex models to estimate their CH_4 emissions (Solazzo et al. 2021).

Spatially disaggregated greenhouse gas emissions are produced as gridded-maps with a $0.1^o \times 0.1^o$ spatial resolution. The EDGAR inventory is updated about once a year with new versions extending the time-series and improving the spatial distribution and magnitude of greenhouse gas emissions. Monthly CH_4 emissions were available for the year 2015 in EDGAR v5.0, whereas only annual estimates were available in previous versions of EDGAR (e.g. EDGAR v4.3.2).

Gridded methane emissions from EDGAR v4.3.2 for the year 2012 (Fig. 3.6a) and from EDGAR v5.0 for the year 2015 (Fig. 3.6c) are used in this thesis. Methane emissions from the UK (including the North Sea) for 2012 in EDGAR v5.0 (Fig. 3.6b) were more than double the emissions in EDGAR v4.3.2 for the same year (Table 3.1). The increase in emissions can be attributed to landfill CH_4 increasing by $\sim$ 1.5 Tg CH_4 yr^{-1} in EDGAR v5.0 across the UK (Table 3.1). UK methane emissions in EDGAR v4.3.2 and v5.0 are dominated by landfill, ruminant animals, and fugitive fossil (e.g. leaks from distribution pipes in the natural gas network) emissions with their proportions varying between versions of EDGAR (Table 3.1).

Whilst an overall increase in UK CH_4 emissions is found in EDGAR v5.0 compared to EDGAR v4.3.2 for the same year, there are large differences in emissions for urban areas such as London, Manchester, and Birmingham, which have smaller CH_4 emissions in EDGAR v5.0 (Fig. 3.6d). The reason for this difference is

unexplained and seems to contrast the general findings that urban areas tend to underestimate CH_4 emissions (Brandt et al. 2014). This shows that emissions in urban areas are particularly uncertain and in need of additional constraints.

Uncertainties of EDGAR emissions data were, until EDGAR v5.0, specified through uncertainty factors for different groups of countries (Crippa et al. 2019). For example, the relative CH_4 uncertainty factor for countries in the EU-15 in EDGAR v4.3.2 for the year 2012 is 32% (Crippa et al. 2019). An uncertainty factor was not provided for the UK nor for the disaggregated emission sectors.

An uncertainty analysis of EDGAR v5.0 2015 CH_4 emissions factors and activity data for energy-, industrial process-, agriculture-, and waste-related emissions for the largest emitting countries was made by Solazzo et al. (2021). For the UK, an uncertainty of 22% was only reported for agricultural related CH_4 emissions, but not for the other emission source sectors.

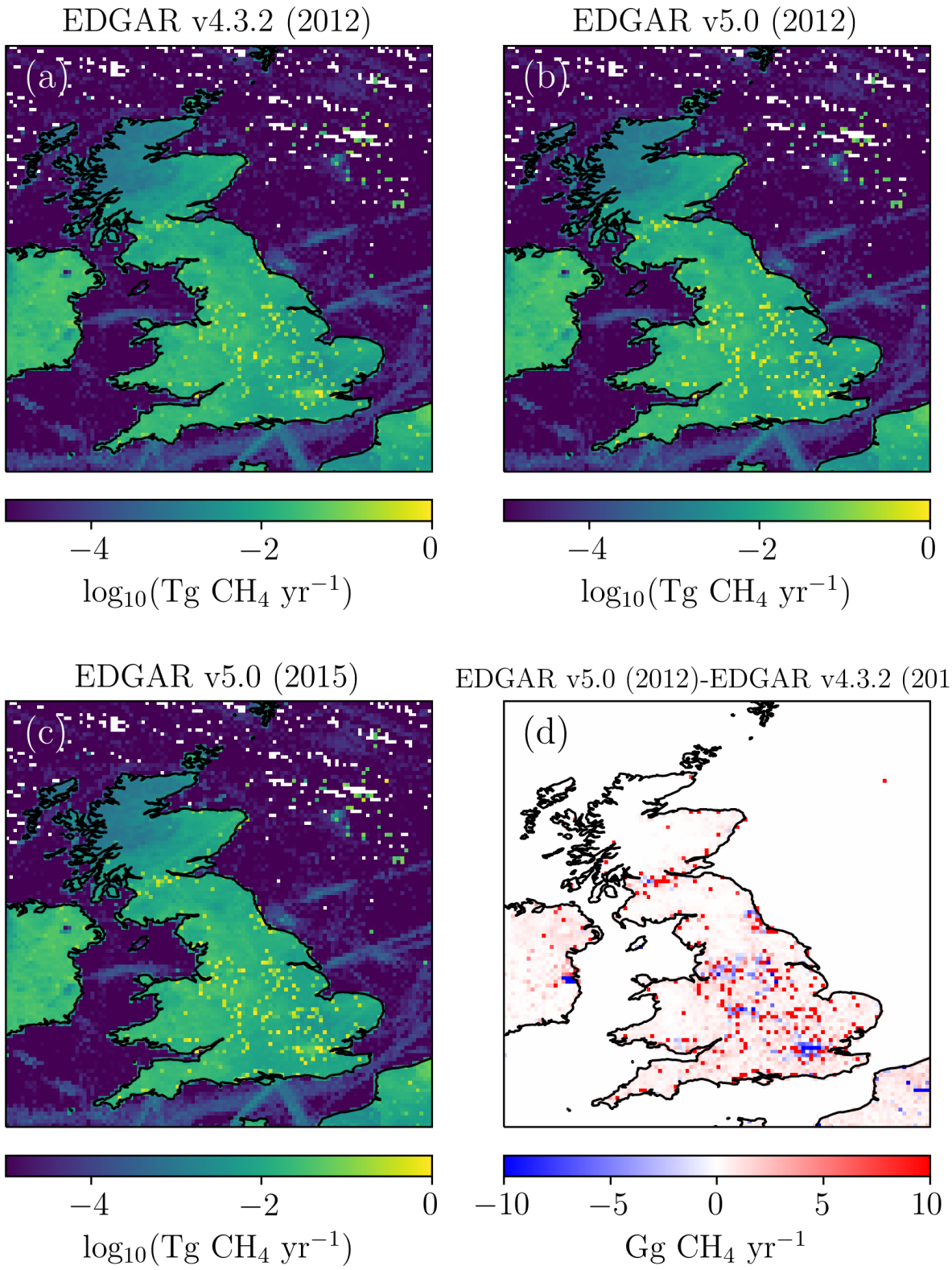


Figure 3.6: Methane emissions over the UK from EDGAR (a) v4.3.2 for the year 2012, (b) v5.0 for the year 2012, (c) v5.0 for the year 2015. The difference between EDGAR v5.0 and EDGAR v4.3.2 for the year 2012 is shown in (d).

Table 3.1: EDGAR v4.3.2 and v5.0 CH_4 emissions for the UK (including the North Sea and the Channel). Proportion of each source sector are shown in parentheses.

Source Sector	IPCC 1996 sector Specification	EDGAR v4.3.2 (2012) (Tg CH_4 yr^{-1})	EDGAR v5.0 (2012) (Tg CH_4 yr^{-1})	EDGAR v5.0 (2015) (Tg CH_4 yr^{-1})
Combustion in energy production and transfer	1A1a	6.7×10^{-3} (0.22%)	9.8×10^{-1} (0.22%)	9.6×10^{-3} (0.21%)
Oil refineries and transformation industry	1A1b, 1A1c, 1A5b1, 1B1b, 1B2a5, 1B2a6, 1B2b5, 2C1b	8.5×10^{-3} (0.28%)	9.0×10^{-3} (0.20%)	7.6×10^{-3} (0.17%)
Combustion from industry	1A2	2.0×10^{-3} (0.07%)	2.1×10^{-3} (0.05%)	2.8×10^{-3} (0.06%)
Aviation	1A1a	1.2×10^{-4}(0.01%)	2.1×10^{-4}(0.00%)	2.3×10^{-4}(0.00%)
Road vehicles	1A3b	7.8×10^{-3} (0.26%)	7.7×10^{-3} (0.17%)	7.3×10^{-3} (0.16%)
Railways, pipelines, off-road transport	1A3c, 1A3e	1.1×10^{-4} (0.00%)	1.1×10^{-4} (0.00%)	1.1×10^{-4} (0.00%)
Shipping	1A3d, 1C2	1.8×10^{-3} (0.06%)	1.6×10^{-3} (0.04%)	1.7×10^{-3} (0.04%)
Non-industrial combustion	1A4	2.3×10^{-2} (0.78%)	3.6×10^{-2} (0.80%)	4.0×10^{-2} (0.87%)
Fugitive fossil	1B1a, 1B2a1, 1B2a2, 1B2a3 1B2a4, 1B2c	0.65 (21.7 %)	0.63 (13.8 %)	0.54 (11.9 %)
Chemical processes	2B	2.2×10^{-3} (0.07 %)	2.2×10^{-3} (0.05 %)	2.2×10^{-3} (0.05 %)
Iron and steel production	1C1a, 1C1c, 2C1d, 1C1e, 2C1f, 2C2	8.6×10^{-6} (0.00%)	5.6×10^{-4} (0.01%)	7.3×10^{-3} (0.02 %)
Enteric fermentation	4A	0.96 (32.1 %)	0.98 (21.6 %)	1.00 (22.0 %)
Manure management	4B	0.17 (5.75%)	0.17 (3.79%)	0.18 (3.92%)
Agricultural soils	4C, 4D	0.0 (0.00%)	0.0 (0.00 %)	0.0 (0.00%)
Agricultural waste burning	4F	2.0×10^{-3} (0.06%)	2.0×10^{-3} (0.04%)	2.4×10^{-3} (0.05%)
Landfills	6A, 6D	1.00 (33.2%)	2.53 (56.0%)	2.6 (57.3%)
Waste water handling	6B	0.13 (4.32%)	0.13 (2.82%)	0.13 (2.81%)
Solid waste incineration	6C	0.03 (1.03%)	0.03 (0.57%)	0.02 (0.51%)
Fossil fuel fires	7A	0.0 (0.00%)	0.0 (0.00%)	0.0 (0.00%)
Total		3.00	4.54	4.56

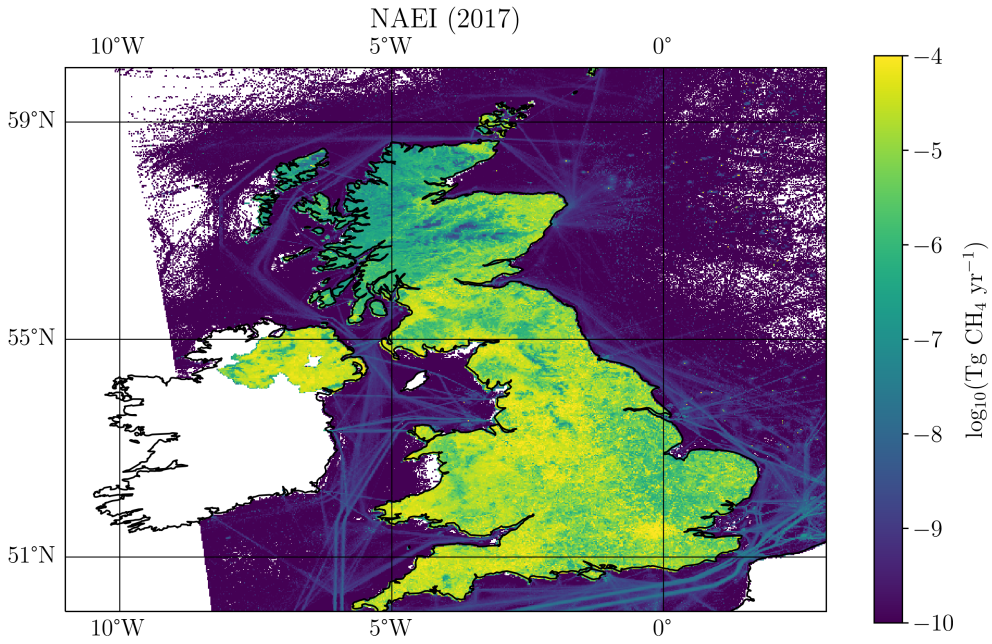


Figure 3.7: Methane emissions, including point source emitters, for the UK from NAEI for the year 2017.

3.2.2 Anthropogenic emissions: UK NAEI

Similar to the EDGAR greenhouse gas emission inventories, the UK National Atmospheric Emissions Inventory (NAEI) provide spatially resolved, disaggregated anthropogenic emission estimates. Methane emissions are available at a 1×1 km^2 spatial resolution for 10 source sectors (Table 3.2) at a yearly temporal resolution. NAEI only produces modelled emissions for the UK and gridded emission maps are only available for the most recent year. Annual CH_4 emissions for the whole UK for different source sectors are available from 1990 onwards.

Emissions are calculated similarly to EDGAR, where an emission factor is combined with activity data. Activity data is sourced from UK statistics, modelled, or provided directly from emission source operators (e.g. emissions from industrial stacks) (NAEI 2017; Ricardo Energy & Environment 2019; Richmond et al. 2019). Emission factors are UK-specific derived from UK research, literature sources, peer-reviewed publications and source operators (Richmond et al. 2019).

Emissions are considered as either "point" sources or "area" sources in NAEI. Point source emitters have a well-defined location and can be directly mapped. Emissions from point sources are usually reported directly from their official source operators (Ricardo Energy & Environment 2019) and are available separately from the sectoral emissions. Area source emitters are defined as sources with smaller and more

widely distributed/diffuse emissions (NAEI 2017). Typically, there is a lack of information about the location and emissions of area sources so appropriate proxy statistics are used to calculate the spatial emissions (Ricardo Energy & Environment 2019; Richmond et al. 2019). The approach for calculating emissions from each source sector varies according to the available data (Ricardo Energy & Environment 2019).

Table 3.2: UK 2017 NAEI CH_4 emissions (and their proportions) for different source sectors along with the correspondence that I used for the allocation of sources between NAEI and EDGAR. Total emissions include point sources.

Source sector	UK NAEI SNAP sector	IPCC 1996 sector specification	UK Emissions (Tg CH_4 yr^{-1})
Combustion in energy production and transfer	SNAP 01	1A1a	3.50×10^{-4} (0.02%)
Non-industrial combustion	SNAP 02	1A4	3.80×10^{-2} (1.83%)
Combustion in industry	SNAP 03	1A2	2.20×10^{-3} (0.11%)
Production processes	SNAP 04	2B, 2C1a, 2C1c, 2C1d, 2C1e, 2C1f, 2C2	7.02×10^{-6} (0.00%)
Extraction and distribution of fossil fuels	SNAP 05	1A1b, 1A1c, 1A5b1, 1B1a, 1B1b, 1B2a, 1B2b5, 1B2c	0.15 (7.21%)
Road transport	SNAP 07	1A3b	3.60×10^{-3} (0.17%)
Other transport	SNAP 08	1A3a, 1A3c, 1A3d, 1A3e, 1C2	1.90×10^{-3} (0.09%)
Waste treatment and disposal	SNAP 09	6A, 6B, 6C, 6D	0.75 (36.1%)
Agriculture	SNAP 10	4A, 4B, 4C, 4D	1.00 (48.1%)
Nature	SNAP 11	5A, 5B, 5C, 5E	0.04 (1.92%)
Point sources			0.08 (3.85%)
Total			2.08

Here, the 2017 gridded NAEI CH_4 emissions are used (Fig. 3.7). Total UK CH_4 emissions are estimated at 2.08 Tg CH_4 yr^{-1} for 2017, which is substantially less than the UK emission estimates in EDGAR v4.3.2 for the year 2012 (3.00 Tg CH_4 yr^{-1}) and EDGAR v5.0 for the year 2015 (4.56 Tg CH_4 yr^{-1}). Methane emissions from the UK in NAEI decreased by approximately 0.33 Tg between 2012 and 2017 (NAEI 2017) indicating

emission reductions over time are not entirely responsible for this discrepancy between inventories.

Agricultural emissions account for around half the 2017 UK CH_4 NAEI emissions (Table 3.2). Waste emissions and fugitive fossil emissions also form a significant part of the UK CH_4 emissions budget, comprising $\sim$ 35% and $\sim$ 7.2% respectively.

The two anthropogenic inventories use different sectoral definitions. The UK NAEI uses CORINAIR Selected Nomenclature for sources of Air Pollution (SNAP) in which sources are allocated to one of 11 categories, whereas EDGAR follows the IPCC 1996 source sector specification where sources are allocated to one of seven categories and then further subdivided. For example, emissions from landfills in EDGAR form a subset of waste sector emissions (category number 6) and are specified as category 6A (Table 3.2), whereas in NAEI all waste emissions are aggregated under SNAP 09. Table 3.2 shows how sources are aligned between these inventories. Land-use change emissions are also modelled in NAEI (SNAP 11; Table 3.2) but are not included in EDGAR.

Uncertainties in NAEI emissions maps are quantified through data "quality ratings" as there is no internationally agreed approach for estimating spatially resolved emission uncertainties (Richmond et al. 2019). Data quality ratings range from 1 (highest quality) to 5 (lowest quality) for area sources, and 1 (highest quality) to 2 (lowest quality) for point sources. Point source data are considered more accurate and precise in their emissions and locations. Point source data with a quality rating of 1 are associated with emissions that are precisely "known" and a quality rating of 2 denotes modelled point source data. Quality ratings for area sources are based on the quality of the spatially resolved data and its reliability. Whilst this approach does not provide a full numerical uncertainty analysis of the emissions it does indicate where improvements in the emissions maps are needed.

3.2.3 Wetland emissions: WetCHARTs

Methane emissions from wetlands are excluded from the EDGAR and NAEI inventories, which only report anthropogenic greenhouse gas emissions. As wetlands are the largest natural source of CH_4 emissions they cannot be discounted from studies of regions that likely have significant amounts of CH_4 emissions from wetlands.

WetCHARTs (Bloom et al. 2017) provides estimates of global, monthly wetland CH_4 emissions based on an ensemble of data and models. These include satellite-derived surface water extent and precipitation reanalyses,

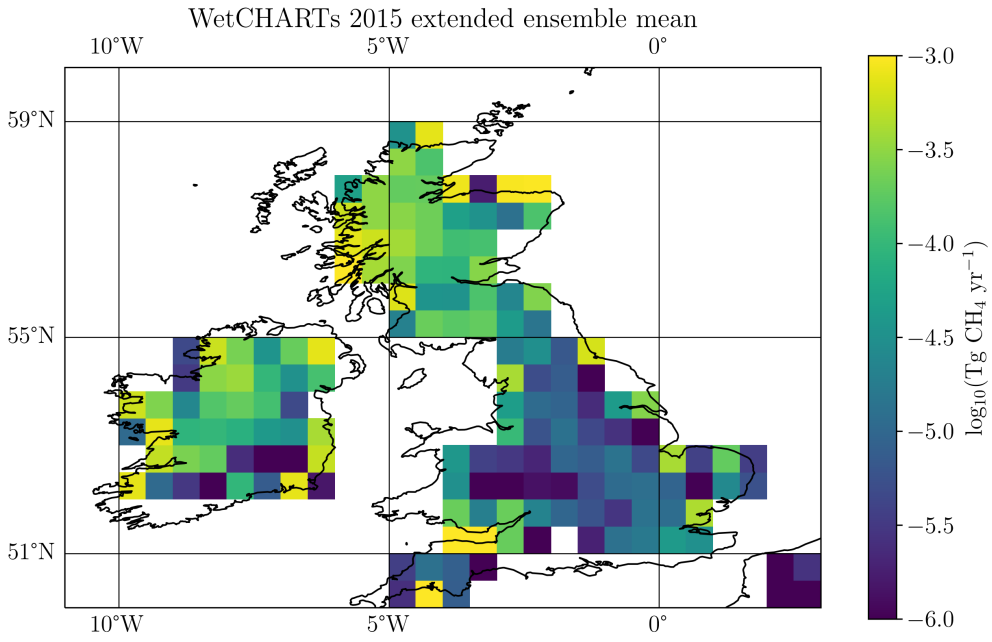


Figure 3.8: WetCHARTs 2015 extended ensemble mean CH_4 emissions over the UK.

nine heterotrophic respiration simulations and three CH_4:C temperature dependent parameterisations.

Two model outputs, both with $0.5^o \times 0.5^o$ spatial resolution, are available from WetCHARTs. The full-ensemble of wetland emissions is for 2009-2010 and uses 324 ensemble members. The extended-ensemble wetland emissions, available for 2001-2015, is a subset of the full-ensemble using 18 ensemble members. The mean of the 18 models in the 2015 extended-ensemble WetCHARTs emissions (Fig. 3.8) is used as they are the most recently available wetland estimates in WetCHARTs. Numerical uncertainties for WetCHARTs are not included in the extended-ensemble data product. Instead, the standard deviation of the ensemble estimates can be used.

Wetland emissions total $1.74 \times 10^{-2} \pm 1.36 \times 10^{-2} (1\sigma)$ Tg CH_4 yr^{-1} in the UK, where $\pm 1\sigma$ represents the standard deviation of the 18 ensemble estimates for the year 2015. Wetland emissions across the UK are much smaller than agricultural, waste and natural gas emissions in the anthropogenic inventories but slightly larger than CH_4 emissions from road transport and non-industrial combustion (Table 3.2). Seasonal changes in wetland emissions are captured in WetCHARTs with emissions largest in August and smallest in April.

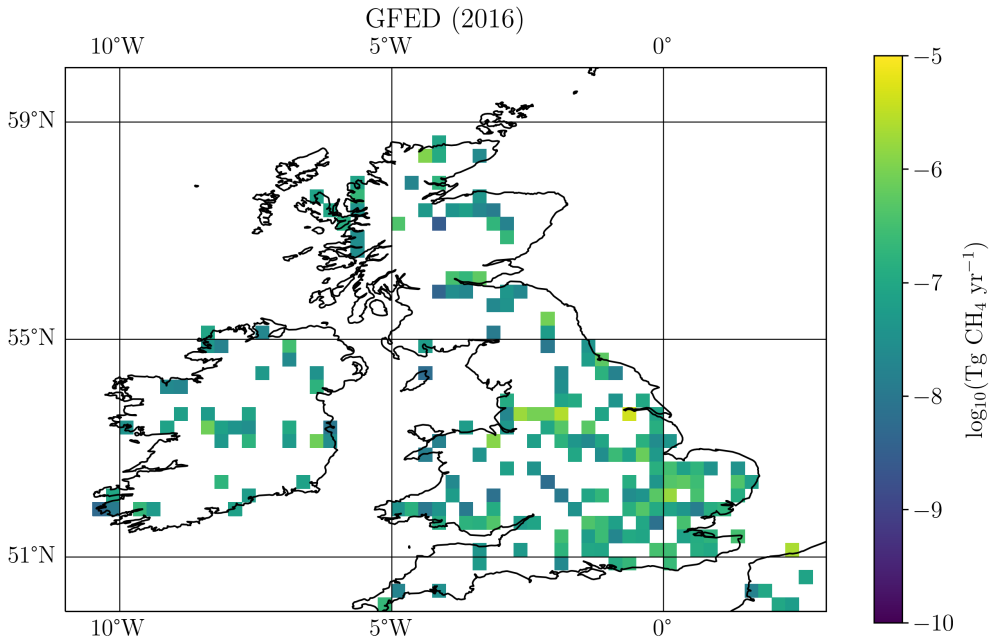


Figure 3.9: Biomass burning CH_4 emission estimates from GFEDv4.1s over the UK for the year 2016.

3.2.4 Biomass burning emissions: GFED

Large-scale CH_4 biomass burning emissions are not included in the gridded EDGAR and NAEI emissions. These inventories do include biomass burning emissions from waste incineration and agricultural waste burning. In EDGAR, agricultural waste burning and waste incineration emissions are separate from other agricultural and waste CH_4 emissions (Table 3.1). Whereas in NAEI, which has fewer disaggregated emission source sectors, they form part of the agricultural and waste source gridded emissions respectively (Table 3.2).

Agricultural waste burning emissions include the burning of farm waste such as crop residues and untreated wood (UK Environment Agency 2019). For waste incineration in the UK, approximately 27% of incinerated material* is wood (DEFRA 2021) and 34% is household waste, which may include other biomass material. Current UK policy (DEFRA 2021) is shifting municipal waste disposal from landfilling to incineration, which could potentially lead to an increase in regional biomass burning CH_4 emissions in the future.

The Global Fire Emissions Database (GFED) is a widely used global biomass burning emissions database (Saunois et al. 2020). The GFED was developed to better understand how fires impact the carbon cycle, air-quality and the climate (Van Der Werf et al. 2017). The fourth version of GFED (GFEDv4.1s; Van Der Werf

*For waste incineration without energy recovery.

Table 3.3: UK GFED biomass burning CH_4 emissions (and their proportion) by fire type and associated emissions factors for each kg of dry matter (DM).

GFED fire type	CH_4 emission factor g CH_4 kg^{-1} DM	UK CH_4 emissions (Tg CH_4 yr^{-1})
Agricultural waste burning	5.82	8.98×10^{-5}(67%)
Boreal forest	5.96	0.0 (0%)
Temperate forest	3.36	3.89×10^{-5} (29%)
Deforestation	5.07	0.0 (0%)
Peat fires	20.8	0.0 (0%)
Savanna, grassland and shrubland	1.94	4.81×10^{-6} (4%)

et al. 2017), which includes small fire emissions (Randerson et al. 2012), is used here. GFED is based on the Carnegie-Ames-Stanford approach (CASA) biogeochemical model and satellite observations of burned areas (Randerson et al. 2012; Van Der Werf et al. 2017).

Fire emissions from agricultural waste burning, peat fires, tropical deforestation, temperate boreal fires, savanna, and grassland and shrubland fires are captured in GFED at $0.25^o \times 0.25^o$ spatial resolution and monthly temporal resolution from 1997 to 2016. Emissions from 2016 were used for this thesis and were calculated by converting the dry matter emissions to CH_4 emissions using the emissions factors in Table 3.3. Collectively, GFEDv4.1s estimates biomass burning emits 1.42×10^{-4} Tg CH_4 yr^{-1} in the UK. The distribution of these emissions across the UK is shown in Fig. 3.9.

Agricultural waste burning is found to be the largest source of biomass burning CH_4 emissions in the UK (Table 3.3) forming nearly two-thirds of the biomass burning CH_4 budget. The rest of the budget is from savanna, grassland and shrubland fires, and temperate forest fires. Emissions from agricultural waste burning are slightly smaller in GFED than in EDGAR. To avoid double counting emissions, agricultural waste burning emissions were excluded from GFED.

3.2.5 Processing emissions data

Gridded emissions data need to be processed when being used with the atmospheric transport model output. The spatial grids of the emissions data and atmospheric model output must exactly match. This means the spatial domain, spatial resolution, and grid-cell boundaries must all align. When the spatial parameters of the

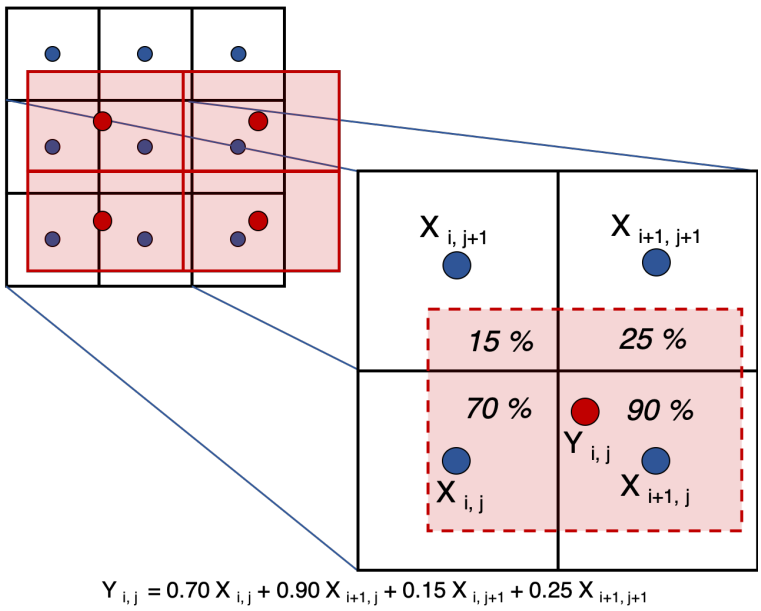


Figure 3.10: Schematic illustrating the process of regridding higher-resolution spatial data (black boxes with blue circles) to a lower-resolution with different grid-cell boundaries (red boxes with red circles).

gridded emissions data do not exactly match those of the atmospheric model output, the emissions data need to be “re-gridded”.

A conservative approach is taken for regridding emissions data of a higher spatial resolution to a lower spatial resolution. The proportion of each overlapping grid cell in the higher resolution data with the lower resolution regridded data grid cells is calculated as illustrated in Fig. 3.10. Emissions from each of the higher-resolution grid cells are multiplied by the proportion of overlap with the lower-resolution grid cell and summed to calculate the emission coming from the regridded data grid cell. An example is shown in Fig. 3.10 where the overlap of four higher-resolution grid cells with the lower resolution (regridded) grid cell are 70%, 90%, 15%, and 25%. The proportion of overlap is multiplied by the respective emission from their higher resolution grid cell ($X_{i,j}$, $X_{i+1,j}$, $X_{i,j+1}$, $X_{i+1,j+1}$) and summed to calculate the emission value for the regridded grid cell $Y_{i,j}$.

3.3 Atmospheric model

The general procedure for simulating CH_4 concentrations is to use an atmospheric model to “transport" surface emissions to a receptor site (e.g. the measurement site at Imperial College London) over a specified duration. In this thesis, the Numerical Atmospheric dispersion Modelling Environment (NAME) developed by the UK

Met Office (Jones et al. 2007) is used. The different parameter specifications used in NAME to generate different back-trajectories are described below along with the approach for simulating CH_4 concentrations using emissions inventories and NAME back-trajectories.

3.3.1 Overview of NAME

NAME is a Lagrangian dispersion model initially developed in 1986 to predict the spread and deposition of nuclear fallout from the Chernobyl disaster. Since then the modelling capabilities of NAME have been improved and extended to meet a wide range of applications including the modelling of volcanic ash clouds (e.g. Webster et al. 2012) and the spread of air-borne diseases (e.g. Hagenaars et al. 2011) at both short-range and global scales.

The atmospheric transport of trace gases emitted from sources to a single or multiple receptor sites can be modelled in NAME by tracking the advection of model particles (sometimes referred to as “theoretical particles") through the atmosphere. As NAME is a Lagrangian particle dispersion model it can be set to run forwards or backwards in time. In theory, the same source-receptor relationship should be obtained when running NAME in forwards or backwards mode. The source-receptor relationship is more efficiently calculated when NAME is run backwards (Arnold et al. 2018), particularly when the number of sources exceeds the number of receptor locations (Manning et al. 2011).

Running NAME in forwards mode involves calculating the dispersion of model particles emitted from sources and tracking the particles to receptor locations for some specified amount of time. When NAME is run backwards, the back-trajectories of particles arriving at the receptor site over some specified duration is calculated. In this way, back-trajectories can be used to determine the likely origin of trace gases arriving at a receptor site.

An advantage of running NAME in forwards mode is that source parameters (e.g. emission rate, location, height) can be included in the NAME input file to improve the accuracy of the source dispersion plume. However, a much larger number of model particles are needed compared to running NAME backwards, particularly if assessing source-receptor relationships that span distances greater than tens of kilometers and/or at a high spatial resolution. A sufficiently large number of particles arriving at the receptor site is needed as the particle number model error is defined as the inverse square-root of the number of particles per grid cell (Jones et al. 2007). A small number of particles in a grid cell could be considered as statistical noise from the dispersion plume.

Larger particle numbers at the receptor site can be achieved when NAME is run backwards. Specific details about the sources (e.g. the height emissions are released into the atmosphere), cannot be included when running NAME backwards. Details about the receptor site (e.g. height) can be specified in the NAME input file.

NAME is driven by a random walk turbulence scheme combined with meteorological data from the Met Office's Unified Model (UM); a numerical weather prediction model. The random walk scheme is coupled with meteorological data to force the transport of model particles rather than let particles be entirely driven by their own physics (Jones et al. 2007).

3.3.2 Back-trajectories from NAME

NAME back-trajectories are outputted as the time-integrated near surface (0-40 magl) air concentration (g s m^{-3}) in each grid cell resulting from a specific release rate (g s^{-1}) from the receptor site. "Footprints" of surface emission sensitivities are calculated by dividing the back-trajectory air concentration by the total mass emitted during the 1 h release time and multiplying by the geographical area of each grid cell. Each cell of the footprint describes the impact an emission from that grid cell would have on the concentration at the receptor site at a certain time (Arnold et al. 2018; Manning et al. 2011; Rigby et al. 2012).

The UM global meteorological fields used in NAME have a $0.1406^o \times 0.0938^o$ spatial resolution and the UKV UM meteorological fields used for the UK part of the model domain have a $0.0135^o \times 0.0135^o$ spatial resolution for the period considered. As atmospheric CH_4 can be considered chemically inert on the spatiotemporal scales used in this thesis, the NAME parameters for representing chemistry, deposition, and radioactive decay

Table 3.4: NAME model parameters used for each set of footprints.

Footprint ID	Horizontal spatial resolution	Particle release rate	Back-trajectory duration	Model domain
25 km	$0.352^o \times 0.234^o$	2×10^4 h^{-1}	30 days	-97.9 ^{o}E to 38.7 ^{o}E 10.8 ^{o}N to 79.2 ^{o}N
10 km	$0.10^o \times 0.10^o$	2×10^4 h^{-1}	6 days	-25.0 ^{o}E to 25.0 ^{o}E 30.0 ^{o}N to 70.0 ^{o}N
2 km	$0.02^o \times 0.02^o$	1.5×10^4 h^{-1}	6 days	-10.5 ^{o}E to 4.8 ^{o}E 49.3 ^{o}N to 61.8 ^{o}N

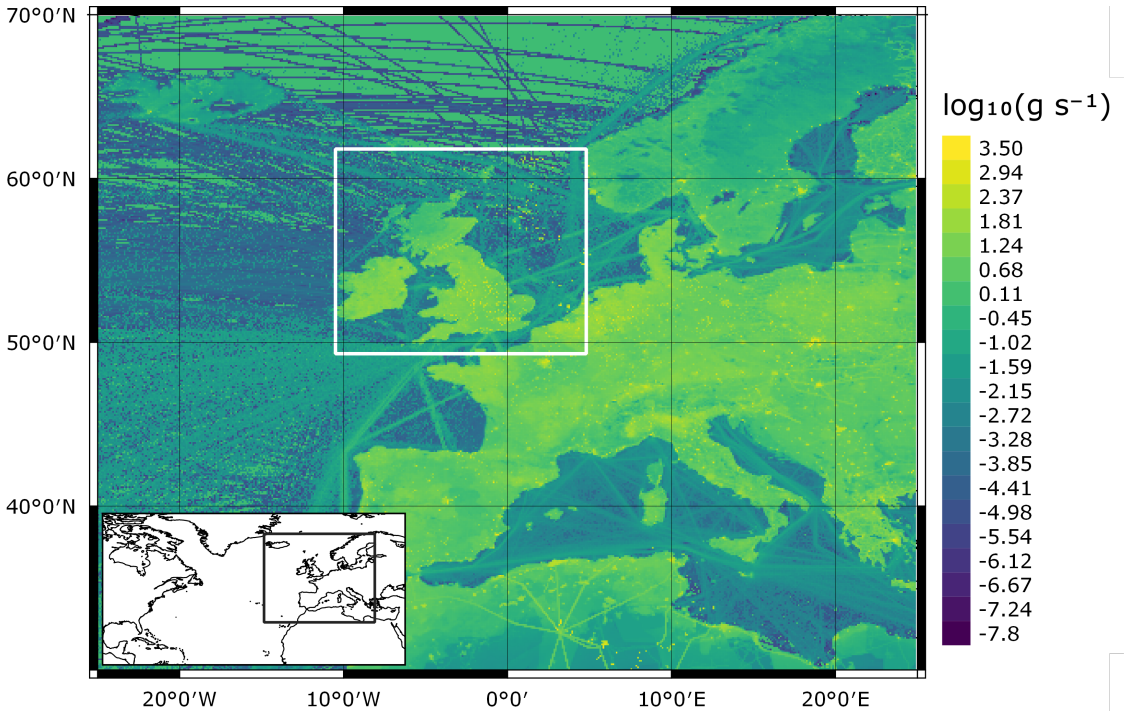


Figure 3.11: The NAME footprint modelling domains. The inset map denotes the area encompassed by the 25 km footprints. The black box denotes the domain of the 10 km footprints, which is shown in the main frame along with the $0.1^o \times 0.1^o$ EDGAR v4.3.2 methane emissions for the year 2012. The white box surrounding the British Isles denotes the 2 km footprint domain.

were not used.

As the transport model is three-dimensional, model particles can begin at the surface, travel to a high altitude and then return to the surface. It is only when particles are in the lowest 40 magl that they are recorded in the NAME model output (Arnold et al. 2018; Jones et al. 2007).

Three sets of hourly footprints, each with a different horizontal spatial resolution, are used in this thesis. Footprints with a spatial resolution of ~ 25 km (Table 3.4) were used for simulating CH_4 across a network of seven sites in the UK and Republic of Ireland (including the ICL measurement site). Footprints with spatial resolutions of ~ 10 km and ~ 2 km (Table 3.4) were generated for additional ICL model-measurement comparisons.

The domain of the 2 km resolution footprints covers the British Isles and a small portion of northern Europe, the domain of the 10 km footprints covers most of Europe, and the domain of the 25 km resolution footprints

extends to central North America (Fig. 3.11 ; Table 3.4). The 2 km and 10 km footprints used a 6-day back-trajectory duration whereas the 25 km footprints used a 30-day back-trajectory duration. Particle release rates of 2×10^4 h^{-1} were used for the 25 km and 10 km back-trajectories and 1.5×10^4 h^{-1} for the 2 km back-trajectories.

3.3.3 Estimating model uncertainty in NAME

Information available about atmospheric transport model uncertainty is usually given in the context of atmospheric inversion modelling. Derivation of model uncertainties is not ubiquitous nor often analysed. It is only in recent years that an analysis of model uncertainties has been considered (e.g. Brophy et al. 2019, Fischer et al. 2017). An atmospheric model uncertainty analysis conducted by Jeong et al. (2013) states the model uncertainty is the sum of uncertainties from: (i) the number of theoretical particles used in the model, (ii) the aggregation error due to the averaging of fluxes within a grid cell, (iii) the error due to estimating the background within the model domain (which is used as the air-concentration boundary value), (iv) a meteorological error arising from errors in simulating the planetary boundary layer (PBL) height, wind speed and direction.

Taking these criteria as the starting point, the particle number error for NAME is the inverse square root of the number of particles (σ_N) (Jones et al. 2007). An aggregation error is not assigned, but differences due to flux aggregation can be evaluated when comparing NAME back-trajectories for the same time and locations but with different spatial resolutions (Chapter 4). Simulations of fossil fuel CO_2 in Europe conducted by Wang et al. (2017) found that the aggregation error made a minor contribution to the atmospheric model uncertainty. The background error is taken as the standard deviation of each calculated baseline concentration* (σ_{BG}).

For the meteorological uncertainty, the approach used in Arnold et al. (2018) is adapted. Arnold et al. (2018) use the simulated PBL height (calculated in the UM) as a proxy for the uncertainty in the model. This is captured in the term f_{BLH}, given as:

$$f_{BLH} = \left[\frac{Max(\text{BLH-In})}{Min(\text{BLH-In})} \times \frac{\tau}{Min(\text{BLH})} \times \text{sgn}(Max(\text{BLH-In})) \right]. \tag{3.2}$$

Here, Max(BLH-In) and Min(BLH-In) denote the maximum and minimum simulated PBL heights relative to the air inlet in a 3 h moving window, respectively. Min(BLH) denotes the minimum PBL height in the 3 h window and τ is an arbitrarily defined threshold value, which is set close to the height of the air inlet at the

*Baseline concentrations are defined as concentrations that are well-mixed and representative of the midlatitude Northern Hemisphere background (Manning et al. 2021).

receptor site.

The first fraction on the right-hand-side in Eq. (3.2) represents the variability in the PBL height over the 3 h period. This is scaled by the second fraction on the right-hand-side in Eq. (3.2) which denotes the proximity of the PBL to the air inlet of the measurement site. The impact on observations is smaller when the PBL is varying at higher altitudes (i.e. larger than τ) than when the PBL is varying at lower altitudes (Arnold et al. 2018). The impact of a low PBL is two-fold. Firstly, there is a higher possibility of measuring air from above the PBL which is not captured in the model. Secondly, at times when the PBL height is lower very local emissions have a greater influence. Here, emissions become trapped under the PBL and are less diluted resulting in local pollutants having a larger signal. The sgn(Max(BLH-In)) term is included in Eq. (3.2) to distinguish times when the PBL height drops below the inlet height. In these instances f_{BLH} is negative.

The PBL heights from the UM are used to calculate f_{BLH}. Planetary boundary layer heights dropped below the air inlets in the UK measurement network on average 19% of the time when using data from all hours. When excluding data from nighttime hours (18:00-08:00 UTC), the PBL was below air inlets on average 1% of the time.

In keeping with the framework developed by Arnold et al. (2018), the uncertainty of the transport model (σ_{model}) is calculated as:

$$\sigma_{model} = \sqrt{\sigma_N^2 + (\sigma_{bg} f_{BLH})^2}. \tag{3.3}$$

A median model uncertainty of 10.1 ppb is obtained when considering data from all hours and 6.0 ppb when excluding nighttime data.

3.3.4 Simulating CH_4

Footprints were combined with gridded emissions to simulate CH_4 mole fractions above the background mole fractions outside the footprint domain (i.e. excess CH_4 mole fractions) for the different emission source sectors.

Simulated atmospheric $\delta^{13}CH_4$ (δ_a) were calculated from a weighted average of the isotopic signatures of individual source sector excess CH_4 using the NAME simulations, and the background $\delta^{13}CH_4$ (δ_{bg}) at Mace Head following:

$$\delta_a = \frac{\delta_{bg} C_{bg} + \Sigma_i (\delta_i C_i)}{C_{bg} + \Sigma_i C_i}. \tag{3.4}$$

Where C_i and δ_i are the excess CH_4 mole fractions and isotopic signature signature of the different source sectors, and C_{bg} and δ_{bg} are the background CH_4 mole fractions and $\delta^{13}CH_4$ values, respectively.

Background $\delta^{13}CH_4$ values were calculated from flask measurements at Mace Head by following the method outlined in Manning et al. (2021). Footprints at Mace Head are used to assess which measurements were not influenced by significant emissions and are suitable as background (baseline) measurements. A curve of multiple harmonics (e.g. Jones et al. 2015) is fitted to the background measurements at Mace Head from January 2018 to May 2020. I extrapolated to October 2020 by fitting a linear trend to the data and assuming the same seasonal cycle to obtain a time series of daily $\delta^{13}CH_4$ values that match the period of ICL observations.

Table 3.5 lists the isotopic signature assigned to each source sector in the UK NAEI and EDGAR inventories, based on the UK-specific isotopic source signatures from Zazzeri et al. (2017). For anthropogenic source sectors that did not have a UK-specific isotopic source signature (petroleum refining, 1A1b, and Oil, 1B2a, in EDGAR) global values from Sherwood et al. (2017) were used. Some source sectors are composed of multiple sources with different isotopic source signatures. For example, the waste sector includes landfill site and waste water CH_4 emissions. In this case, the weighted average of the different sources, based on the UK emissions reported to the UNFCCC (`https://di.unfccc.int/comparison_by_category`) were used to calculate the isotopic source signature of that source sector.

Simulations of $\Delta^{14}CH_4$ were similarly generated. Fossil fuel sources were assigned $\Delta^{14}CH_4$ signatures of -1000‰ and biogenic sources were assigned $\Delta^{14}CH_4$ signatures of 0‰ for the year 2018 (Table 3.5; further details are given within Chapter 5).

Table 3.5: The allocation of methane isotopic signatures of $\delta^{13}CH_4$ and $\Delta^{14}CH_4$ for different methane sources using NAEI sectors. The correspondence between NAEI and EDGAR source sectors are given in Table 3.2

Source sector	UK NAEI SNAP sector	$\delta^{13}CH_4$ $\pm 1\sigma$ (‰)	$\Delta^{14}CH_4$ (‰)	References
Combustion in energy production and transfer	SNAP 01	-25 ± 3	-1000	Zazzeri et al. (2017) Sherwood et al. (2017)
Non-industrial combustion	SNAP 02	-25 ± 3	-1000	Zazzeri et al. (2017)
Combustion in industry	SNAP 03	-25 ± 3	-1000	Zazzeri et al. (2017)
Production processes	SNAP 04	-25 ± 3	-1000	Zazzeri et al. (2017)
Extraction and distribution of fossil fuels	SNAP 05	-37 ± 3	-1000	Zazzeri et al. (2017) Sherwood et al. (2017)
Road transport	SNAP 07	-20 ± 3	-1000	Zazzeri et al. (2017)
Other transport	SNAP 08	-20 ± 3	-1000	Zazzeri et al. (2017)
Waste treatment and disposal	SNAP 09	-57 ± 3	0^{+30}_{-3}	Zazzeri et al. (2017) Graven et al. (2019)
Agriculture	SNAP 10	-64 ± 3	0^{+30}_{-3}	Zazzeri et al. (2017) Graven et al. (2019)
Wetlands (WetCHARTs)		-71 ± 1	0^{+30}_{-3}	Fisher et al. (2017)
Biomass burning (GFED)		-28 ± 3	0^{+30}_{-3}	Zazzeri et al. (2017)

3.4 Remote sensing measurements from TROPOMI

3.4.1 Overview of TROPOMI

The TROPOspheric Monitoring Instrument (TROPOMI) is the satellite instrument on board the Copernicus Sentinel-5 Precursor (S-5P) satellite. Launched in October 2017, S-5P is in a sun-synchronous orbit 824 km above the Earth's surface. TROPOMI makes daily observations with near-global coverage of atmospheric methane, and other trace gases, with overpasses occurring at 13:30 local time. Retrievals have a pixel resolution of 5.5×7.0 km^2 since August 2019 (and 7.0×7.0 km^2 before August 2019), which is much higher than previous satellite instruments (Jacob et al. 2016). The high spatial resolution and high signal-to-noise ratio of TROPOMI's retrievals facilitates the detection and quantification of CH_4 emissions from smaller scale sources (e.g. Pandey et al. 2019) to larger scale sources (e.g. Gouw et al. 2020) and inversion modelling, which requires high-quality data.

Total atmospheric columns of dry-air CH_4 mixing ratios (XCH_4) are measured by TROPOMI in the short-wave infrared (SWIR) spectral band at 2.3 μm and near-infrared (NIR) at 0.76 μm (Veefkind et al. 2012).

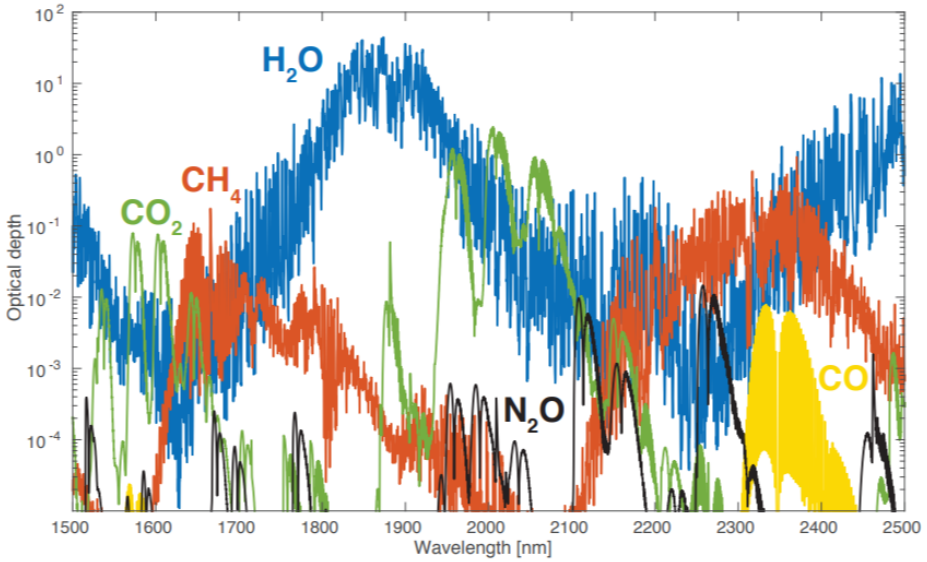


Figure 3.12: Atmospheric optical depths of major trace gases in the spectral range 1.5-2.5μm. The calculation is for the US Standard Atmosphere (Anderson et al. 1986) with surface concentrations adjusted to 399 ppm CO_2, 1.9 ppm CH_4 , 330 ppb N_2O, and 80 ppb CO. The line-by-line data have been smoothed with a spectral resolution of 0.1 nm (full width at half maximum). Figure and caption from Jacob et al. (2016).

Measurements in the SWIR are ideal for inferring CH_4 emissions as the atmosphere is nearly transparent and a near-uniform sensitivity of the troposphere can be achieved (Frankenberg et al. 2006; Jacob et al. 2016). Clouds, however, hinder measurements in the SWIR as solar radiation is reflected back to space preventing below-cloud observations.

Whilst the CH_4 optical depth is stronger at 2.3 μm than at 1.65 μm (Fig. 3.12) back-scattered solar radiation is three times weaker at 2.3 μm than at 1.65 μm (Jacob et al. 2016). Retrievals of CO can also be made at 2.3 μm (Fig. 3.12) but atmospheric CO_2 cannot be retrieved at 2.3 μm as there is no neighbouring CO_2 band. This means the CO_2 proxy method for retrieving CH_4 columns (Frankenberg et al. 2006), as used by GOSAT for observing XCH_4, cannot be used and instead a full-physics approach for retrieving XCH_4 (Butz et al. 2009) is used in the retrieval algorithm for TROPOMI XCH_4 observations. Whilst the full-physics approach uses the near O_2-band to inform on atmospheric aerosols, the CO_2 proxy method uses the ratio of CH_4:CO_2 retrievals from their neighbouring bands to cancel out the aerosol effects - which are assumed the same for CO_2 and CH_4. XCH_4 is obtained by combining the ratio with the modelled CO_2 (Frankenberg et al. 2006).

3.4.2 Overview of TROPOMI's retrieval algorithm

TROPOMI uses a full-physics approach for retrieving atmospheric CH_4 column abundances. In the full-physics approach, the scattering properties of the surface and atmosphere, which are simultaneously retrieved, are fitted as part of the retrieval (Veefkind et al. 2012) where additional fitting variables are used to describe the scattering. The fitting parameters in TROPOMI's retrieval are: the partial CH_4 columns in 12 atmospheric layers; total columns of water vapour, CO and aerosol particles; the surface albedo and the wavelength shifts in Earth radiance and solar irradiance spectra (Hu et al. 2016; Hu et al. 2018a).

The RemoTeC algorithm (Butz et al. 2009; Butz et al. 2011), which has been previously used for XCH_4 retrievals from GOSAT (Jacob et al. 2016; Butz et al. 2011), is used to derive the XCH_4 data product from TROPOMI retrievals (Hu et al. 2016). The algorithm calculates the state vector, $\mathbf{x}$, from TROPOMI radiance measurements, $\mathbf{y}$, and forward-model simulated TROPOMI measurements, $\mathbf{F}$, (Lorente et al. 2021):

$$\mathbf{y} = \mathbf{F}(\mathbf{x}) + e_y + e_F. \tag{3.5}$$

Here, e_y and e_F are the measurement noise error and forward model error, respectively. The state vector, $\mathbf{x}$, is found through an inversion approach with regularisation methods used as there is not sufficient information to independently retrieve every state vector element (Lorente et al. 2021). A prior estimate is used in the

regularisation (Hu et al. 2016; Hu et al. 2018a), but as instruments measuring in the SWIR have uniform sensitivity of the full atmospheric methane column, these prior estimates do not significantly contribute to the retrieved columns (Jacob et al. 2016). The TROPOMI XCH_4 product is calculated from the partial sub-column number densities and converted to a mixing-ratio using meteorological input data from ECMWF (European Centre for Medium-Range Weather Forecasts).

The XCH_4 precision is given as the standard deviation of the retrieval noise. Mission requirements for both the accuracy and precision of XCH_4 retrievals to be less than 1% are largely met (Hu et al. 2018a; Lorente et al. 2021), with an average 1σ precision of 0.6% achieved for single observations (Butz et al. 2012). Further details of the TROPOMI CH_4 retrieval algorithm can be found in Hu et al. (2016).

3.4.3 Data products and quality

TROPOMI XCH_4 retrievals are made in the SWIR band with a spectral resolution of 0.25 nm and spectral sampling interval of ~ 0.1 nm (Hu et al. 2016). Observations are made every one second and have a swath (the dimension across the track of the satellite) of 2600 km and 7 km across the track (Fig. 3.13) per observation. As Sentinel-5P makes 14-15 orbits per day TROPOMI outputs data products with near daily global coverage and high spatial resolution, which increases the probability of pixels having clear-sky scenes and thus high data quality (Veefkind et al. 2012).

Operational TROPOMI data files contain the XCH_4 data product, XCH_4 precision values, surface albedo, aerosol optical depth, pixel data quality values (where quality values of 1 denote clear-sky scenes and are the highest quality data) and surface albedo corrected XCH_4 (referred to as "bias-corrected") data product.

The S-5P data product guide (Apituley et al. 2021) recommends using the bias-corrected XCH_4 product and filtering out pixels with quality values less than 0.5. Pixels with data quality values of 0.5 are almost equivalent to pixels with quality values of 1 (the highest quality data where XCH_4 has been filtered for smooth topography, viewing zenith angle ($< 60^o$), solar zenith angle ($< 70^o$) and aerosol optical thickness <0.3 in the NIR band; Veefkind et al. 2012) except for an irradiance deconvolution condition that filters out row-specific pixels across the track. Furthermore, some pixels with too low CH_4 concentrations may still be present for quality values larger than 0.5 (Apituley et al. 2021). Additional data quality issues that are known but not covered by the quality flags include stripes of erroneous CH_4 values in the flight direction, and the precision values for single overpasses should be doubled when requiring an overall uncertainty (https://mpc-vdaf.tropomi.eu/).

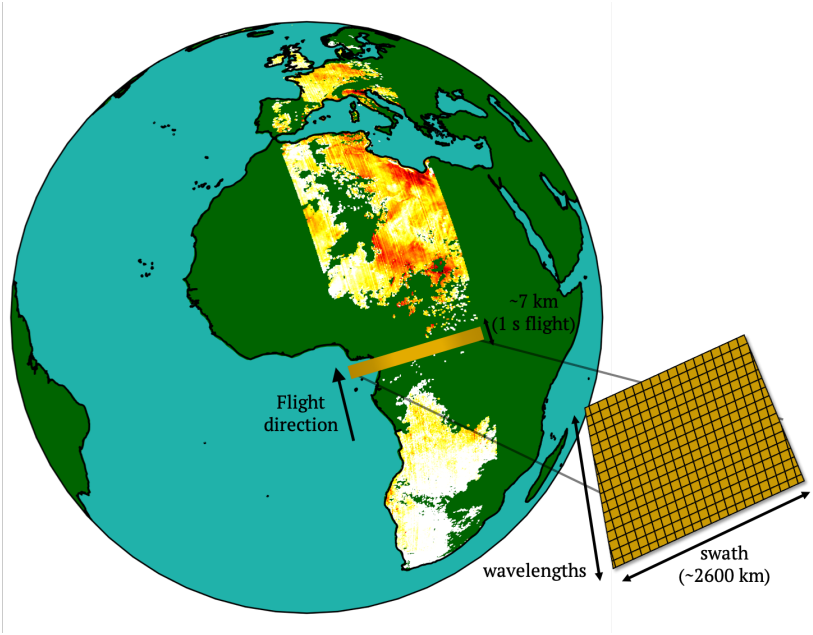


Figure 3.13: TROPOMI measuring principle with a XCH_4 retrieval superimposed.

This is to reflect the scatter in single sounding errors from the data validation. Stripes of CH_4 values are only apparent in single-overpasses and do not typically appear when combining retrievals over a longer period.

The TROPOMI XCH_4 product also contains a column averaging kernel that describes the sensitivity of the retrieved column to partial columns in different atmospheric layers. An explanation of the use of the column averaging kernel is given below.

3.4.4 Data validation

TROPOMI retrieval errors may arise from light collection, spectroscopic data, the radiative transfer model, and clouds. To validate TROPOMI observations, ground-based measurements from the Total Carbon Column Observing Network (TCCON) (Wunch et al. 2011) are used. The TCCON uses ground-based Fourier-transform spectroscopic instruments to measure the same dry-air XCH_4 column as TROPOMI but with a much higher signal-to-noise ratio and a well-defined light path (Jacob et al. 2016). Retrievals from TCCON are calibrated to the World Meteorological Organization and are validated by comparison to aircraft profile measurements (Wunch et al. 2011).

A comparison of the corrected and uncorrected XCH_4 TROPOMI products with 13 TCCON stations distributed around the globe by Lorente et al. (2021) found a mean bias of -3.4 ppb for the bias-corrected XCH_4 product

and -17.0 ppb for the uncorrected XCH_4 product. The overall negative bias is attributed to a strong XCH_4 underestimation from low surface albedo values (Fig. 3.14a), which when corrected for (using a spline fit) partly reduces the overall bias (Lorente et al. 2021). A lot of scatter is observed in the XCH_4 - surface albedo plot (Fig. 3.14a) and XCH_4 - aerosol optical thickness (Fig. 3.14b) plot for TROPOMI and TCCON data. Applying the surface albedo correction produced by Lorente et al. (2020) will leave some pixels uncorrected. Correcting for bias introduced by the aerosol optical thickness is more difficult as there are few data points with high aerosol optical thickness values and there appears to be no correlation for lower aerosol optical thickness values and TROPOMI-TCCON XCH_4 (Fig. 3.14b). Larger differences in the XCH_4 TROPOMI-TCCON data seem to occur for aerosol optical thickness values larger than 0.10. Filtering out these data may improve the quality of the TROPOMI XCH_4 data product.

A mean bias of -12.5 ± 14.9 ppb is found between TROPOMI and GOSAT XCH_4 by Lorente et al. (2021). Relative to GOSAT, TROPOMI underestimates XCH_4 in the tropics in South America and in the African continent. At higher temperate latitudes, there is better agreement between GOSAT and TROPOMI (Fig. 3.15).

Here, I used the bias-corrected XCH_4 TROPOMI product filtered to retain pixels with data quality values of 1 and filtered to remove pixels with aerosol optical thicknesses larger than 0.10.

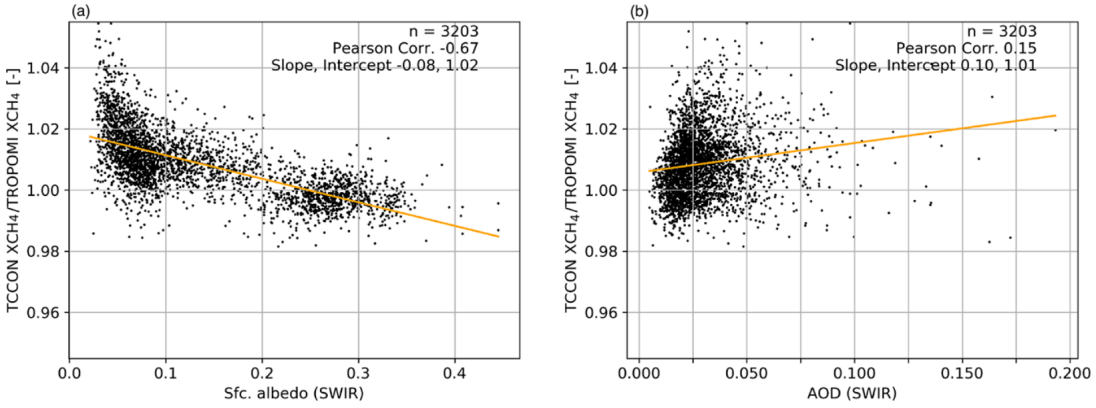


Figure 3.14: Ratio of XCH_4 measurements by TCCON and TROPOMI as a function of (a) retrieved surface albedo in the SWIR spectral range, (b) retrieved aerosol optical depth (AOD) in the SWIR spectral range. Figure and caption from Lorente et al. 2021.

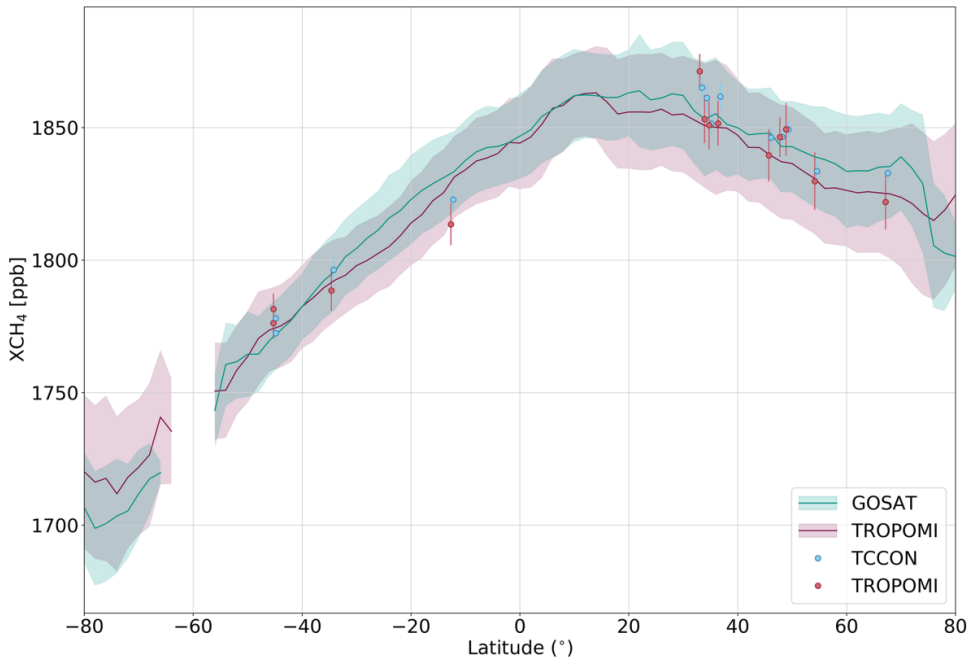


Figure 3.15: Latitudinal distribution of XCH_4 measured by TROPOMI and GOSAT and the TROPOMI and TCCON collocations over the selected stations for validation. The shaded bands indicate the 1σ standard deviation around the mean. (Figure and caption from Lorente et al. 2021).

3.4.5 Data processing

The operational TROPOMI data product from November 2018 to October 2020 was processed using the HARP Python module (https://stcorp.github.io/harp/doc/html/index.html) which is designed for ingesting, processing and inter-comparing satellite data. TROPOMI data products are not on a uniform spatial grid. The longitudinal-latitudinal bounds of each pixel given in the data file are not uniformly spaced due to viewing angle of TROPOMI during the overpasses. Having the data products on a uniform spatial grid is desirable, particularly if comparing to other sources of gridded data or if being used in inversion modelling.

Bias-corrected XCH_4 retrievals were gridded to $0.08^o \times 0.08^o$ spatial resolution in HARP to closely match the spatial-resolution of the TROPOMI retrievals. Bias-corrected XCH_4 pixels were filtered to retain those with data quality values of 1 and aerosol optical depth less than 0.10 to create a "high-quality" dataset of TROPOMI XCH_4 for the UK. After this data processing, approximately 2.98% of retrievals from this period had sufficient XCH_4 pixel coverage and density for parts of the UK (e.g. London, or the southeast) but only eight days* (1.09%) had pixels with sufficient UK-wide coverage and pixel density. Cloud coverage is likely

*The eight days are: 15 Feb. 2019, 26 Feb. 2019, 27 Jun. 2019, 20 Apr. 2020, 21 Apr. 2020, 6 May 2020, 17 Sep. 2020, 21 Sep.

the main factor that results in a small number of high-quality TROPOMI XCH_4 retrievals for across the UK.

Negligible differences (<3 ppb) were found between the filtered operational bias-corrected XCH_4 product and the Lorente et al. (2021) surface albedo corrected XCH_4 product over the UK between January 2018 and November 2020.

3.5 CAMS XCH_4 analysis and forecast products

The Copernicus Atmosphere Monitoring Service (CAMS, http://atmosphere.copernicus.eu) is part of the Copernicus European Earth observation programme. Daily analyses and forecasts of atmospheric trace gas concentrations and aerosol concentrations are provided through near-real time CAMS global data products. CAMS has been providing daily analysis and five day forecasts of atmospheric CO_2 and CH_4, using the ECMWF Integrated Forecasting System (IFS) that incorporates modelling and data assimilation, since 2015 (ECMWF 2021; Agustí-Panareda et al. 2019).

The CAMS global reanalysis product for atmospheric methane and the CAMS global atmospheric composition forecast atmospheric methane data product are used in this thesis for analysing and comparing TROPOMI XCH_4 retrievals over the UK.

3.5.1 CAMS EGG4 greenhouse gas reanalysis data product

The CAMS global greenhouse gas reanalysis (EGG4) is part of the fourth generation ECMWF global reanalysis of atmospheric composition (EAC4) that focuses on atmospheric CO_2 and CH_4. The reanalysis products consist of a three-dimensional time-consistent atmospheric composition field (Inness et al. 2019).

The process of reanalysis combines observations and model data into a consistent dataset by using an atmospheric model based on physical-chemical laws and data assimilation (ECMWF 2021). Data assimilation is based on the principle of combining a previous forecast with new observations to produce a new estimate of the state of the atmosphere called the "analysis" (Inness et al. 2019). A data assimilation approach means biases between different sets of observations can be estimated and concentrations of atmospheric pollutants at locations where there is low data coverage can also be estimated (Ramonet et al. 2021).

2020.

The atmospheric XCH_4 reanalysis product is available at three-hour time intervals and has $0.75^o \times 0.75^o$ spatial resolution and 60 vertical model levels from the surface to an atmospheric layer with pressure of 0.1 hPa. (ECMWF 2021).

Between 2010-2020 the reanalysis product tends to produce lower surface methane concentrations and negative biases in comparison to the control run*. The reanalysis product tends to overestimate the CH_4 total columns compared to most of the mid- and high-latitude TCCON stations with a relative difference of up to 2.5% (Ramonet et al. 2021). Measurements from TCCON and partial column measurements from Network for the Detection of Atmospheric Composition Change (NDACC) sites suggest the stratospheric part of the reanalysis could be overestimating (Ramonet et al. 2021).

Since 2017, however, the control run has been underestimating XCH_4, particularly in the tropospheric columns (Ramonet et al. 2021). The development of a negative bias may be due to the EDGAR v4.2 anthropogenic emissions (for the year 2010) that are used in the CAMS reanalysis dataset. Growth in anthropogenic emissions since 2010 is not captured in the model. Wetland CH_4 emissions from LPJ-WHyMe model (Spahni et al. 2011) and the CH_4 sink dataset from (Bergamaschi et al. 2009) are also included in the data assimilation. Total column CH_4 and CO_2 satellite data from the MetOp and GOSAT satellites have been used since 2019 in the data assimilation to correct the atmospheric concentrations (Massart et al. 2014), but emissions and surface fluxes remain unchanged in the assimilation; (Barré et al. 2021).

Negative CH_4 biases appear more frequently in 2019-2020, especially in the northern hemisphere. Underestimation of XCH_4 in more recent years is thought to be due to the tropospheric part of the reanalysis (Ramonet et al. 2021).

3.5.2 CAMS atmospheric composition forecast data product

Five-day forecasts of CH_4 are provided by the IFS as part of the CAMS greenhouse gas products (Agustí-Panareda et al. 2019). The IFS 4D-Var assimilation system (Engelen et al. 2009; Massart et al. 2014; Massart et al. 2016), which is adapted to assimilate column-averaged CO_2 and CH_4, produces analyses every 12 hours at 00:00 UTC and 12:00 UTC. A four-day forecast is produced after the 00:00 UTC analysis at a medium-

*The control run has the same settings as the reanalysis but does not include the data assimilation. For 2017-2020 the CAMS hb7h GHG analysis experiment is used to produce the control run.

resolution (approximately 25×25 km^2, with 137 vertical model levels). The four-day medium-resolution forecast is merged with the high-resolution forecast (approximately 9×9 km^2, with 137 vertical model levels) for the previous day.

Observations of XCO_2 and XCH_4 from GOSAT and MetOp satellites are included in the assimilation and used to constrain the forecast model. Satellite observations do not correct emissions in the 25 km resolution analyses. Instead they mainly provide a correction to the forecast initial condition concentrations in the free troposphere and above. Emissions are, however, the main influence on the four-day 25 km forecast (that is used to initialise the 9 km forecast; Barré et al. 2021) at lower altitudes.

Surface concentrations of CH_4 and CO_2 from stations in the Integrated Carbon Observation System (ICOS) network and column measurements from TCCON and NDACC stations are used to validate the analysis and high-resolution forecast experiments. Negative CH_4 biases ranging -10 ppb to -50 ppb are generally found in the XCH_4 forecast data product (Sudarchikova et al. 2021). Between April and July 2020, however, positive biases of XCH_4 were found at most of the northern hemispheric ICOS stations (Sudarchikova et al. 2021).

Atmospheric methane concentration forecasts from IFS cycles 45R1 (starting June 2018 using CAMS e-suite experiment gznv) and 46R1 (starting September 2019 using CAMS o-suite experiment h9sp) are used in this thesis. The CAMS forecast IFS cycle 45R1 is initialised from GHG analysis experiment gwx3 with IFS model resolution Tco1279 (9 km) and 137 vertical levels. Anthropogenic emissions from EDGAR v4.2FT for the year 2010 are used in this IFS cycle. The CAMS forecast IFS cycle 46R1 is initialised from GHG analysis experiment h72g with IFS model resolution Tco1279 (9 km) and 137 vertical levels. CAMS forecasts in IFS cycle 46R1 uses CAMS-GLOB-ANTv2.1 anthropogenic emissions for 2018 (https://atmosphere.copernicus.eu/anthropogenic-and-natural-emissions), which is based on EDGAR emissions, national emission reports, and other existing emission inventories.

3.5.3 CAMS data processing

The CAMS reanalysis and atmospheric composition forecast CH_4 data products were obtained for the eight days between November 2018 and October 2020 when TROPOMI observed sufficient high-quality XCH_4 coverage of the UK (Section 3.4.5). Both sets of CAMS data products were processed using the Python HARP module.

Partial XCH_4 columns in the CAMS data products are given for the vertical *model* levels not *pressure* levels. Each model level in the CAMS data product represent the bounds of each vertical layer ("half-levels"). The corresponding atmospheric pressure levels at the layer interfaces are calculated from the ECMWF surface pressure field (P_s) using:

$$P_{k+1/2} = a_{k+1/2} + b_{k+1/2} P_s, \tag{3.6}$$

where $a_{k+\frac{1}{2}}$ and $b_{k+\frac{1}{2}}$ are constants defined for each model half-level (ECMWF 2015). The pressure associated with the middle of each k^{th} layer (the "full-level") is calculated from:

$$P_k = \frac{1}{2}(P_{k+1/2} + P_{k-1/2}). \tag{3.7}$$

3.5.4 CAMS data setup

The TROPOMI column averaging kernels should be used when comparing the CAMS XCH_4 data products (or any other XCH_4 data product) with the TROPOMI retrievals (Apituley et al. 2021). Column averaging kernels describe the sensitivity of the retrieved CH_4 column to partial columns. The procedure for preparing the CAMS data products for comparison with TROPOMI retrievals is described in Apituley et al. (2021) and below.

The prepared CAMS mixing-ratio product, $XCH_{4,avg}^{CAMS}$ is, by definition, the ratio of the CH_4 number density ($VCH_{4,avg}^{CAMS}$ in units of cm^{-2}) to the total dry-air column number density ($Vdryair^{CAMS}$):

$$XCH_{4,avg}^{CAMS} = VCH_{4,avg}^{CAMS} / Vdryair^{CAMS}. \tag{3.8}$$

Where $VCH_{4,avg}^{CAMS}$ is given relative to the prior data included in the RemoTeC algorithm for TROPOMI retrievals:

$$VCH_{4,avg}^{CAMS} = VCH_4^{prior} + \sum_{i=1}^{N} a_i (\partial VCH_{4,i}^{CAMS} - \partial VCH_{4,i}^{prior}). \tag{3.9}$$

Here, VCH_4^{prior} is the prior methane total column number density provided in the TROPOMI data products; N the number of vertical layers in the TROPOMI retrieval; a_i is the column averaging kernel for the i^{th} layer; and $\partial VCH_{4,i}^{CAMS}$ is the corresponding partial methane column in CAMS. As the vertical grid in CAMS has a finer resolution than the vertical layers in TROPOMI XCH_4 , CAMS XCH_4 values within each i^{th} layer are averaged (Apituley et al. 2021).

Chapter 4

Measurements and modelling of CH_4 concentrations and $\delta^{13}CH_4$ in central London

"You will be astonished when I tell you what this curious play of carbon amounts to."

— Michael Faraday, *A Course of Six Lectures on the Chemical History of a Candle (ed. 1861)*

Abstract

Top-down greenhouse gas measurements can be used to independently assess the accuracy of bottom-up emission estimates. Atmospheric CH_4 mole fractions and $\delta^{13}CH_4$ measurements from Imperial College London since early 2018 using a Picarro G2201-i analyser are reported. Measurements from March 2018 to October 2020 were compared to simulations of CH_4 mole fractions and $\delta^{13}CH_4$ produced using the NAME dispersion model coupled with the UK National Atmospheric Emissions Inventory, UK NAEI, and the global inventory, EDGAR, with model spatial resolutions of ~ 2 km, ~ 10 km, and ~ 25 km. Simulation-measurement comparisons are used to evaluate the London emissions and source apportionment in the global (EDGAR) and UK national (NAEI) emission inventories. Observed mole fractions were underestimated by 30% to 35% in the NAEI simulations. On the other hand, a good correspondence between observations and EDGAR simulations was seen. There was no correlation between the measured and simulated $\delta^{13}CH_4$ values for either NAEI or EDGAR, however, suggesting the inventories' sectoral attributions are incorrect. On average, natural gas sources accounted for 20% to 28% of the above background CH_4 in the NAEI simulations, and only 6% to 9% in the EDGAR simulations. In contrast, nearly 84% of isotopic source values calculated by Keeling plot analysis (using measurement data from 13:00-17:00 UTC) of individual pollution events

were higher than -45‰, suggesting the primary CH_4 sources in London are actually natural gas leaks. The simulation-observation comparison of CH_4 mole fractions suggests that total emissions in London are much higher than the NAEI estimate (0.04 Tg CH_4 yr^{-1}) but close to, or slightly lower than the EDGAR estimate (0.10 Tg CH_4 yr^{-1}). However, the simulation-observation comparison of $\delta^{13}CH_4$ and the Keeling plot results indicate that emissions due to natural gas leaks in London are being underestimated in both the UK NAEI and EDGAR.

4.1 Introduction

Urban areas are greenhouse gas (GHG) emission hotspots that account for 70% of anthropogenic GHG emissions (IPCC 2014a). Collectively, they form the single largest anthropogenic contribution to climate change (Duren and Miller 2012; Hopkins et al. 2016) making them important targets for GHG emissions mitigation. Urban areas account for 21% of global anthropogenic CH_4 emissions (Marcotullio et al. 2013) and over 40% of global CH_4 emissions from the waste, energy and transport sectors are from cities (Marcotullio et al. 2013).

The London region enclosed within the London orbital motorway comprises 0.65% of the UK's land area yet accounts for 2.7% of the UK's annual CH_4 emissions and 9.1% of the UK's annual fugitive (e.g. leaks from the natural gas distribution network) CH_4 emissions reported in NAEI (NAEI 2017). Waste sector emissions account for 52% of London CH_4 emissions and fossil fuel sources of CH_4 form 41%, with the remaining 7% of London emissions attributed to domestic combustion and land use change (e.g. emissions of CH_4 from the River Thames) (NAEI 2017).

Historically, emission inventory estimates of CH_4 tend to underestimate emissions in comparison to atmospheric measurements in urban regions (Brandt et al. 2014), including in London. Atmospheric measurements can be used to independently evaluate inventory estimates as measurements of the well-mixed atmosphere do not form part of the evidence used to estimate emission inventories. Eddy-covariance measurements made from the BT Tower in central London between 2012-2014 found emissions (72 ± 3 t CH_4 km^{-2} yr^{-1}) were more than double the NAEI inventory values for London (Helfter et al. 2016). Although no isotopic nor tracer measurements were made in this study, inventory-measurement differences were attributed to natural gas leaks or effluent CH_4 being underestimated in the inventory (Helfter et al. 2016). Zazzeri et al. (2017) concluded from $\delta^{13}CH_4$ isotopic measurements that gas leaks were underestimated in the emission inventories after

finding many large gas leaks in mobile measurement surveys. However, a study using aircraft measurements from a single flight over the London region in 2016 suggested the UK NAEI was overestimating CH_4 emissions and they needed to be scaled down by 0.71 (0.66-0.79) to be consistent with the aircraft measurements on this particular day (Pitt et al. 2019). Additional London measurements are needed to better understand CH_4 emissions from different sources and how they compare to updated inventories. In particular, long-term measurements of isotopic composition could provide more robust source attribution than CH_4 measurements alone or isotopic measurements from field campaigns.

Attributing emissions to specific sources can be challenging when CH_4 sources are collocated. Isotopic measurements of $\delta^{13}CH_4$ are a well-established approach for discriminating between sources of CH_4 (e.g. Fisher et al. 2017; France et al. 2016; Tans 1997; Zazzeri et al. 2017). Sources can be differentiated by their distinct isotopic signatures (Sherwood et al. 2017). In the UK, waste CH_4 emissions have an average $\delta^{13}CH_4$ value of -58‰ and natural gas emissions have an isotopic signature of -36‰ (Zazzeri et al. 2017) with uncertainties of ±3‰. The isotopic signatures of some sources have been found to exhibit spatiotemporal variations (Feinberg et al. 2018) so it is preferable to use regional values, when available, for interpreting atmospheric $\delta^{13}CH_4$ measurements (Feinberg et al. 2018; Hoheisel et al. 2019; Zazzeri et al. 2017).

Discrepancies between atmospheric measurements and bottom-up estimates have similarly been found in other urban regions. Methane observations in Boston, USA found natural gas emissions were 2-3 times higher than the emissions estimates from a customised inventory comprised of local data (McKain et al. 2015). Another more recent measurement campaign using five sites in the Boston urban area from 2012 to 2020 also found natural gas emissions were approximately three times higher than bottom-up estimates (Sargent et al. 2021). It was suggested that a large component of missing inventory emissions in the Boston area were from transmission and end-use stages of natural gas distribution (Sargent et al. 2021). In Paris, Xueref-Remy et al. (2020) conducted mobile surveys for CH_4 and $\delta^{13}CH_4$ over 2012-2015 and found that emissions from the waste water treatment sector were being underestimated in the AIRPARIF 2013 inventories.

Instruments capable of making continuous measurements of atmospheric $\delta^{13}CH_4$ have recently become available, yet only a few studies have deployed them to attribute CH_4 emissions in areas of mixed sources. Venturi et al. (2020) measured $\delta^{13}CH_4$ in Florence, Italy over a few months in 2017 and found that CH_4 emissions in the city were mainly due to natural gas emissions. In Cabauw, Netherlands Röckmann et al. (2016) deployed a dual isotope mass spectrometric system and a quantum cascade laser spectrometer to

measure $\delta^{13}CH_4$. Model-observation comparisons of $\delta^{13}CH_4$ across five months found simulations using the EDGAR inventory overestimated fossil fuel CH_4 sources for this region. Assan et al. (2018) used a Picarro G2201-i to measure $\delta^{13}CH_4$, along with other atmospheric tracers, near a natural gas compressor station and found local sources were dominated by natural gas CH_4, with traffic-related and ruminant sources also present. The first network of continuous atmospheric $\delta^{13}CH_4$ measurements, using cavity ring-down spectroscopy (CRDS), comprised of four tall towers in the Marcellus Shale gas region, Pennsylvania (Miles et al. 2018) showed mean differences between flask and in situ $\delta^{13}CH_4$ were between 0.02‰ and 0.08‰, demonstrating CRDS has the capacity to make high-precision $\delta^{13}CH_4$ measurements that align with flask measurements.

In this chapter, over two years of continuous measurements of CH_4 mole fractions and $\delta^{13}CH_4$ values made from the South Kensington campus of Imperial College London, in central London are presented. These measurements form the longest in situ $\delta^{13}CH_4$ measurement campaign in central London reported to date. The time span of these measurements allowed relationships between anthropogenic sources at different times of the year to be explored, minimise the impact of anomalous pollution events, and assess the impact of the first UK COVID-19 lockdown on CH_4 mole fractions and $\delta^{13}CH_4$ in London. An automated Keeling plot analysis was created to determine the isotopic source values (δ_s) of individual pollution events. Since previous London CH_4 studies there have been revisions to the global and UK national emissions inventories. It is important, particularly in urban areas, that updated inventories are evaluated to ensure reported source values are accurate for city-wide mitigation policies to be effective. Unlike some previous London studies, I compare observations with atmospheric transport model simulations using EDGAR 2012 v4.3.2. (Chapter 3, Section 3.2.1) and UK NAEI 2017 (Chapter 3, Section 3.2.2) bottom-up inventory estimates and their source apportionment for the London region. The NAME atmospheric model (Chapter 3, Section 3.3) is used to transport these emissions under three different spatial resolutions to simulate the excess CH_4 mole fractions and $\delta^{13}CH_4$ at ICL.

4.2 Methods

4.2.1 Keeling plot analysis

Measurements of CH_4 mole fractions and $\delta^{13}CH_4$ values were made at ICL using a Picarro G2201-i isotopic analyser as described in Chapter 3. Based on Allan precision values of less than 0.1‰ (Chapter 3, Section 3.2), 20-minute averaged methane measurements were used to evaluate CH_4 emissions and sources in the London area.

The Keeling plot technique (Keeling 1958; Keeling 1961; Pataki et al. 2003; Chapter 2, Section 2.6.2) was used to assess isotopic signatures (δ_s) of local and regional sources by analysing data across three different moving time intervals or "windows" that were 12 hours, three days and seven days in length. Isotopic signatures obtained with the 12-h window are expected to emphasise sources local to the measurement site, particularly the local emissions that accumulate in the nocturnal boundary layer. For the 3-day and 7-day time windows data from 13:00-17:00 are used as this is when the planetary boundary layer (PBL) is at its largest and δ_s values are more representative of sources from the wider area. For all three time windows an orthogonal distance regression was applied to the 20-minute averaged data using an automated algorithm, similar to Röckmann et al. (2016). To ensure a coherent pollution event was captured, the δ_s value from each moving window was retained if the mole fractions varied by more than 150 ppb.

The selection criteria for including a pollution event in the Keeling plot analysis considers the variation in mole fractions (i.e. the mole fraction peak strength) within a moving window. Considering variations in $\delta^{13}CH_4$ could potentially lead to pollution events with source signatures near background $\delta^{13}CH_4$ values being excluded in the analysis, as does using the correlation coefficient of a Keeling plot as a measure of the coherency of a pollution event.

To specify the magnitude of a pollution event for which δ_s could be well-characterised with the measurement uncertainty of the Picarro instrument, the recovery of an isotopic source signature in pseudo-data for peak strengths from 50 ppb to 300 ppb (increasing in 50 ppb increments; Fig. 4.1) was evaluated. Ideal pollution events were constructed with a range of distinct isotopic signatures (-35‰, -40‰, -46‰ and, -65‰) using a mass balance approach with Gaussian white noise of 0.2‰ standard deviation added to represent measurement uncertainty. For each peak strength and isotopic signature 1000 simulations were run and the δ_s values determined. Larger variations in δ_s across simulations for pollution events with smaller peak strengths are seen (Fig. 4.1). Standard deviations of δ_s for simulated pollution events with the same peak strength but with different isotopic signatures are within 0.1‰, for peak strengths 150 ppb or larger (Table 4.1), of each other and decrease exponentially with increasing peak strength size (Fig. 4.2). Based on these simulations pollution events of at least 100 ppb are considered for which δ_s can be well-characterised with the measurement uncertainty.

Isotopic source values were calculated with ICL atmospheric measurements using peak strengths of 100, 150, and 200 ppb for 12-h, 3-day and 7-day moving windows. Whilst smaller peak strengths return a larger number

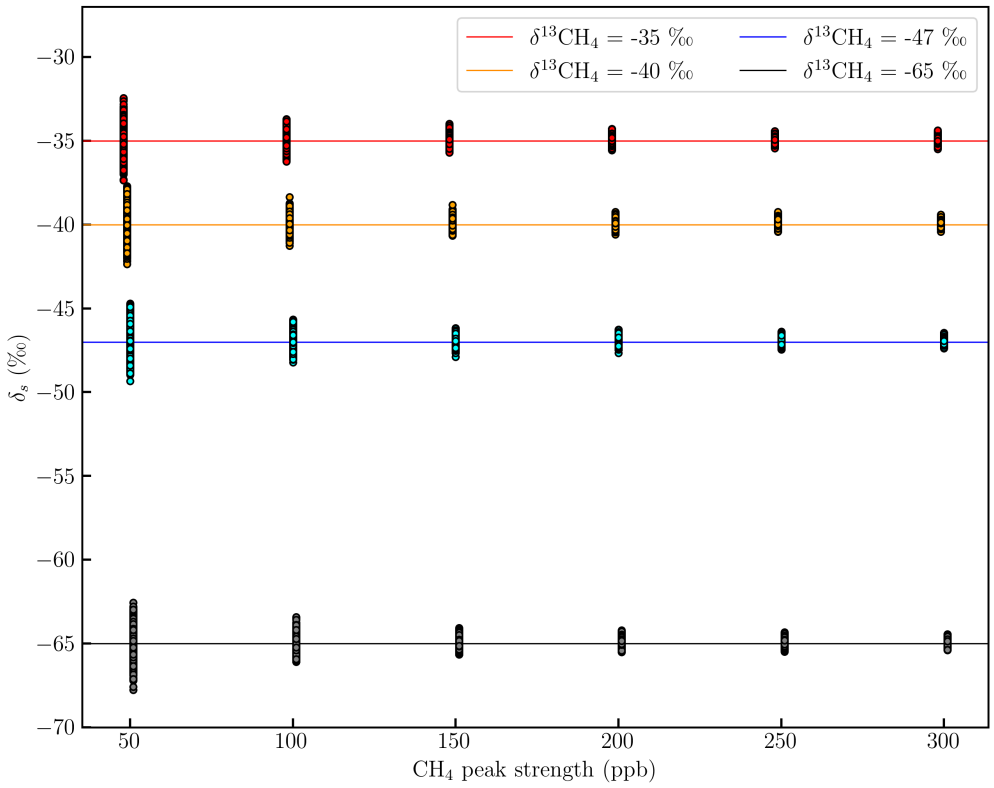


Figure 4.1: Isotopic source values for ideal pollution events with different isotopic signatures and peak strengths.

of δ_s values, their mean standard error increases and the range of δ_s values include unrealistic values (Table 4.2). For the 3-day and 7-day windows, nearly three times the proportion of δ_s values between -30‰ and -35‰ are observed in the 100 ppb and 150 ppb peak strengths in comparison to the 200 ppb δ_s values. For the 12-h window there were not any large differences in the proportions of 12-h δ_s<-45‰ for the different peak strengths (Table 4.2) compared to the 3-day and 7-day windows. Based on these analyses a peak strength of 150 ppb was chosen.

4.2.2 Atmospheric simulations

Simulations of atmospheric CH_4 were performed by using NAME back-trajectories with spatial resolutions of ~ 25 km, ~ 10 km and ~ 2 km (Chapter 3, Section 3.3.2), which were used to calculate footprints of surface emission sensitivities. As the spatial domains of the footprints differ (Table 3.4), nested footprints were created that used the higher resolution footprints for the inner domain and the coarser footprints for the outer domain(s); Table 4.3.

Table 4.1: Keeling plot pseudo-data peak strength mean and 1σ.

	Isotopic signature (δ_s)			
Pseudo-data peak strength	-35‰	-40‰	-47‰	-65‰
50 ppb	-34.8 ± 0.83	-39.9 ± 0.76	-46.9 ± 0.81	-64.9 ± 0.85
100 ppb	-34.9 ± 0.39	-39.9 ± 0.39	-46.9 ± 0.41	-64.9 ± 0.43
150 ppb	-34.9 ± 0.27	-39.9 ± 0.27	-46.9 ± 0.27	-64.9 ± 0.27
200 ppb	-34.9 ± 0.21	-39.9 ± 0.21	-46.9 ± 0.20	-64.9 ± 0.21
250 ppb	-34.9 ± 0.17	-39.9 ± 0.17	-46.9 ± 0.16	-64.9 ± 0.17
300 ppb	-34.9 ± 0.14	-39.9 ± 0.14	-46.9 ± 0.15	-64.9 ± 0.14

As previously described, footprints are combined with gridded emissions to simulate excess CH_4 mole fractions and $\delta^{13}CH_4$. To compare the simulated excess CH_4 mole fractions to the measurements at ICL, daily background CH_4 mole fractions from the Mace Head Observatory (Chapter 3, Section 3.3.4) are subtracted from the 20-minute averaged measurements at ICL. $\delta^{13}CH_4$ values are simulated following Eq. 3.4 and using the $\delta^{13}CH_4$ isotopic signatures in Table 3.5 and the MHD background mole fractions and MHD $\delta^{13}CH_4$ (Chapter 3, Section 3.3.4).

Anthropogenic emissions from EDGAR v4.3.2 for the year 2012 and from NAEI for the year 2017, where point source emissions were added using the locations of the point sources, are used. These were the most recent versions of these emission inventories at the time simulations were performed. There have since been updates in both EDGAR and NAEI. The NAEI is only available for the UK, so for simulations using the NAEI a hybrid emissions map was created with NAEI emissions for the UK and EDGAR emissions for outside the UK. Wetland emissions from the mean of the 2015 extended ensemble WetCHARTs inventory and biomass burning emissions from GFED v4.1s (excluding agricultural waste burning emissions) are also used.

The four sets of anthropogenic emissions for the London area are shown in Fig. 4.3a-d. The UK NAEI emissions are approximately 2.5 times smaller than the EDGAR emissions for the London area (Table 4.4; Fig. 4.3e), but 8% smaller than the EDGAR emissions across the UK and North Sea (Fig. 4.3f). Emissions from the North Sea account for around 0.45 Tg CH_4 yr^{-1} in EDGAR and 0.04 Tg CH_4 yr^{-1} in NAEI (not including point source emissions). The 2 km NAEI and 10 km EDGAR show high emissions from individual grid cells that are smoothed out in the coarser 25 km EDGAR grid (Fig. 4.3a) and 25 km NAEI grid (Fig. 4.3c).

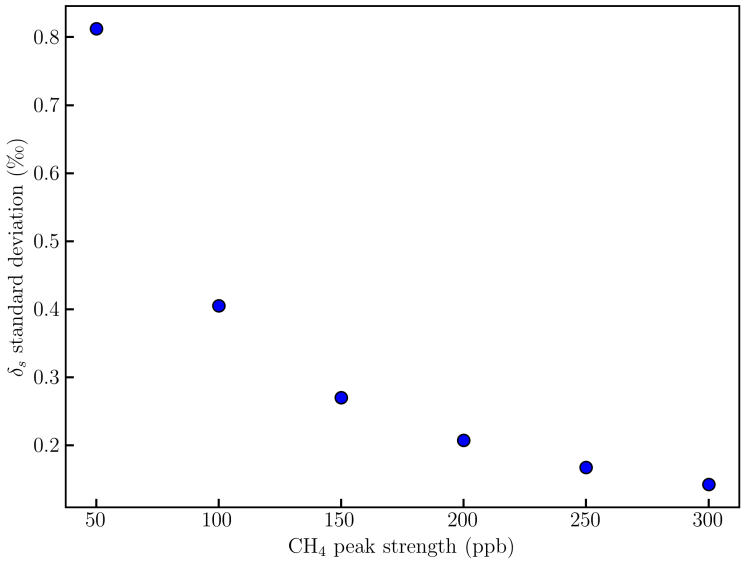


Figure 4.2: Standard deviations of the recovered isotopic source values for different peak strengths.

Subtracting the 25 km NAEI emissions from the 25 km EDGAR emissions (Fig. 4.3e-f) indicates the largest differences between inventories were in cities; London, Birmingham and the Leeds-Sheffield area, which have higher emissions in the EDGAR inventory. This shows that emissions in urban areas are particularly uncertain and in need of additional constraints.

Four combinations of footprints coupled with anthropogenic emissions data are used: (i) the 25 km footprints combined with the EDGAR emissions (EDGAR-25km); (ii) the 10 km footprints nested in the 25 km footprints combined with the EDGAR emissions (EDGAR-10km); (iii) the 25 km footprints combined with the UK NAEI emissions for the UK and the EDGAR emissions for the rest of the domain (NAEI-25km); and (iv) the 2 km footprints nested in the 10 km and 25 km footprints combined with the UK NAEI emissions for the UK and EDGAR for the rest of the domain (NAEI-2km). These are summarised in Table 4.3.

4.3 Results

4.3.1 Measurements

The 20-minute averaged CH_4 mole fractions from March 2018 to October 2020 along with the Mace Head background values are shown in Fig. 4.4a. Mole fractions ranged from 1895 ppb to 3924 ppb in the ICL measurements with a mean value of 2083 ± 145 (1σ) ppb. ICL mole fractions measured during the afternoon (13:00-17:00) had a smaller mean value, 2028 ± 73 (1σ) ppb, and a lower maximum value, 2477 ppb, showing

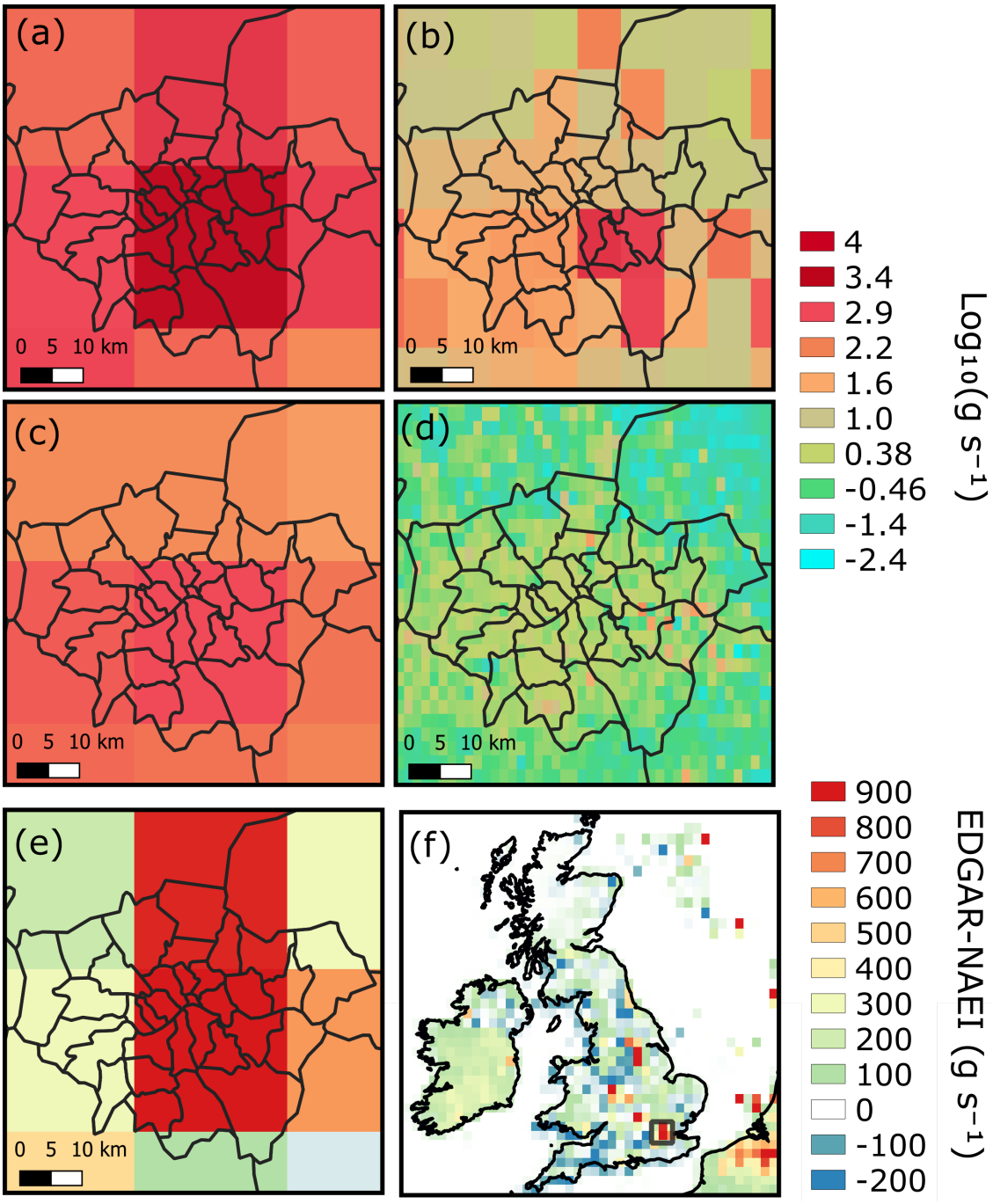


Figure 4.3: London CH_4 emissions from (a) EDGAR v4.3.2 (2012) scaled at $0.352^o \times 0.234^o$, (b) EDGAR at $0.10^o \times 0.10^o$, (c) UK NAEI (2017) scaled at $0.352^o \times 0.234^o$ and (d) UK NAEI scaled at $0.02^o \times 0.02^o$. The NAEI scaled at $0.352^o \times 0.234^o$ subtracted from the EDGAR emissions (in g s^{-1}) for London is shown in (e) and for the UK in (f). The London region in relation to the UK is shown by the black box in (f).

Table 4.2: Imperial College London isotopic source values summary for different peak strengths and window sizes.

Moving window	Peak strength (ppb)	Number of δ_s values	Range of δ_s values (‰)	Mean standard error on δ_s (‰)	$\delta_s \leq -45$ (%)
12-h	100	1664	[-69.6, -13.2]	3.83	23.7
	150	1046	[-66.3, -24.8]	2.77	24.8
	200	706	[-61.1, -25.6]	2.31	23.9
3-d	100	82	[-65.0, -19.5]	8.02	32.9
	150	41	[-55.8, -28.9]	5.18	36.9
	200	27	[-55.2, -30.9]	3.50	44.4
7-d	100	83	[-60.8, -24.1]	5.57	34.9
	150	47	[-55.2, -27.8]	3.65	31.9
	200	27	[-55.2, -30.9]	3.50	44.4

that higher concentrations are observed during the night-time from the build-up of emissions in the nocturnal boundary layer (Fig. 4.4b). The daily Mace Head background mole fractions ranged from 1907-1973 ppb and had a mean value of 1939 ± 13 (1σ) ppb. During the first UK COVID-19 lockdown period (23 March 2020-15 June 2020) there are more days with higher CH_4 mole fractions compared to the preceding months (Fig. 4.4a). Average CH_4 mole fractions before and during the COVID-19 lockdown period did not change (Fig. 4.5a).

The $\delta^{13}CH_4$ measurements at ICL are shown in Fig. 4.4c along with the calculated Mace Head background $\delta^{13}CH_4$ values. The mean $\delta^{13}CH_4$ at ICL for this period is -47.1 ± 0.9 (1σ)‰ with values ranging from -52.4‰ to -42.3‰. The afternoon $\delta^{13}CH_4$ mean was similar; -47.2 ± 0.8 (1σ)‰. Mace Head background $\delta^{13}CH_4$ averaged -47.6 ± 0.2 (1σ)‰ and ranged from -48.0‰ to -47.4‰. Observed $\delta^{13}CH_4$ at ICL was

Table 4.3: Summary of atmospheric CH_4 simulations at ICL. WetCHARTs and GFEDv4.1s were used for wetland and biomass burning emissions in all simulations.

Simulation	Footprints	Anthropogenic emissions
EDGAR-25km	25 km	EDGAR
EDGAR-10km	10 km nested in 25 km	EDGAR
NAEI-25km	25 km	NAEI in UK, EDGAR outside UK
NAEI-2km	2 km nested in 10 km nested in 25 km	NAEI in UK, EDGAR outside UK

Table 4.4: EDGAR and NAEI emissions for the UK and London. $\delta^{13}CH_4$ is the weighted average of different emission sectors using isotopic source signatures in Table 3.5.

Region	EDGAR emissions (Tg CH_4 yr^{-1})	NAEI emissions (Tg CH_4 yr^{-1})	EDGAR $\delta^{13}CH_4$ signature (‰)	NAEI $\delta^{13}CH_4$ signature (‰)
UK	3.00	2.00	-57.1	-50.7[a]
London	0.10	0.04	-53.7	-47.7

[a] Average excludes CH_4 shipping emissions, which changes UK average $\delta^{13}CH_4$ to -30.5 ‰.

generally higher than $\delta^{13}CH_4$ at Mace Head during 2018, but excursions both higher and lower than the background are seen during 2019-20. A mean increase of 0.05‰ in $\delta^{13}CH_4$ is observed at ICL during the first UK COVID-19 lockdown period. There are seasonal increases in atmospheric $\delta^{13}CH_4$ of around 0.03‰ per month at MHD during this period suggesting the change in ICL $\delta^{13}CH_4$ during the UK COVID-19 lockdown period is not significant in comparison to the concurrent Northern hemispheric $\delta^{13}CH_4$ seasonal changes.

The ICL mole fractions were detrended by fitting a first-order polynomial to Mace Head data to find the trend between 2018-2020 with the mole fraction on 1 March 2018 set as the reference point, t_{ref}. Detrended mole fractions were binned by month to evaluate seasonal variations (Fig. 4.5a). A seasonal cycle is observed with a CH_4 minimum occurring in July for both ICL and Mace Head measurements. Smaller interquartile ranges and smaller maximum values in the ICL mole fractions are observed in the summer months. Smaller CH_4 mole fraction enhancements have been observed in other urban studies. Helfter et al. (2016) found London CH_4 fluxes were 17% lower in the summer months than during the winter. Similar observations were made in Los Angeles (Verhulst et al. 2017) and Boston (McKain et al. 2015) in the USA. Smaller summertime CH_4 mole fractions measured at ICL could be attributed to seasonality in anthropogenic emissions - natural gas CH_4 emissions in Boston displayed some seasonality with lower emissions during the summer (McKain et al. 2015) - or could be due seasonal variations in the PBL. A deeper PBL is expected during the summer months, compared to winter months, because of increased insolation meaning larger enhancements would be expected in the winter compared to the summer (Verhulst et al. 2017).

Diurnal cycles are observed in the detrended ICL mole fractions with daily minimums between 13:00 and 15:00 (Fig. 4.6a) with generally smaller mole fractions between April and September. Differences in the diurnal cycles throughout the week vary depending on the time of year, which has also been seen in CH_4 mole

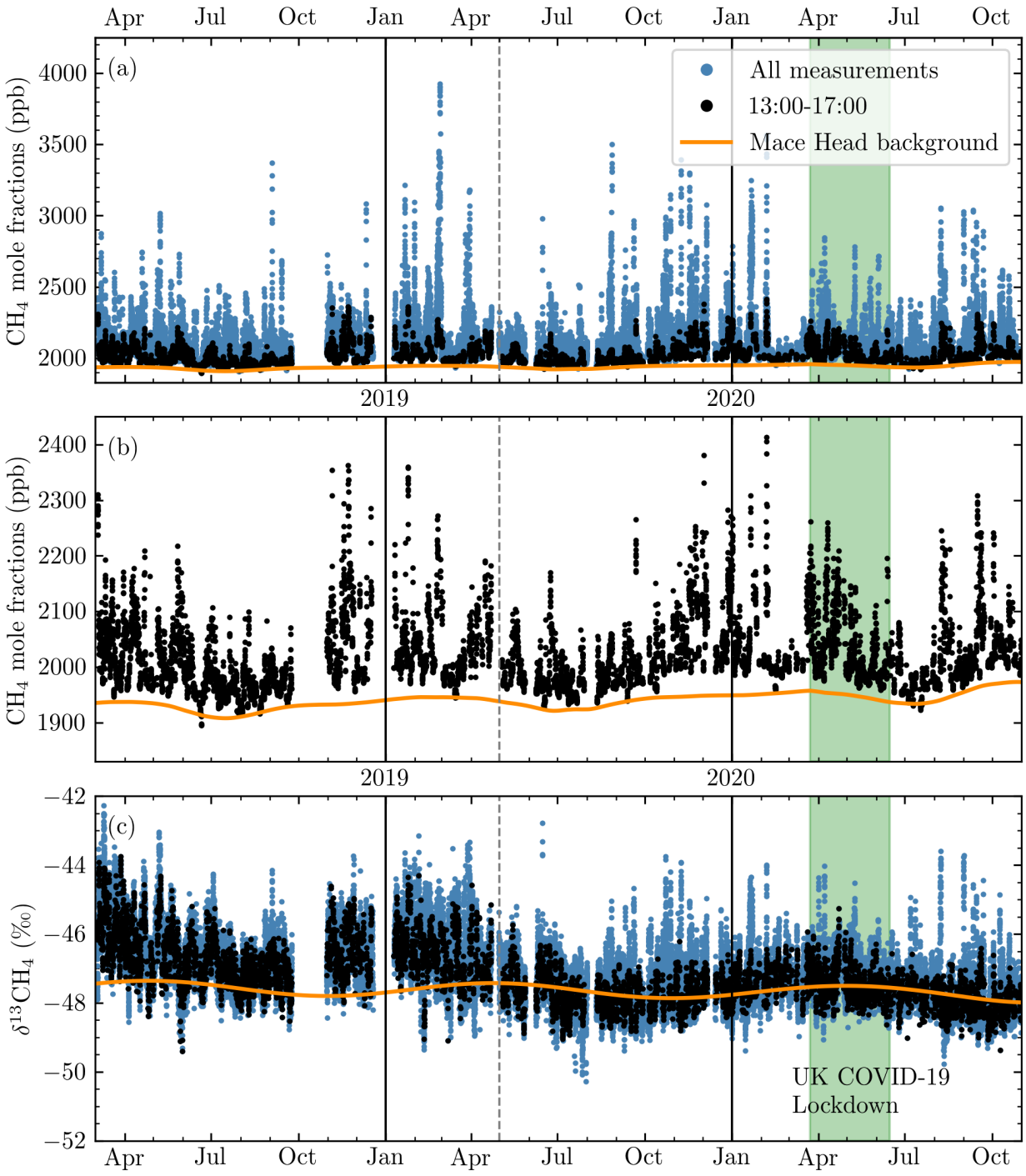


Figure 4.4: The 20-minute averaged measured (a) mole fractions, (b) 13:00-17:00 mole fractions and (c) $\delta^{13}CH_4$ values at ICL, along with the daily Mace Head background values from March 2018-October 2020. Afternoon (13:00-17:00) data are shown in black. The period of the first UK national COVID-19 lockdown is denoted by the green region. The grey dashed line denotes when the standard and target tanks were changed.

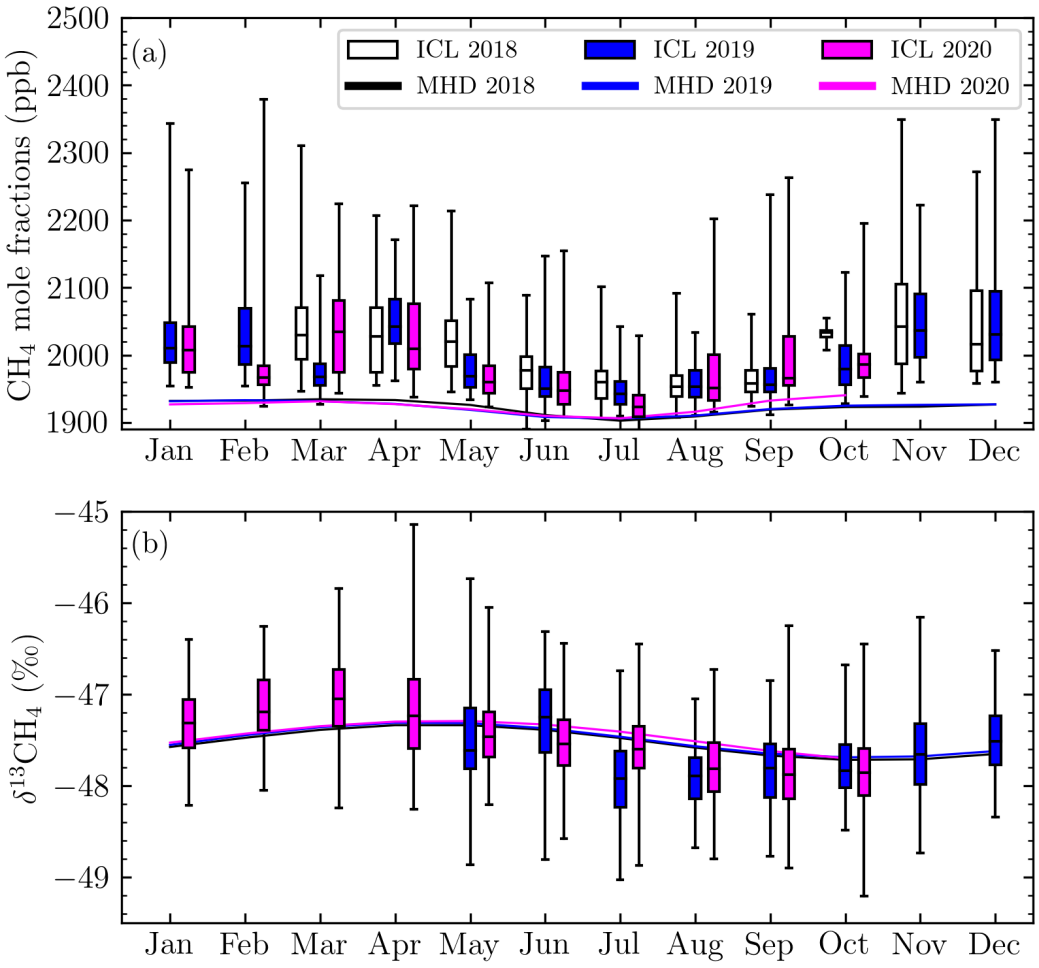


Figure 4.5: Seasonal cycles of detrended 20-minute measurements of (a) mole fractions and (b) $\delta^{13}CH_4$ at ICL (box plots) and Mace Head (lines) where values deviate about March 1, 2018 (t_{ref}) for mole fractions and about May 1, 2019 (t_{ref}) for $\delta^{13}CH_4$.

fraction measurements in Florence, Italy (Venturi et al. 2020). Differences in diurnal cycles could be due to seasonal variations in i) the PBL depth, ii) anthropogenic emissions (Helfter et al. 2016; Verhulst et al. 2017), or iii) the growth rate of the convective layer which is more rapid during the summer than winter -with lower mixing heights in the winter (Helfter et al. 2016). The average nocturnal build-up of CH_4 is significantly larger on Monday and Tuesday in the July-August-September (JAS) averaged mole fractions compared to the rest of the week (Fig. 4.6a), whereas the October-November-December (OND) averaged mole fractions have relatively similar levels of CH_4 nocturnal build-up throughout the week.

Here, the analysis focuses on $\delta^{13}CH_4$ measurements from May 2019 onwards as large unexplained variations

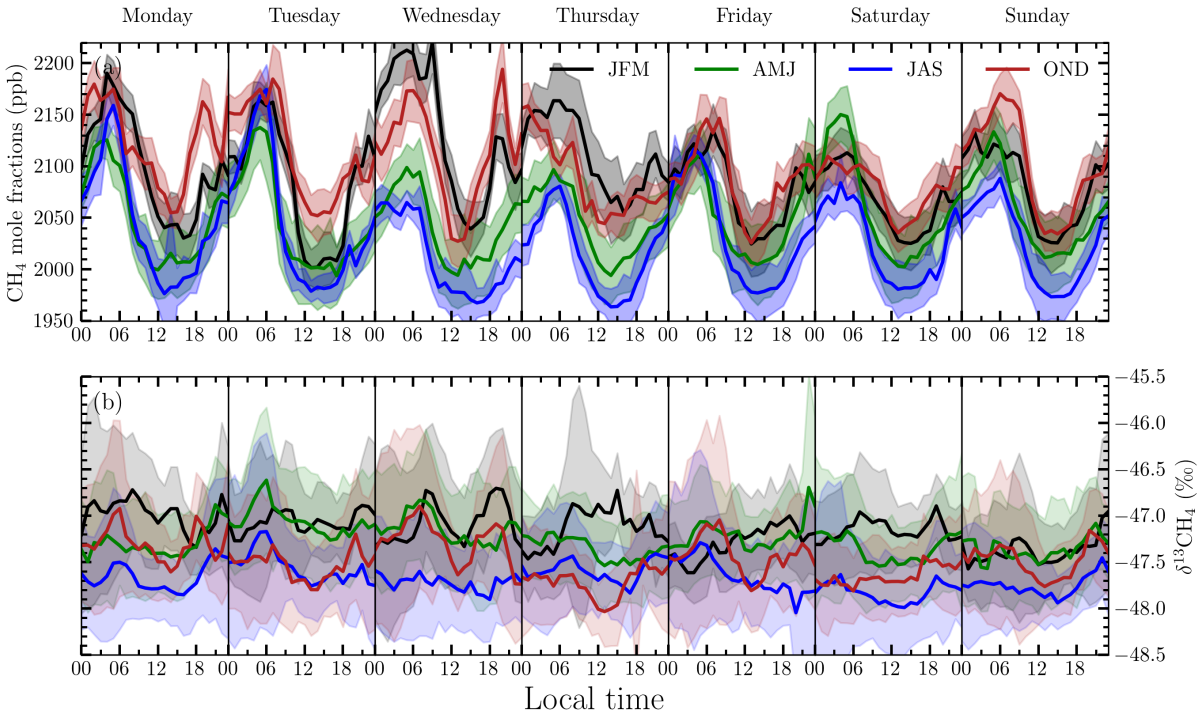


Figure 4.6: Weekly detrended 20-minute averages of (a) mole fractions and (b) $\delta^{13}CH_4$ at ICL (values normalised to 1 March 2018 and 1 May 2019, t_{ref}, respectively). Measurements are grouped by season of year and binned by hour-of-day and day-of-week. The 1σ range is included on both panels.

in one of the reference tanks before May 2019 result in larger $\delta^{13}CH_4$ uncertainties (Chapter 3, Section. 3.1.2). Afternoon measurements of $\delta^{13}CH_4$ at ICL were detrended by fitting a first-order polynomial to Mace Head background $\delta^{13}CH_4$ from 2018-2020 with $\delta^{13}CH_4$ on 1 May 2019 set as the reference point, t_{ref}, (Fig. 4.5b). ICL median $\delta^{13}CH_4$ between January and March were generally higher than the Mace Head background, and generally lower from July through to September. The $\delta^{13}CH_4$ ICL measurements averaged into hourly intervals tend to exhibit lower $\delta^{13}CH_4$ during the afternoon but no well-defined diurnal or weekly cycle (Fig. 4.6b).

4.3.2 Keeling plot analyses

Three moving time windows of lengths 12 h, three days, and seven days were used in the automated Keeling plot algorithm to find δ_s values between May 2019 and October 2020 (Fig. 4.7-4.8). The calculated δ_s values may correspond to an individual source sector (Table 3.5), but they can reflect mixtures of different sources influencing the measured air in each time window, where the δ_s is a weighted average of the different sources. Isotopic source values lower than -47‰ suggest the sources are primarily biogenic (waste and/or agriculture),

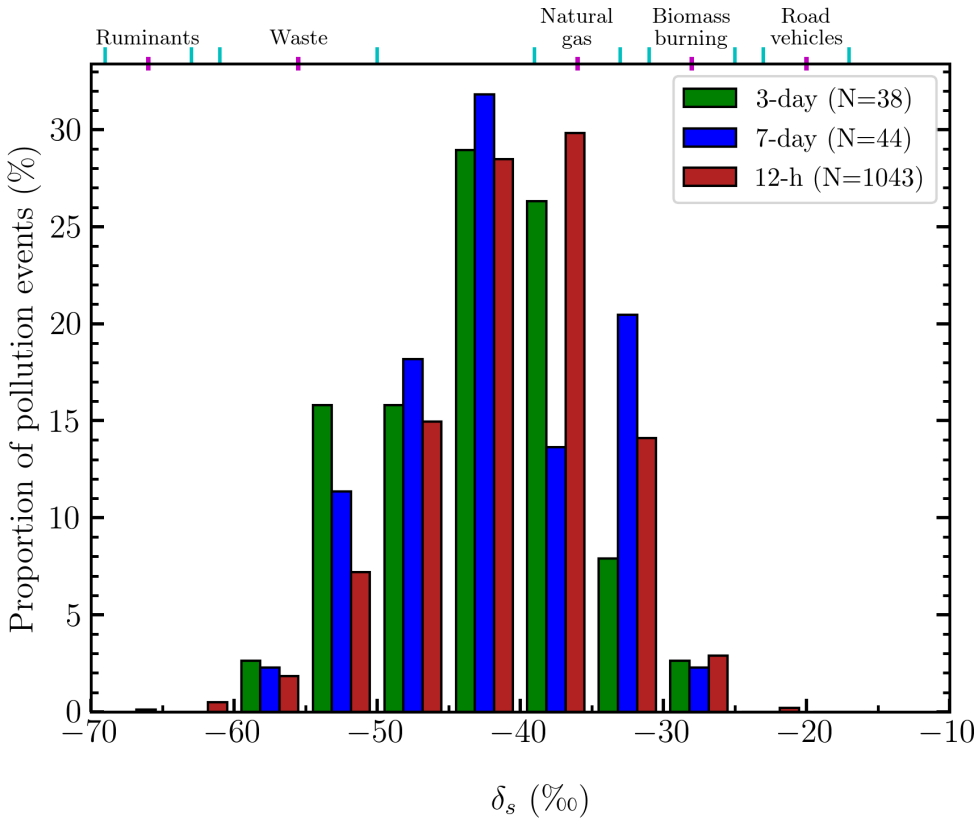


Figure 4.7: The distributions of the isotopic source values from Keeling plot analysis sorted into 5‰ bins. The ranges of UK isotopic signatures for different source sectors from Zazzeri et al. (2017) are shown at the top for reference.

and δ_s values higher than -47‰ suggest the sources are primarily from gas leaks from the CH_4 gas distribution network (i.e. natural gas leaks), where -47‰ is the midpoint between the waste and the natural gas CH_4 isotopic signatures (Table 3.5). Isotopic source values are sorted into 5‰ bins therefore -45‰ is used to distinguish between primarily biogenic and primarily natural gas CH_4 sources.

The 12-h moving windows, using measurements from all hours, returned 1043 δ_s values, of which 24.5% were ≤ -45‰. Most of the 12-h pollution events occurred during the nocturnal CH_4 build-up and the large number of δ_s values >-45‰ suggests natural gas sources are primarily driving the nocturnal CH_4 build-up around ICL. Natural gas leaks are expected to have a signature of -36 ± 3‰ in London (Zazzeri et al. 2017). Average uncertainties in δ_s were 2.8‰ in the 12-h windows.

The 3- and 7-day windows using 13:00-17:00 measurements returned 38 and 44 δ_s values, respectively, and

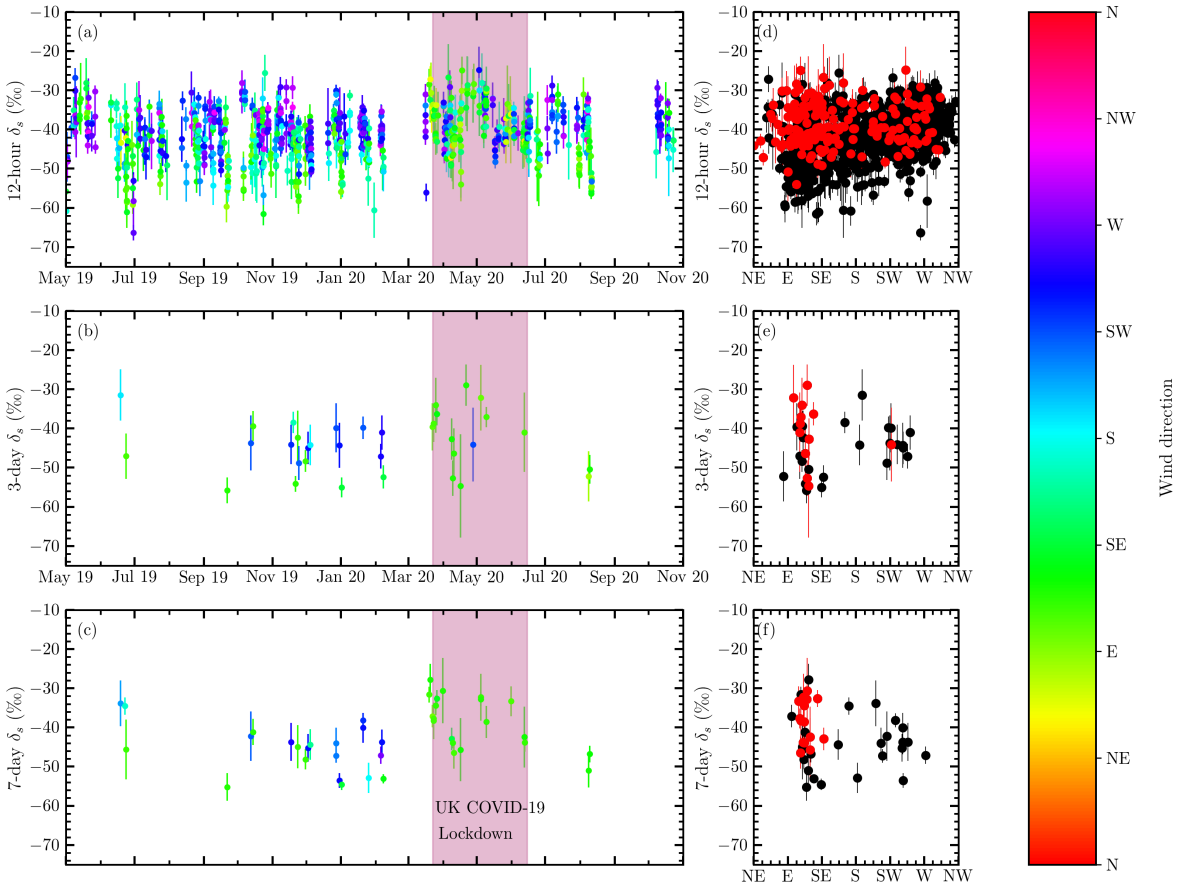


Figure 4.8: Time-series and correlation plots of isotopic source values for (a,d) 12-h; (b,e) 3-day; (c,f) 7-day windows. The marker colour (as shown in the colour-bar) denotes the mean wind direction from the start of the window to the peak of the pollution event (a-c). Black markers indicate times when wind direction data was not available. The UK COVID-19 lockdown period is shown in pink in time series and denoted by red markers in the correlation plots (d-f).

have higher proportions of biogenic influences than obtained with 12-h windows. In the 3-day windows, 26.3% of δ_s values were ≤ -45‰ and in the 7-day windows, 20.5% of δ_s values were ≤ -45‰. Still, a majority of pollution events had δ_s values >-45‰, showing that natural gas leaks are the main source of CH_4 pollution at ICL sampled in the afternoon and arising from larger-scale regional influences, in addition to the presumably more local sources sampled in the night. Average uncertainties in δ_s were 4.4‰ in the 3- and 7-day windows.

δ_s values between -30‰ and -25‰ may arise from a mixture of vehicular and natural gas CH_4 but they have peak strengths smaller than 200 ppb and they comprise less than 5% of the isotopic source values, indicating CH_4 emissions from the nearby roads and power station are small.

The relationship between wind direction and δ_s values was explored (Fig. 4.8) but consistent patterns were not found, which reflects the collocation and heterogeneity of sources in London. Some events with low isotopic signatures and wind direction in the southerly or south-westerly direction may be influenced by the sewage or landfill sites south or southwest of ICL (Fig. 3.2). δ_s values observed during the first UK COVID-19 lockdown period were ~ 2‰ higher in the 12-h windows and ~ 5‰ higher in the 3- and 7-day windows compared to the months before and after the lockdown. However, during the first UK COVID-19 lockdown period there was an unusual predominance of easterly winds.

4.3.3 Simulations of methane: simulated CH_4 mole fractions

Afternoon simulations of CH_4 mole fractions are compared with the afternoon observations at ICL in Fig. 4.9 for 2020 (Fig. 4.10, 4.11 for 2018 and 2019) and in Fig. 4.12 for all years. As previously highlighted, afternoon mole fractions are less sensitive to local emissions and provide a more accurate representation of regional-scale CH_4 sources and mole fraction variations. Afternoon weather conditions tend to be represented better in models as errors in the modelled planetary boundary layer are considered smaller during the afternoon (Brophy et al. 2019; Jeong et al. 2013). Simulated CH_4 using UK NAEI tends to be lower than the ICL measurements. Simulated mole fractions using EDGAR emissions are expected be larger than mole fractions from simulations using NAEI as emissions in EDGAR are 2.5 times larger than the NAEI emissions for the London area (Table. 4.4).

Linear regressions (Fig. 4.12a-d), RMSE and median simulation-observation differences (Fig. 4.12e-h) are used to compare the simulations with the observations. Linear regression coefficients are very similar when using an ordinary least squares and an orthogonal distance regression.

Though EDGAR-10km comparisons (Fig. 4.12b) have slopes closest to one, the EDGAR-10km comparisons also have the largest RMSE (61.9 ppb; Table 4.5), whereas the other simulation-measurement RMSE are between 44.5 ppb (EDGAR-25km; Table 4.5) and 53.7 ppb (NAEI-2km; Table 4.5). The larger RMSE values in EDGAR-10km simulations could be due to the very large simulation-observation differences of a few data points (as seen in the upper left of Fig. 4.12b).

Distributions of simulation-observations (Fig. 4.12e-h) show 13:00-17:00 median values are closer to zero

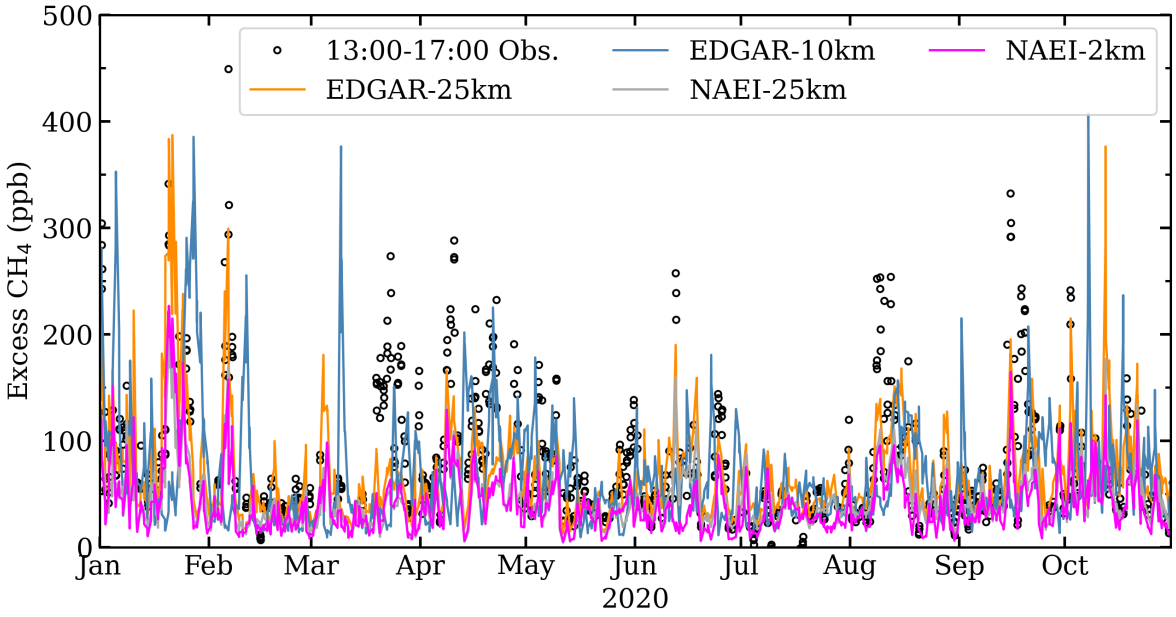


Figure 4.9: Excess simulated and observed 13:00-17:00 mole fractions at ICL for 2020 where the Mace Head background has been subtracted from the ICL measurements.

in simulations using EDGAR emissions over the UK than when NAEI emissions are used. EDGAR-10km has a median simulation-measurement difference of 0.93 ppb. The NAEI-25km and NAEI-2km simulation-measurement distributions have afternoon median values of -19.6 ppb and -22.5 ppb respectively (Fig. 4.12g-h).

A scaling factor, β, can be applied to each simulation data point so that it exactly matches the corresponding measured excess mole fraction data point, ΔC_{obs}. Scaling factors are calculated as:

$$\beta = \Delta C_{obs} / C_{sim}. \tag{4.1}$$

Since ΔC_{obs} are the Mace Head background mole fractions subtracted from the ICL measurements, background mole fractions exert the most leverage on the values of β that are calculated. Background mole fractions

Table 4.5: Simulation-observation 13:00-17:00 RMSE values, scaling factors and correlation coefficients.

Simulation	RMSE	β Median (Q1-Q3)	ρ
EDGAR-25km	44.5 ppb	0.97 (0.72-1.29)	0.74
EDGAR-10km	61.9 ppb	1.07 (0.80-1.46)	0.66
NAEI-25km	52.3 ppb	1.46 (1.12-1.97)	0.77
NAEI-2km	53.7 ppb	1.65 (1.26-2.25)	0.77

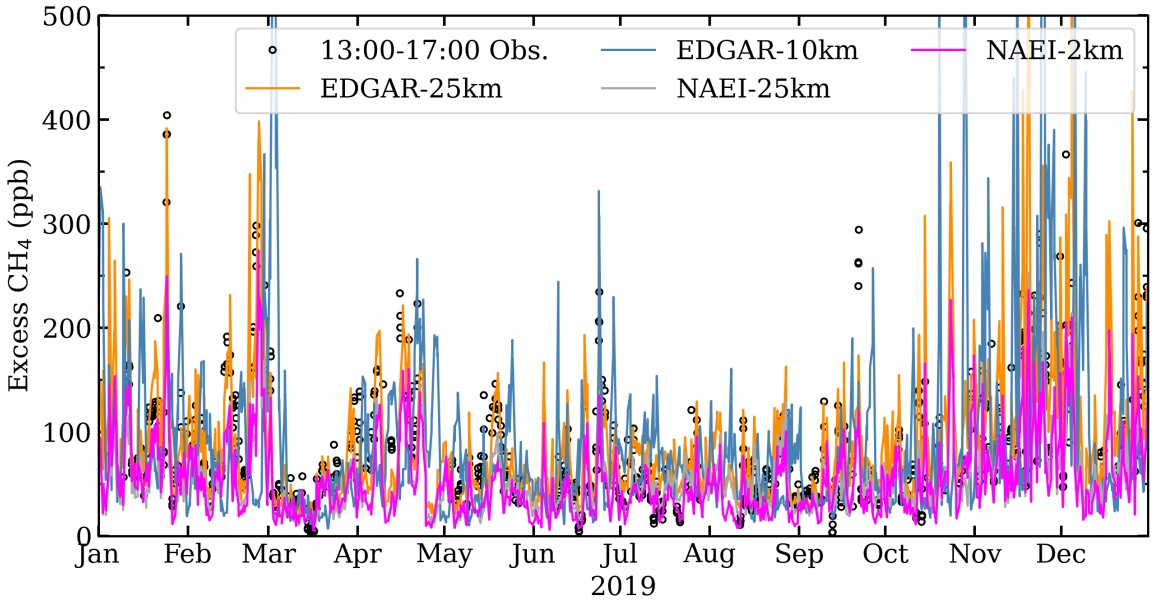


Figure 4.10: Excess simulated and observed 13:00-17:00 mole fractions at ICL for 2019 where the Mace Head background has been subtracted from the ICL measurements.

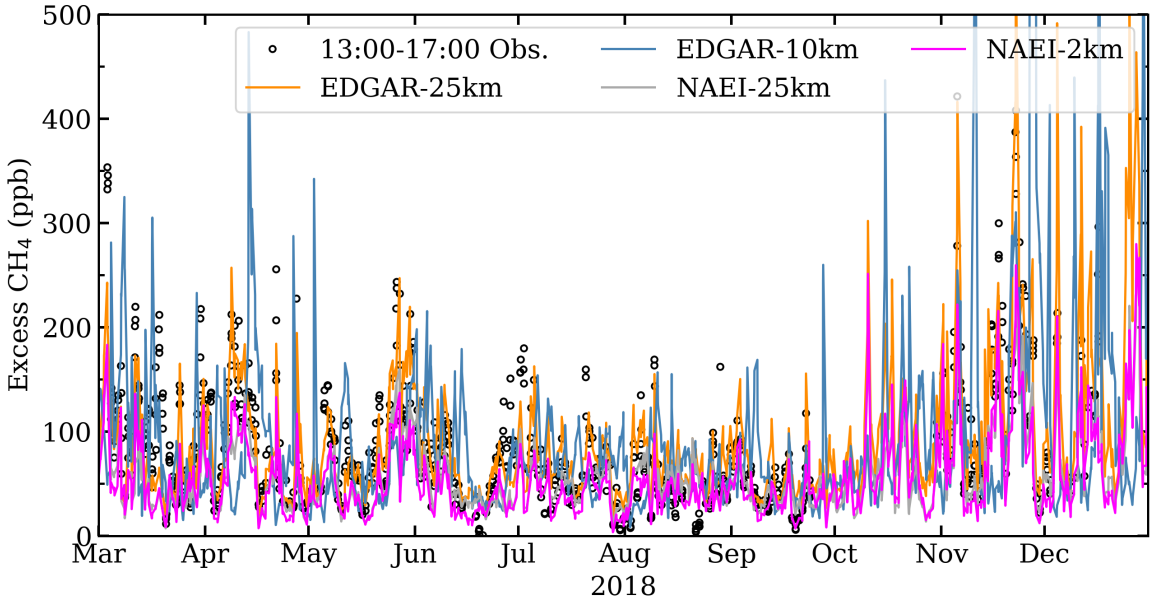


Figure 4.11: Excess simulated and observed 13:00-17:00 mole fractions at ICL for 2018 where the Mace Head background has been subtracted from the ICL measurements.

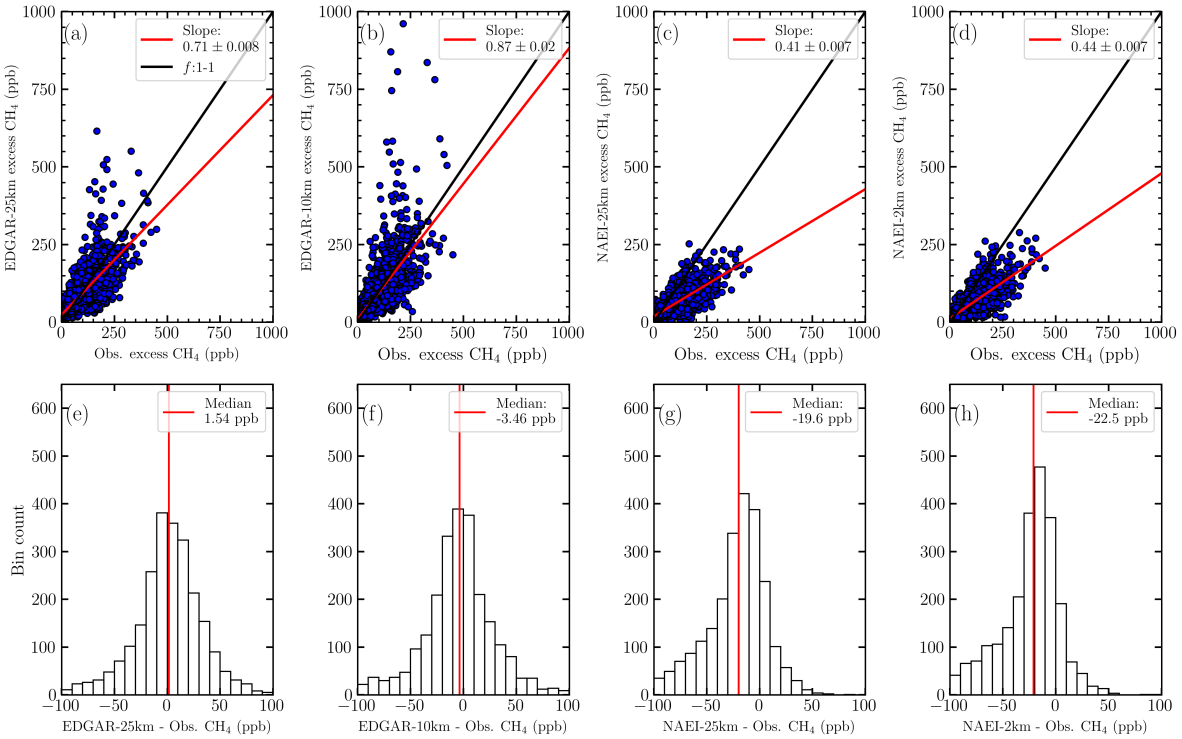


Figure 4.12: Simulation-observation comparisons of excess mole fractions using linear regressions (top row) and distributions of the simulation-observation differences (bottom row) for (a, e) EDGAR-25km; (b, f) EDGAR-10km; (c, g) NAEI-25km; (d, h) NAEI-2km from March 2018 to October 2020.

that are too low or too high could introduce bias into the excess measured mole fractions and thus β. This is accounted for by varying each daily background mole fraction by randomly sampling from a Gaussian distribution centred on the daily background value and using the daily standard deviation to vary the mole fraction background and calculate the β values 150 times. The mean β value for each data point is then calculated and the median and interquartile values of β for the whole period are reported in Table 4.5.

The median β scaling factors are more similar in the 13:00-17:00 data with EDGAR simulations having scaling factors closer to one (Table 4.5) suggesting a strong correspondence between the EDGAR emissions and the observations. On average, 13:00-17:00 NAEI-2km simulations need to be scaled by 1.61 and NAEI-25km by 1.42. The interquartile ranges of β scaling factors are between 0.57 for EDGAR-25km simulations and 0.99 for NAEI-2km simulations, implying β is quite variable and may suggest that observation-simulation differences are not entirely systematic.

Increasing the spatial resolution in the simulated mole fractions had a small effect in comparison to the

differences between using NAEI and EDGAR emissions for the UK. The conservative gridding approach (Chapter 3, Section 3.4.5) ensures emissions across a region will be the same for all spatial resolutions. Differences will arise as a result of the width of the different back-trajectory plumes and the emissions grid cells they intersect.

4.3.4 Simulations of methane: simulated $\delta^{13}CH_4$ values

Simulated $\delta^{13}CH_4$ values are consistently ^{13}C-depleted relative to the background in all simulations (Fig. 4.13, 4.14), which contrasts with the observations that show $\delta^{13}CH_4$ excursions both above and below the background (Fig. 4.13). The simulated range in $\delta^{13}CH_4$ in NAEI-25km and NAEI-2km is only 0.2‰, which reflects the strong similarity between the mean isotopic source signature for London of -47.7‰ in NAEI (Table 4.4) and the background $\delta^{13}CH_4$ (-48.0‰ to -47.4‰). EDGAR-25km and EDGAR-10km also underestimated the variation in $\delta^{13}CH_4$ as isotopically heavy pollution events were missing, even though the isotopically light spikes are often exaggerated in EDGAR-10km, as was found for the mole fractions. The mean isotopic source signature for London is -53.7‰ in EDGAR (Table 4.4) due to a large proportion of emissions from waste (93%) and a small proportion from natural gas (3%). The proportion of emissions from natural gas is higher in NAEI (41%), but the mean isotopic source signature for London in both NAEI and EDGAR are much lower than the median in the isotopic source signatures calculated in the Keeling plot analysis (-41.6‰; Fig. 4.7).

Simulation-observation comparisons in Fig. 4.15a-d do not show any correlation between the measurements and the simulations. The simulation-observation difference distributions (Fig. 4.15e-h) are all negatively skewed and have mean differences ranging from -0.63‰ - in the NAEI-2km data - to -0.80‰ - in the EDGAR-25km simulations. This indicates the source apportionment in the NAEI and EDGAR inventories have fossil-fractions that are too low, and their sources may be distributed too homogeneously.

To test whether the underestimates in excess CH_4 mole fractions and in $\delta^{13}CH_4$ in the NAEI simulations could be explained solely by underestimated emissions from natural gas leaks $\delta^{13}CH_4$ is recalculated in NAEI-25km and NAEI-2km by assuming all the missing simulated CH_4 is natural gas CH_4. Scaling factors for the simulated natural gas mole fractions, calculated from the overall CH_4 scaling factors (Table 4.5), are 3.7 for NAEI-25km and 4.1 for NAEI-2km. The recalculated $\delta^{13}CH_4$ shows much smaller excursions below background $\delta^{13}CH_4$ and now some excursions above background $\delta^{13}CH_4$ (Fig. 4.16), particularly in NAEI-2km where the correlation between observed and simulated $\delta^{13}CH_4$ increased from 0.37 to 0.56. With this scaling fossil sources of CH_4 comprise 43% and 52% of added CH_4 mole fractions in the NAEI-

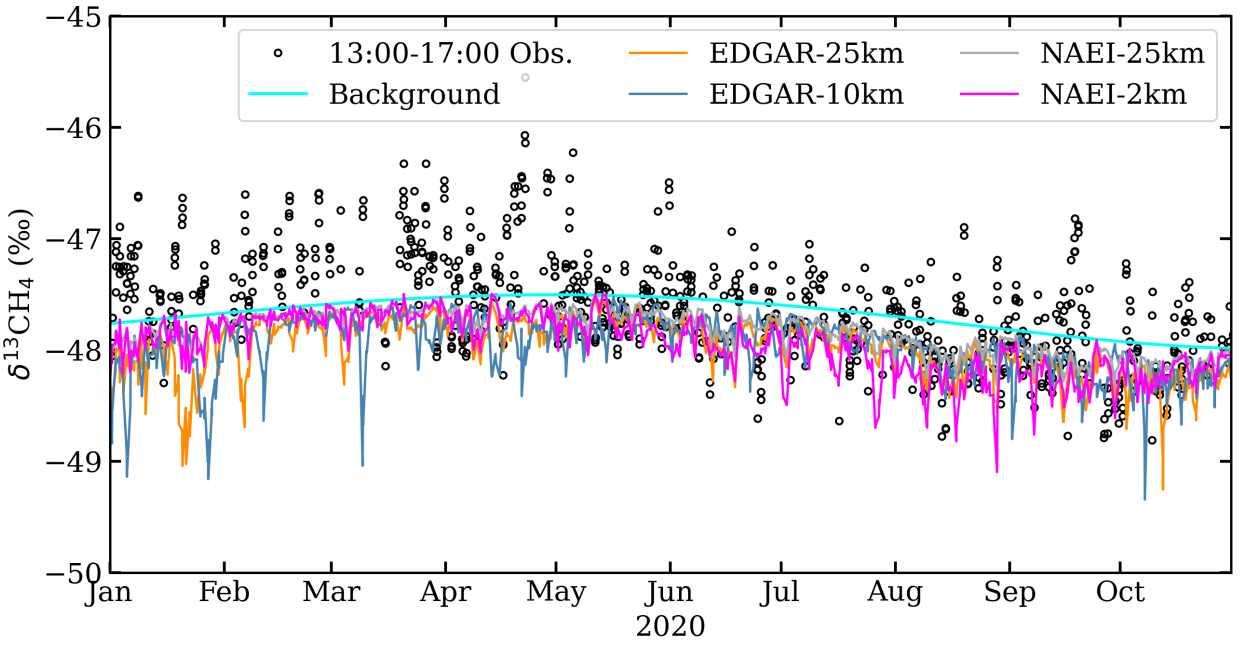


Figure 4.13: Simulated and measured $\delta^{13}CH_4$ values for 2020 using 13:00-17:00 data.

25km and NAEI-2km simulations, respectively. However, it appears that the recalculated $\delta^{13}CH_4$ reflects a rather homogeneous fossil-fraction in excess CH_4 with an isotopic signature near to background $\delta^{13}CH_4$, which therefore produces very small variations in $\delta^{13}CH_4$ in contrast with the observations. This indicates the locations of natural gas and waste emissions in London are more spatially distinct than in the NAEI inventory.

4.3.5 Sectoral source apportionment in the simulations

The mean source apportionment at ICL for each set of simulations are given in Table 4.6. In all four sets of simulations, simulated CH_4 mole fractions from the waste sector dominated at ICL, accounting for between 30.0% (NAEI-2km) and 71.1% (EDGAR-25km) of added CH_4 (Table 4.6). Whilst waste CH_4 at ICL was more than three times larger than any other source sector in EDGAR-25km and EDGAR-10km, waste CH_4 mole fractions were lower and more comparable to natural gas CH_4 mole fractions in NAEI-25km and NAEI-2km simulations. Natural gas CH_4 at ICL formed the third largest source in the NAEI-25km (20.4%) and second largest in the NAEI-2km (28.3%) but it was significantly smaller in EDGAR-25km (6.2%) and EDGAR-10km (8.1%). Agricultural sources at ICL accounted for the second largest source in EDGAR-25km (13.8%), EDGAR-10km (18.8%) and NAEI-25km (22.2%). Note the source apportionment of added CH_4 mole fractions differs between simulations and emission inventories since atmospheric measurements at ICL

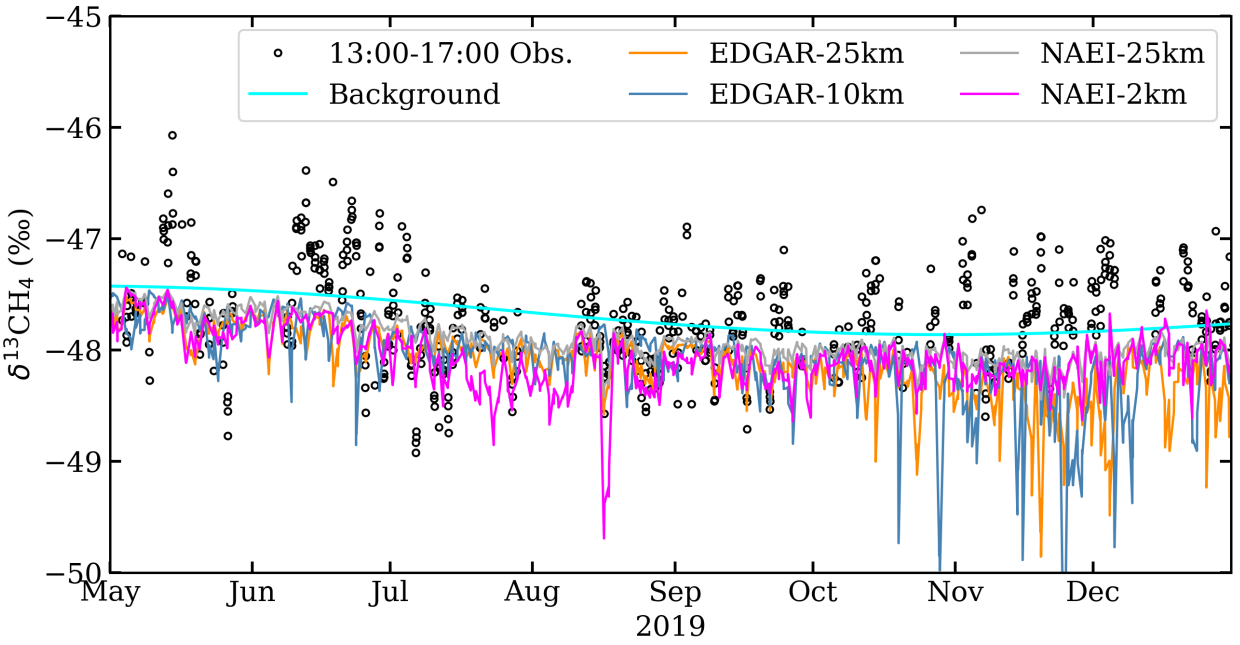


Figure 4.14: Simulated and measured $\delta^{13}CH_4$ values for 2019 using 13:00-17:00 data.

do not have equal sensitivity to methane emissions from across London. Hence the use of NAME footprints for calculating the different sensitivities at different times.

Higher resolution simulations decreased the proportion of waste sources and increased the proportion of natural gas CH_4 sources. The distribution of emissions in lower resolution simulations are likely to unrealistically smooth the point source emissions from landfills across the London area, increasing the probability of the back-trajectories interacting with emissions from these grid cells. For example, NAEI-2km waste emissions are located towards the outskirts of London (Fig. 4.17d) but NAEI-25km waste emissions are uniformly distributed across London (Fig. 4.17c). Natural gas emissions are located near the centre of London (Fig. 4.18d) but not uniformly distributed in the coarser resolution emissions due to the absence of natural gas emissions on the outskirts/ outside of London (Fig. 4.18c).

Simulated CH_4 from biomass burning sources (GFEDv4.1s) were negligible (< 0.2%; Table 4.6) in comparison to the contributions from other sources. However, CH_4 from wetlands formed a significant proportion of added CH_4 (6.0% – 9.8%; Table 4.6), with higher contributions during the summer. A pollution event on 16 August 2019 that had a low isotopic source signature coincided with an 80 ppb simulated wetland mole fraction on the same day.

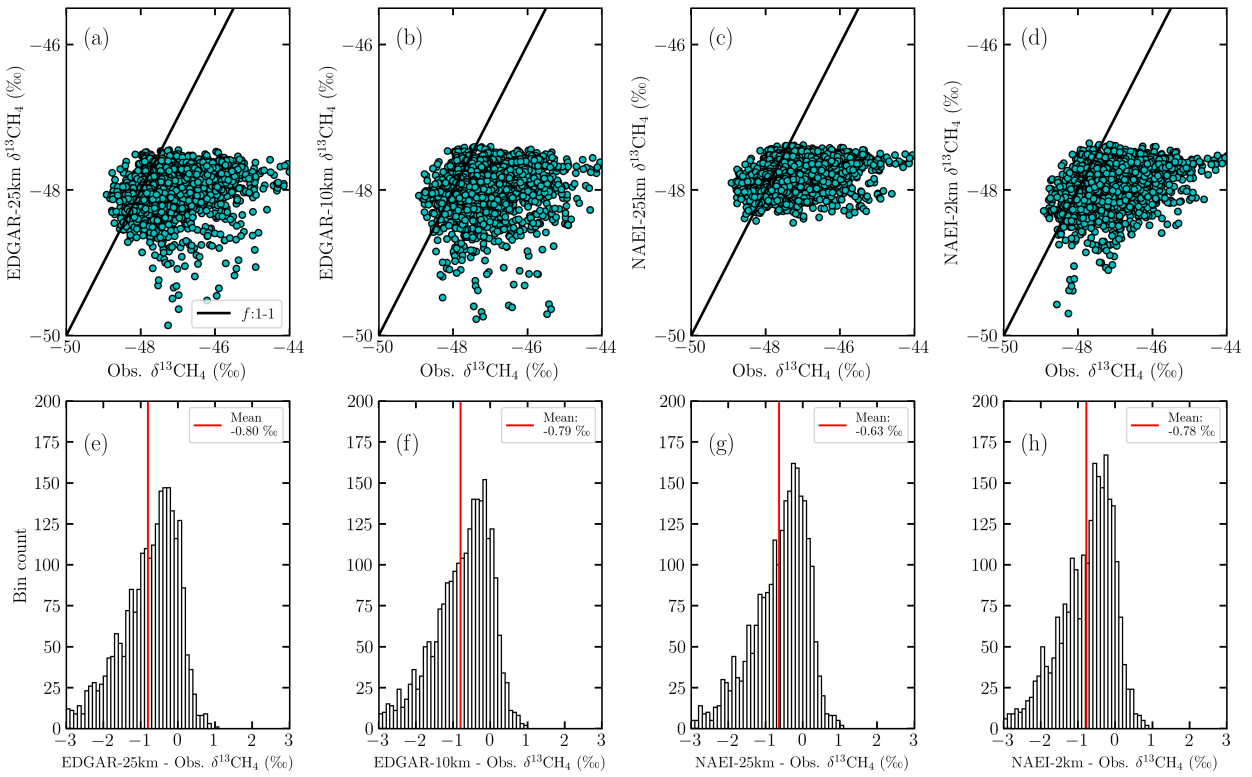


Figure 4.15: Simulation-observation comparisons of $\delta^{13}CH_4$ using point-by-point comparisons (top row) and distributions of the simulation-measurement differences (bottom row) for (a, e) EDGAR-25km; (b, f) EDGAR-10km; (c, g) NAEI-25km; (d, h) NAEI-2km.

4.4 Discussion

Continuous measurements of CH_4 mole fractions and $\delta^{13}CH_4$ in central London show, through Keeling plot analyses, a range of different CH_4 sources exist in London. Most isotopic source values are >-45‰ indicating a high fossil-fraction of added CH_4 for central London. Comparisons between measurements and the simulated excess mole fractions show a good correspondence between the EDGAR-25km, EDGAR-10km simulations and observations. The NAEI simulations at 2 km and 25 km significantly underestimate the observations, but retain a good correlation. The NAEI emissions for London need to be scaled by 1.52 (1.39-1.65) and EDGAR emissions by 0.99 (0.92-1.07), when using the 13:00-17:00 data, which is more representative of the London area and has smaller errors in the modelled boundary layer mole fractions than when night-time data is included. In contrast, a correlation is not observed between the measured and simulated $\delta^{13}CH_4$ values. Unlike the simulated mole fractions, simulated $\delta^{13}CH_4$ values are dependent on the source sector spatial distributions in the emissions inventories. Simulations of $\delta^{13}CH_4$ fail to capture any $\delta^{13}CH_4$ excursions above

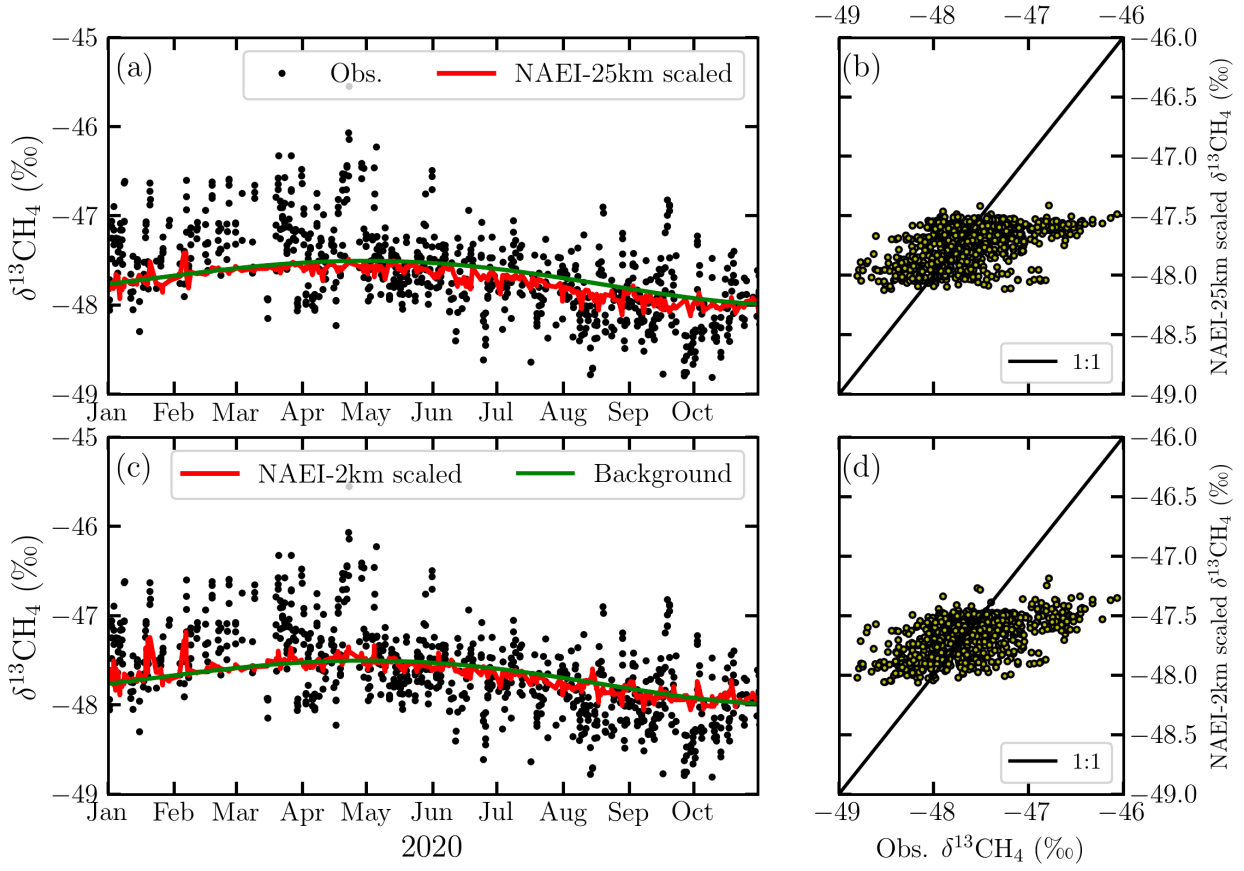


Figure 4.16: Time-series comparison of simulated (a) NAEI-25km and (c) NAEI-2km $\delta^{13}CH_4$ recalculated by scaling the simulated natural gas mole fractions, along with observations for afternoon hours. Simulation-observation comparisons of $\delta^{13}CH_4$ using linear regressions for (b) NAEI-25km and (d) NAEI-2km for 2020 afternoon hours.

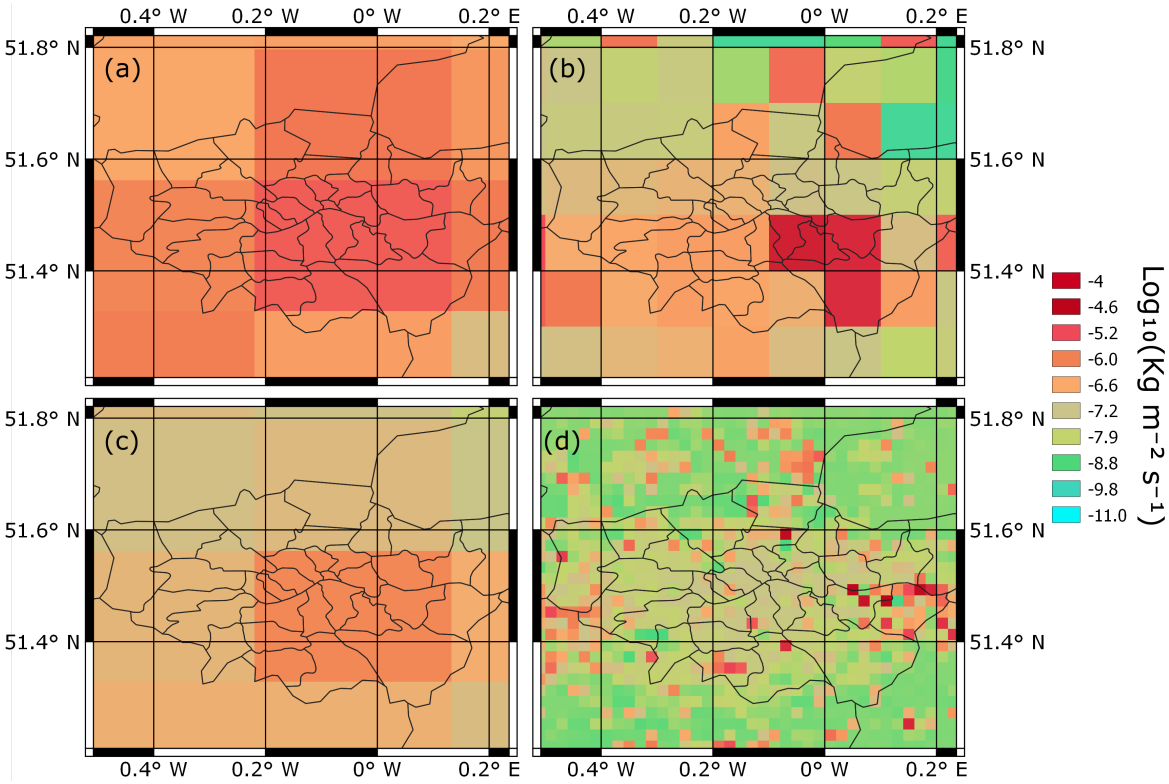


Figure 4.17: London waste emissions from EDGAR gridded at (a) $0.352^o \times 0.234^o$, (b) $0.10^o \times 0.10^o$ and UK NAEI gridded at (c) $0.352^o \times 0.234^o$ and (d) $0.02^o \times 0.02^o$.

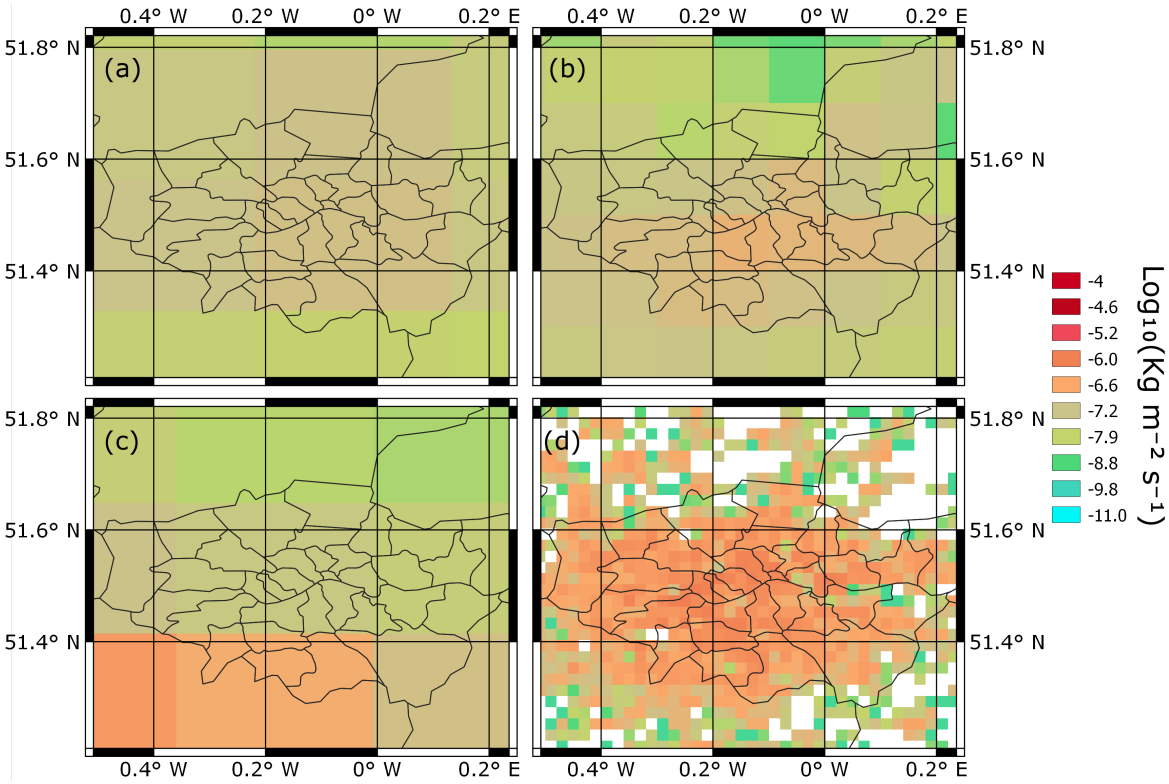


Figure 4.18: London natural gas emissions from EDGAR gridded at (a) $0.352^o \times 0.234^o$, (b) $0.10^o \times 0.10^o$ and UK NAEI gridded at (c) $0.352^o \times 0.234^o$ and (d) $0.02^o \times 0.02^o$.

Table 4.6: Mean simulated source apportionment for excess CH_4 at Imperial College London and in the CH_4 emissions for London.

Source sector	Imperial EDGAR-25km (%)	Imperial EDGAR-10km (%)	Imperial NAEI-25km (%)	Imperial NAEI-2km (%)	Total London EDGAR (%)	Total London NAEI (%)
Biomass burning	0.1	0.1	0.1	0.1	-	-
Combustion	2.3	3.4	3.2	3.7	2.9	5.5
Natural gas	7.4	8.7	17.8	22.6	3.3	41.2
Road vehicles	0.3	0.4	0.3	0.4	0.3	0.8
Agricultural	18.3	24.3	26.9	30.1	0.3	0.8
Waste	62.7	52.6	38.7	30.0	93.2	52.0
Wetlands	8.9	10.5	13.0	13.1	-	-

the background as seen in the observations suggesting the NAEI and EDGAR inventories are underestimating natural gas emissions for the London area.

Under-reported natural gas emissions are reflected in all four $\delta^{13}CH_4$ simulations, where there are few simulated values above the background in contrast to the observations. While the EDGAR-25km and EDGAR-10km mole fraction simulations are most comparable to the observed mole fractions, discrepancies in simulated $\delta^{13}CH_4$ show that the apportionment of sources is incorrect in EDGAR. Over 90% of EDGAR CH_4 emissions for London are allocated to the waste sector, which would require leak rates in natural gas infrastructure to be very low, in contrast to observations in other cities with older infrastructure (e.g. McKain et al. 2015). In EDGAR v5.0, a newer version of the EDGAR inventory, not only are CH_4 emissions for the UK larger but these increases have been attributed to waste sector emissions. There may be even larger discrepancies between urban observation and simulations when using EDGAR v5.0 emissions. The underestimation of mole fractions in the NAEI-25km and NAEI-2km might be accounted for by missing natural gas emissions in the NAEI inventory for London. Scaling the natural gas mole fractions in the NAEI simulations to match the overall excess mole fraction (which increased the natural gas fraction from 22.6% to 52.1%) improved the correspondence between the observations and simulated $\delta^{13}CH_4$ slightly, however, it appears the spatial allocation of waste and natural gas emissions in the inventory is too homogeneous. Overall, it does not seem possible to improve the model-data comparison for both CH_4 mole fractions and $\delta^{13}CH_4$ without increasing CH_4 emissions from natural gas leaks in the London area in the inventories. More explicit use of $\delta^{13}CH_4$ and CH_4 data with high-resolution NAME simulations in an inversion framework including consideration of uncertainties in measured, background and modelled $\delta^{13}CH_4$ and CH_4 could help to specify the fossil-fraction

in London more precisely.

Previous ground-based measurement campaigns in London found inventory emissions were underestimated. Helfter et al. (2016) reported mean annual measured emissions of 72 ± 3 t CH_4 km^{-2} yr^{-1}, which was more than double the London inventory estimate. Assuming their measured emissions are representative of the Greater London area, this is approximately equivalent to 0.11 Tg CH_4 yr^{-1}. This is similar to the EDGAR v4.3.2 (2012) estimate of 0.10 Tg CH_4 yr^{-1} for the same London area (Table 4.4). Simulation-observation comparisons of ICL CH_4 mole fractions are in good agreement with the EDGAR emissions estimate suggesting total London CH_4 emissions have not significantly changed since the Helfter et al. (2016) measurement campaign. The median differences between the NAEI simulations and ICL measurements are not as large as those found by Helfter et al. (2016) suggesting some improvement in the NAEI emission estimates for London, but with some sources still underestimated.

Isotopic measurements of $\delta^{13}CH_4$ by Zazzeri et al. (2017) indicated a predominance of fossil fuel CH_4 in central London that was not seen in the NAEI inventory, which estimated 29% of London CH_4 emissions were natural gas CH_4 at that time (compared to 41% in the current inventory). Whether fossil fuel CH_4 was underreported or misattributed was an open question as Zazzeri et al. (2017) did not use an atmospheric transport model to generate simulations that could be compared with observed concentrations. Here, the model-data analysis provides evidence that the NAEI inventory does appear to underestimate natural gas leaks, in agreement with the hypothesis presented in Zazzeri et al. (2017).

The results from these continuous long-term CH_4 and $\delta^{13}CH_4$ measurements show that they can be used for effective evaluation of CH_4 emissions from natural gas and waste sources in urban areas. Measurements from a single site would be significantly enhanced by a larger urban network of CH_4 and $\delta^{13}CH_4$ measurements encompassing the spatial heterogeneity in different CH_4 sources. Measuring from a greater height would also be useful as this would increase the geographical size of the footprint and allow greater mixing of individual sources before measurement.

Measurements of other tracers, such as deuterium, radiocarbon or ethane, would provide additional constraints on the London CH_4 source apportionment.

4.5 Conclusion

This chapter presents over two years of atmospheric measurements of CH_4 mole fractions and $\delta^{13}CH_4$ from Imperial College London. Isotopic source values from Keeling plot analysis revealed a predominance of natural gas CH_4 with source values higher than -45‰ in 74% – 80% of the afternoon data. In contrast, simulated sectoral contributions using UK NAEI and EDGAR inventories showed the largest fractions from waste sectors, leading to a simulated underestimation of observed $\delta^{13}CH_4$. These results suggest that natural gas leaks in London are under-reported in both inventories, consistent with previous studies in London and some other global cities.

Chapter 5

Developing a framework for regional source attribution using atmospheric measurements of CH_4 concentrations, $\delta^{13}CH_4$ and $\Delta^{14}CH_4$

"Science calculates / all things that live between the cosmic rays / and earthbound nitrogen in equilibrium / take in and give off carbon radiation / by rate of fifteen point three disintegrations / per gram per minute and at dying all / cease to take in and give off irreplaced / their whole accumulation pulse by pulse / the steady running down runs down the ages / to a half-life past five thousand years"

— Ann Deagon, *Carbon 14 (1974)*

Abstract

Sources of regional methane emissions can be identified through isotopic and tracer measurements. Isotopic measurements of atmospheric $\delta^{13}CH_4$ are a well-established approach for attributing methane sources but $\delta^{13}CH_4$ source signatures have large uncertainties. Radiocarbon measurements of atmospheric methane ($\Delta^{14}CH_4$) could provide additional constraints on methane source attribution as fossil CH_4 sources are devoid of radiocarbon but non-fossil CH_4 sources contain measurable amounts of radiocarbon. $\Delta^{14}CH_4$ measurements therefore provide clear distinctions between fossil and non-fossil CH_4 sources. In this chapter, a combined CH_4-$\delta^{13}CH_4$-$\Delta^{14}CH_4$ framework is presented for quantifying and detecting regional scale changes in methane fossil-fractions and sources based on relationships of CH_4-$\delta^{13}CH_4$-$\Delta^{14}CH_4$, $\Delta^{14}CH_4$-CH_4 and $\Delta^{14}CH_4$-$\delta^{13}CH_4$. The utility of the regional framework is explored by using pseudo-data simulations created by combining NAME back-trajectories with gridded emissions data for a network of seven measurement

sites in the UK and Republic of Ireland. Two sets of pseudo-data generated for the year 2018 are used. One set of pseudo-data uses 2015 EDGAR v5.0 emissions (EDGAR5) and the second set uses 2017 NAEI emissions for the UK and 2012 EDGAR v4.3.2 emissions for the rest of the model domain (NAEI-EDGAR4). Slopes of $\Delta^{14}CH_4$-CH_4 pseudo-data have mean differences of 24% (4% – 27%) between EDGAR5 and NAEI-EDGAR4 simulations across the UK network. Pseudo-data $\Delta^{14}CH_4$-$\delta^{13}CH_4$ slopes differ by 32% (0% – 54%) across the network with the largest differences between the sets of simulations occurring at Imperial College London, where added concentrations of methane are higher. Larger average differences between the sets of simulations of $\Delta^{14}CH_4$-$\delta^{13}CH_4$ suggest $\Delta^{14}CH_4$-$\delta^{13}CH_4$ measurements could provide more accurate constraints of UK sources. Simulations of nuclear power plant (NPP) $^{14}CH_4$ emissions suggest median influences of 5.1‰ to 31.9‰ in atmospheric $\Delta^{14}CH_4$ across the UK network, with increases of up to 600‰ sometimes occurring. Removing pseudo-data at times when NPPs are upwind reduces their impact on $\Delta^{14}CH_4$ but does not completely eliminate NPP influences. NPP influences should therefore be accounted for in UK studies of $\Delta^{14}CH_4$.

5.1 Introduction

There are large uncertainties associated with CH_4 emissions reported for different source sectors at a regional scale (Bergamaschi et al. 2015; Zazzeri 2016; Lunt et al. 2021a). Measurements of CH_4 isotopes have been used to provide crucial, empirical constraints on the source apportionment of methane emissions. Atmospheric $\delta^{13}CH_4$ measurements, for example, are an established approach for evaluating sources of methane (France et al. 2016; Nisbet et al. 2016; Zazzeri 2016; Hoheisel et al. 2019; Saboya et al. 2022). In situ laser spectroscopy instruments are now capable of making precise atmospheric $\delta^{13}CH_4$ measurements that can be used for CH_4 source attribution (Röckmann et al. 2016; Saboya et al. 2022; Menoud et al. 2020). With the $\delta^{13}CH_4$ signature of pollution events being well-characterised with the measurement uncertainty for pollution events of at least 100 ppb above the background (Chapter 4, Section 4.2.1). Although there are measurement stations in the UK that have been making continuous, in situ $\delta^{13}CH_4$ measurements (e.g. HFD) only continuous in situ $\delta^{13}CH_4$ measurements from ICL have been reported in the literature (Saboya et al. 2022). Atmospheric $\delta^{13}CH_4$ measurement uncertainties of up to 0.07‰ have been achieved with a recent laser spectroscopy measurement system (Rennick et al. 2021) that is currently deployed at the Heathfield measurement site, south of London. Whilst this means small changes in atmospheric $\delta^{13}CH_4$ can be detected this does not necessarily improve the attribution of methane sources to large CH_4 emission events unless the $\delta^{13}CH_4$ signatures of specific sources are also precisely quantified. The $\delta^{13}CH_4$ signatures used for characterising methane sources are found to

have large ranges (Sherwood et al. 2017) and spatiotemporal variations (Feinberg et al. 2018) which limits the extent atmospheric $\delta^{13}CH_4$ measurements can be used for source attribution. The UK $\delta^{13}CH_4$ signatures of specific sources have been quantified (Zazzeri et al. 2015; Zazzeri et al. 2017) and used to identify CH_4 events from in situ measurements of CH_4 concentrations and $\delta^{13}CH_4$ in the UK (e.g. Saboya et al. 2022).

Atmospheric measurements of radiocarbon in methane ($\Delta^{14}CH_4$) have previously been used for constraining CH_4 sources and fossil-fractions, F (e.g. Kessler et al. 2008; Levin et al. 1992; Levin et al. 1985). Since fossil fuel emissions are devoid of radiocarbon and biogenic CH_4 emissions have $\Delta^{14}CH_4$ values similar to contemporary atmospheric $\Delta^{14}CO_2$ (Lassey et al. 2007b; Lassey et al. 2007a) a clear difference between fossil and non-fossil fuel CH_4 can be made. Graven et al. (2019) developed a methodology for distinguishing between fossil fuel and non-fossil fuel CH_4 sources based on atmospheric $\Delta^{14}CH_4$-CH_4 slopes (Fig. 5.1a, Table 5.1). The change in atmospheric $\Delta^{14}CH_4$ per ppb of added CH_4 concentration is larger when there is a higher proportion of fossil CH_4 observed (Table 5.1). For an entirely fossil CH_4 source (i.e. F=100%) the change in $\Delta^{14}CH_4$ per ppb of added CH_4 is around four times more than for an entirely biogenic CH_4 source (Fig. 5.1a, Graven et al. 2019). Figure 5.1a also shows there are smaller uncertainties in F for larger added CH_4 concentrations. Larger added CH_4 concentration values are more useful for inferring fossil-fractions, particularly if F is variable. In this way, fossil-fractions of large CH_4 pollution events can be interpreted from slopes of $\Delta^{14}CH_4$-CH_4.

Graven et al. (2019) tested their $\Delta^{14}CH_4$-CH_4 framework in a regional setting by using EDGAR and USA Gridded Environmental Protection Agency (GEPA) CH_4 emissions to create pseudo-data for a measurement network in California. Pseudo-data $\Delta^{14}CH_4$-CH_4 slopes suggested $\Delta^{14}CH_4$ and CH_4 concentration measurements could provide useful regional scale information on biogenic and fossil CH_4 emissions and could indicate errors in the spatial variations of the emission inventory fossil-fractions. Simulations using GEPA emissions were in better agreement with measurements of atmospheric CH_4 concentrations and $\Delta^{14}CH_4$ made in 2009 in Los Angeles by Townsend-Small et al. (2012) demonstrating this framework could be used with atmospheric measurements to evaluate emission inventories at a regional scale.

Nuclear power plants with pressurised water reactors (PWRs) are large sources of $^{14}CH_4$. Whilst PWR fluxes have a negligible impact on atmospheric methane concentrations they drive atmospheric $\Delta^{14}CH_4$ to higher values (Fig. 5.1a; Lassey et al. 2007b; Kunz 1985; Graven et al. 2019). There are over 40 operational PWRs in the UK and Europe emitting $^{14}CH_4$, and their impact has been observed in previous $\Delta^{14}CH_4$ measurement

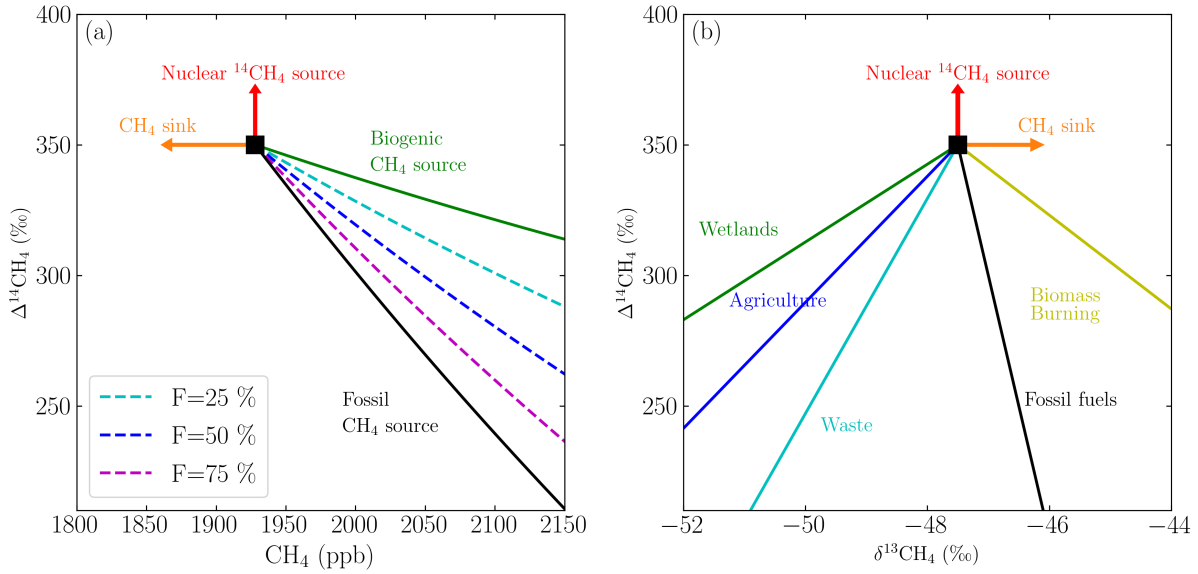


Figure 5.1: The expected changes in (a) CH_4 concentrations and $\Delta^{14}CH_4$ from the background (black square) with reference $\Delta^{14}CH_4$-CH_4 slopes for different methane fossil-fractions. (b) $\delta^{13}CH_4$ and $\Delta^{14}CH_4$ changes from the background due to different methane sources and the tropospheric OH sink with reference $\Delta^{14}CH_4$-$\delta^{13}CH_4$ slopes for key source sectors. The $\Delta^{14}CH_4$ signature for biospheric sources is for the year 2018, and $\delta^{13}CH_4$ signatures are from Zazzeri et al. (2017).

campaigns made in Europe (Eisma et al. 1995; Levin et al. 1992). Radiocarbon emissions from European NPPs are measured on site and reported as an annual value in the RADD database (RADD 2017; EPRI 2010; Van der Stricht and Janssens 2005). Globally, NPP $^{14}CH_4$ emissions are estimated from reported NPP electrical output data as NPP $^{14}CH_4$ measurements are globally sparse. An emission factor is used to relate NPP electrical output (power production) to $^{14}CH_4$ emissions, which are assumed to be directly proportional (Lassey et al. 2007b; Lassey et al. 2007a; Zazzeri et al. 2018; Graven and Gruber 2011). Emission factors for the same type of reactor (used at different facilities) have been found to span nearly two orders of magnitude, with yearly temporal variations also found for the same reactor (Graven and Gruber 2011; Zazzeri et al. 2018).

Details regarding NPP $^{14}CH_4$ venting times or when there are larger releases of $^{14}CH_4$ are not reported in RADD. This introduces a large source of uncertainty when using radiocarbon for methane source quantification as NPP influences need to be accounted in regions where a large number of NPPs are present. NPP influences could potentially be minimised by making measurements of $\Delta^{14}CH_4$ at times when NPPs are downwind of the measurement site. However, depending on the vicinity of the measurement site to a PWR NPP, measurements of $\Delta^{14}CH_4$ could be constantly influenced by NPP $^{14}CH_4$ emissions. Atmospheric models could be used to

establish source-receptor relationships between NPPs and potential measurement sites at different times of the year as a way to estimate the $\Delta^{14}CH_4$ bias from NPP radiocarbon emissions. Quantifying the influences of NPPs on $\Delta^{14}CH_4$ is needed to ensure accurate CH_4 fossil-fraction values are being inferred from measurements.

Graven et al. (2019) modelled the impact of NPP radiocarbon emissions on pseudo $\Delta^{14}CH_4$ data at sites in the California network using two nearby NPPs: Diablo Canyon (in California) and Palo Verde (in Nevada). Their simulations suggested median $\Delta^{14}CH_4$ increases of 0‰ to 7‰ across the measurement network, but under certain meteorological conditions $\Delta^{14}CH_4$ increased by over 40‰. Although the shortest distance between a measurement site and a NPP is $\sim$ 180 km, NPP $^{14}CH_4$ emissions still significantly influenced $\Delta^{14}CH_4$ values across the California measurement network. NPP emissions should therefore be accounted in $\Delta^{14}CH_4$ studies in California.

Recently, a radiocarbon sampling system was developed to make atmospheric $\Delta^{14}CH_4$ measurements without having to transport large volumes of air whilst achieving a measurement precision of 5.4‰ (Zazzeri et al. 2021). The setup of this system means there is potential for it to be portable and to make more regular $\Delta^{14}CH_4$ measurements from a range of locations, including at UK stations that are currently measuring atmospheric $\delta^{13}CH_4$. Combined measurements of $\Delta^{14}CH_4$ and $\delta^{13}CH_4$ could provide additional observational constraints on UK CH_4 source emissions and also be used to determine how the $\delta^{13}CH_4$ signature of fossil CH_4 changes over time (Graven et al. 2019).

There have been few measurement campaigns of concurrent CH_4, $\delta^{13}CH_4$ and $\Delta^{14}CH_4$. This is likely due to a combination of the high costs of atmospheric radiocarbon measurements, which are also time consuming, the uncertainty in quantifying the impact of NPP $^{14}CH_4$ emissions and the labour intensity of conducting concurrent CH_4, $\delta^{13}CH_4$ and $\Delta^{14}CH_4$ measurements. Measurements of $\delta^{13}CH_4$ in Los Angeles 2009 indicated a large proportion of CH_4 emissions were due to fossil fuel leaks with concurrent $\Delta^{14}CH_4$ samples found to be depleted (262‰ to 208‰) relative to the measured background values of $\sim$ 350‰ (Townsend-Small et al. 2012). High-variability in $\Delta^{14}CH_4$ measurements made it difficult to infer fossil-fractions from $\Delta^{14}CH_4$-CH_4 slopes. Atmospheric measurements of $\Delta^{14}CH_4$ and $\delta^{13}CH_4$ in the Athabasca oil sands region, Canada from 2019 were used to distinguish between different sources of fossil CH_4 emissions coming from surface coal mining and from tailing ponds CH_4 (Gonzalez Moguel et al. 2022). Neither of these campaigns explored the impact of NPPs on their atmospheric $\Delta^{14}CH_4$ measurements.

Graven et al. (2019) also explored the utility of using added CH_4 concentrations and $\Delta^{14}CH_4$ changes from the background ($\Delta\Delta^{14}CH_4$) for differentiating between a business-as-usual (BAU) emissions scenario and a targeted emissions reduction scenario in California for the year 2030. In the target scenario added CH_4 concentrations are decreased by 36% to 39% compared to 2013-2014 baseline emissions. Whilst there are decreases in biogenic CH_4 emissions in the BAU scenario these are balanced by an increase in fossil CH_4 emissions. $\Delta^{14}CH_4$-CH_4 slopes were able to differentiate between pseudo-data generated for the target and BAU scenarios, where generally steeper slopes were found for the BAU scenario. $\Delta^{14}CH_4$-CH_4 slopes indicate 2030 fossil-fractions of 29% in the target scenario and 35% in the BAU scenario. However, scenarios with the same or similar fossil-fractions would have similar $\Delta^{14}CH_4$-CH_4 slopes; making it difficult to distinguish between scenarios. The magnitudes of added CH_4 concentrations or additional isotopic measurements (e.g. $\delta^{13}CH_4$) could be used to distinguish between such scenarios (Graven et al. 2019).

In this chapter, the modelling framework developed by Graven et al. (2019) is extended to include atmospheric $\delta^{13}CH_4$ isotopic data. A multi-isotopic approach is expected to produce tighter constraints on CH_4 emissions and their source distributions across a regional network. Here, pseudo-data for the UK-DECC network plus the Imperial College London, Weybourne Atmospheric Observatory (WAO) and Heathfield measurement stations are used to test the regional CH_4-$\delta^{13}CH_4$-$\Delta^{14}CH_4$ framework. Pseudo-data are generated for each of these sites for the year 2018 using 25 km NAME back-trajectories combined with 2015 EDGAR v5.0 and 2017 NAEI emissions. The influence of NPP $^{14}CH_4$ emissions on $\Delta^{14}CH_4$ at the UK measurement sites is also explored through source-receptor simulations used to quantify i) the reactors that have the largest influences and ii) meteorological conditions that could minimise the impact of UK $\Delta^{14}CH_4$ from NPPs.

Future CH_4 emissions under two different Shared Socioeconomic Pathways (SSP) scenarios from the sixth Coupled Model Intercomparison Project (CMIP6) are also used to explore differences in UK $\delta^{13}CH_4$ and $\Delta^{14}CH_4$ for the year 2030. Here, the multi-isotopic framework is used to assess if differences between future emission scenarios can be detected, which could be potentially useful for tracking future CH_4 emissions in the UK.

5.2 Methods

5.2.1 Joint CH_4-$\delta^{13}CH_4$-$\Delta^{14}CH_4$ regional framework

The method for using atmospheric CH_4 concentrations and isotopic measurements to inform on regional sources follows a mass balance approach similar to what was used in the previous chapter.

Atmospheric CH_4 concentrations at the measurement/receptor site (C_a) of interest are assumed to be equal to the sum of a background component that represents the global or hemispheric time-varying background (C_{bg}) and added concentrations or enhancements from regional CH_4 sources that are not yet fully mixed into the background (C_s). In general, added concentrations are aggregated into N source sectors:

$$C_a = C_{bg} + C_s = C_{bg} + \sum_{i}^{N} C_i. \tag{5.1}$$

Where, for example, added concentrations could be simply split between fossil and non-fossil CH_4 sources ($N = 2$). Added concentrations could alternatively be aggregated into a larger number of different source sectors where, for instance, there are contributions from ruminants, landfill sites, wetlands etc. The sink component is excluded from Eq. 5.1 as the atmospheric transport and mixing timescales that are considered for the regional modelling in this chapter are much shorter than the CH_4 tropospheric lifetime (Manning et al. 2011; Graven et al. 2019).

Top-down atmospheric concentration measurements can, at best, only inform on the total CH_4 enhancement, assuming reasonable background concentration measurements are available. To constrain the added concentrations from different CH_4 source sectors additional tracer measurements (e.g. $\delta^{13}CH_4$ and $\Delta^{14}CH_4$) are required. In general, for N methane source sectors in Eq. 5.1, $N - 1$ tracer measurements are needed to constrain the added concentrations for each of the N source sectors.

An approximate mass balance of $^{13}CH_4$ can be constructed by multiplying each term in Eq. 5.1 by its respective $\delta^{13}CH_4$ isotopic signature (δ_i), which is approximately the ratio $^{13}CH_4/^{12}CH_4$:

$$\delta_a C_a = \delta_{bg} C_{bg} + \sum_{i}^{N} \delta_i C_i. \tag{5.2}$$

For UK regional modelling, the $\delta^{13}CH_4$ isotopic signatures from Zazzeri et al. (2017) are used and assigned to the same source sectors used in the previous chapter (Table 3.5) and are shown in Table 5.2.

An approximate mass balance of $^{14}CH_4$ can be constructed in the same way as $^{13}CH_4$:

$$\Delta_a C_a = \Delta_{bg} C_{bg} + \sum_i^N (\Delta_i C_i) + A_{nuc}. \tag{5.3}$$

By definition a value of -1000‰ is used for the $\Delta^{14}CH_4$ signature of fossil fuel CH_4 (Δ_f). $\Delta^{14}CH_4$ values of biogenic and biomass burning CH_4 sources reported by Quay et al. (1999) found similar mean values for agriculture, landfill and wetlands but the $\Delta^{14}CH_4$ of measured biomass burning methane differed from biogenic sources by $\sim$ 13 pM (870‰). The $\Delta^{14}CH_4$ of biomass burning methane depends on the age of the biomass material. Methane emitted from sources of older organic material will have higher or lower $\Delta^{14}CH_4$ depending on the age of the material (e.g. Garnett et al. 2013). $\Delta^{14}CH_4$ values of biospheric methane sources (Δ_b) have not been recently quantified but can be estimated using contemporary atmospheric $\Delta^{14}CO_2$ values with a turnover time that represents the carbon residence time between uptake by photosynthesis and release as atmospheric CH_4. As agricultural and waste CH_4 comprise 90% of biogenic CH_4 emissions in the 2017 UK NAEI and are estimated to have a turnover time of 0 years (Quay et al. 1999; Wahlen et al. 1989), a biospheric turnover time of 0 years is assumed for all UK biospheric sources. This gives a value of 0‰ for the year 2018 (Graven et al. 2019; Graven et al. 2020; Graven et al. 2017). The uncertainty in Δ_b will be due to the combined uncertainties in $\Delta^{14}CO_2$ (estimated at 2-3‰; Miller et al. 2013) and the biogenic turnover time. Using a biogenic turnover time of 6 years (as suggested from global simulations by Lassey et al. (2007a)) gives Δ_b = 30.4‰ (Graven et al. 2017) for the year 2018, which changes Δ_a in the UK $\Delta^{14}CH_4$ simulations by, on average, $\sim$ 6‰. The change in Δ_a due to Δ_b values with different turnover times is comparable to the instrument precision of $\Delta^{14}CH_4$ measurements (5.4‰; Zazzeri et al. 2021) and implies from the $\Delta^{14}CH_4$-CH_4 slope values in Table 5.1 that added concentrations larger than 16.4 ppb are needed to distinguish a source with a fossil-fraction of 0% and a fossil-fraction of 100% without overlapping uncertainties due to uncertainty in Δ_b.

An additional term is included in the $^{14}CH_4$ mass balance (Eq. 5.3) that captures $^{14}CH_4$ emissions from NPPs (A_{nuc}). This term is not included in Eq. 5.1 since $^{14}CH_4$ emissions represent a negligible proportion of the total carbon budget. A factor of 1000‰/R_{14}, where R_{14} is the modern $^{14}C/C$ standard, is included in A_{nuc} to ensure the terms in Eq. 5.3 are consistent.

With this notation, the methane fossil-fraction (F) can be written as:

$$F = \frac{C_f}{C_s} = \frac{C_f}{C_a - C_{bg}}, \tag{5.4}$$

where C_f are the added fossil CH_4 concentrations. The mass balance in Eq. 5.1 shows the total CH_4 enhancements can be written as $C_a - C_{bg}$.

Graven et al. (2019) demonstrated that slopes of $\Delta^{14}CH_4$-CH_4 are linked to different fossil-fraction values (Fig. 5.1a). Combining Eq. 5.1, Eq. 5.3 and Eq. 5.4, fossil-fractions can be directly calculated from the slope or y-intercept of a linear regression applied to $\Delta^{14}CH_4$-$CH_4{}^{-1}$ using:

$$\Delta_a = -\frac{1}{C_a}(F(\Delta_f - \Delta_b) + \Delta_b - \Delta_{bg})C_{bg} + (F(\Delta_f - \Delta_b) + \Delta_b + A_{nuc}), \tag{5.5}$$

which is derived in Appendix A. Since the fossil-fraction is the proportion of fossil CH_4 enhancements, then added CH_4 concentrations can be split between fossil and non-fossil CH_4. Where non-fossil CH_4 has a $\Delta^{14}CH_4$ isotopic signature represented by Δ_b in Eq. 5.5. Table 5.1 shows the expected $\Delta^{14}CH_4$-CH_4 slope values calculated from Eq. 5.5 using a concentration background value of 1928 ppb (for the year 2018), Δ_{bg} = 350‰ (Townsend-Small et al. 2012) and Δ_b=0‰. Alternatively, the fossil-fraction can be calculated from $\Delta^{14}CH_4$-CH_4 measurements using:

$$F = \frac{1}{C_a - C_{bg}}\left(C_a\left(\frac{\Delta_a - \Delta_b}{\Delta_f - \Delta_b}\right) - C_{bg}\left(\frac{\Delta_{bg} - \Delta_b}{\Delta_f - \Delta_b}\right) - \frac{A_{nuc}}{\Delta_f - \Delta_b}\right), \tag{5.6}$$

which is also derived in Appendix A.

Fossil-fractions can similarly be calculated using measurements of $\delta^{13}CH_4$ (δ_a) and CH_4:

$$F = \frac{1}{C_a - C_{bg}}\left(C_a\left(\frac{\delta_a - \delta_b}{\delta_f - \delta_b}\right) - C_{bg}\left(\frac{\delta_{bg} - \delta_b}{\delta_f - \delta_b}\right)\right), \tag{5.7}$$

which is also derived in Appendix A. Eq. 5.7 assumes reasonable background $\delta^{13}CH_4$ measurements are available and also aggregates added CH_4 concentrations into fossil and non-fossil sources.

Table 5.1: $\Delta^{14}CH_4$-CH_4 slope values for different methane fossil-fractions estimated for the year 2018. Biogenic $\Delta^{14}CH_4$ signature is estimated at 0‰ for the year 2018. Slopes are calculated from Eq. 5.5.

Fossil-fraction	$\Delta^{14}CH_4$-CH_4 slope (‰ ppb^{-1})
0%	-0.12
25%	-0.22
50%	-0.37
75%	-0.52
100%	-0.63

As the framework being used in this chapter consists of two isotopic tracers, $\Delta^{14}CH_4$ and $\delta^{13}CH_4$, added concentrations can therefore be constrained for three aggregated source sectors (C_1, C_2, C_3). This is more clearly seen when using matrices to express the system of linear equations, Eq. 5.1-5.3;

$$\begin{pmatrix} C_a \\ \Delta_a \\ \delta_a \end{pmatrix} = \frac{1}{C_a} \begin{pmatrix} C_a & C_a & C_a & C_a \\ \Delta_{bg} & \Delta_1 & \Delta_2 & \Delta_3 \\ \delta_{bg} & \delta_1 & \delta_2 & \delta_3 \end{pmatrix} \begin{pmatrix} C_{bg} \\ C_1 \\ C_2 \\ C_3 \end{pmatrix} + \frac{1}{C_a} \begin{pmatrix} 0 \\ A_{nuc} \\ 0 \end{pmatrix}. \tag{5.8}$$

Where Δ_i and δ_i are the corresponding $\Delta^{14}CH_4$ and $\delta^{13}CH_4$ signatures for added CH_4 sector C_i, which are assumed to be known. Gaussian elimination, for example, can be used to find the values of C_1, C_2, C_3 in Eq. 5.8 (assuming all the terms in the 3×4 matrix are known), which are analytically expressed as:

$$C_1 = \left(\frac{\delta_1 - \delta_3}{\delta_2 - \delta_3} - \frac{\Delta_1 - \Delta_3}{\Delta_2 - \Delta_3}\right)^{-1} \left(C_a \left(\frac{\delta_a - \delta_3}{\delta_2 - \delta_3} - \frac{\Delta_a - \Delta_3}{\Delta_2 - \Delta_3}\right) - C_{bg} \left(\frac{\delta_{bg} - \delta_3}{\delta_2 - \delta_3} - \frac{\Delta_{bg} - \Delta_3}{\delta_2 - \delta_3}\right) + \frac{A_{nuc}}{\Delta_2 - \Delta_3}\right), \tag{5.9}$$

$$C_2 = \left(\frac{\delta_2 - \delta_3}{\delta_1 - \delta_3} - \frac{\Delta_2 - \Delta_3}{\Delta_1 - \Delta_3}\right)^{-1} \left(C_a \left(\frac{\delta_a - \delta_3}{\delta_1 - \delta_3} - \frac{\Delta_a - \Delta_3}{\Delta_1 - \Delta_3}\right) - C_{bg} \left(\frac{\delta_{bg} - \delta_3}{\delta_1 - \delta_3} - \frac{\Delta_{bg} - \Delta_3}{\delta_1 - \delta_3}\right) + \frac{A_{nuc}}{\Delta_1 - \Delta_3}\right), \tag{5.10}$$

$$C_3 = C_a - C_{bg} - C_1 - C_2. \tag{5.11}$$

For the UK, added concentrations could, for example, be split between "fossil" (C_1), "agricultural" (C_2) and "other biospheric" (C_3) sources, which would primarily consist of waste methane - since waste and agricultural CH_4 form 90% of UK biogenic methane sources (NAEI 2017). Weighted $\delta^{13}CH_4$ isotopic source signatures - calculated using the sectoral CH_4 emissions from NAEI and $\delta^{13}CH_4$ isotopic signatures from Zazzeri et al. (2017) - could be used for each of the three source sectors in this joint CH_4-$\delta^{13}CH_4$-$\Delta^{14}CH_4$ approach.

Eq. 5.9 can be used to calculate the fossil-fraction from $\Delta^{14}CH_4$ and $\delta^{13}CH_4$ measurements by letting variables with subscript 1 denote fossil CH_4 and subscript 2 denote non-fossil CH_4; for example, $C_1 = C_f$ (fossil CH_4), $C_2 = C_b$ (biospheric CH_4) and $C_3 = 0$, and dividing each term by $C_a - C_{bg}$:

$$F = \left(\frac{\delta_f}{\delta_b} - \frac{\Delta_f}{\Delta_b}\right)^{-1} \left(\frac{C_a}{C_a - C_{bg}} \left(\frac{\delta_a}{\delta_b} - \frac{\Delta_a}{\Delta_b}\right) - \frac{C_b}{C_a - C_{bg}} \left(\frac{\delta_{bg}}{\delta_b} - \frac{\Delta_{bg}}{\Delta_b}\right) + \frac{A_{nuc}}{\Delta_b (C_a - C_{bg})}\right). \tag{5.12}$$

Large added CH_4 concentrations from different source sectors have distinct $\Delta^{14}CH_4$-$\delta^{13}CH_4$ slopes (Fig. 5.1b; Table 5.2). Fossil fuel sources of CH_4 produce the largest changes in atmospheric $\Delta^{14}CH_4$ per ‰ change of $\delta^{13}CH_4$ (Table 5.2) and wetland sources the smallest change (Table 5.2). For fossil and non-fossil CH_4 with values close to the background $\Delta^{14}CH_4$-$\delta^{13}CH_4$ slope values are less ambiguous than $\Delta^{14}CH_4$-CH_4 slope values. Fossil CH_4 have positive $\Delta^{14}CH_4$-$\delta^{13}CH_4$ slopes whereas biogenic CH_4 sources have negative

$\Delta^{14}CH_4$-$\delta^{13}CH_4$ slopes (Fig. 5.1b). $\Delta^{14}CH_4$-$\delta^{13}CH_4$ slopes are, however, dependent on the biospheric $\Delta^{14}CH_4$ signature and $\delta^{13}CH_4$ signatures used. For example, a change of +2‰ in the fossil $\delta^{13}CH_4$ signature results in a steeper slope with an additional −17‰ change in $\Delta^{14}CH_4$ per ‰ change in $\delta^{13}CH_4$ (i.e. going from -100 to -117). The distinct $\Delta^{14}CH_4$-$\delta^{13}CH_4$ slopes for different biogenic sources means there is potential for imposing constraints on agricultural and waste CH_4 sources (the largest two sources in the UK) and not just fossil and non-fossil CH_4 emissions with this framework. These further distinctions between biogenic sources are driven by $\delta^{13}CH_4$ measurements.

Uncertainties in the slopes of $\Delta^{14}CH_4$-$\delta^{13}CH_4$ are calculated by propagating uncertainties reported for $\delta^{13}CH_4$ isotopic signatures (Zazzeri et al. 2017), background and measurement; and the uncertainties of $\Delta^{14}CH_4$ isotopic signatures, measurement and background. $\Delta^{14}CH_4$ uncertainties for biospheric sources are calculated by combining a ±3‰ uncertainty in $\Delta^{14}CO_2$ measurements (Miller et al. 2013), 30‰ uncertainty for the turnover time and 11% variability in the background value (Lassey et al. 2007b). The difference in $\Delta^{14}CO_2$ between a 0 year and 6 year turnover time for the year 2018 (30‰) is used as the uncertainty of the turnover time. Average biospheric $\Delta^{14}CH_4$ uncertainties of 5.6‰ are calculated for slopes of $\Delta^{14}CH_4$-$\delta^{13}CH_4$ (calculated in Appendix B). Whilst $\Delta^{14}CH_4$-$\delta^{13}CH_4$ slopes do not have overlapping uncertainties, uncertainties for biomass burning are likely to be larger than calculated due to larger range of possible turnover times of the biomass material being combusted.

Daily background CH_4 concentrations and $\delta^{13}CH_4$ values were obtained using atmospheric measurements from the Mace Head measurement station as described in Chapter 3. Background measurements are interpolated to ensure daily values are obtained for the whole period. Background CH_4 and $\delta^{13}CH_4$ had average values of $1928 \pm 9(1\sigma)$ ppb and $-47.6 \pm 0.1(1\sigma)$‰ for 2018. $\Delta^{14}CH_4$ measurements in air representative of the hemispheric background have not been made for over 10 years. Measurements made by Townsend-Small et al. (2012) in Los Angeles in 2009 suggest a $\Delta^{14}CH_4$ background around 350‰ (Table 5.2) with a measurement uncertainty between 5‰ to 11‰. Global and regional variability in background $\Delta^{14}CH_4$ (Δ_{bg}) is difficult to assess due to there being very few measurements. Annual global data from 1986-2000 have standard deviations of 7‰ (Lassey et al. 2007a) but regional variability may be larger (Graven et al. 2019).

5.2.2 Deviations in atmospheric $\delta^{13}CH_4$ and $\Delta^{14}CH_4$ from the background

Changes in $\delta^{13}CH_4$ and $\Delta^{14}CH_4$ from their respective background values are used in the source attribution approach presented in this chapter. Using deviations of $\delta^{13}CH_4$ and $\Delta^{14}CH_4$ from the background removes

Table 5.2: $\Delta^{14}CH_4$-$\delta^{13}CH_4$ slope values for different sources of methane along with their respective $\delta^{13}CH_4$ and $\Delta^{14}CH_4$ signatures. $\delta^{13}CH_4$ isotopic signatures from Zazzeri et al. (2017) and non-fossil $\Delta^{14}CH_4$ signatures for the year 2018 are used. Weighted-mean fossil and biospheric values are calculated using 2017 NAEI emissions for each source sector. $\Delta^{14}CH_4$-$\delta^{13}CH_4$ slopes are calculated from Eq. 5.15.

Source sector	$\delta^{13}CH_4$ signature (‰)	$\Delta^{14}CH_4$ signature (‰)	$\Delta^{14}CH_4$-$\delta^{13}CH_4$ slope (‰ ‰$^{-1}$)
Agriculture	$-64.0 \pm 3.0(1\sigma)$	0^{+30}_{-3}	$+21.3 \pm 4.4$
Biomass burning	$-28.0 \pm 3.0(1\sigma)$	0^{+30}_{-3}	-17.9 ± 3.2
Fossil fuels	$-34.1 \pm 3.0(1\sigma)$	-1000 ± 0	-100.0 ± 22.2
Waste	$-57.0 \pm 3.0(1\sigma)$	0^{+30}_{-3}	$+37.2 \pm 12.4$
Wetlands	$-71.0 \pm 1.0(1\sigma)$	0^{+30}_{-3}	$+15.0 \pm 2.4$
Background	$-47.6 \pm 0.1(1\sigma)$	350	
Weighted-mean fossil	$-34.1 \pm 3.0(1\sigma)$	-1000	
Weighted-mean biospheric	$-61.0 \pm 3.0(1\sigma)$	0	

seasonal and long-term trends whilst allowing methane fossil-fractions and source values to be interpreted from slopes of $\Delta^{14}CH_4$-CH_4 and $\Delta^{14}CH_4$-$\delta^{13}CH_4$.

For a measurement site uninfluenced by NPP $^{14}CH_4$ emissions the mass balance equations (Eq. 5.1-5.3) can be used to understand how the proportion of fossil CH_4 enhancements affects deviations in $\delta^{13}CH_4$ and $\Delta^{14}CH_4$ from their background values,

$$\delta_a - \delta_{bg} = \frac{1}{C_a} \sum_i^N C_i(\delta_i - \delta_{bg}), \tag{5.13}$$

and

$$\Delta_a - \Delta_{bg} = \frac{1}{C_a} \sum_i^N C_i(\Delta_i - \Delta_{bg}), \tag{5.14}$$

where Eq. 5.13 and Eq. 5.14 are derived in Appendix A. As shown in Fig. 5.2a, added CH_4 concentrations that have a larger proportion of biospheric CH_4 result in negative deviations in $\delta^{13}CH_4$ from the background ($\Delta\delta^{13}CH_4$), whereas added CH_4 that is predominantly from fossil fuels results in positive deviations in $\Delta\delta^{13}CH_4$. However, the magnitude of added CH_4 concentrations drives the magnitude of $\Delta\delta^{13}CH_4$, where larger added CH_4 concentrations for the same fossil-fractions produce larger $\Delta\delta^{13}CH_4$ values (Fig. 5.2a).

For changes in $\Delta^{14}CH_4$ from the background ($\Delta\Delta^{14}CH_4$), both fossil and biospheric methane lead to negative

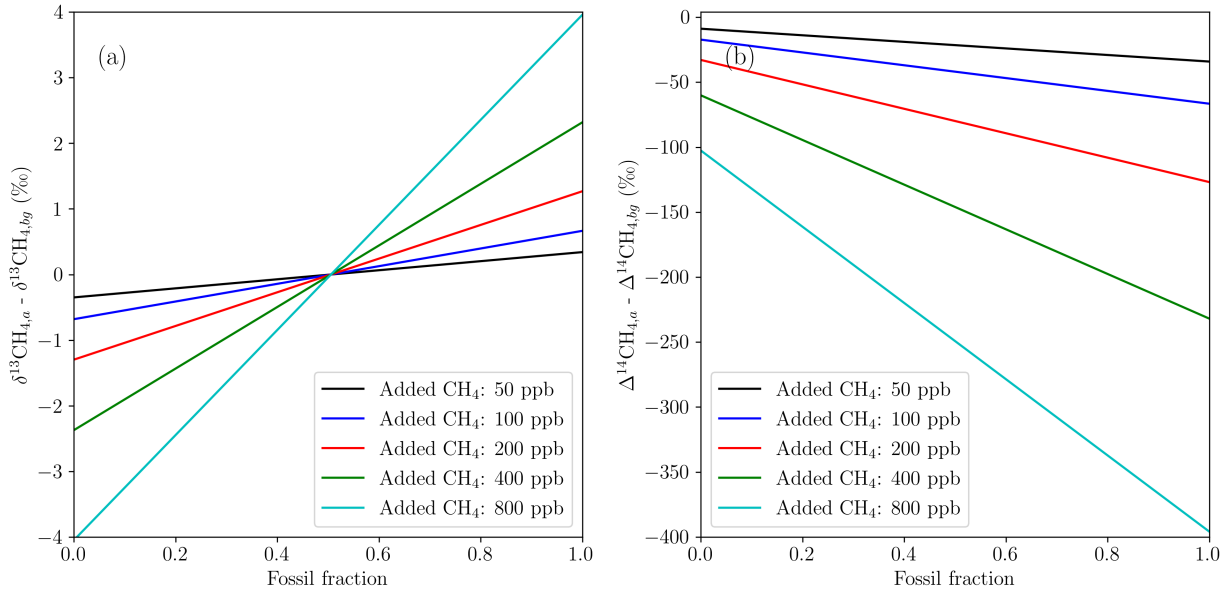


Figure 5.2: Schematic to show the deviations in isotopic values from the background for various added CH_4 concentrations of different fossil-fraction values. Panel (a) shows the deviations in $\delta^{13}CH_4$ from the background and panel (b) shows the deviations in $\Delta^{14}CH_4$ from the background.

$\Delta\Delta^{14}CH_4$ values (Fig. 5.2b). Larger fossil-fractions produce $\Delta\Delta^{14}CH_4$ values with larger magnitudes. Similar to $\Delta\delta^{13}CH_4$ it is the magnitude of added CH_4 concentrations that drive the larger $\Delta\Delta^{14}CH_4$ values (Fig. 5.2b).

Equations 5.13 and 5.14 can be combined to calculate the $\Delta^{14}CH_4$-$\delta^{13}CH_4$ slopes of different sources by letting $N = 1$ and calculating the changes for individual source sectors (see Appendix A for derivation), which are given in Table 5.2,

$$\frac{\Delta_a - \Delta_{bg}}{\delta_a - \delta_{bg}} = \frac{\sum_i^N C_i(\Delta_i - \Delta_{bg})}{\sum_i^N C_i(\delta_i - \delta_{bg})}. \tag{5.15}$$

In this way, a combined isotopic approach can be used to calculate and constrain CH_4 sources rather than relying on using a single isotopic approach.

5.2.3 Pseudo-data across the UK measurement network

Added CH_4 concentrations, $\delta^{13}CH_4$ and $\Delta^{14}CH_4$ pseudo-data were generated for seven measurement sites in the UK and Republic of Ireland (Fig. 5.3). The network of sites, shown in Fig. 5.3, consists of: two coastal sites - Mace Head (MHD) and Weybourne (WAO) observatories; four tall-tower sites - Bilsdale (BSD), Heathfield (HFD), Ridgehill (RGL), Tacolneston (TAC); and the Imperial College London (ICL) measurement station located in central London (Table 5.3). Some of these measurement sites have been used in previous

methane measurement and modelling studies (e.g. Ganesan et al. 2015; Lunt et al. 2021a; Saboya et al. 2022) and are being used as part of the ongoing Detection and Attribution of Regional greenhouse gas Emissions in the UK (DARE-UK) project (dareuk.blogs.bristol.ac.uk). All these sites have made measurements of atmospheric CH_4 concentrations from various sampling heights (Table 5.3; Stanley et al. 2018). It is only at ICL that atmospheric measurements of CH_4, $\delta^{13}CH_4$ and $\Delta^{14}CH_4$ have been made (Saboya et al. 2022; Zazzeri et al. 2021). As only a few $\Delta^{14}CH_4$ measurements have been made at ICL the combined utility of CH_4 concentrations, $\delta^{13}CH_4$ and $\Delta^{14}CH_4$ has not yet been explored for evaluating CH_4 sources in the London area.

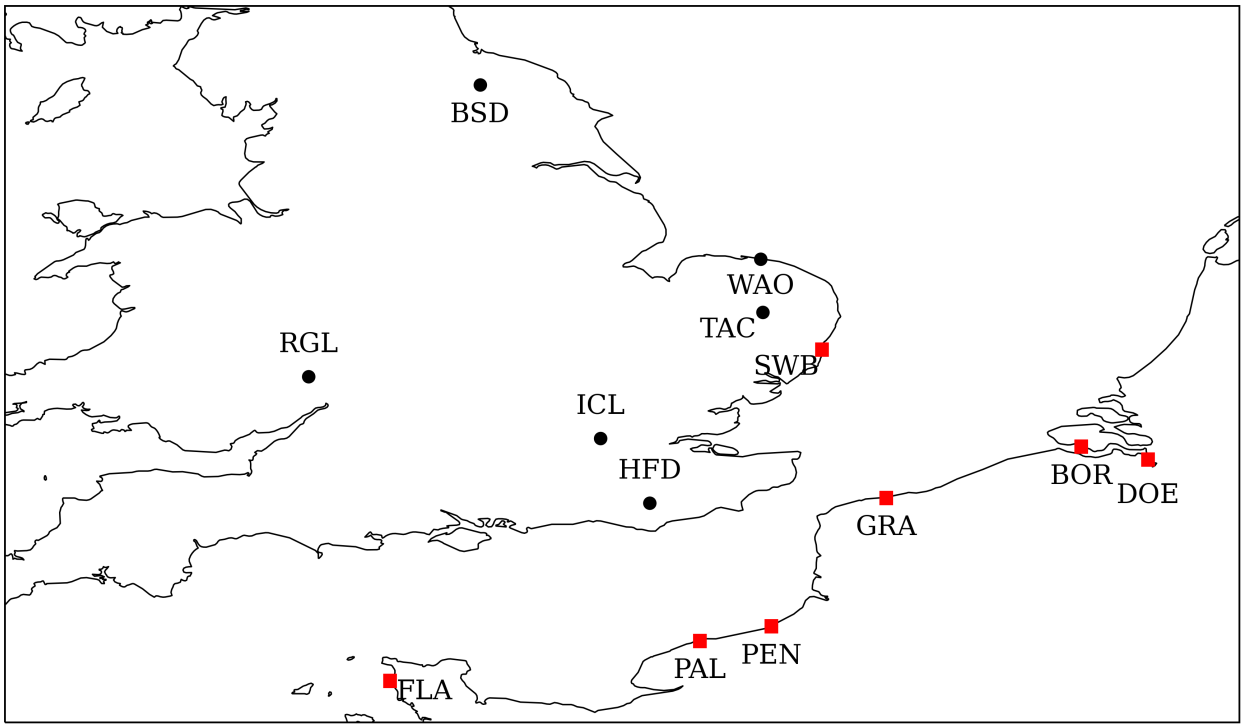


Figure 5.3: UK measurement network of sites (black circles) along with nearby PWR nuclear power plants (red squares).

5.2.3.1 Contemporary CH_4 simulations

Pseudo-data were generated by combining 25 km resolution NAME back-trajectories from 09:00-15:00 (with the same model parameters as described in the Chapter 3) for the year 2018 with methane emissions inventory data. Daytime pseudo-data are used since they are more representative of regional sources and emissions as model errors are smaller (6 ppb; Chapter 3, Section 3.3.3). Times when the PBL height in the UM output was below the inlet height were removed from the pseudo-data. Anthropogenic emissions from the UK National

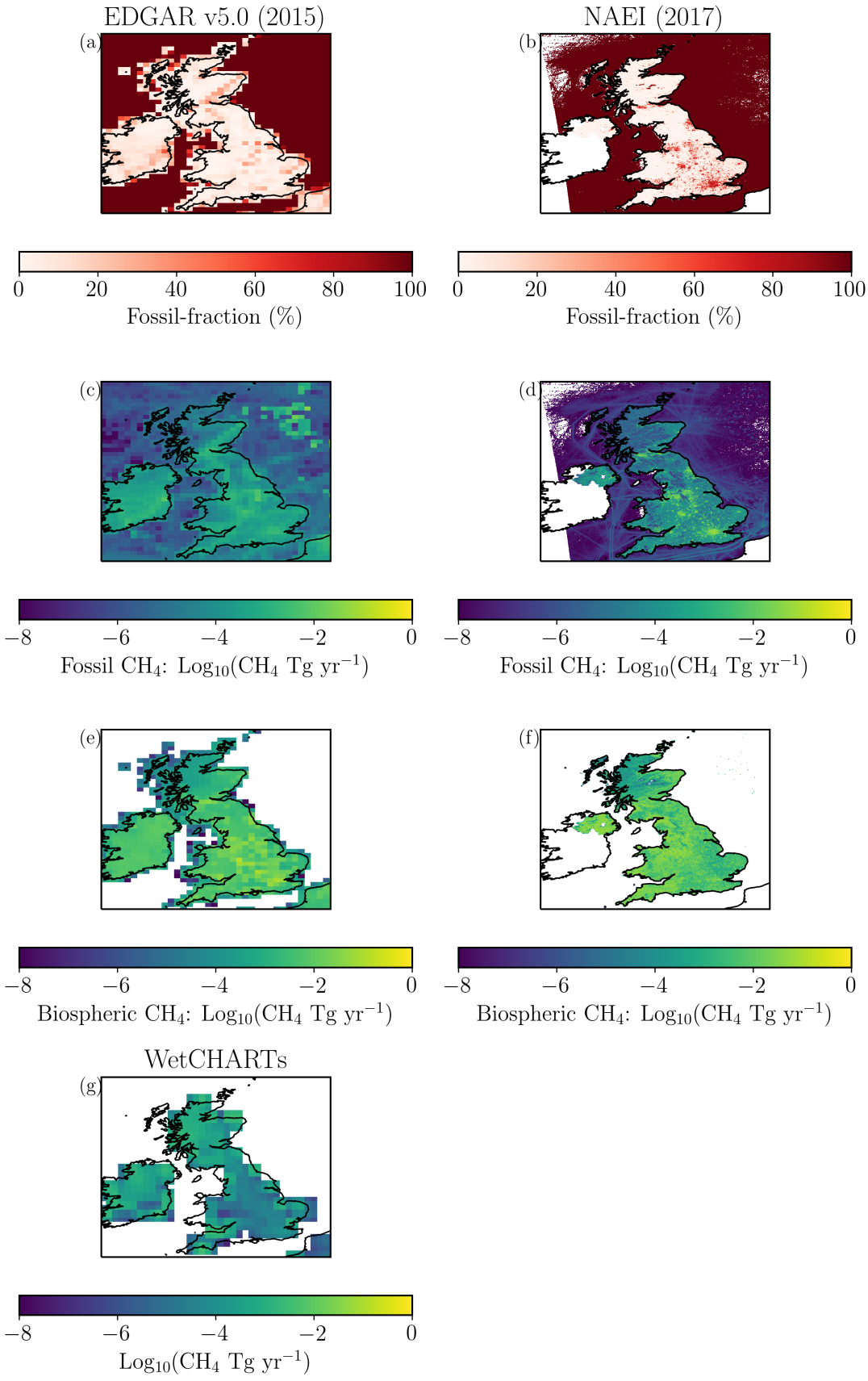


Figure 5.4: Anthropogenic CH_4 emissions from EDGAR v5.0 (2015) (a,c,e), 2017 UK NAEI (b,d,f) and 2015 mean extended ensemble WetCHARTs emissions (g). Fossil-fractions are shown in the first row, fossil CH_4 emissions in the second row and biospheric CH_4 emissions in the third row.

Table 5.3: Locations and sampling heights of UK and Republic of Ireland measurement sites used in the simulations.

Measurement site	Code	Latitude (^oN)	Longitude (^oE)	Sampling height (m.a.g.l.)
Bilsdale	BSD	54.3586	-1.1503	250
Heathfield	HFD	50.9767	0.2295	100
Imperial College London	ICL	51.4988	-0.1749	26
Mace Head	MHD	53.3264	-9.9039	10
Ridge Hill	RGL	51.9975	-2.4500	90
Tacolneston	TAC	52.5177	1.1386	185
Weybourne	WAO	52.5702	1.0719	20

Atmospheric Emissions Inventory (NAEI) for the year 2017, Emissions Database for Global Atmospheric Research (EDGAR) v4.3.2 inventory for the year 2012 (Janssens-Maenhout et al. 2012) and v5.0 inventory for the year 2015 (Crippa et al. 2019) (Fig. 5.4a-f) are used to generate two sets of contemporary simulations. The first set of simulations uses EDGAR v5.0 for the whole of the model domain (EDGAR5). The second set uses a UK hybrid emissions map with NAEI emissions for the UK and EDGAR v4.3.2 emissions for the rest of the model domain (NAEI-EDGAR4).

Total UK emissions (including CH_4 from the North Sea) are higher in EDGAR v5.0 (4.18 Tg CH_4 yr^{-1}) than in NAEI (2.08 Tg CH_4 yr^{-1}). However, both inventories have similar methane fossil-fractions for the UK (14% – 15%; Table 5.4), which could be too low based on results presented in the previous chapter. Wetland CH_4 emissions from the mean of the 2015 WetCHARTs extended ensemble inventory (Fig. 5.4g) are used in both sets of simulations along with biomass burning CH_4 emissions from the GFED inventory.

Simulations of $\delta^{13}CH_4$ and $\Delta^{14}CH_4$ were produced using Eq. 5.1, Eq. 5.2 and Eq. 5.3 with the isotopic signatures for the respective source sectors shown in Table 5.2 and the simulated added CH_4 concentrations for the different source sectors.

5.2.3.2 Projected SSP CH_4 simulations for 2030

The shared socioeconomic pathways (O'Neill et al. 2014) are a set of future warming scenarios created to understand our world under alternative emission mitigation scenarios. These scenarios range from GHG emission reductions that align with the most stringent goals of the Paris Agreement (SSP1-1.9) to high GHG emissions with minimal mitigation controls in place (SSP5-8.5). A suite of scenarios were explored in CMIP6

Table 5.4: Methane emission inventory values for the UK reported in Tg CH_4 yr^{-1} for different source sectors in contemporary (EDGAR and NAEI) emissions and projected (SSP1-1.9 and SSP5-8.5) emissions. Relative contributions of each sector are in brackets and fossil-fractions are denoted by the column F.

	Total	F	Agriculture	Energy	Industrial Combustion	Residential Combustion	Transport	Waste
EDGAR v5.0 2015	4.57	13.6%	1.18 (25.9%)	0.55 (12.1%)	0.02 (0.4%)	0.04 (0.8%)	0.02 (0.4%)	2.76 (60.5%)
NAEI 2017	2.01	15.4%	1.00 (49.8%)	0.24 (11.9%)	0.01 (0.5%)	0.04 (2.0%)	0.02 (1.0%)	0.70 (34.8%)
CMIP6 2015	2.56	15.6%	1.08 (42.2%)	0.35 (13.7%)	0.01 (0.4%)	0.03 (1.2%)	0.02 (0.8%)	1.08 (42.2%)
SSP1-1.9 2030	1.28	10.2%	0.83 (64.8%)	0.10 (7.8%)	0.01 (0.8%)	0.01 (0.8%)	0.02 (1.6%)	0.32 (25.0%)
SSP5-8.5 2030	3.08	14.9%	1.15 (37.3%)	0.44 (14.3%)	0.01 (0.3%)	0.02 (0.6%)	0.02 (0.6%)	1.47 (47.7%)

to produce monthly $0.5^o \times 0.5^o$ spatially resolved global emission trajectories from 2015 to 2100 for different anthropogenic sources and different atmospheric trace gas species.

For SSP CMIP6 emissions, 2015 is used as a transitional year between historic and future model runs. Anthropogenic emissions are extrapolated to 2015 using historic emissions data from Hoesly et al. (2018). UK methane emissions for all sources in 2015 SSP CMIP6 are estimated at 2.56 Tg CH_4 yr^{-1}, which is close to the 2017 UK NAEI CH_4 emission estimate. The fossil-fraction in 2015 SSP CMIP6 emissions is close to the NAEI fossil-fraction (Table 5.4) with similar emission values between the different source sectors, except for waste CH_4 emissions which are $\sim$ 0.4 Tg CH_4 yr^{-1} larger in the CMIP6 emissions than in NAEI. There are much larger differences between CMIP6 and EDGAR v5.0 emissions, with waste emissions in EDGAR more than double the value in CMIP6 methane emissions (Table 5.4). Differences between gridded emissions could be attributed to model extrapolation and the different historical datasets used in SSP CMIP6 emissions (Gidden et al. 2019).

Monthly CH_4 emissions from SSP1-1.9 and SSP5-8.5 for the year 2030 are used to evaluate the utility of CH_4 concentrations, $\delta^{13}CH_4$ and $\Delta^{14}CH_4$ for exploring differences between scenarios in the UK. Following a

mass balance approach, simulated above background (i.e. excess) CH_4 concentrations for 2030 are created by combining the 2030 SSP emissions with 2018 NAME back-trajectories from April, August and December for all measurement sites.

Projected changes in CH_4 background concentrations under SSP1-1.9 and SSP5-8.5 are needed to simulate future $\delta^{13}CH_4$ and $\Delta^{14}CH_4$. Meinshausen et al. (2020) produced Northern hemispheric background CH_4 concentrations for different SSPs using the MAGICC climate-carbon-cycle model (Meinshausen et al. 2011). Under SSP1-1.9 a CH_4 concentration background of 1838.9 ppb is expected and under SSP5-8.5 a CH_4 concentration background of 2067.3 ppb is expected for the year 2030. Projected changes in tropospheric OH concentrations are included in MAGICC with changes in CH_4 emissions modelled to affect tropospheric OH concentrations. As a result, there is an overall effect where CH_4 lifetimes are generally shorter in lower emissions scenarios and longer in higher emission scenarios (Meinshausen et al. 2020).

Simulating atmospheric $\Delta^{14}CH_4$ in the UK requires constraints on the background and biogenic $\Delta^{14}CH_4$ values. There are currently no published values for how global atmospheric $\Delta^{14}CH_4$ evolves under different future scenarios so a value of 350‰ is used as the background $\Delta^{14}CH_4$ value for 2030. As biogenic $\Delta^{14}CH_4$ signatures are closely linked to atmospheric $\Delta^{14}CO_2$ values, projections of $\Delta^{14}CO_2$ under different future scenarios can be used to constrain how the biogenic $\Delta^{14}CH_4$ signature evolves over time. Projections of $\Delta^{14}CO_2$ from Graven et al. (2020) are used with a biospheric turnover time of 0 years. This gives 2030 biospheric $\Delta^{14}CH_4$ values of -1.5‰ and -38.3‰ for SSP1-1.9 and SSP5-8.5 scenarios, respectively. The impact of NPP $^{14}CH_4$ emissions are not included in the 2030 $\Delta^{14}CH_4$ simulations.

Similarly, changes in the global $\delta^{13}CH_4$ values, fossil and biogenic signatures of $\delta^{13}CH_4$ are needed for 2030 simulations of $\delta^{13}CH_4$ in the UK. As there are also no projections for how global $\delta^{13}CH_4$ values will evolve and as changes in $\delta^{13}CH_4$ signatures are somewhat unpredictable values from Table 5.2 for the year 2018 are used.

5.2.4 Simulating nuclear power plant $^{14}CH_4$ emissions

There are 42 operational PWR NPPs within the modelling domain used for generating pseudo-data. Most of these NPPs are over 400 km from the UK measurement sites but there are seven nearby that could potentially have a significant impact on atmospheric $\Delta^{14}CH_4$ across the UK (Fig. 5.3; Table 5.5). Sizewell B (SWB) is the only PWR in the UK and is located on the east coast of England near TAC and WAO measurement sites.

However, $^{14}CH_4$ emissions from SWB (152 μg $^{14}CH_4$ h^{-1}) are around half the value of $^{14}CH_4$ emissions from other NPPs near the UK. The Gravelines (GRA) NPP facility in northwest France (Fig. 5.4h) consists of six 900 MW reactors making it the largest NPP in western Europe and seventh largest in the world. Gravelines is only $\sim$ 165 km from central London and therefore $^{14}CH_4$ emissions from this NPP, which are reported as 552 μg $^{14}CH_4$ h^{-1}, are likely to have a notable influence on $\Delta^{14}CH_4$ across the UK.

Table 5.5: The pressurised water reactor nuclear power plants that are closest to the UK and Republic of Ireland measurement sites with their respective 2016 $^{14}CH_4$ emissions as reported in Zazzeri et al. (2018).

Reactor name	Code	Latitude (^oN)	Longitude (^oE)	Emissions (μg CH_4 h^{-1})
Borssele	BOR	51.4316	3.7176	65.9
Doel	DOE	51.3252	4.2594	389
Flamanville	FLA	49.5358	-1.8814	349
Gravelines	GRA	51.0161	2.1442	552
Paluel	PAL	49.8581	0.6331	344
Penly	PEN	49.9756	1.2119	319
Sizewell B	SWB	52.2150	1.6197	152

In the United Kingdom advanced gas-cooled reactors (AGRs) have been used for nuclear power generation since the 1980's (Nonbøl 1996). As AGRs use carbon dioxide in the coolant they are sources of atmospheric $^{14}CO_2$ (Nonbøl 1996; Wenger et al. 2019). Whilst AGRs are not reported as sources of $14CH_4$, it may be possible that some atmospheric $14CH_4$ is emitted from AGRs as low concentrations of methane are used to inhibit the radiolytic oxidation of CO_2 in the coolant (Nonbøl 1996). However, AGR $14CH_4$ emissions are not reported in the literature or RADD database and are therefore not included in the simulations or analysis of NPP $14CH_4$ presented in this chapter.

The 2016 (most recent) annual PWR NPP $^{14}CH_4$ emissions reported in Zazzeri et al. (2018) are used to construct an emissions map of NPPs in the modelling domain that is then combined with the 25 km NAME back-trajectories to estimate A_{nuc} in Eq. 5.3. Since hourly pseudo-data are used in the simulations, PWR $^{14}CH_4$ emissions are downscaled by assuming constant, uniform emissions throughout the year. The impact of individual reactor $^{14}CH_4$ emission on $\Delta^{14}CH_4$ at the UK sites is explored by simulating $^{14}CH_4$ emissions separately for each PWR in Table 5.5. This approach for quantifying NPP-measurement site relationships has been previously used in other radiocarbon studies (Wenger et al. 2019; Graven et al. 2019).

5.3 Results

5.3.1 Contemporary simulations for 2018 using EDGAR and NAEI emissions

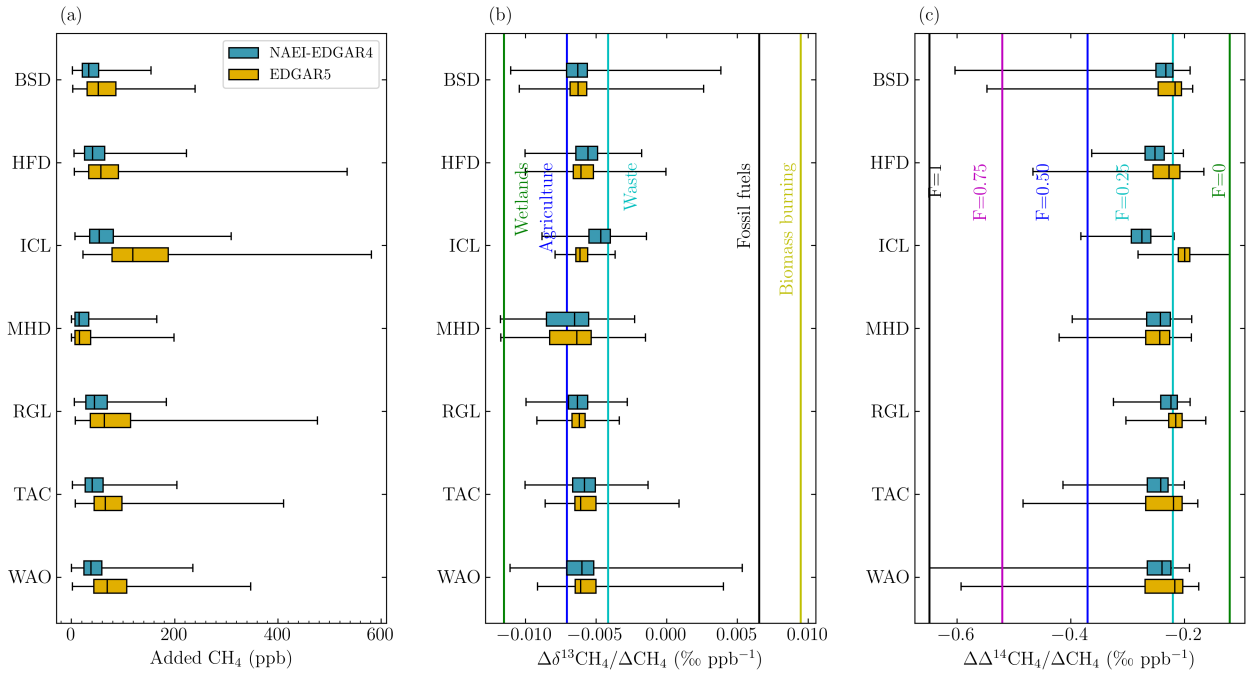


Figure 5.5: Boxplot distributions of (a) added concentrations, (b) $\Delta\delta^{13}CH_4/CH_4$, (c) $\Delta\Delta^{14}CH_4/CH_4$ for EDGAR5 and NAEI-EDGAR4 simulations. NPP influences are not included in $\Delta\Delta^{14}CH_4/CH_4$ and boxplots show the full range of simulated data. Reference lines for $\Delta\delta^{13}CH_4/CH_4$ sources are shown in (b) which are calculated from UK $\delta^{13}CH_4$ signatures (Zazzeri et al. 2017). Fossil-fraction reference lines are also shown in (c) for the year 2018.

Figure 5.5a shows the distributions of simulated added CH_4 concentrations at the measurement sites for 2018. In both sets of simulations added CH_4 concentrations are largest at Imperial and smallest at MHD, with the other five sites having similar median values and distributions. Median added CH_4 concentrations are between 50 ppb and 100 ppb across the sites in both NAEI-EDGAR4 and EDGAR5 simulations. The low median added CH_4 concentrations suggest the simulated average $\Delta\delta^{13}CH_4$ and $\Delta\Delta^{14}CH_4$ values are generally going to be small in magnitude as indicated in Fig. 5.2.

Differences of added CH_4 concentrations between EDGAR5 and NAEI-EDGAR4 are largest at ICL where EDGAR5 is on average 65 ppb higher than NAEI-EDGAR4. As presented in the previous chapter, NAEI

emissions were underestimating measured CH_4 concentrations at ICL by 30% – 35% for the London area. The larger added CH_4 concentrations in EDGAR5 are therefore likely to be in better agreement with measurements of atmospheric methane concentrations at ICL.

Simulated $\Delta\delta^{13}CH_4$ values divided by their added CH_4 concentrations are shown in Fig. 5.5b along with reference lines for methane sources calculated using UK $\delta^{13}CH_4$ signatures (Zazzeri et al. 2017). Large ranges in $\Delta\delta^{13}CH_4/\Delta CH_4$ values reflects the high variability in sources close to each of the measurement sites. Reference lines suggest most UK methane emissions are due to a mixture of agriculture and waste emissions, but there are $\Delta\delta^{13}CH_4/\Delta CH_4$ values that indicate the presence of fossil methane. However, this approach for source attribution relies on precise $\delta^{13}CH_4$ signatures where small changes in these values could lead to CH_4 emissions being misattributed. For example, the reference lines for agricultural and waste sources are close and will have overlapping uncertainty ranges. Therefore small changes in $\delta^{13}CH_4$ signatures could potentially result in some waste emissions being attributed to the agricultural sector, or conversely.

Figure 5.5c shows the simulated $\Delta\Delta^{14}CH_4$ values divided by their added CH_4 concentrations where values closer to -0.70 are indicative of CH_4 with $F = 1$ and values closer to -0.12 are indicative of $F = 0$ (Table 5.1). Simulated $\Delta\Delta^{14}CH_4/\Delta CH_4$ values show low fossil-fraction values across the UK with generally small variability, but some sites (e.g. WAO and TAC) show larger variability with some data points indicative of high F values (likely a result of being close to the Bacton natural gas terminal). Large differences in $\Delta\Delta^{14}CH_4/\Delta CH_4$ are seen between simulations for ICL, where fossil-fractions are generally lower in EDGAR5 simulations than NAEI-EDGAR4. In the previous chapter, NAEI emissions were found to be underreporting fossil CH_4 emissions for the London area in comparison to $\delta^{13}CH_4$ measurements at ICL, suggesting fossil CH_4 is also underreported in EDGAR v5.0 for the London area.

Two-dimensional histograms of $\Delta\Delta^{14}CH_4$-ΔCH_4 and $\Delta\Delta^{14}CH_4$-$\Delta\delta^{13}CH_4$ are shown in Fig. 5.6 for HFD, ICL and TAC. In the sites shown, $\Delta\Delta^{14}CH_4$-ΔCH_4 slopes suggest fossil-fractions are close to 10% for both sets of simulations, with slightly steeper slopes for ICL NAEI-EDGAR4 simulations (Fig. 5.6e). Slopes of $\Delta\Delta^{14}CH_4$-ΔCH_4 in NAEI-EDGAR4 and EDGAR5 simulations at the other UK sites have similar values (Table 5.6). On average there are relative differences of 24% between the NAEI-EDGAR4 and EDGAR5 $\Delta\Delta^{14}CH_4$-ΔCH_4 slopes.

There are larger differences between simulations of EDGAR5 and NAEI-EDGAR4 in the $\Delta\Delta^{14}CH_4$-$\Delta\delta^{13}CH_4$

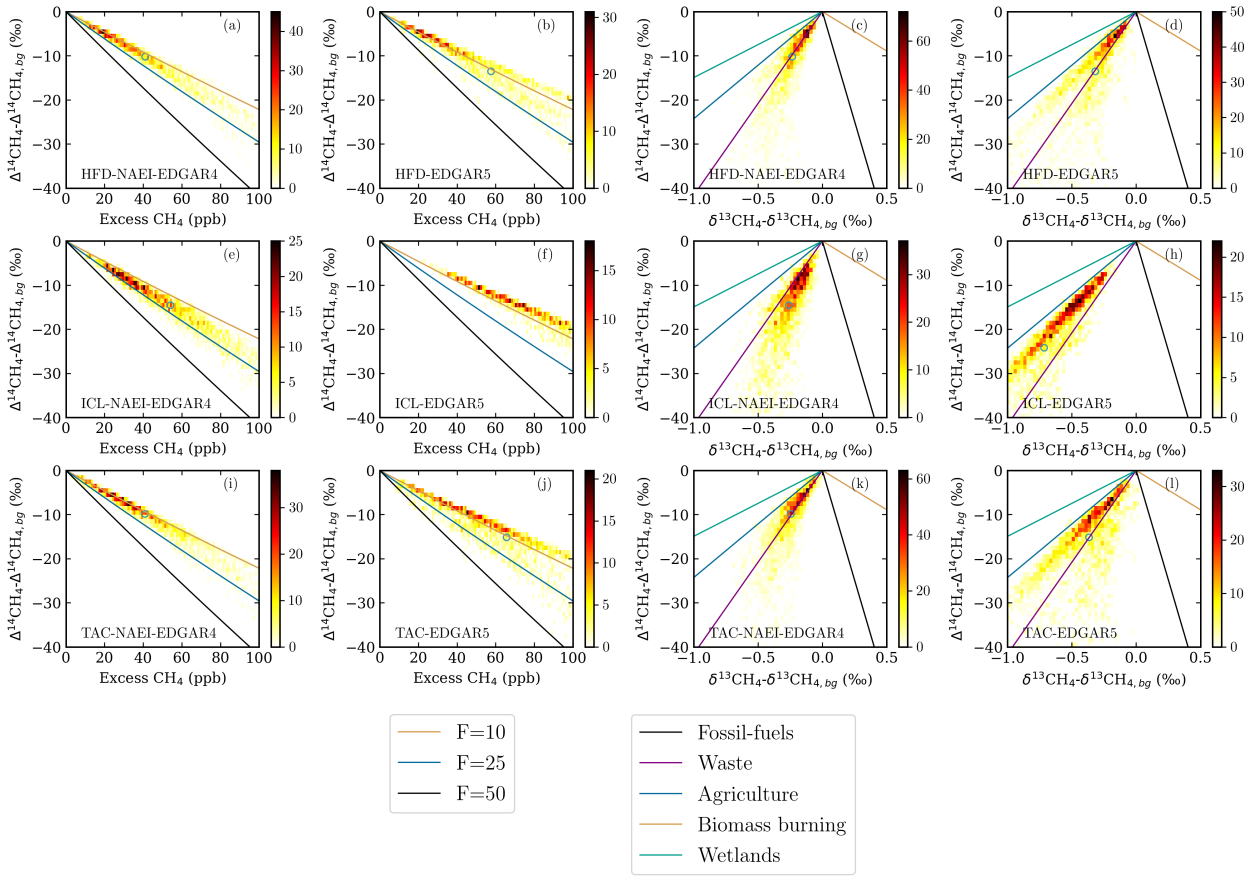


Figure 5.6: Two-dimensional histograms of $\Delta\Delta^{14}CH_4$-ΔCH_4 (columns 1 and 2) and $\Delta\Delta^{14}CH_4$-$\Delta\delta^{13}CH_4$ (columns 3 and 4) for HFD (top row), ICL (middle row) and TAC (bottom row). Median values are shown by the blue marker on each panel. Reference lines for F values and CH_4 sources are also shown.

two-dimensional histograms (Table 5.6) with average differences of 32.3%. Larger added CH_4 concentrations produce larger $\Delta^{14}CH_4$-$\delta^{13}CH_4$ deviations from their background values (Fig. 5.6) reducing the ambiguity of which sources are driving the CH_4 enhancements. $\Delta\Delta^{14}CH_4$-$\Delta\delta^{13}CH_4$ pseudo-data in EDGAR5 simulations mostly fall between the waste and agriculture CH_4 reference lines, whereas in NAEI-EDGAR4 $\Delta\Delta^{14}CH_4$-$\Delta\delta^{13}CH_4$ pseudo-data are closer to the waste CH_4 reference line. Most of the added CH_4 concentrations at these sites have small magnitudes making it difficult to distinguish between waste and agricultural emissions.

However, differences between simulations are largest at ICL (47% – 54%; Table 5.6) where NAEI-EDGAR4 pseudo-data form much steeper $\Delta\Delta^{14}CH_4$-$\Delta\delta^{13}CH_4$ slopes and have data points closer to the fossil fuel $\Delta\Delta^{14}CH_4$-$\Delta\delta^{13}CH_4$ reference line. The larger differences between NAEI-EDGAR4 and EDGAR5 pseudo-data at ICL are a result of the larger differences in the NAEI and EDGAR v5.0 emissions source apportionment for

Table 5.6: $\Delta\Delta^{14}CH_4$-ΔCH_4 and $\Delta\Delta^{14}CH_4$-$\Delta\delta^{13}CH_4$ pseudo-data slope values for each of the measurement sites calculated using a least-squares fit. Relative differences between slope values for different simulations are also shown. NPP influences are not included.

	Gradient		Relative difference	
Measurement site	$\Delta\Delta^{14}CH_4$-ΔCH_4	$\Delta\Delta^{14}CH_4$-$\Delta\delta^{13}CH_4$	$\Delta\Delta^{14}CH_4$-ΔCH_4	$\Delta\Delta^{14}CH_4$-$\Delta\delta^{13}CH_4$
BSD (NAEI-EDGAR4)	-0.266	42.79	18%	22%
BSD (EDGAR5)	-0.219	33.50		
HFD (NAEI-EDGAR4)	-0.284	55.31	27%	41%
HFD (EDGAR5)	-0.206	32.63		
ICL (NAEI-EDGAR4)	-0.291	67.35	47%	54%
ICL (EDGAR5)	-0.154	31.07		
MHD (NAEI-EDGAR4)	-0.249	43.49	4%	0.2%
MHD (EDGAR5)	-0.240	43.57		
RGL (NAEI-EDGAR4)	-0.252	43.35	21%	17%
RGL (EDGAR5)	-0.199	35.93		
TAC (NAEI-EDGAR4)	-0.281	52.01	24%	47%
TAC (EDGAR5)	-0.214	27.53		
WAO (NAEI-EDGAR4)	-0.281	50.45	25%	45%
WAO (EDGAR5)	-0.212	27.97		

the London area. As shown in the previous chapter, there are large uncertainties in the source apportionment of urban areas (Brandt et al. 2014).

Despite the smaller simulated added CH_4 concentrations at HFD and TAC (Fig. 5.6) NAEI-EDGAR4 and EDGAR5 simulations have different $\Delta\Delta^{14}CH_4$-$\Delta\delta^{13}CH_4$ slopes for each site. At HFD and TAC, NAEI-EDGAR4 and EDGAR5 $\Delta\Delta^{14}CH_4$-$\Delta\delta^{13}CH_4$ slopes have relative differences of 41% and 47%, respectively (Table 5.6). Slopes of $\Delta\Delta^{14}CH_4$-$\Delta\delta^{13}CH_4$ in NAEI-EDGAR4 and EDGAR5 are sufficiently distinct that atmospheric measurements of $\Delta^{14}CH_4$ and $\delta^{13}CH_4$ could likely be used to evaluate which emissions inventory is in better agreement with UK observations.

5.3.2 Nuclear power plant $\Delta^{14}CH_4$ influences across the UK

The simulated influences of NPP emissions on $\Delta^{14}CH_4$ varies strongly across the measurement sites (Fig. 5.7). Sites in southeast England (HFD, ICL, TAC, WAO) were most influenced by NPP emissions (Fig. 5.7), where mean $\Delta^{14}CH_4$ increases range between 75.8‰ at ICL and 114.3‰ at HFD (Table 5.7). Large mean increases in $\Delta^{14}CH_4$ are driven by a few very large episodes as seen in the distributions of NPP $\Delta^{14}CH_4$ increases,

which are positively skewed (Fig. 5.7). As such, median values are more representative of the average NPP $\Delta^{14}CH_4$ increases across the UK. Median NPP $\Delta^{14}CH_4$ increases are much lower than the mean values and range between 15.7‰ at WAO and 31.9‰ at TAC (for southeast UK sites; Table 5.7, Fig. 5.7).

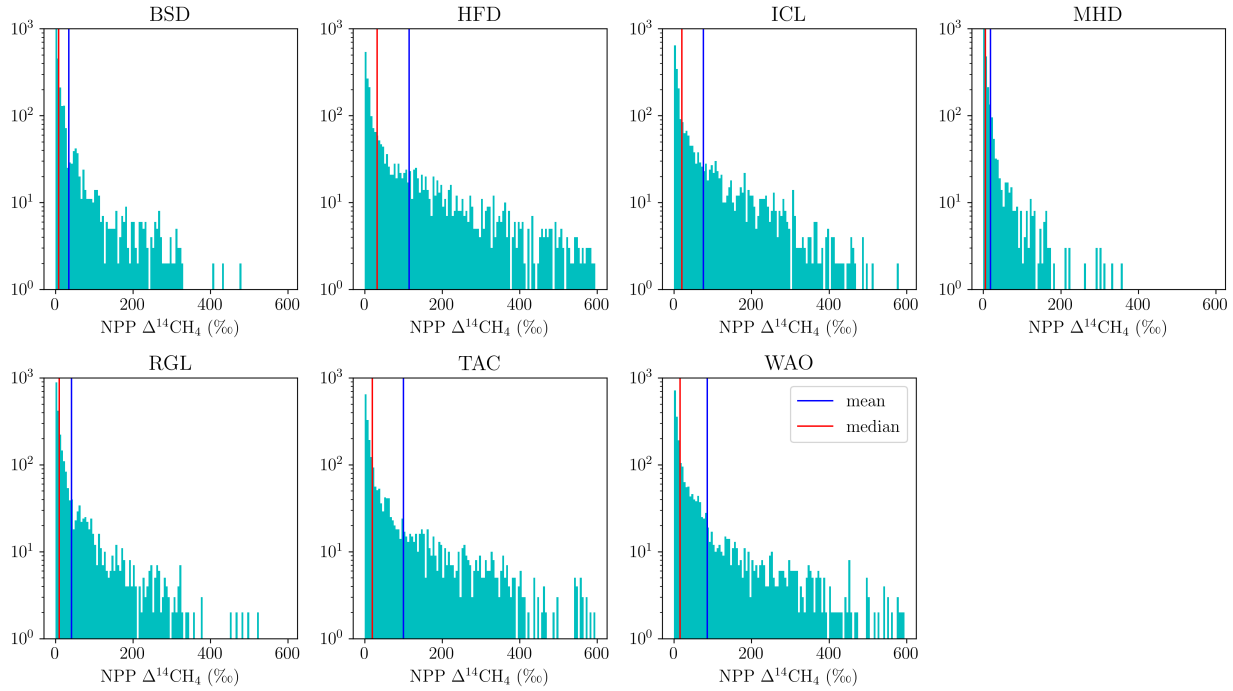


Figure 5.7: Histograms of modelled NPP $\Delta^{14}CH_4$ influences at each of the measurement sites binned at 5‰ intervals. Mean and median values are indicated. Note, y-axis scale is logarithmic.

The $\Delta^{14}CH_4$ distributions for EDGAR5 and NAEI-EDGAR4 simulations with and without NPP contributions for the different sites are shown in Fig. 5.8. There are significant increases in the distributions of $\Delta^{14}CH_4$ values at all the measurement sites, but these increases are smaller for sites further away from any NPPs, such as MHD. As a result of being closer to NPPs, there is higher variability in $\Delta^{14}CH_4$ values at HFD, ICL, TAC and WAO than at the sites further away (Fig. 5.8).

Figure 5.9 shows two-dimensional histograms of $\Delta\Delta^{14}CH_4$-ΔCH_4 and $\Delta\Delta^{14}CH_4$-$\Delta\delta^{13}CH_4$ that include NPP influences in $\Delta^{14}CH_4$. The inclusion of NPP $\Delta^{14}CH_4$ influences produces more scattered $\Delta^{14}CH_4$-CH_4 and $\Delta^{14}CH_4$-$\delta^{13}CH_4$ values and drives the median $\Delta^{14}CH_4$ in each set of simulations to higher values. In the two-dimensional histograms, sources of methane inferred from pseudo-data plots of $\Delta\Delta^{14}CH_4$-$\Delta\delta^{13}CH_4$ suggest a much larger proportion of waste CH_4 in the EDGAR5 simulations than is shown in Fig. 5.6

Table 5.7: NPP $\Delta^{14}CH_4$ influence statistics for each of the measurement sites.

Site	Mean NPP $\Delta^{14}CH_4$ increase (‰)	Median NPP $\Delta^{14}CH_4$ increase (‰)	% of NPP $\Delta^{14}CH_4$ increases $\leq$ 5 ‰
BSD	34.2	7.7	38.9
HFD	114.3	31.9	21.3
ICL	75.8	19.7	25.2
MHD	18.1	5.1	49.5
RGL	41.3	9.4	34.8
TAC	99.9	19.7	25.3
WAO	85.5	15.7	28.0

and reported in the EDGAR v5.0 inventory. However, pseudo-data plots of $\Delta\Delta^{14}CH_4$-$\Delta\delta^{13}CH_4$ in the NAEI-EDGAR4 simulations have smaller deviations from the background when NPPs are included making it more difficult to interpret the methane sources at the measurement sites (Fig.5.6).

It is clear that NPP $\Delta^{14}CH_4$ influences heavily distort the interpretation of $\Delta^{14}CH_4$-CH_4 and $\Delta^{14}CH_4$-$\delta^{13}CH_4$ data slopes in the UK. Without accounting for or minimising NPP influences the methane fossil-fractions and sources could be falsely interpreted.

Less than 1% of $\Delta^{14}CH_4$ values across the UK network were not influenced by NPP emissions. However, between 21.3% and 49.5% of the $\Delta^{14}CH_4$ pseudo-data across the UK were increased by only 5‰ (approximately the measurement uncertainty for atmospheric $\Delta^{14}CH_4$; Zazzeri et al. 2021) or less as a result of NPP influences (Table 5.7). Whilst this suggests there are constant NPP influences across the UK throughout the year, these data also indicate that a large proportion of NPP $\Delta^{14}CH_4$ influences are too small to be detected with current instrumentation. Therefore, there are times or certain meteorological conditions when NPP influences on $\Delta^{14}CH_4$ in the UK can be minimised. However, the spatial resolution used for simulating NPPs likely impacts the magnitude and variations of $\Delta^{14}CH_4$ across the UK. As most NPPs are over 100 km from the measurement sites coarser resolution back-trajectories are computationally favourable. However, SWB is only 45 km from TAC and coarser resolution back-trajectories could likely overestimate the $\Delta^{14}CH_4$ influences from SWB at the nearby measurement sites. In this instance, higher-resolution back-trajectories would likely produce more accurate source-receptor relationships for NPPs closer to the UK.

Meteorological data from the Met Office's Unified Model are used to find times when NPPs were upwind and downwind of the measurement sites. At times when NPPs were upwind of the measurement sites ($\sim$ 7% of

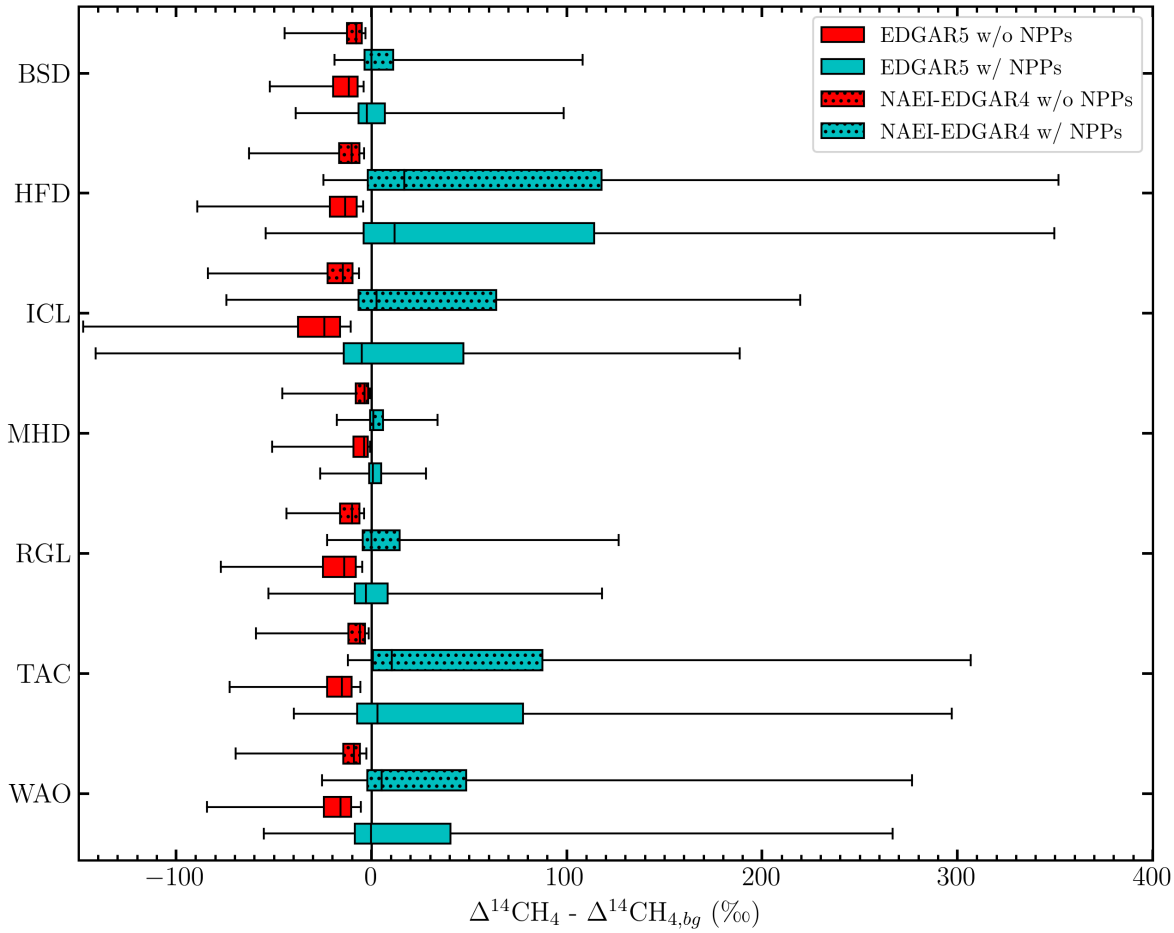


Figure 5.8: Boxplot distributions of $\Delta\Delta^{14}CH_4$ at each of the sites with (cyan) and without (red) NPP influences for EDGAR5 and NAEI-EDGAR4 simulations.

data) $\Delta^{14}CH_4$ values were on average between 6.3‰ (at MHD) and 376‰ (at WAO) higher (Fig. 5.10a) and exhibited large variability, particularly at the measurement sites close to NPPs. During downwind conditions, NPPs increased $\Delta^{14}CH_4$ values on average between 2.8‰ at MHD and 5.8‰ at ICL (Fig. 5.10a). Whilst these small average increases do not significantly affect $\Delta^{14}CH_4$ values, NPPs introduce a bias in $\Delta^{14}CH_4$ when used for interpreting fossil-fractions and methane sources, especially as most of the average increases are within the 5.4‰ instrument measurement uncertainty (Zazzeri et al. 2021).

This simple filtering for wind direction produces significant reductions in the NPP influences on $\Delta^{14}CH_4$, even for measurement sites close to NPPs, such as TAC and WAO which have average reductions in NPP $\Delta^{14}CH_4$ influences of 351‰ and 372‰, respectively.

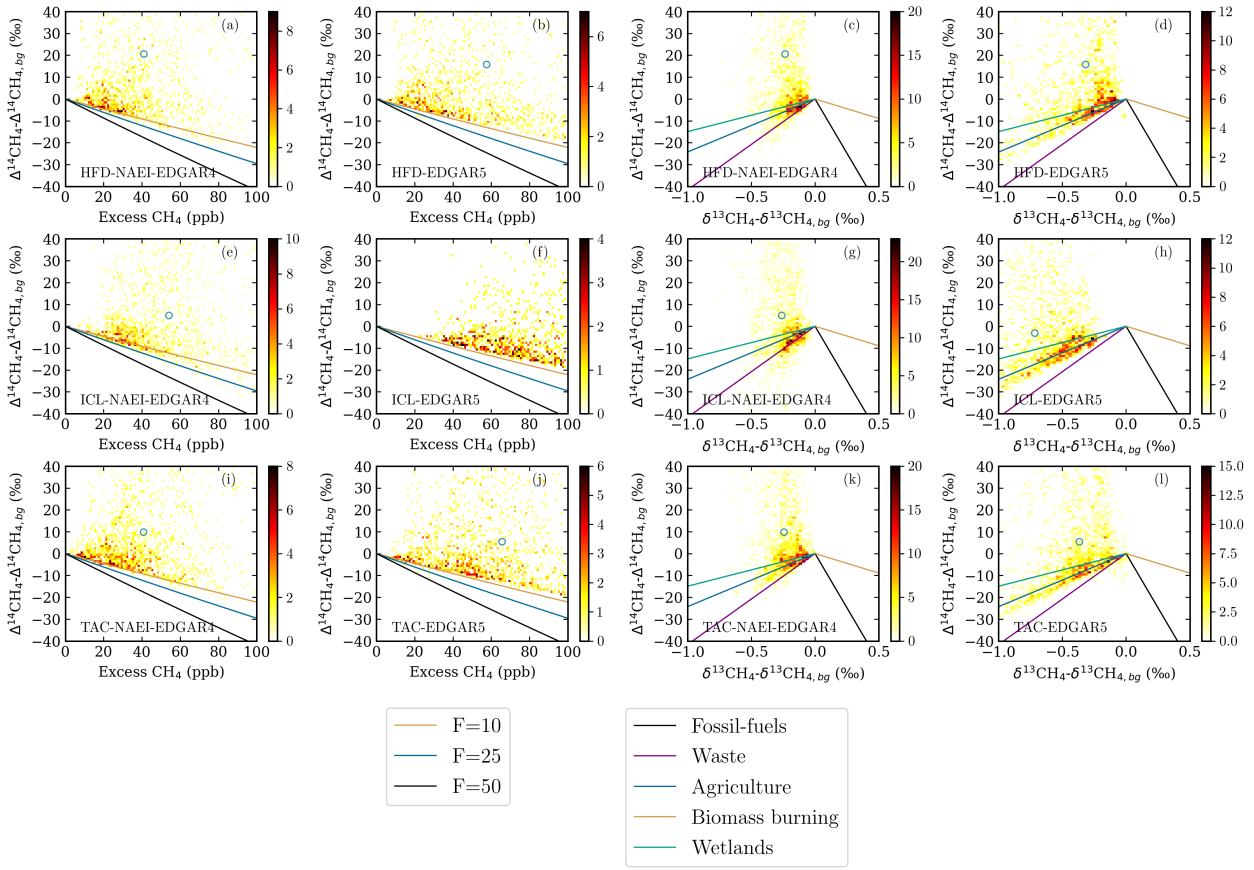


Figure 5.9: Two-dimensional histograms of $\Delta\Delta^{14}CH_4$-ΔCH_4 (columns 1 and 2) and $\Delta\Delta^{14}CH_4$-$\Delta\delta^{13}CH_4$ (columns 3 and 4) for HFD (top row), ICL (middle row) and TAC (bottom row) with NPP $\Delta^{14}CH_4$ influences included. Median values are shown by the blue marker on each panel. Reference lines for F values and CH_4 sources are also shown.

CH_4, $\Delta^{14}CH_4$ and $\delta^{13}CH_4$ EDGAR5 pseudo-data at Imperial College London and Ridge Hill at times when NPPs are downwind are plotted in Fig. 5.10b-e. The downwind $\Delta\Delta^{14}CH_4$-ΔCH_4 pseudo-data no longer form distinct slopes nor closely match the $\Delta\Delta^{14}CH_4$-ΔCH_4 pseudo-data slopes that do not include NPP influences. At ICL, there there is a lot of scatter in $\Delta\Delta^{14}CH_4$-ΔCH_4 pseudo-data plots. Whilst there are no positive $\Delta\Delta^{14}CH_4$ values at ICL, the influence of NPPs is evident when compared to $\Delta\Delta^{14}CH_4$-ΔCH_4 pseudo-data plots without NPP influences (Fig. 5.10b). In contrast, the influence of NPPs on downwind pseudo-data at RGL is noticeable with positive $\Delta\Delta^{14}CH_4$ values shown in plots of $\Delta\Delta^{14}CH_4$-ΔCH_4 pseudo-data (Fig. 5.10c). Similarly, $\Delta\Delta^{14}CH_4$-$\Delta\delta^{13}CH_4$ pseudo-data are impacted by NPPs and pseudo-data no longer form distinct slopes but have scattered values. $\Delta\Delta^{14}CH_4$-$\Delta\delta^{13}CH_4$ pseudo-data slopes at ICL are now indicative of a mixture of waste and agricultural methane sources and no fossil fuel methane (Fig.

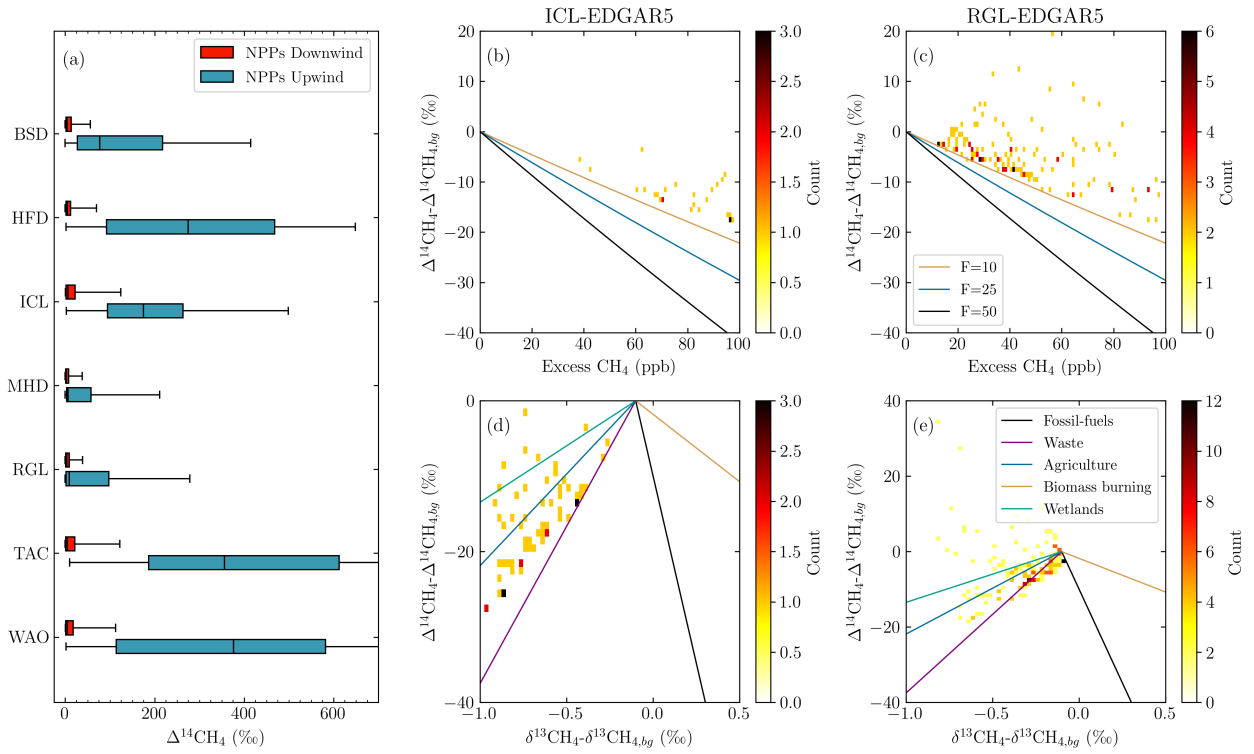


Figure 5.10: Panel (a) distributions of simulated NPP $\Delta^{14}CH_4$ influences at the measurement sites under upwind and downwind conditions. Two-dimensional histograms of $\Delta\Delta^{14}CH_4$-ΔCH_4 and $\Delta\Delta^{14}CH_4$-$\Delta\delta^{13}CH_4$ for ICL (b,d) and RGL (c,e) from EDGAR5 simulations with data when NPPs are downwind. Fossil-fraction and methane source reference lines are shown.

5.10d). However, wind direction filtering does reduce some of the impact of NPP emissions on $\Delta^{14}CH_4$ in comparison to the pseudo-data two-dimensional histograms that include NPP influences. Filtering for wind direction could result in methane emissions from areas between NPPs and the measurement sites not being captured in the analysis which could potentially result in emissions in the southeast UK (Fig. 5.3) not being accurately attributed or constrained. Whilst wind direction filtering at sites such as ICL does remove positive $\Delta\Delta^{14}CH_4$ values there are still influences from NPPs that could distort interpretations of $\Delta^{14}CH_4$ measurements. Therefore NPP influences should always be accounted for in UK radiocarbon studies.

Average increases in $\Delta^{14}CH_4$ from the seven PWRs closest to the measurement sites varies across the network (Table 5.8). At measurement sites furthest from the NPPs (e.g. BSD) the magnitude of individual reactor influences on $\Delta^{14}CH_4$ are proportional to their emission rates (Table 5.5), with GRA $^{14}CH_4$ emissions producing the largest increases in $\Delta^{14}CH_4$ and BOR $^{14}CH_4$ emissions producing the smallest increases in $\Delta^{14}CH_4$ at BSD.

For sites in the southeast, NPP proximity determines which reactor has the largest average impact on $\Delta^{14}CH_4$ (Table 5.8). For example, at TAC and WAO Sizewell B $^{14}CH_4$ emissions produce a larger average impact on $\Delta^{14}CH_4$ than emissions from Gravelines NPP. Even through radiocarbon emissions from GRA are more than three times the emissions from SWB, GRA is ~ 140 km south of SWB and atmospheric transport dilutes the influence of GRA emissions.

Atmospheric transport model resolution also has a role in the simulated influences of PWRs. The 25 km NAME back-trajectories for each of the UK sites were combined with point source NPP emissions to simulate their influence on $\Delta^{14}CH_4$ across the UK. The spatial resolution of back-trajectories may impact the frequency and variability of NPP contributions. Back-trajectories with a higher spatial resolution typically have plumes that are narrower and less disperse than coarser resolution back-trajectories. Plumes in higher resolution back-trajectories are therefore less likely to intersect the NPPs further from the measurement sites and could lead to NPP $\Delta^{14}CH_4$ influences being underestimated. Conversely, coarser resolution back-trajectories could produce more disperse plumes that overestimate NPP $\Delta^{14}CH_4$ influences. Validating the back-trajectory resolution that is most suitable for quantifying NPP influences presents a significant challenge.

Table 5.8: Mean increases in $\Delta^{14}CH_4$ from each of the seven individual NPPs near the measurement sites. Values in ‰.

Site	BOR	DOE	FLA	GRA	PAL	PEN	SWB
BSD	0.3	1.4	2.2	3.9	2.0	1.9	1.4
HFD	0.9	4.7	7.9	16.9	19.1	12.6	5.3
ICL	0.8	4.0	6.7	8.7	7.1	6.1	3.4
RGL	0.3	1.4	5.5	2.7	2.3	1.7	1.5
TAC	0.9	4.0	4.3	17.9	6.8	5.9	20.9
WAO	1.2	5.0	3.7	12.7	4.6	4.3	16.7

5.3.3 Future simulations for 2030 using CMIP6 SSP emissions

5.3.3.1 Changes between 2015 and 2030 in emissions across the UK

Under SSP1-1.9, UK CH_4 emissions in 2030 decreased by 1.28 Tg CH_4 compared to 2015 emissions, with the largest reductions occurring in the agricultural (23.1%), waste (70.4%) and energy (71.4%; e.g. leaks from the natural gas distribution network) CH_4 emission sectors (Table 5.4, Fig. 5.11). In SSP5-8.5, UK CH_4 emissions increase by 20.3% in 2030 relative to 2015 UK emissions, with the largest increases occurring in

the agricultural (6.5%), waste (36.1%) and energy sectors (25.7%; Table 5.4, Fig. 5.11).

Figure 5.11 shows the percentage changes in CH_4 emissions between 2030 and 2015 under SSP1-1.9 and SSP5-8.5 for agricultural, energy, waste and total CH_4 emissions across the UK. In the sectoral emissions spatial variations in emission changes are less than 1% in SSP1-1.9 and SSP5-8.5. However, larger variations in the spatial changes in total CH_4 emissions are seen (Fig. 5.11a-b). The largest changes in the UK occur in the southeast where under SSP1-1.9 there are larger reductions and under SSP5-8.5 there are increases in CH_4 emissions.

5.3.3.2 Future changes in CH_4, $\delta^{13}CH_4$ and $\Delta^{14}CH_4$ across the UK

Similar to contemporary simulations, added CH_4 concentrations, $\Delta\delta^{13}CH_4/\Delta CH_4$ and $\Delta\Delta^{14}CH_4/\Delta CH_4$ are compared under SSP1-1.9 and SSP5-8.5 scenarios for the year 2030 (Fig. 5.12). Most of the added CH_4 concentrations in the SSP simulations are smaller than 100 ppb (Fig. 5.12a). This implies simulated $\Delta\delta^{13}CH_4$ and $\Delta\Delta^{14}CH_4$ values will likely be small in magnitude and therefore make it difficult to distinguish between CH_4 sources and fossil-fractions from plots of $\Delta\Delta^{14}CH_4$-ΔCH_4 and $\Delta\Delta^{14}CH_4$-$\Delta\delta^{13}CH_4$. Median added CH_4 concentrations are 1.5 ppb to 9.0 ppb higher under SSP5-8.5 compared to 2015 SSP estimates and 4.1 ppb to 22.2 ppb smaller under SSP1-1.9 compared to 2015 SSP estimates across the UK sites (Fig. 5.12a).

$\Delta\delta^{13}CH_4/\Delta CH_4$ values in SSP1-1.9 and SSP5-8.5 simulations for 2030 are both positive and negative reflecting the presence of fossil and biospheric methane sources close to the measurement sites (Fig. 5.12b). As a result of smaller added CH_4 concentrations in SSP1-1.9 simulations, $\Delta\delta^{13}CH_4/\Delta CH_4$ have median values of 0‰ ppb^{-1} at all the sites except MHD and RGL. Compared to EDGAR5 and NAEI-EDGAR4 $\Delta\delta^{13}CH_4/\Delta CH_4$, SSP1-1.9 and SSP5-8.5 values are generally less negative due to differences in the source distributions of CH_4 emissions.

Distributions of $\Delta\Delta^{14}CH_4/CH_4$ values in the SSP1-1.9 and SSP5-8.5 simulations are quite similar (Fig. 5.12c). However, median $\Delta\Delta^{14}CH_4/CH_4$ values are generally less negative in the SSP5-8.5 simulations compared to SSP1-1.9 simulations for HFD, ICL and MHD, which is indicative of a smaller fossil-fraction. This contrasts the higher methane fossil-fraction in the SSP5-8.5 emissions (Table 5.4), which may suggest large biospheric emission sources in the vicinity of the measurement sites. However, median $\Delta\Delta^{14}CH_4/\Delta CH_4$ at MHD and RGL are more negative in SSP5-8.5 than SSP1-1.9 simulations reflecting the larger fossil-fraction in SSP5-8.5. Distributions of $\Delta\Delta^{14}CH_4/\Delta CH_4$ indicate there is high variability in the methane fossil-fraction values at the

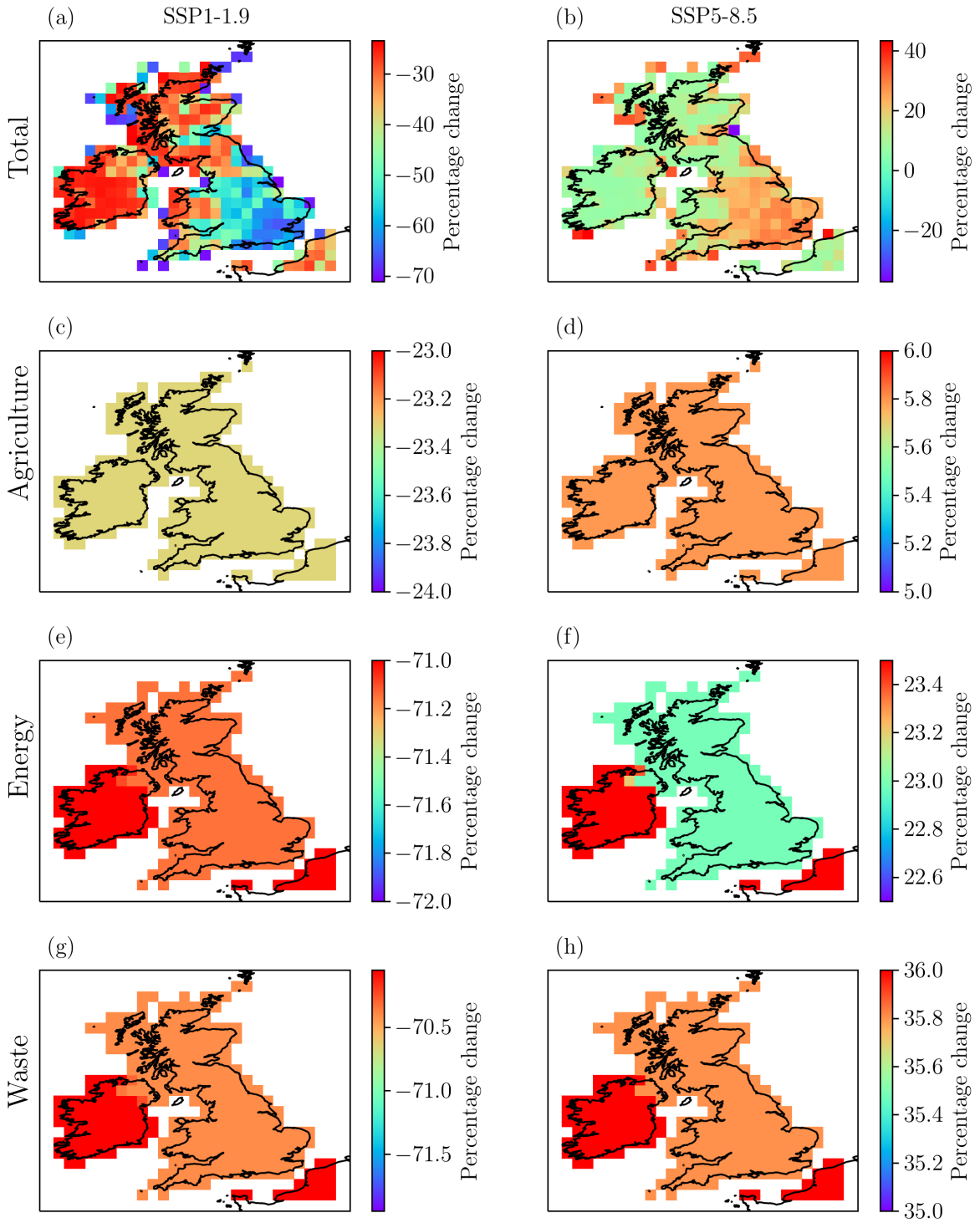


Figure 5.11: Relative differences between 2015 and 2030 SSP1-1.9 (left column) and SSP5-8.5 (right column) methane emissions over the UK for total (top row), agricultural (second row), energy (third row) and waste (bottom row) sectors.

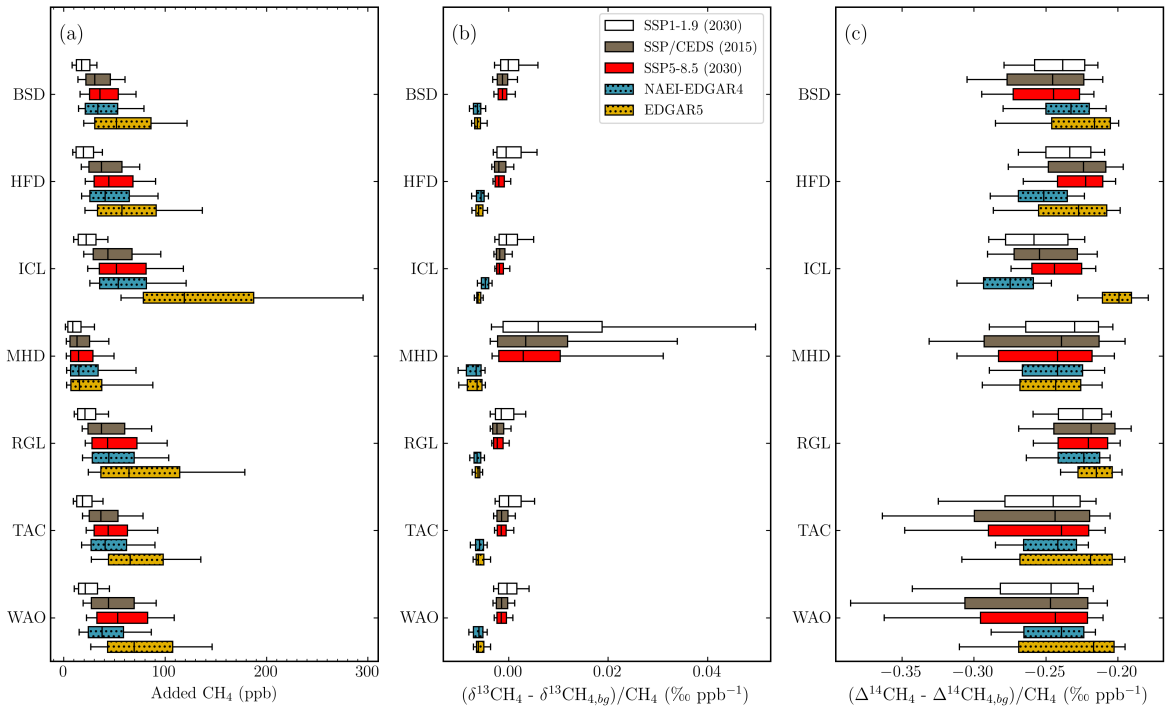


Figure 5.12: Boxplot distributions of (a) added concentrations, (b) $\Delta\delta^{13}CH_4$ and (c) $\Delta\Delta^{14}CH_4$ for EDGAR5, NAEI-EDGAR4, SSP1-1.9, SSP5-8.5 simulations. NPP influences are not included and boxplots show the full range of simulated data.

different measurement sites in the SSP1-1.9 and SSP5-8.5 simulations. This could make it difficult when using atmospheric $\Delta^{14}CH_4$ measurements to determine whether UK emissions are following a path that better aligns with a SSP1-1.9 or SSP5-8.5 pathway.

Two-dimensional histograms of $\Delta\Delta^{14}CH_4$-ΔCH_4 and $\Delta\Delta^{14}CH_4$-$\Delta\delta^{13}CH_4$ for SSP1-1.9 and SSP5-8.5 simulations at HFD, ICL and TAC are shown in Fig. 5.13. The smaller added CH_4 concentrations in SSP1-1.9 simulations introduce larger uncertainties in the fossil-fractions that are interpreted from plots of $\Delta\Delta^{14}CH_4$-ΔCH_4. Whilst the larger added CH_4 concentrations in SSP5-8.5 simulations reduces the uncertainty of fossil-fraction estimates interpreted from $\Delta\Delta^{14}CH_4$-ΔCH_4 plots, F values are shown to be more variable. Therefore distinguishing between the SSP1-1.9 and SSP5-8.5 scenarios relies heavily on the magnitudes of added CH_4 concentrations. Pseudo-data slopes of $\Delta\Delta^{14}CH_4$-ΔCH_4 at each of the measurement sites are calculated using a least-squares regression for both scenarios. Pseudo-data $\Delta\Delta^{14}CH_4$-ΔCH_4 slopes differ between SSP1-1.9 and SSP5-8.5 scenarios by 3% to 10% across the measurement sites, with the largest differences occurring at ICL.

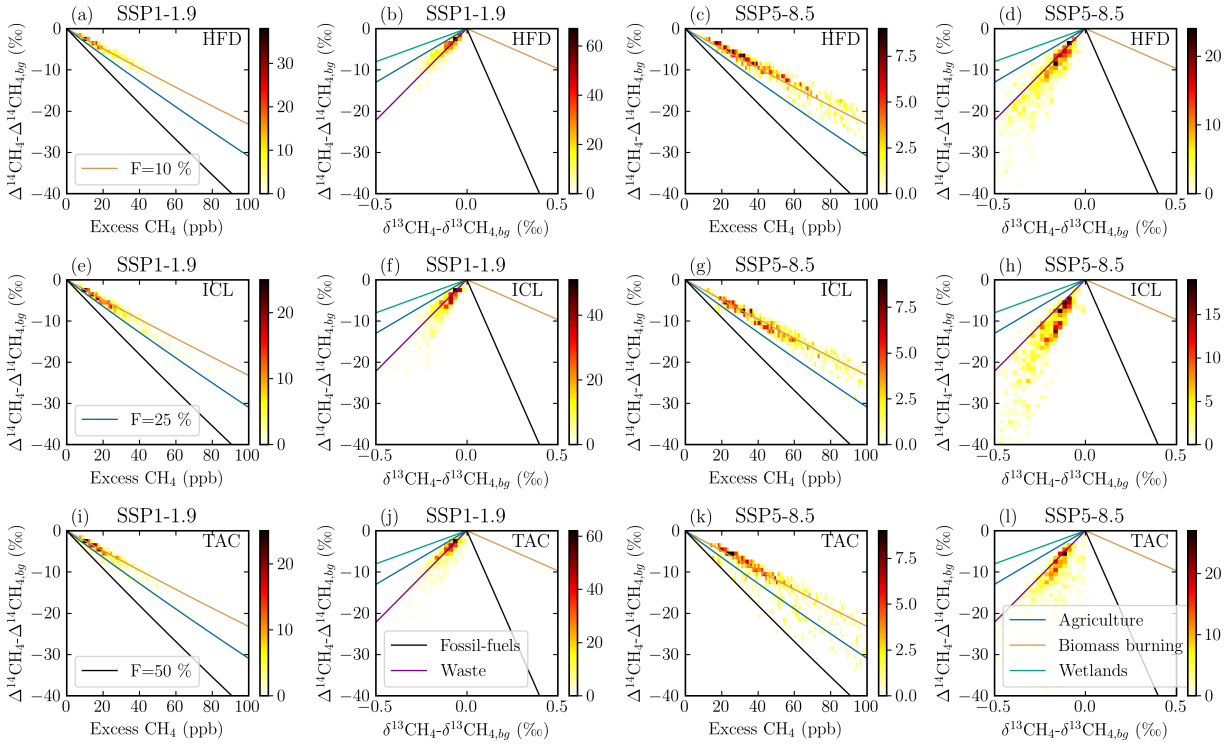


Figure 5.13: Two-dimensional histograms of simulated $\Delta\Delta^{14}CH_4$-ΔCH_4 and $\Delta\Delta^{14}CH_4$-$\Delta\delta^{13}CH_4$ for HFD, ICL and TAC under SSP1-1.9 and SSP5-8.5 emission scenarios.

In the two-dimensional $\Delta\Delta^{14}CH_4$-$\Delta\delta^{13}CH_4$ histograms (Fig. 5.13) there are larger distinctions between SSP1-1.9 and SSP5-8.5 pseudo-data, where differences in slopes are between 10% to 29%, with the largest differences at ICL. SSP5-8.5 $\Delta\Delta^{14}CH_4$-$\Delta\delta^{13}CH_4$ generally have a larger number of data points between the waste and fossil fuel reference lines than seen in SSP1-1.9 $\Delta\Delta^{14}CH_4$-$\Delta\delta^{13}CH_4$. This is most noticeable at ICL, and is also seen in the TAC $\Delta\Delta^{14}CH_4$-$\Delta\delta^{13}CH_4$ histograms. Although larger added CH_4 concentrations reduce the source attribution uncertainty, methane sources can still be interpreted (at least as biogenic or fossil) when there are smaller added concentrations, which is more difficult to do when using only a $\Delta\Delta^{14}CH_4$-ΔCH_4 framework for the UK. With enough data points, slopes of $\Delta^{14}CH_4$-$\delta^{13}CH_4$ could potentially be used for discerning between future methane emission pathways.

5.4 Discussion

In this chapter a regional multi-isotopic framework for interpreting methane fossil-fractions and sources from CH_4, $\delta^{13}CH_4$ and $\Delta^{14}CH_4$ was presented. In this framework different methane fossil-fractions form distinct

$\Delta^{14}CH_4$-CH_4 slopes and similarly different methane sources form distinct $\Delta^{14}CH_4$-$\delta^{13}CH_4$ slopes. The utility of this framework was tested by generating contemporary and future pseudo-data for a network of measurement sites across the UK. Fossil-fractions from different contemporary simulations and future scenarios had similar slopes but differed between contemporary NAEI-EDGAR4 and EDGAR5 simulations by 4% to 47% and by 3% to 10% in the SSP1-1.9 and SSP5-8.5 simulations, respectively. Smaller added concentrations in SSP1-1.9 make it more difficult to distinguish from SSP5-8.5 simulations. Slopes of $\Delta^{14}CH_4$-CH_4 were more discernible between simulations at ICL where added methane concentrations were larger than at the other UK sites. However, larger differences were found between simulations across the UK measurement sites in plots of $\Delta^{14}CH_4$-$\delta^{13}CH_4$. This is likely a result of $\Delta^{14}CH_4$-$\delta^{13}CH_4$ reference lines being less ambiguous between different methane sources for smaller added concentrations. Therefore suggesting concurrent $\Delta^{14}CH_4$-$\delta^{13}CH_4$ measurements could potentially be more useful for evaluating the source attribution of UK methane emission inventory estimates.

The extent this CH_4-$\delta^{13}CH_4$-$\Delta^{14}CH_4$ framework is useful for interpreting isotopic measurements from the UK relies on the accuracy of the pseudo-data simulations used to test the framework. For example, if the emissions used in the simulations are too low across the UK, then smaller added CH_4 concentrations are generated. The use of $\Delta^{14}CH_4$-CH_4 for interpreting UK fossil-fractions is then undervalued since the smaller added concentrations imply larger uncertainties in the fossil-fractions. Lunt et al. (2021a) found good agreement between methane emissions from NAEI and those calculated from atmospheric CH_4 measurements from BSD, HFD, MHD, RGL and TAC in an inversion setup, which were on average ~ 0.10 Tg CH_4 yr^{-1} lower than NAEI between 2013-2020. The largest posterior-prior differences ($\sim 9.5 \times 10^{-3}$ kg m^{-2} yr^{-1}) in these inversions occurred in the north near BSD and in the London area (Lunt et al. 2021a). It is therefore likely that the pseudo-data concentrations generated for most of the UK sites used in this chapter will be in reasonable agreement with their corresponding atmospheric CH_4 measurements. Therefore, as the simulations suggest, regional scale fossil-fraction differences may be difficult to interpret from plots of $\Delta^{14}CH_4$-CH_4 data at some of the UK sites (e.g. RGL).

Pseudo-data used in the $\Delta^{14}CH_4$-CH_4 California study (Graven et al. 2019) generally had larger added CH_4 concentrations across the measurement network than the simulated values used in the UK. Graven et al. (2019) detected larger regional differences in the fossil-fractions suggesting the $\Delta^{14}CH_4$-CH_4 approach is better suited to regions, such as California, where there are larger methane concentrations.

Atmospheric $\delta^{13}CH_4$ and concentration measurements from Saboya et al. (2022) found 2017 NAEI emissions were underestimated in London and that the proportion of fossil CH_4 sources were too low in the NAEI and EDGAR v4.3.2 inventories compared to observations. It is therefore more likely that $\Delta^{14}CH_4$-CH_4 plots of ICL measurements would be more useful than implied by the simulations since there are larger added CH_4 concentrations in the ICL measurements (Saboya et al. 2022).

Comparisons of $\Delta^{14}CH_4$-$\delta^{13}CH_4$ pseudo-data across the UK sites yielded larger differences between simulations and are potentially more useful for interpreting regional scale differences in UK methane sources than only using $\Delta^{14}CH_4$-CH_4 data. The additional constraint of $\delta^{13}CH_4$ isotopic data means there are smaller uncertainties between the sources for smaller added concentrations. However, the $\Delta^{14}CH_4$-$\delta^{13}CH_4$ approach relies on precisely known $\delta^{13}CH_4$ source signatures, which in reality will have some uncertainty (e.g. ±3 ‰; Zazzeri et al. 2015).

The large number of NPPs in the vicinity of the UK means $^{14}CH_4$ emissions from these sources need to be accounted for in UK $\Delta^{14}CH_4$ studies. Simulated NPP emissions resulted in median $\Delta^{14}CH_4$ influences of 5.1‰ to 31.9‰ across the UK, with instances when $\Delta^{14}CH_4$ increased by nearly 600‰. Whilst UK median $\Delta^{14}CH_4$ increases are much larger than the average 0‰ to 7‰ increase across California from NPP emissions (Graven et al. 2019), UK median $\Delta^{14}CH_4$ increases are similar to those measured in Heidelberg in 1988-89 (Levin et al. 1992).

However, a simple filtering for wind direction reduces median NPP $\Delta^{14}CH_4$ influences to 2.8‰ to 5.8‰ across the UK sites. Median increases are close to or within the 5.4‰ measurement uncertainty of $\Delta^{14}CH_4$ (Zazzeri et al. 2021). However, there are still NPP influences at times when NPPs are downwind of the measurement stations and are shown to distort the interpretation of $\Delta^{14}CH_4$-CH_4 and $\Delta^{14}CH_4$-$\delta^{13}CH_4$ plots. Whilst there is potential to reduce NPP influences, methane emissions from the area between the measurement sites and NPPs (e.g. the southeast of the UK) are not going to be captured.

Further exploration into variations of NPP influences on $\Delta^{14}CH_4$ using different model spatial resolutions is needed. Different spatial resolutions used in the simulations are likely to produce different estimates of the magnitude of NPP influences - particularly from NPPs close to the measurement sites. Higher resolution simulations could be more suitable for modelling NPP $\Delta^{14}CH_4$ influences from the closest PWRs, but computationally expensive for NPPs further away.

Additional isotopic or other tracer measurements could be included in this framework or used to target regions close to NPPs that could affect $\Delta^{14}CH_4$. Ethane, for example, is emitted from fossil fuel methane sources and considered to not be emitted from biogenic methane sources (e.g. Helmig et al. 2016). However, quantifying the source apportionment from atmospheric ethane measurements requires knowing the methane:ethane emission ratios of fossil methane sources (Hausmann et al. 2016). Ethane has been used for constraining methane sources in the UK through an inversion model (Ramsden et al. 2022) where it was also demonstrated that biases in the source attribution can arise when incorrect methane:ethane ratios are used. This is analogous to the uncertainties of the $\delta^{13}CH_4$ isotopic signatures used for source attribution. In this regard, radiocarbon tracer measurements can provide tighter fossil fuel methane constraints, but only if NPP $\Delta^{14}CH_4$ influences can be accounted for or minimised and the biogenic $\Delta^{14}CH_4$ signature is known.

As in Graven et al. (2019), hourly pseudo-data from the afternoon for a network of measurement sites were used for the UK. However, it is unlikely for concurrent CH_4, $\delta^{13}CH_4$ and $\Delta^{14}CH_4$ measurements to be made at this frequency at seven measurement sites. Pseudo-data indicate that measurements at ICL would be a suitable location to apply this framework. The larger differences between simulations and larger added concentrations make it more likely for $\Delta^{14}CH_4$-CH_4 and $\Delta^{14}CH_4$-$\delta^{13}CH_4$ measurements in London to be useful for evaluating emission inventories.

5.5 Conclusion

This chapter presented a combined CH_4-$\delta^{13}CH_4$-$\Delta^{14}CH_4$ framework for interpreting regional methane sources and fossil-fractions from slopes of $\Delta^{14}CH_4$-$\delta^{13}CH_4$ and $\Delta^{14}CH_4$-CH_4, respectively. Simulations suggest $\Delta^{14}CH_4$-CH_4 data could be useful for assessing regional differences in UK fossil-fractions. However, $\Delta^{14}CH_4$-$\delta^{13}CH_4$ simulations suggest a joint isotopic approach is more valuable, particularly for urban areas, such as London, where there are larger added CH_4 concentrations that can improve the constraints of sources interpreted from $\Delta^{14}CH_4$-CH_4 data. Larger differences between the NAEI-EDGAR4 and EDGAR5 simulations of $\Delta^{14}CH_4$-$\delta^{13}CH_4$ than $\Delta^{14}CH_4$-CH_4 across the UK suggest atmospheric $\Delta^{14}CH_4$-$\delta^{13}CH_4$ measurements could be more useful for assessing regional differences in methane sources across the UK and for evaluating the source apportionment of emission inventories. Simulations suggest that NPP influences on UK $\Delta^{14}CH_4$ are large on average and whilst their impact can be reduced by filtering for times when NPPs are downwind, NPP influences should be accounted for when interpreting $\Delta^{14}CH_4$ measurements.

Chapter 6

Assessing the utility of TROPOMI XCH_4 retrievals for the UK

"Look again at that dot. That's here. That's home. That's us."

— Carl Sagan, *Pale Blue Dot, 1994*

Abstract

Satellite measurements of atmospheric methane have been previously used for detecting and quantifying CH_4 emissions. TROPOMI, launched onboard the Sentinel-5 Precursor satellite in 2017, provides high-resolution, daily retrievals of atmospheric methane columns which are ideal for informing on regional scale methane emissions. After data quality filtering, approximately 3% of TROPOMI retrievals between 2018-2020 are found to be useful for UK applications. This is a much smaller proportion of successful retrievals than obtained in previous regional TROPOMI CH_4 studies targeted at other countries. Within this observation period total methane columns (XCH_4) have a mean value of $1860.4 \pm 10.6 (1\sigma)$ ppb for the UK. There are small regional differences in the TROPOMI XCH_4 values across the UK with no discernible XCH_4 gradient observed between London and the surrounding areas in the southeast UK. This contrasts the distinct CH_4 emissions gradient between London and the rest of the southeast that is observed in the UK national emissions inventory. TROPOMI retrievals over the UK are in good agreement with modelled XCH_4 values from the Copernicus Atmosphere Monitoring Service (CAMS) reanalysis and forecast data products (adjusted for global bias) finding absolute median differences of 4.5 ppb and 7.6 ppb respectively. The largest CAMS-TROPOMI XCH_4 differences occur for pixels with higher surface albedo values suggesting there remains some surface

albedo bias in the TROPOMI XCH_4 measurements despite data quality filtering. CAMS forecasts and reanalysis XCH_4 have average XCH_4 gradients of approximately 10 ppb and 5 ppb, respectively, between London and its surrounding areas. As these spatial gradients are smaller than the TROPOMI instrument precision, TROPOMI measurements cannot be used to accurately inform on spatial differences of CH_4 in the UK. TROPOMI retrievals were also used to search for plumes coming from Drax power station, which has reported emissions of 3126 t CH_4 yr^{-1}, but satisfactory plumes were not observed in the 2018-2020 retrievals. These findings indicate that TROPOMI XCH_4 retrievals from this period are not useful for informing on UK methane gradients nor detecting emissions from UK point sources.

6.1 Introduction

Satellite measurements of atmospheric methane enable a unique approach for frequent monitoring of global CH_4 sources. Compared to ground-based measurements satellite observations can cover larger areas, provide global spatial constraints on the distribution of CH_4 emissions and can measure over places that are not easily accessible to ground-based instruments.

Until 2018, GOSAT provided the main satellite constraint of total atmospheric methane column (XCH_4) measurements. XCH_4 measurements from GOSAT have been used in a range of regional studies to quantify and better understand CH_4 emissions from different sources (e.g Lunt et al. 2016; Feng et al. 2017; Ganesan et al. 2017; Pandey et al. 2016; Turner et al. 2015). For example, GOSAT observations used in different inversion models found that coal-related methane emissions from China were being overestimated in the EDGAR inventory (Turner et al. 2015; Ganesan et al. 2017; Maasakkers et al. 2019). Similarly, Ganesan et al. (2017) found waste and ruminant CH_4 emissions in India were being overestimated in the EDGAR v.4.2 inventory.

Since 2018, TROPOMI XCH_4 measurements have provided additional spaceborne constraints on atmospheric CH_4. The high spatial resolution of TROPOMI retrievals (5.5×7 km^2), compared to GOSAT retrievals (10.5×10.5 km^2), makes TROPOMI XCH_4 measurements well-suited for regional scale inversions, informing on regional scale spatial patterns of CH_4 and other applications. For example, methane emissions from six coal mines in Queensland, Australia were collectively estimated at 570 ± 98 Gg CH_4 yr^{-1} from using TROPOMI measurements in a cross-sectional flux approach (Chapter 6, Section 6.2.4), which is seven times larger than reported in the Australian emission inventory (Sadavarte et al. 2021). Plant et al. (2022) used CO and CH_4

TROPOMI measurements to estimate emissions from eight US cities*. They found urban CH_4 emissions were on average 70% larger than reported in the 2015 EDGAR v5.0 inventory. GOSAT and TROPOMI XCH_4 measurements used in a joint global inversion model produced posterior emission estimates for Europe that were 7 Tg CH_4 yr^{-1} smaller than reported in the prior EDGAR v4.3.2 inventory for the year 2012 (Qu et al. 2021). The large prior-posterior differences from this inversion study were attributed to reductions in fossil fuel CH_4 emissions across Europe (Qu et al. 2021). However, to date, there are no published studies using TROPOMI XCH_4 measurements in a regional-scale inversion model.

There are also currently no published studies that use TROPOMI, or other satellite, methane measurements targeted at the UK. The spatial resolution and instrument precision of GOSAT makes it challenging to quantify methane emissions from smaller, cloudy places such as the UK (Palmer et al. 2021). Any successful GOSAT retrievals for the UK would therefore likely result in a sparse XCH_4 dataset. The higher spatial resolution and near daily global coverage of TROPOMI retrievals means there is potential for monitoring spatiotemporal changes of XCH_4 across the UK and constraining the spatial distributions of UK methane emissions. However, the 5 ppb to 10 ppb instrument precision of TROPOMI (Hu et al. 2018b) makes it unlikely for small spatiotemporal XCH_4 changes or small pollution events to be captured in the retrievals.

To directly compare regional XCH_4 gradients observed in TROPOMI retrievals to spatially distributed CH_4 emissions reported in gridded inventories, such as NAEI and EDGAR, an atmospheric transport model is needed. An inversion model, which accounts for atmospheric transport, could be used to calculate a posterior emissions estimate using TROPOMI measurements. However, an inversion could be computationally expensive and time consuming, especially if the high-resolution TROPOMI retrievals are retained in the inversion model. Alternatively, a model XCH_4 dataset that combines emission estimates and an atmospheric transport model could be used to assess whether there are substantial regional differences with TROPOMI and if performing an inversion would be informative.

CAMS (Copernicus Atmospheric Monitoring Service) produce modelled estimates of global XCH_4 using a data assimilation approach (Chapter 3, Section 3.5). Emission inventories, the atmospheric IFS model and atmospheric measurements – including GOSAT measurements – are used to generate consistent atmospheric XCH_4 datasets. CAMS reanalysis XCH_4 (Chapter 3, Section 3.5.1) uses observations and a previous XCH_4 forecast to produce an updated state of the atmosphere. Globally, CAMS reanalysis underestimates CH_4

*Boston, Philadelphia, Washington DC, Baltimore, Portland, Kansas City, New York City and Atlanta.

observations from the Total Carbon Column Observing Network (TCCON) by 5 ppb to 20 ppb (Ramonet et al. 2021). CAMS also produce daily XCH_4 forecasts (Chapter 3, Section 3.5.2), which are found to underestimate global XCH_4 observations by ~ 25 ppb on average (Barré et al. 2021). The negative biases in CAMS reanalysis and forecasts are thought to be due to a bias in the tropospheric component of the IFS model (Ramonet et al. 2021). Barré et al. (2021) used a high-pass Gaussian filter to remove some of the bias in CAMS forecasts so global comparisons with TROPOMI retrievals could be used to evaluate large point source emitters.

Some studies have used TROPOMI retrievals for quantifying emissions from large point sources or pollution events (e.g. Pandey et al. 2019; Varon et al. 2019). Drax power station (Fig. 6.1) is one of the UK's largest power stations generating 6% of the UK's electricity (drax 2022). Drax is also one of the UK's largest methane point source emitters and is estimated in the 2019 NAEI inventory to emit 3126 t CH_4 yr^{-1} (or 0.36 t CH_4 hr^{-1}; assuming constant emissions). Drax power station used to be a coal-fuelled plant but by March 2021 was converted to be entirely fuelled by wood pellets (drax 2022). Observations from TROPOMI used in this chapter cover the period when Drax was using a combination of wood pellets and coal for electrical generation.

In this chapter, the data coverage of TROPOMI XCH_4 retrievals from November 2018 to October 2020 are assessed for the UK and used to analyse regional gradients of XCH_4. CAMS reanalysis and forecast datasets are compared with TROPOMI measurements to assess the extent CAMS XCH_4 capture the spatial differences observed in TROPOMI retrievals and if TROPOMI XCH_4 could provide additional constraints on regional CH_4 gradients in the UK. TROPOMI XCH_4 retrievals are also used to search any for visible plumes coming from Drax power station that could be used to quantify its emission rate using the cross-sectional flux approach.

6.2 Data products and methods

6.2.1 Overview of TROPOMI XCH_4 data products and processing

Daily TROPOMI operational data products (as described in Chapter 3, Section 3.4) from 1 November 2018 to 31 October 2020 were analysed to find retrievals with high-quality XCH_4 pixels over the UK. Data products are processed using the HARP Python module and pixels are aligned to a uniform $0.08^o \times 0.08^o$ spatial grid, which closely matches the TROPOMI 7×7 km^2 pixel resolution over some of the observational period considered (from August 2019 the pixel resolution is 5.5×7 km^2; Hu et al. 2018b).

Figure 6.2 shows the 2018-2020 averaged values for the uncorrected XCH_4 data product, the bias-corrected XCH_4 product and the bias-corrected, filtered to retain pixels with aerosol optical thickness (AOT) <0.1 XCH_4 data product over the UK. An average XCH_4 of $1848.0 \pm 11.8(1\sigma)$ ppb is found in the uncorrected methane product, $1860.3 \pm 10.6(1\sigma)$ ppb in the bias-corrected product and $1860.4 \pm 10.6(1\sigma)$ ppb in the bias-corrected

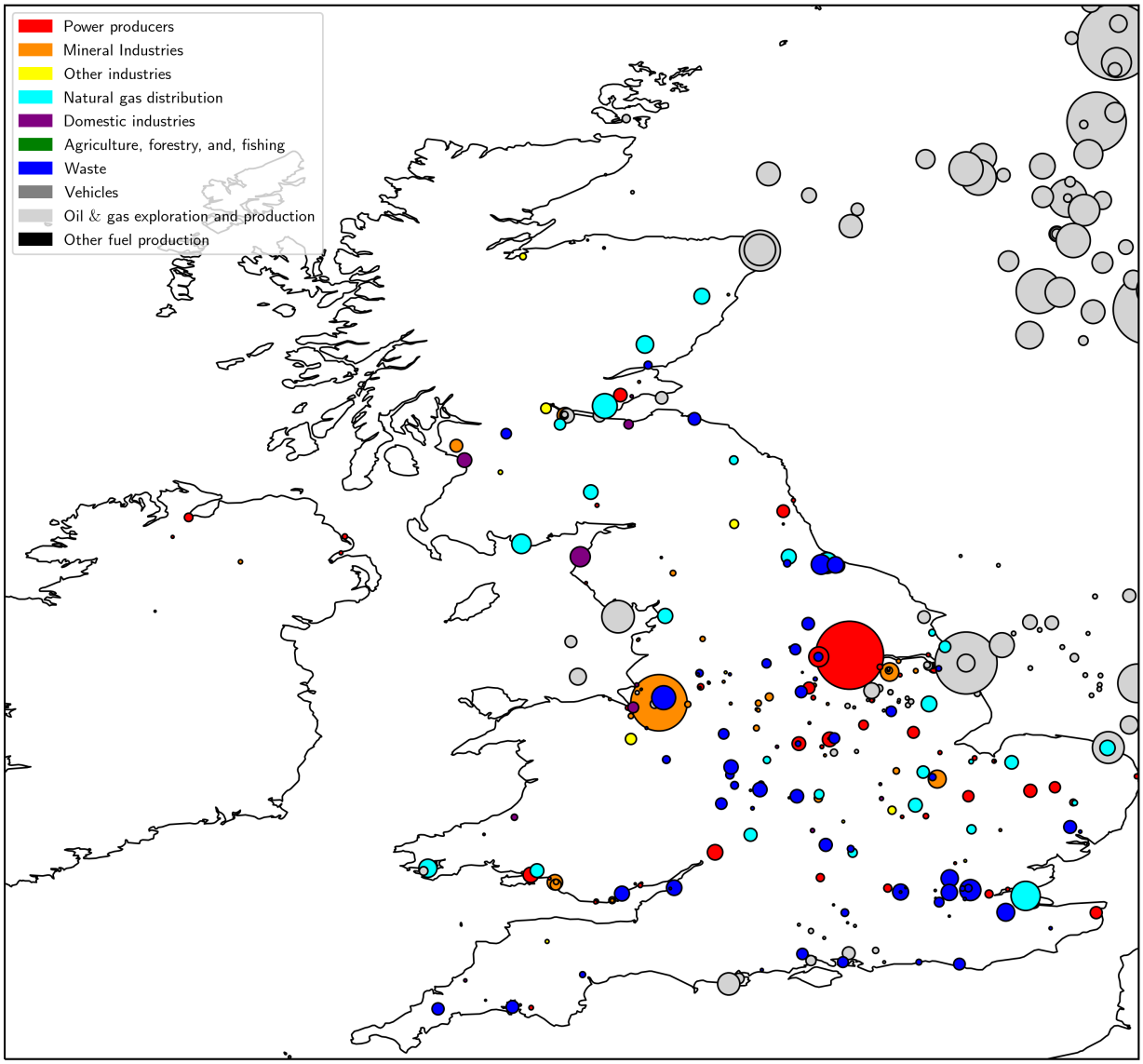


Figure 6.1: 2017 UK NAEI point sources where marker colour denotes the emission source sector and marker size is scaled by the magnitude of emissions. Drax power station is denoted by the large red marker in northeast England.

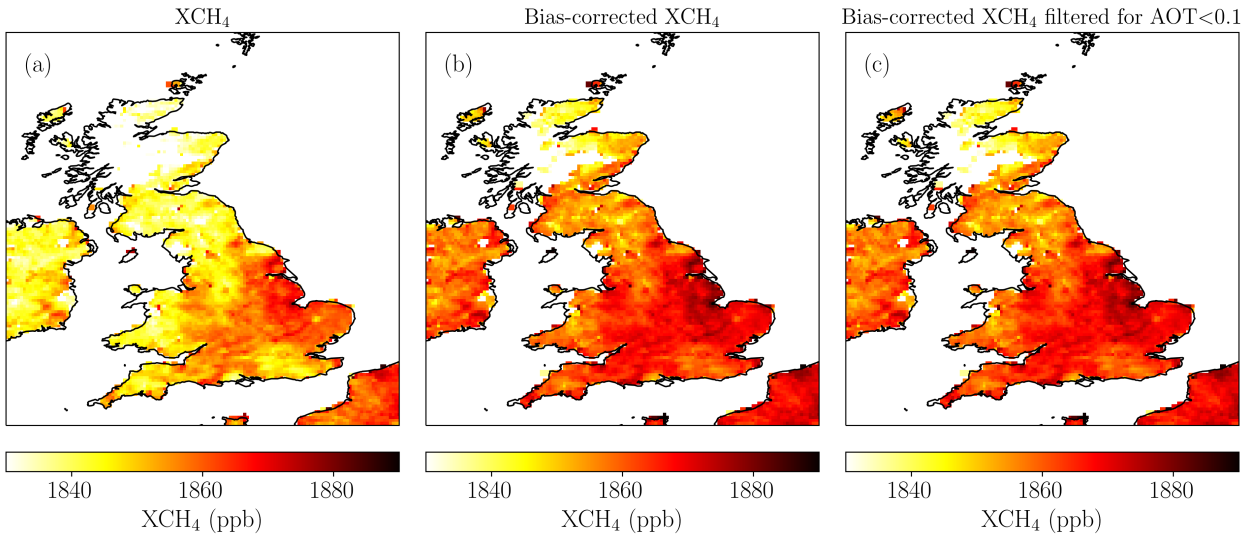


Figure 6.2: UK 2018-2020 averaged TROPOMI XCH_4 for (a) uncorrected product, (b) bias-corrected product and (c) and bias-corrected product with additional filtering to remove pixels with aerosol optical thickness > 0.1.

and AOT-filtered product over the UK. These averages do not include the North Sea as TROPOMI does not retrieve XCH_4 over large aquatic bodies in the observation period considered. XCH_4 pixels are shifted towards higher values in the bias-corrected TROPOMI XCH_4 product compared to the uncorrected XCH_4 product.

The bias correction applied to XCH_4 is to account for the bias introduced from surface albedo values. There is a strong underestimation in retrieved XCH_4 for low albedo values and an overestimation for high albedo values (Fig. 3.14) compared to ground-based FTIR column measurements from across TCCON (Lorente et al. 2021). A similar correction for surface albedo bias is also applied to XCH_4 retrievals made by GOSAT (Hasecamp et al. 2019). Comparing the corrected TROPOMI XCH_4 data with GOSAT finds, globally, the surface albedo bias is removed (Hasecamp et al. 2019). The mean surface albedo across the UK for 2018-2020 is $0.08 \pm 0.01 (1\sigma)$ - shown in Fig. 6.7a - suggesting an approximate underestimation of $\sim 1\%$ in comparison to TCCON observations (Lorente et al. 2021). There are increases in XCH_4 in the bias-corrected product over the UK (Fig. 6.3) with high XCH_4 values towards the east of England that are not seen in the uncorrected XCH_4 product (Fig. 6.2) and large increases in XCH_4 across the west of the UK (Fig. 6.3).

Pixels with AOT>0.10 result in larger deviations in TROPOMI XCH_4 when compared to corresponding TCCON observations (Fig. 3.14; Lorente et al. 2021). Whilst pixels with AOT<0.10 also deviate TROPOMI

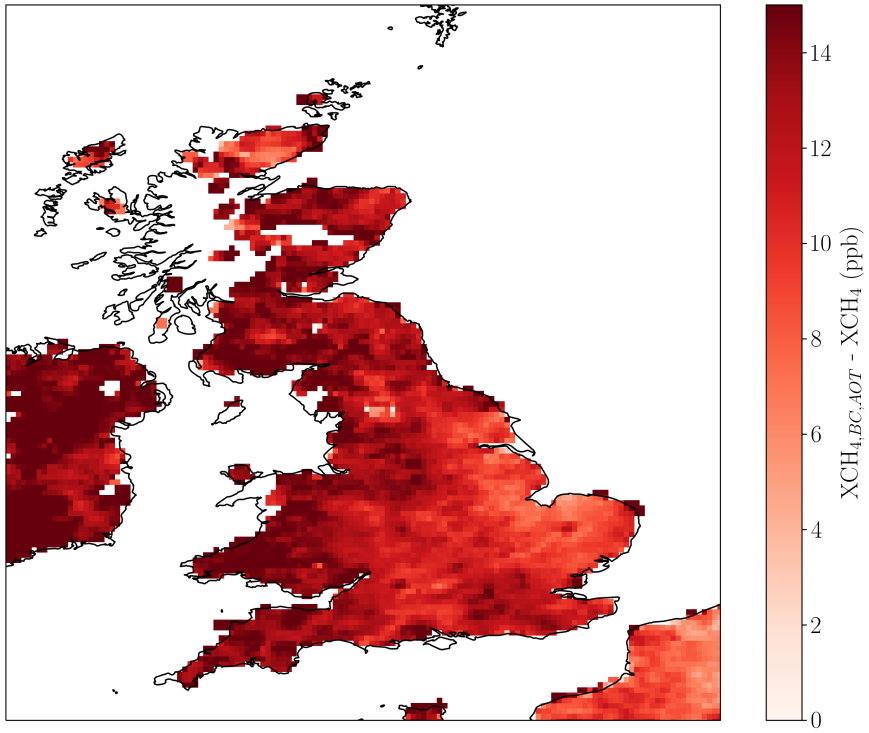


Figure 6.3: UK mean 2018-2020 TROPOMI CH_4 subtracted from the corresponding bias-corrected TROPOMI XCH_4, filtered for AOT<0.10, values.

XCH_4 values in comparison to TCCON observations this deviation is uncorrelated (Fig. 3.14; Lorente et al. 2021). After filtering to remove pixels with AOT>0.10 there is an average AOT of $0.02 \pm 0.01(1\sigma)$ across the UK in this observation period (Fig. 6.7b). AOT-filtering does not lead to a change in the average XCH_4 value nor the XCH_4 standard deviation for bias-corrected data across the UK. Figure 6.4 shows there are differences of up to ±4 ppb for certain pixels in the UK when filtering for AOT<0.1, which is within the 10.6 ppb TROPOMI XCH_4 uncertainty and therefore unlikely to improve the bias-corrected XCH_4 data product across the UK. The results presented in this chapter use the bias-corrected, AOT-filtered XCH_4 data product, and are hereby referred to as just XCH_4.

Applying the filtering and data quality controls to individual retrievals in the 2018-2020 observation period yields eight successful cloud-free scenes with XCH_4 pixels covering most of the UK during this observation period (Table 6.1). Within the UK the number of successful cloud-free scenes varies. For example, 16 successful retrievals are found for the London area during this period of observation.

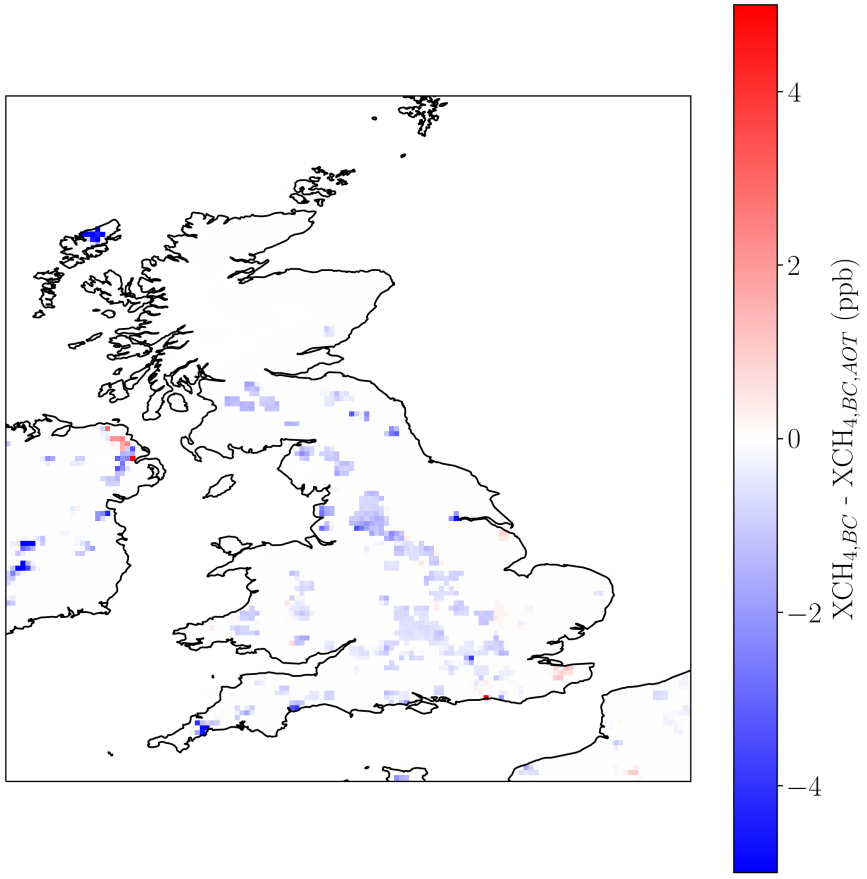


Figure 6.4: Difference between XCH_4 bias-corrected product with filtering for aerosol optical thickness ($XCH_{4BC,AOT}$) and without filtering for aerosol optical thickness (XCH_{4BC}).

6.2.2 Overview of CAMS XCH_4 data products and processing

The CAMS CH_4 global greenhouse gas reanalysis (EGG4) and atmospheric composition forecast data products - as described in Chapter 3, Section 3.5 - use data assimilation with an atmospheric model to produce a consistent data set (Inness et al. 2019; Agustí-Panareda et al. 2019). Partial columns of atmospheric CH_4 from the EGG4 reanalysis product have 60 vertical levels and $0.75^o \times 0.75^o$ horizontal spatial resolution whereas CAMS atmospheric composition forecasts have 137 vertical levels with $0.10^o \times 0.10^o$ horizontal spatial resolution.

CAMS data products corresponding to the eight successful, clear-sky XCH_4 retrievals covering the UK (Table 6.1) are used, with 12:00 UTC CAMS products selected as these are the closest to when local TROPOMI overpasses occur in the UK (13:30 UTC). CAMS data are processed using the HARP Python module and prepared for comparison with TROPOMI XCH_4 as described in Chapter 3, Section 3.5.

6.2.3 Comparing CAMS and TROPOMI XCH_4

Comparison between CAMS XCH_4 products and TROPOMI XCH_4 are made for the individual eight days so any anomalous pixels can be identified and regions in the UK with any significant differences that occur on individual retrievals are not averaged out. Averaged CAMS and TROPOMI XCH_4 data for the eight days in Table 6.1 are also used as a way to represent the UK 2018-2020 averaged XCH_4 data. In this way, UK TROPOMI XCH_4 spatial gradients can be compared to the modelled XCH_4 gradients in CAMS to assess whether small regional differences in CH_4 emissions can be discerned with TROPOMI observations.

Since a negative bias has been previously identified between CAMS XCH_4 and other XCH_4 observations (Ramonet et al. 2021; Barré et al. 2021) a +50 ppb adjustment is applied to CAMS XCH_4 so the UK spatial CAMS-TROPOMI differences can be analysed. Additional regional-scale differences could be due to the size of the troposphere in the CAMS reanalysis IFS model, the anthropogenic methane emissions used in the IFS model, or other reasons.

6.2.4 Cross-sectional flux method

Point source methane emissions can be quantified from TROPOMI XCH_4 retrievals by using the cross-sectional flux (CSF) method (White et al. 1976; Mays et al. 2009; Krings et al. 2011; Tratt et al. 2014). The CSF method is applied to any observed plumes emitted from Drax power station in the TROPOMI XCH_4 retrievals.

The CH_4 flux through one or more plume cross-sections orthogonal to the plume direction is calculated based on a mass balance between the source rate, Q, and the product of the effective wind speed (i.e. the spatial average of the wind field), U_{eff}, and the integrated XCH_4 enhancement, $\bar{C}$, perpendicular to the wind direction (Fig. 6.5):

$$Q = \bar{C}U_{\text{eff}}, \quad \text{with } \bar{C} = \frac{1}{N}\sum_{j=1}^{N}\int \Delta\Omega(x_j, y)dy. \tag{6.1}$$

The XCH_4 enhancement, $\Delta\Omega$ (kg m^{-2}), is calculated by using a local background upwind of the source (Fig. 6.5). To calculate the integrated methane column enhancements, a quadrilateral is mapped over the plume enhancement and divided into equally spaced transects orthogonal to the plume direction downwind of the source. Observations along each transect are integrated perpendicular to the wind direction with the transect length defining the integration limits. xt

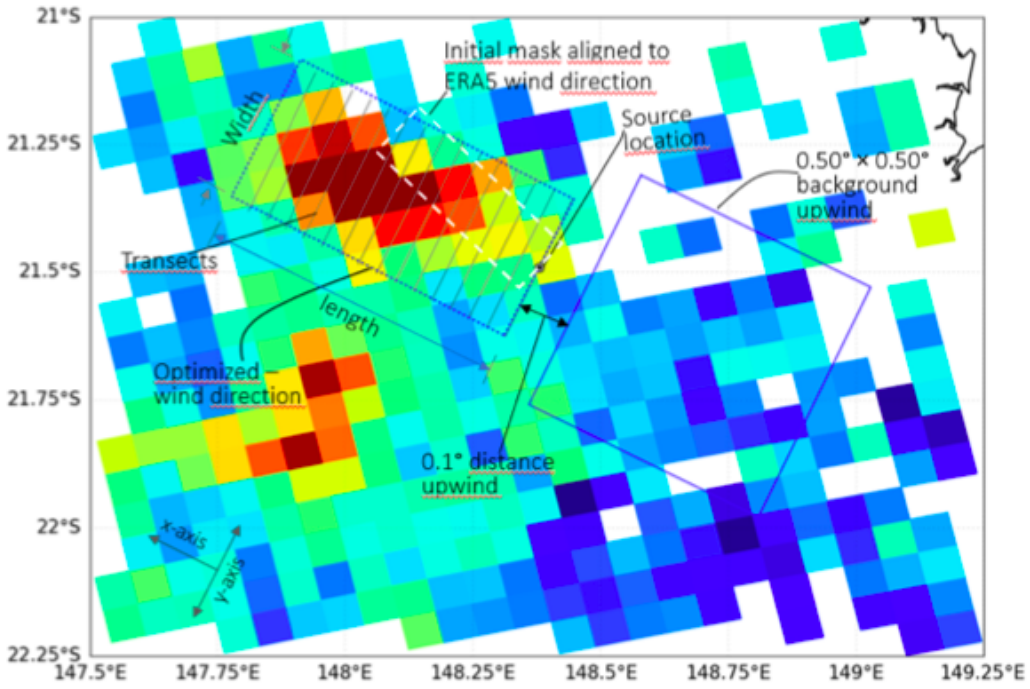


Figure 6.5: Example of the cross-sectional flux method showing the source location (black dot), the upwind background area of $0.5^o \times 0.5^o$ (blue square), initial mask and wind direction (white dotted box), optimized wind direction over the plume (black dotted box), and the transects (grey lines). Figure taken from Sadavarte et al. (2021).

6.3 Results

6.3.1 TROPOMI measurements across the UK

Figure 6.6a shows the 2018-2020 UK XCH_4 averaged values, where a mean XCH_4 value of $1860.4 \pm 10.6(1\sigma)$ ppb is found. The largest averaged TROPOMI XCH_4 values are towards the east midlands and are smallest in north England and across Scotland (Fig. 6.6a).

The spatial distribution of averaged XCH_4 in Fig. 6.6a differs from the spatial distribution of surface CH_4 emissions in NAEI (Fig. 6.6b) that show, for example, a steep emissions gradient between London and its surrounding areas which is not seen in the TROPOMI observations. Where there are low NAEI methane emissions in the east of the UK high XCH_4 are observed in the TROPOMI retrievals. As TROPOMI observations have near-uniform sensitivity throughout the atmospheric column (Jacob et al. 2016) a correlation

between surface emissions and XCH_4 might be expected. Agricultural CH_4 emissions are treated as area sources in NAEI (Ricardo Energy & Environment 2019) and are the largest source of CH_4 emissions in the UK (Fig. 6.6) yet the spatial distribution of agricultural emissions also differs from the distribution of averaged XCH_4 TROPOMI values across the UK (Fig. 6.6).

Figure 6.7a shows the 2018-2020 averaged UK surface albedo and Fig. 6.7b the averaged UK AOT. A higher surface albedo is seen towards the east of the UK, which is also where larger XCH_4 values are observed (Fig. 6.6a). Corresponding surface albedo and XCH_4 values for individual pixels in the UK are plotted in a two-dimensional histogram in Fig. 6.8a which reveals a tight, positive correlation over the range of observed XCH_4. The large XCH_4 values seen in the UK could be due to a bias from the surface albedo that is not entirely corrected for in the TROPOMI bias-corrected XCH_4 product. Similarly, corresponding XCH_4 and AOT values are also plotted as a two-dimensional histogram in Fig. 6.8b but a correlation is not observed.

Figure 6.7c shows the number of clear-sky, high-quality retrievals obtained for each pixel over the UK between 2018-2020. On average, 23 retrievals are obtained per pixel with the number of successful retrievals per pixel ranging from 0 to 69 across the UK. A larger number of retrievals per pixel are found in the south of the UK. For example, the London area has an average of 36 clear-sky retrievals per pixel. The area south of London has the largest number of average retrievals per pixel in the UK with an average of 57 retrievals per pixel. An average

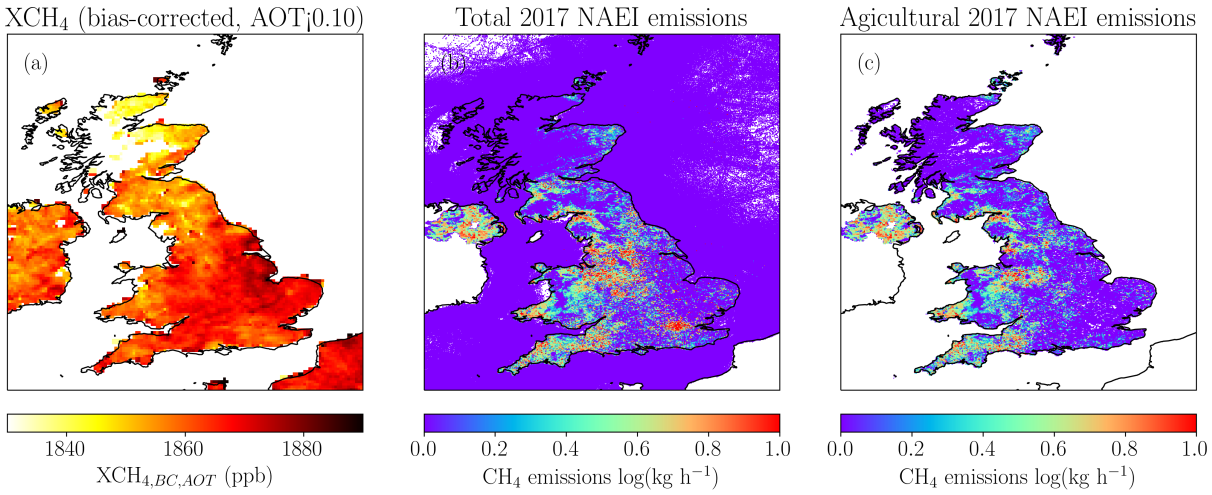


Figure 6.6: (a) TROPOMI averaged XCH_4, (b) total methane NAEI emissions for the year 2017 and (c) agricultural NAEI methane emissions for the year 2017.

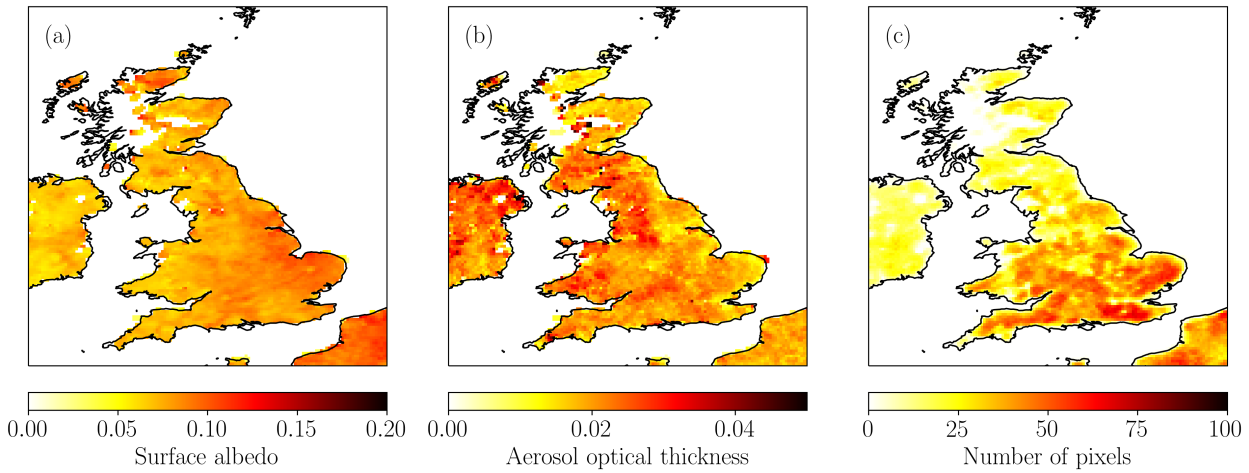


Figure 6.7: UK 2018-2020 averaged TROPOMI (a) surface albedo, (b) aerosol optical thickness (AOT) values and (c) the number of retrievals for each pixel over 2018-2020.

retrieval success rate of 2.98% is calculated for clear-sky scenes in the UK over this period and 4.66% is calculated for London across this period. Comparing the TROPOMI retrieval success rate for the UK with other TROPOMI studies in different locations suggests the retrieval rate is low for the UK. Sadavarte et al. (2021) obtained a retrieval success rate of 5.5% – 9.3% for TROPOMI XCH_4 measurements of coal mines in Queensland, Australia between June 2018 and December 2019. Gouw et al. (2020) found 45.8% of TROPOMI measurements over the Permian Basin in Texas between December 2018-March 2019 could be used. TROPOMI retrievals between December 2018-February 2019, June 2019-August 2019 used to quantify emissions from cites in USA had retrieval success rates between 3.3% for Kansas City to 34.6% for New York City (Plant et al. 2022).

There are eight cloud-free days in the 2018-2020 observation period where TROPOMI XCH_4 values cover most of the UK with a high pixel density (Table 6.1), which corresponds to 1.1% of all retrievals from this period. An average XCH_4 of 1858.7 ppb is found across the UK for these days with XCH_4 values smallest on 27 June 2019 ($1848.2 \pm 11.9(1\sigma)$ ppb) and largest on 21 September 2020 ($1877.1 \pm 10.5(1\sigma)$ ppb). Figures 6.9-6.16 show XCH_4, surface albedo and AOT observations for these individual days. The retrieval on 15 February 2019 (Fig. 6.9) shows lower XCH_4 values in the west of the UK correspond with higher AOT values for the same pixels. Similarly, lower XCH_4 values on the 27 June 2019 correspond with higher AOT values in the southwest UK (Fig. 6.11).

Larger XCH_4 values are consistently seen in the northeast UK, which for some days (e.g. 17 and 21 September 2020) correspond with higher surface albedo values. The retrieval on 6 May 2020 (Fig. 6.14) shows large

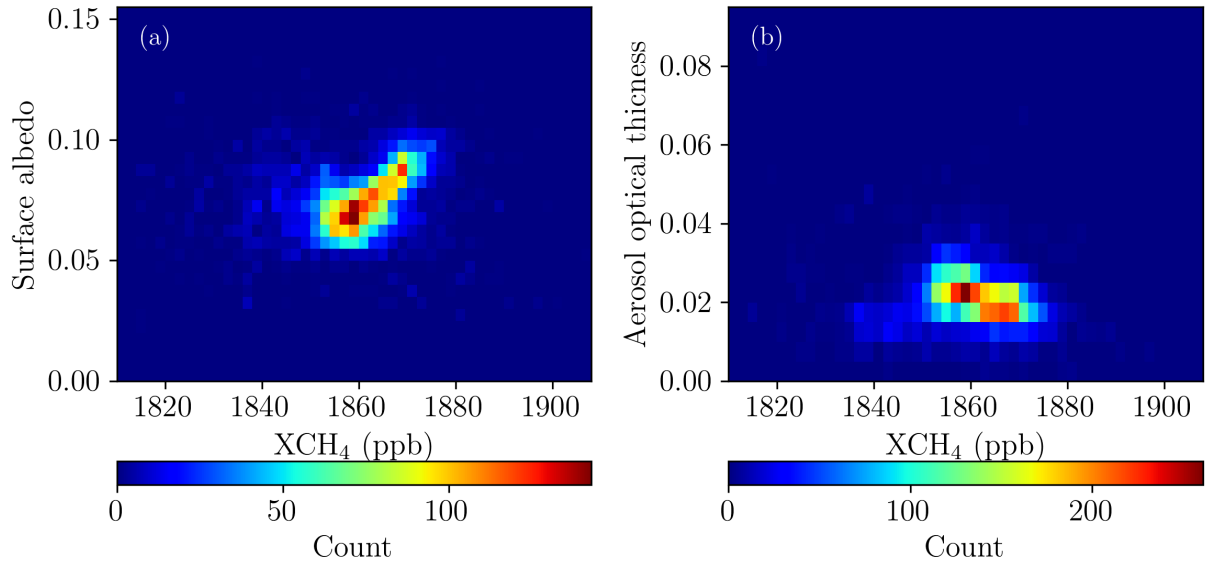


Figure 6.8: Two-dimensional histograms of TROPOMI 2018-2020 averaged a) XCH_4-surface albedo and b) XCH_4-AOT for over the UK.

XCH_4 values in the south which are not correlated with the surface albedo or AOT values on this day suggesting a large pollution event may have occurred.

Stripes in TROPOMI's direction of travel (running from south to north of the UK) are also observed in the individual UK XCH_4 overpasses (Fig. 6.9-6.16). Pixels along the stripes could potentially have erroneous XCH_4 values, likely due to swath position-dependent calibration inaccuracies (Hasecamp et al. 2019).

Surface albedo-XCH_4 two-dimensional histograms (Fig. 6.17) and AOT-XCH_4 two-dimensional histograms (Fig. 6.18) for the dates in Table 6.1 are analysed for correlations on individual overpasses. In contrast to Fig. 6.8a, a correlation between surface albedo and XCH_4 is not always observed. Retrievals on 26 February (Fig. 6.17b), 20 April 2020 (Fig. 6.17d), 17 September (Fig. 6.17g) and 21 September (Fig. 6.17h) show a slight positive correlation between surface albedo and XCH_4 but not as strong as in Fig. 6.8a. Only some days show a correlation between AOT and XCH_4; with a slightly negative correlation seen on 15 February 2019 (Fig. 6.18a) and 21 April 2020 (Fig. 6.18e), but a slightly positive correlation observed on 20 April 2020 (Fig. 6.18d). This implies AOT has an inconsistent impact on the TROPOMI UK XCH_4 values on individual days.

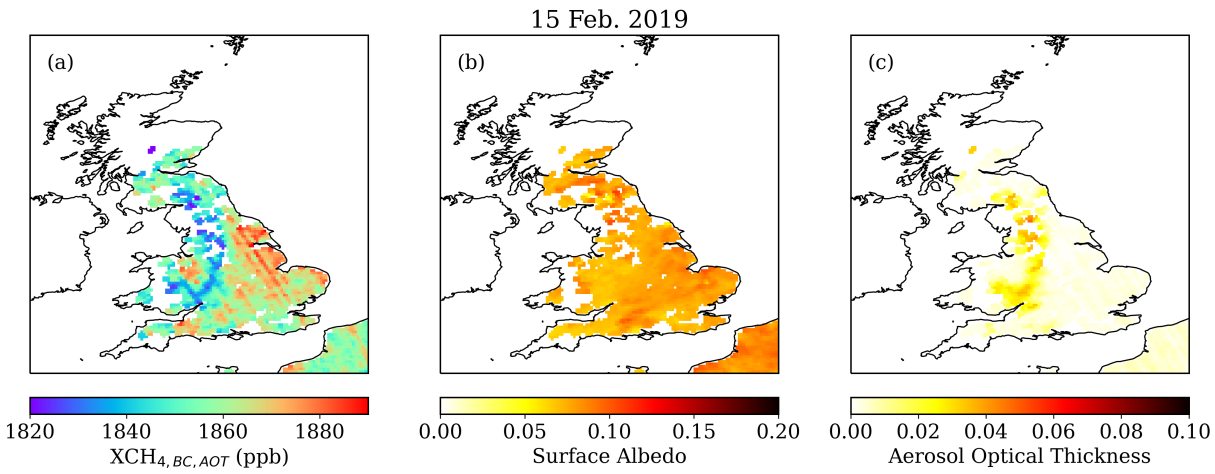


Figure 6.9: TROPOMI XCH_4, surface albedo, AOT data products for 15 February 2019.

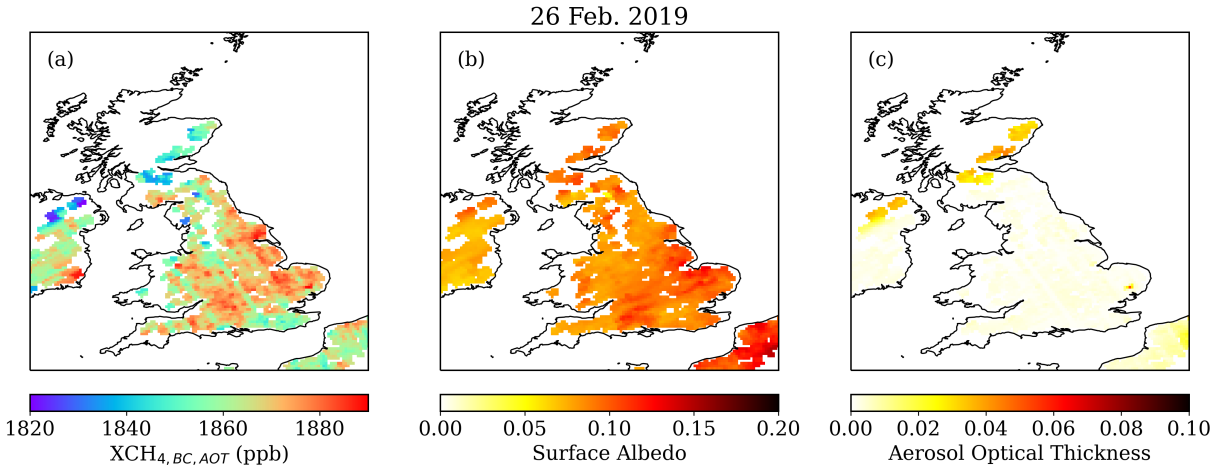


Figure 6.10: TROPOMI XCH_4, surface albedo, AOT data products for 26 February 2019.

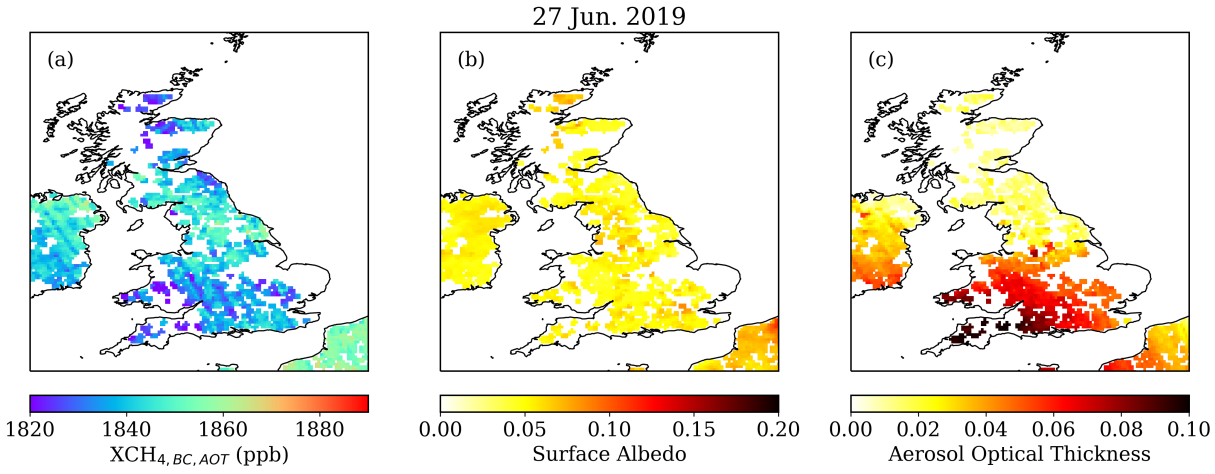


Figure 6.11: TROPOMI XCH_4, surface albedo, AOT data products for 27 June 2019.

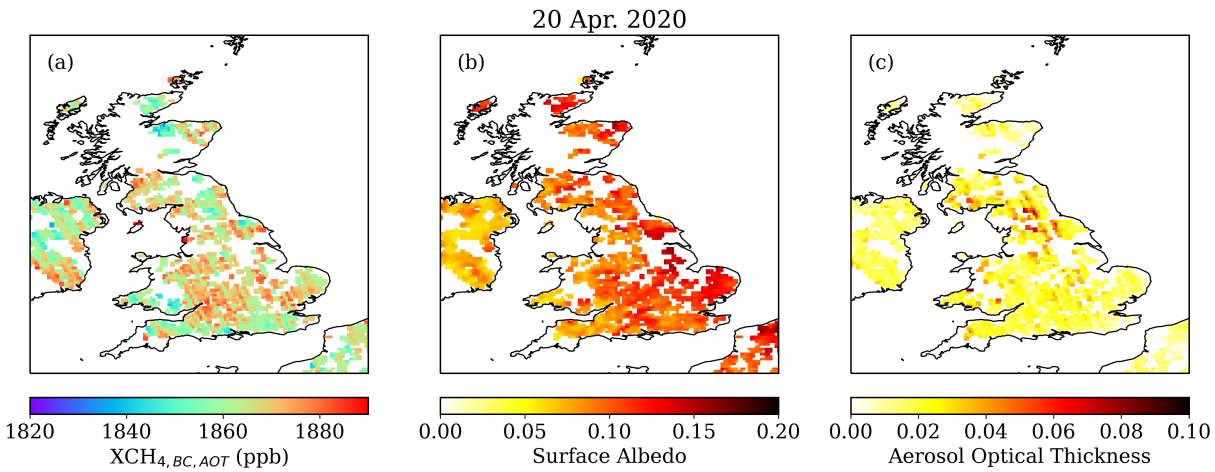


Figure 6.12: TROPOMI XCH_4, surface albedo, AOT data products for 20 April 2020.

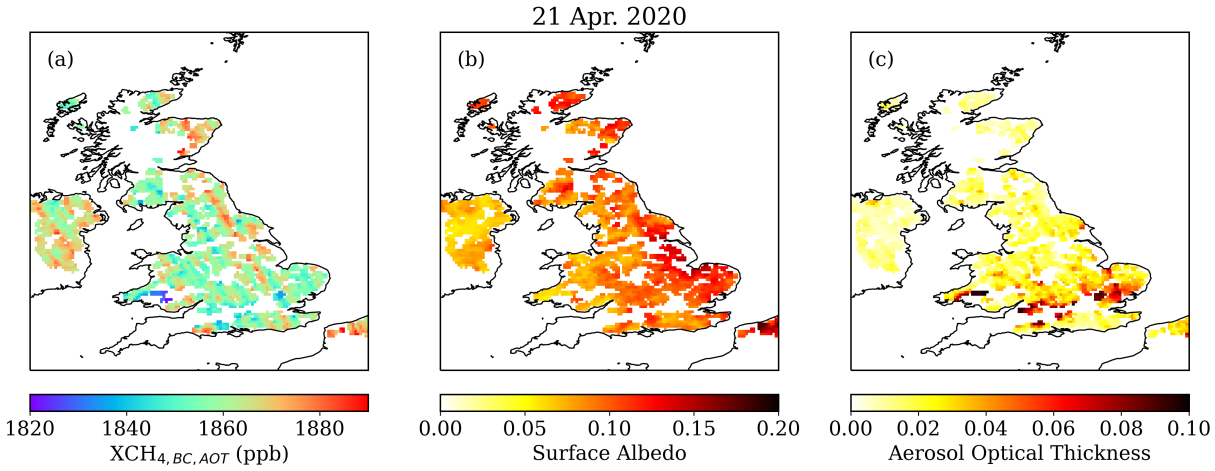


Figure 6.13: TROPOMI XCH_4, surface albedo, AOT data products for 21 April 2020.

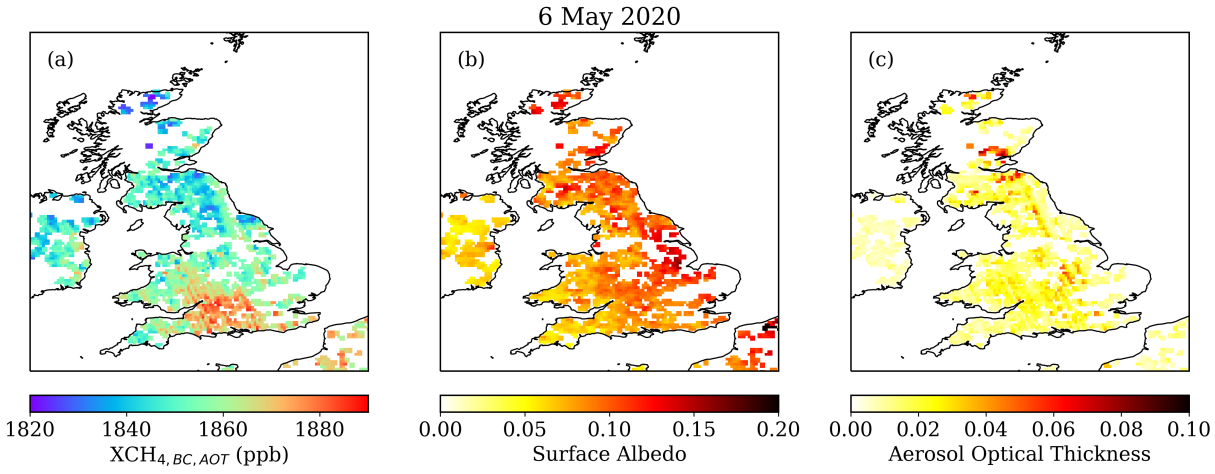


Figure 6.14: TROPOMI XCH_4, surface albedo, AOT data products for 6 May 2020.

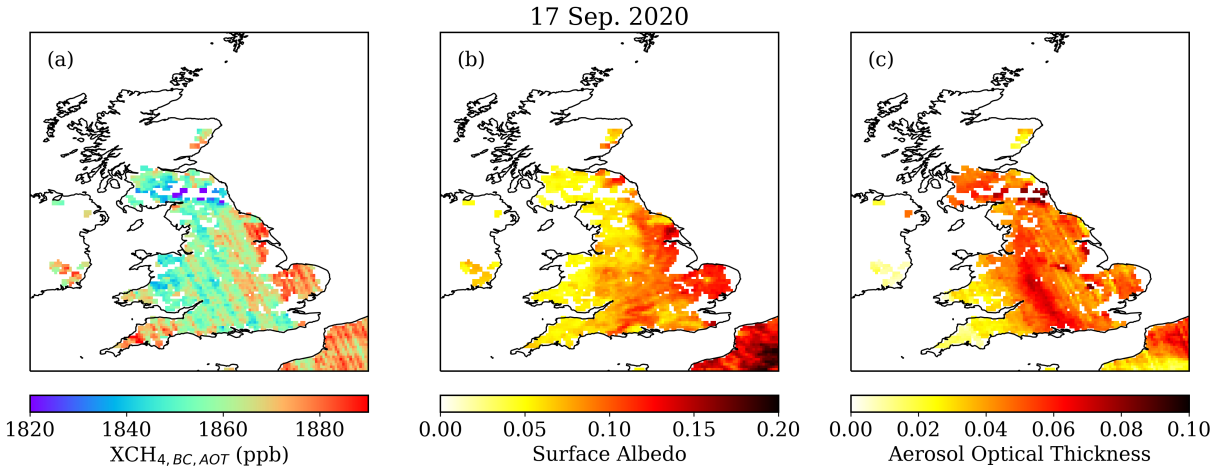


Figure 6.15: TROPOMI XCH_4, surface albedo, AOT data products for 17 September 2020.

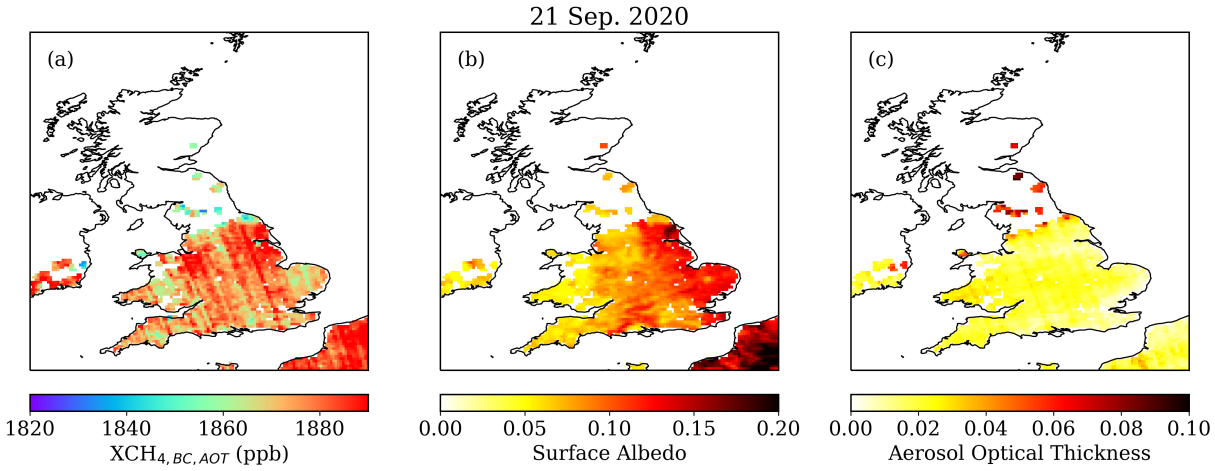


Figure 6.16: TROPOMI XCH_4, surface albedo, AOT data products for 21 September 2020.

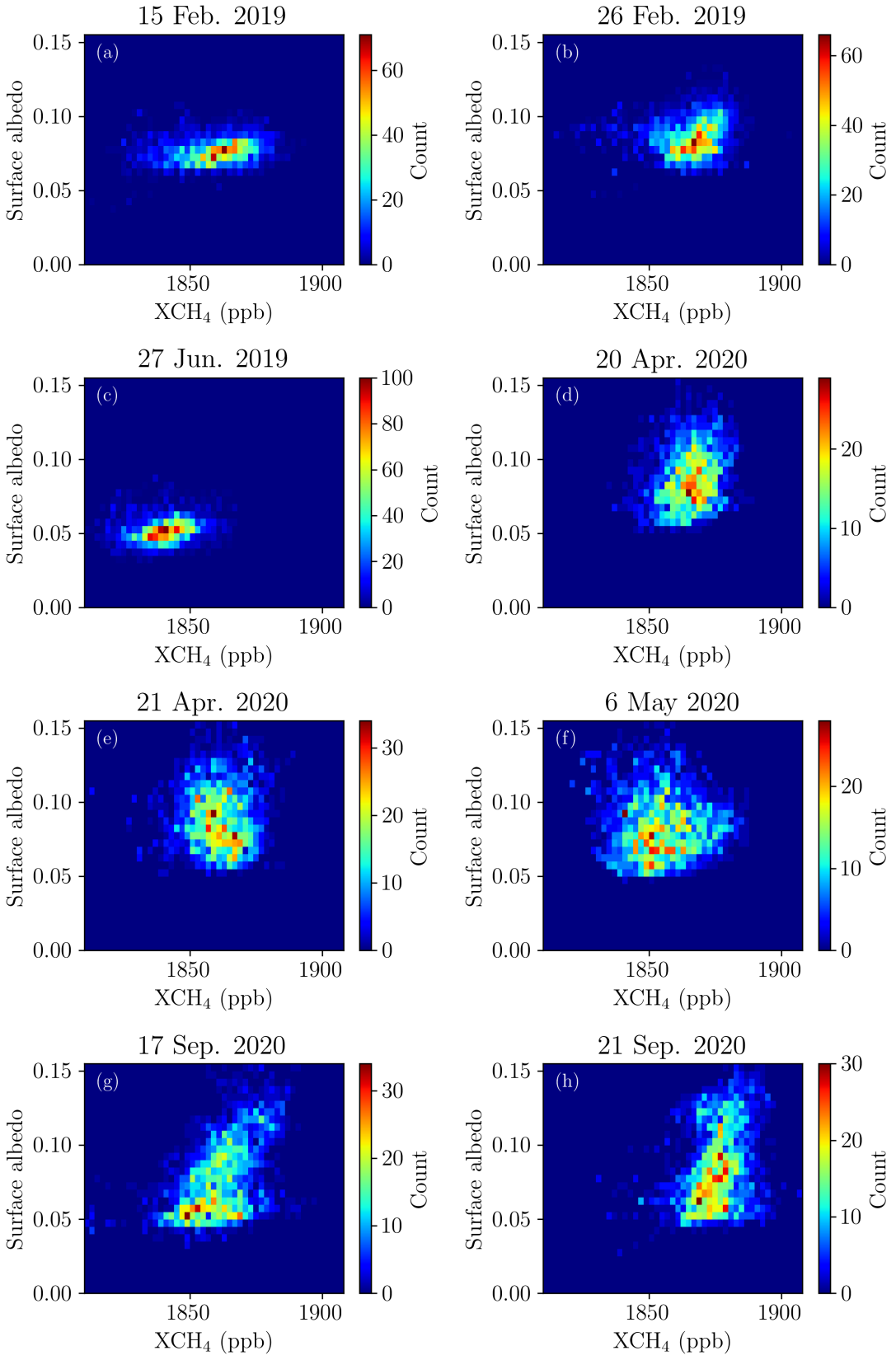


Figure 6.17: Two-dimensional histograms of TROPOMI XCH_4-surface albedo for individual days with clear-sky scenes over the UK.

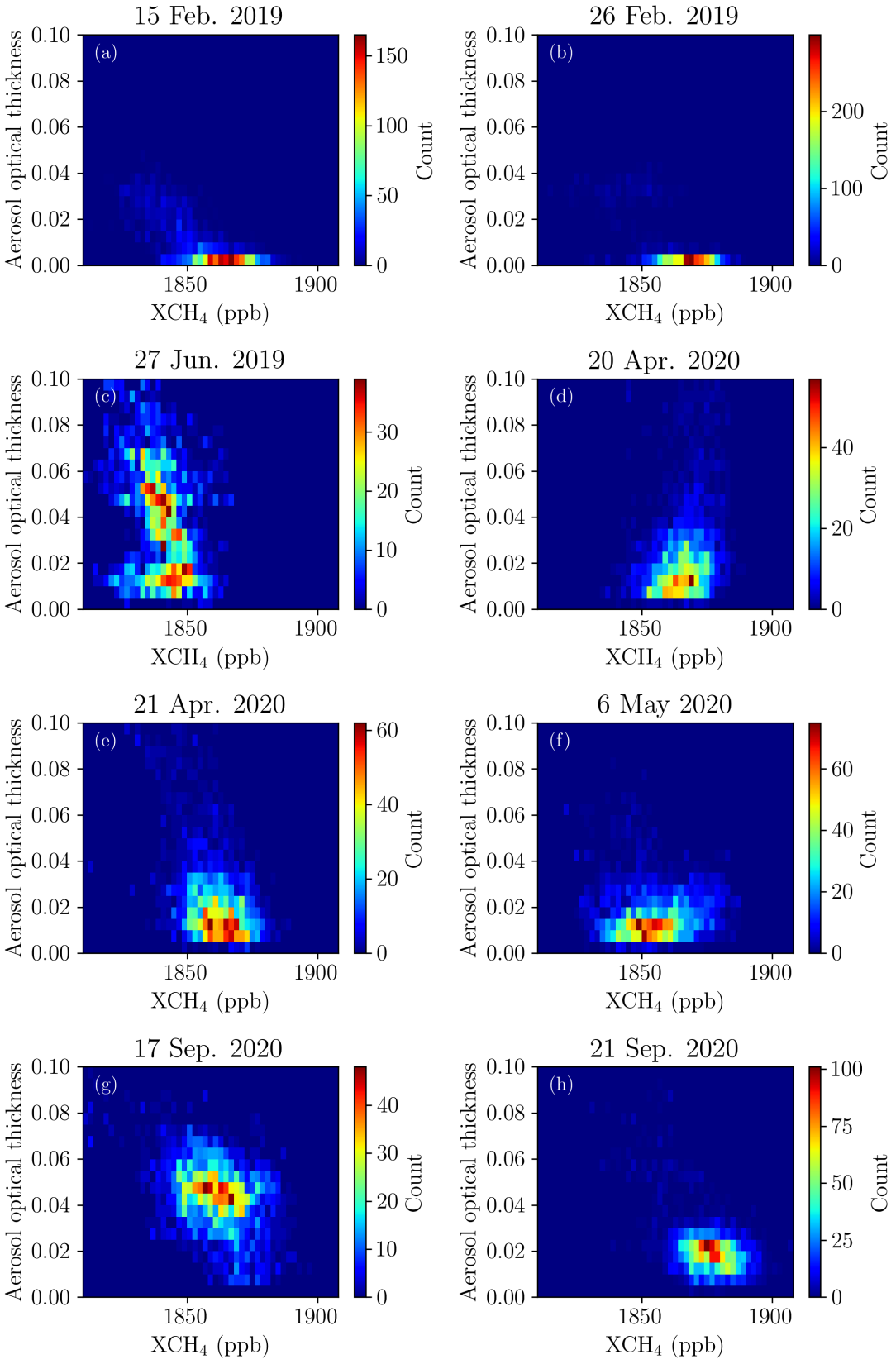


Figure 6.18: Two-dimensional histograms of TROPOMI XCH_4-AOT for individual days with clear-sky scenes over the UK.

Table 6.1: TROPOMI mean XCH_4, surface albedo and AOT for eight individual dates in 2018-2020 with UK-wide clear-sky scenes.

Date	TROPOMI XCH_4 mean (ppb)	Surface albedo mean	AOT mean
15/2/2019	$1850.6 \pm 13.5(1\sigma)$	$0.08 \pm 0.01(1\sigma)$	$0.01 \pm 0.01(1\sigma)$
26/2/2019	$1851.9 \pm 19.2(1\sigma)$	$0.09 \pm 0.02(1\sigma)$	$0.02 \pm 0.02(1\sigma)$
27/6/2019	$1848.2 \pm 11.9(1\sigma)$	$0.06 \pm 0.02(1\sigma)$	$0.02 \pm 0.01(1\sigma)$
20/4/2020	$1859.3 \pm 11.2(1\sigma)$	$0.10 \pm 0.03(1\sigma)$	$0.02 \pm 0.01(1\sigma)$
21/4/2020	$1861.0 \pm 10.0(1\sigma)$	$0.10 \pm 0.03(1\sigma)$	$0.02 \pm 0.01(1\sigma)$
06/5/2020	$1855.8 \pm 10.8(1\sigma)$	$0.09 \pm 0.03(1\sigma)$	$0.01 \pm 0.01(1\sigma)$
17/9/2020	$1865.8 \pm 11.4(1\sigma)$	$0.10 \pm 0.04(1\sigma)$	$0.04 \pm 0.02(1\sigma)$
21/9/2020	$1877.1 \pm 10.5(1\sigma)$	$0.11 \pm 0.04(1\sigma)$	$0.02 \pm 0.01(1\sigma)$
Average	$1858.7 \pm 9.5(1\sigma)$	$0.09 \pm 0.02(1\sigma)$	$0.02 \pm 0.01(1\sigma)$

6.3.2 CAMS-TROPOMI XCH_4 comparison over the UK

Whilst comparisons of 2018-2020 averaged TROPOMI XCH_4 observations with NAEI CH_4 emissions reveal regional differences across the UK (e.g. the gradient between London and southeast UK), this comparison does not account for the atmospheric transport of NAEI CH_4 emissions. To better understand the TROPOMI XCH_4 regional gradients observed over the UK, retrievals are compared with CAMS XCH_4 reanalysis and forecasts, which includes the atmospheric transport of surface emissions to model atmospheric XCH_4.

The eight days with UK-wide TROPOMI XCH_4 pixels (Table 6.1) are used for comparison with CAMS XCH_4 data. Figures 6.19–6.26 show the CAMS reanalysis and forecast XCH_4 values for these individual days. Average XCH_4 values for the UK are 1806.3 ppb in the reanalysis and 1806.9 ppb in the forecasts, which is lower than the average XCH_4 value of $1860 \pm 10.6(1\sigma)$ ppb in the TROPOMI measurements (Table 6.1). The corresponding CAMS forecast and reanalysis XCH_4 have similar median values and interquartile ranges over the UK (Table 6.2). Median values differ by less than 6 ppb; except on 17 September 2020 where CAMS reanalysis and forecasts XCH_4 differ by 12.6 ppb. Small differences between CAMS reanalysis and forecast data are not unexpected since the reanalysis product is used as part of the initialisation for the CAMS atmospheric forecast data.

XCH_4 values are similarly distributed across the UK in the CAMS reanalysis and forecasts, but there are more distinct XCH_4 spatial variations in the forecasts data than in the reanalysis data. For example, there are hotspots

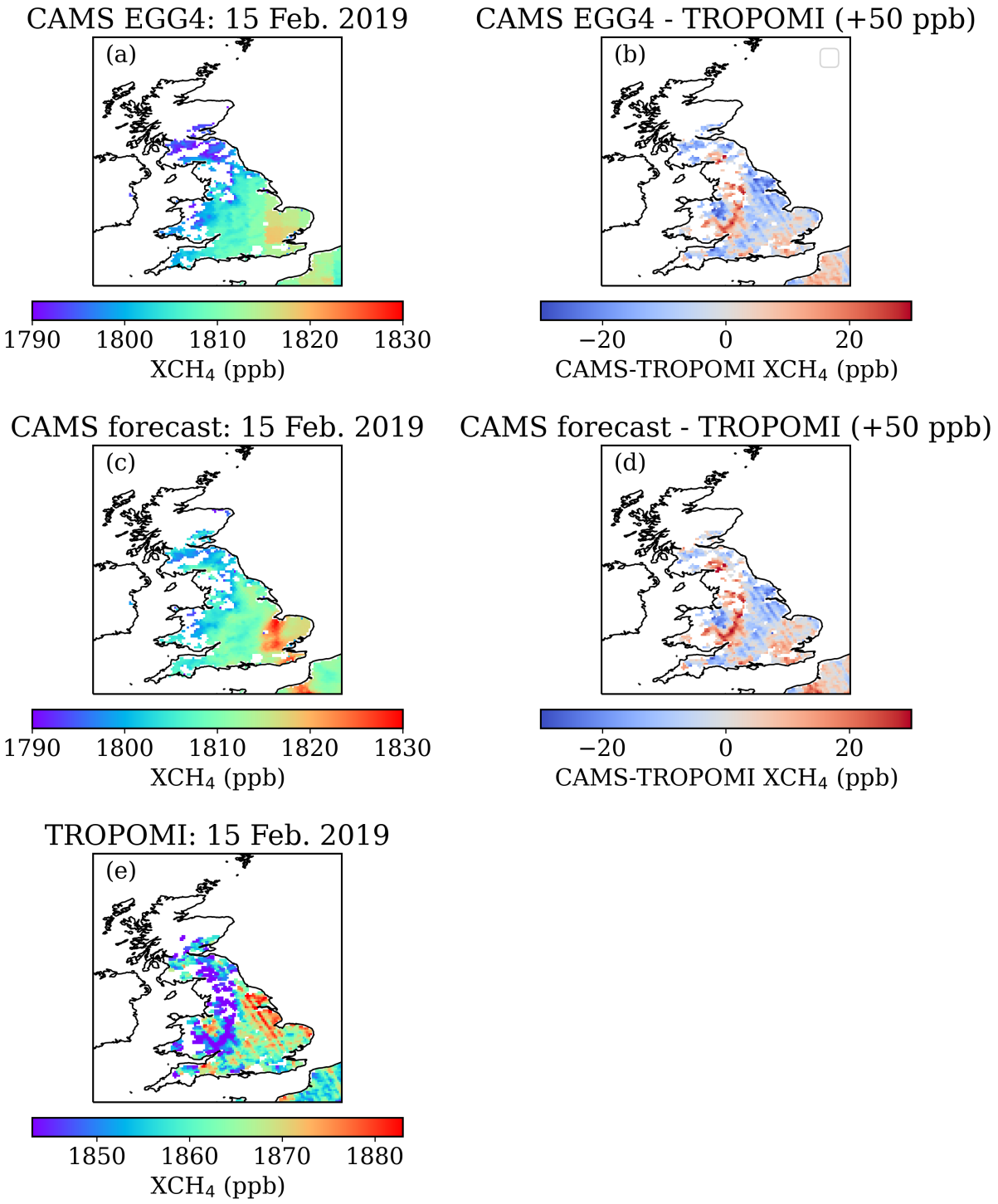


Figure 6.19: (a) CAMS reanalysis (EGG4) XCH_4, (b) CAMS reanalysis - TROPOMI XCH_4, (C) CAMS atmospheric composition forecast XCH_4, (d) CAMS forecast - TROPOMI XCH_4 and (e) TROPOMI XCH_4 for 15 February 2019.

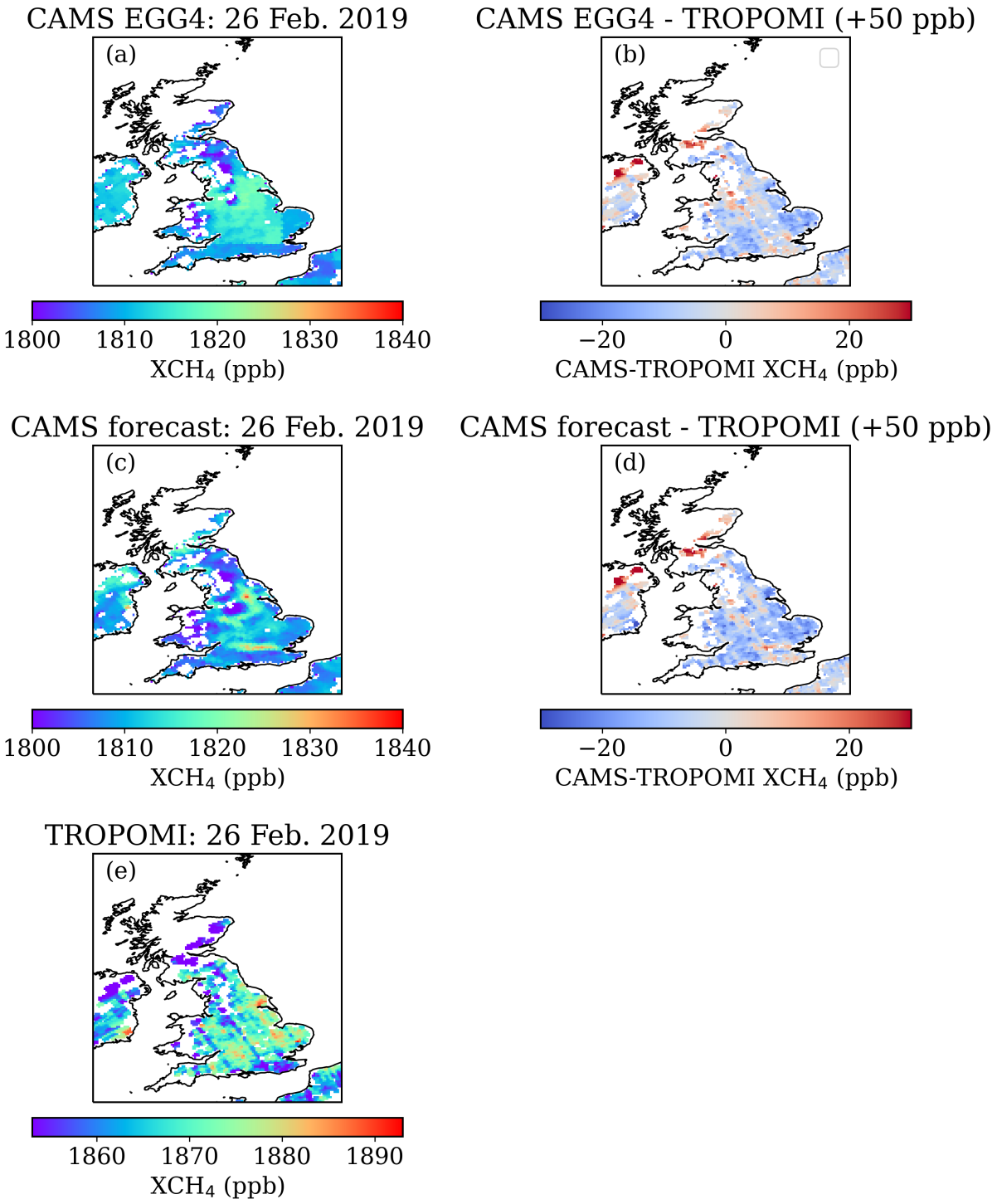


Figure 6.20: (a) CAMS reanalysis (EGG4) XCH_4, (b) CAMS reanalysis - TROPOMI XCH_4, (C) CAMS atmospheric composition forecast XCH_4, (d) CAMS forecast - TROPOMI XCH_4 and (e) TROPOMI XCH_4 for 26 February 2019.

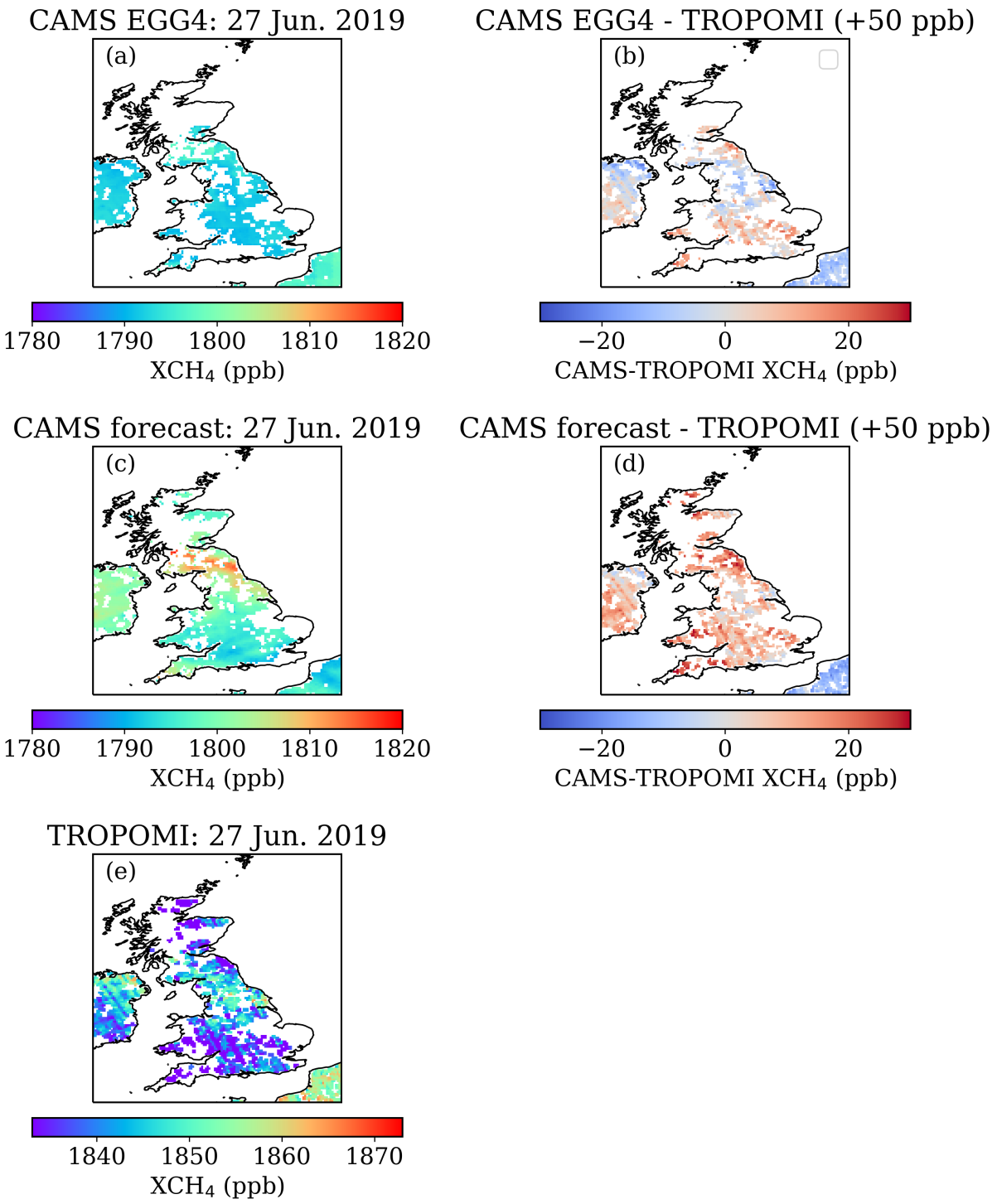


Figure 6.21: (a) CAMS reanalysis (EGG4) XCH_4, (b) CAMS reanalysis - TROPOMI XCH_4, (C) CAMS atmospheric composition forecast XCH_4, (d) CAMS forecast - TROPOMI XCH_4 and (e) TROPOMI XCH_4 for 27 June 2019.

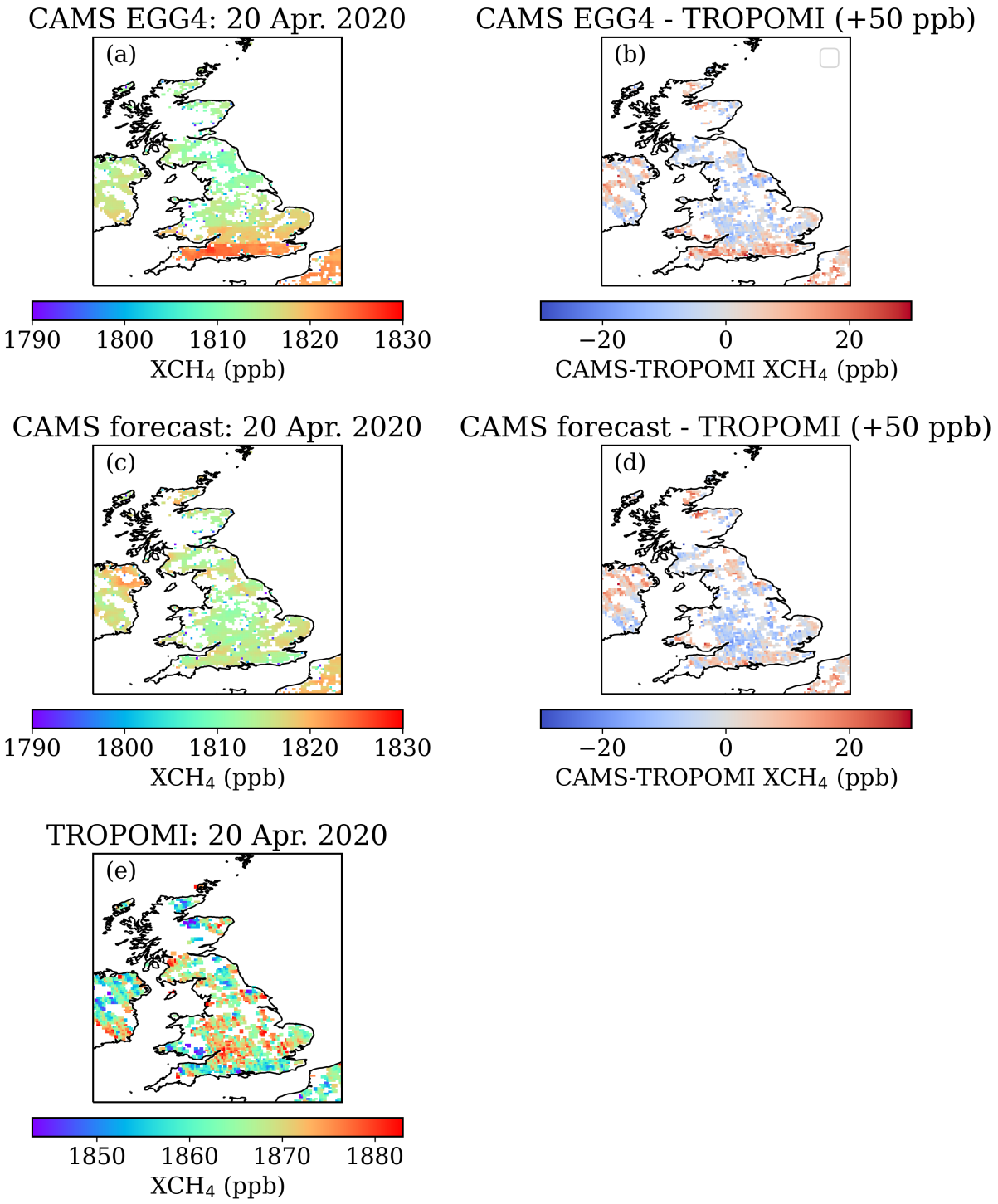


Figure 6.22: (a) CAMS reanalysis (EGG4) XCH_4, (b) CAMS reanalysis - TROPOMI XCH_4, (C) CAMS atmospheric composition forecast XCH_4, (d) CAMS forecast - TROPOMI XCH_4 and (e) TROPOMI XCH_4 for 20 April 2020.

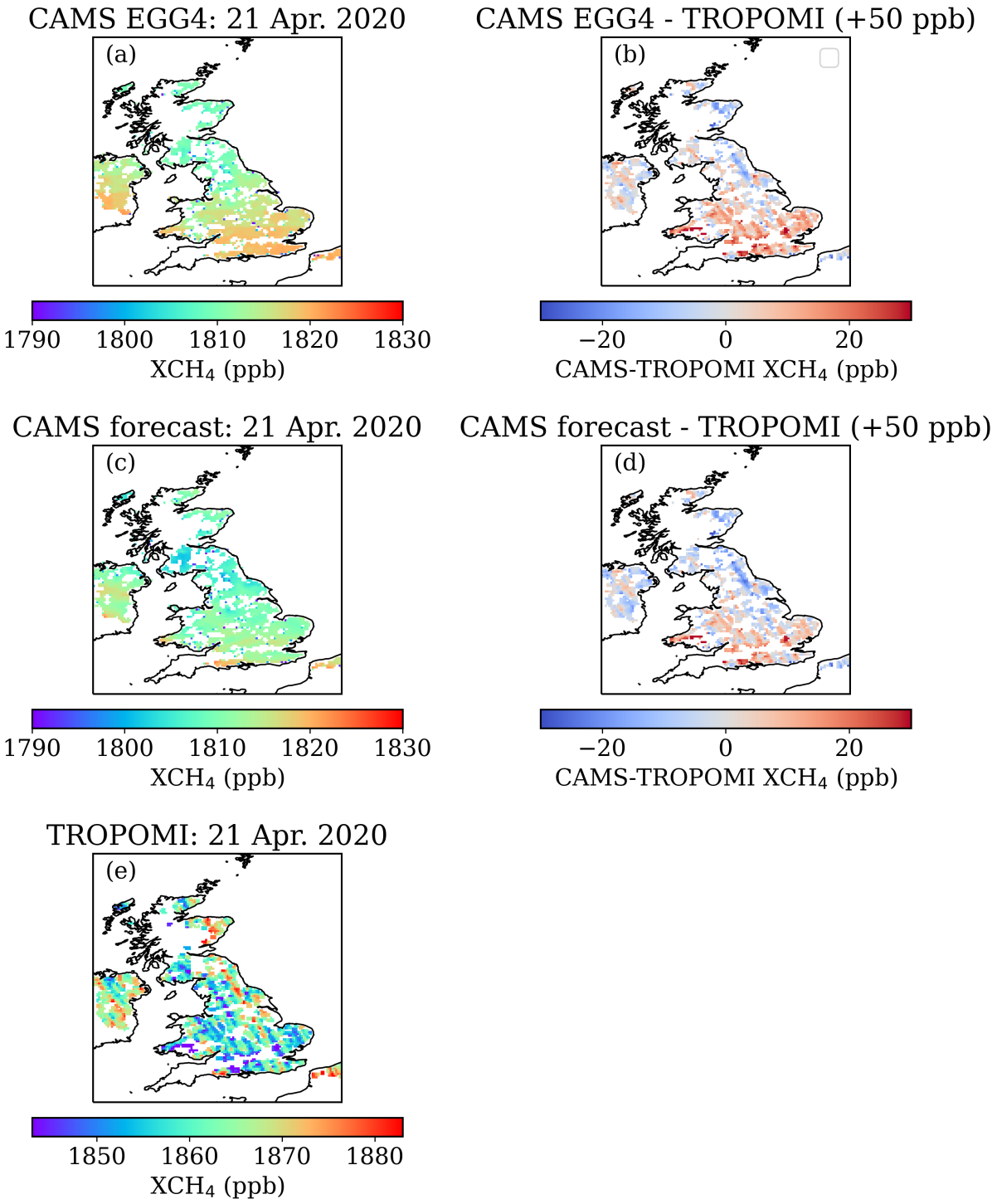


Figure 6.23: (a) CAMS reanalysis (EGG4) XCH_4, (b) CAMS reanalysis - TROPOMI XCH_4, (C) CAMS atmospheric composition forecast XCH_4, (d) CAMS forecast - TROPOMI XCH_4 and (e) TROPOMI XCH_4 for 21 April 2020.

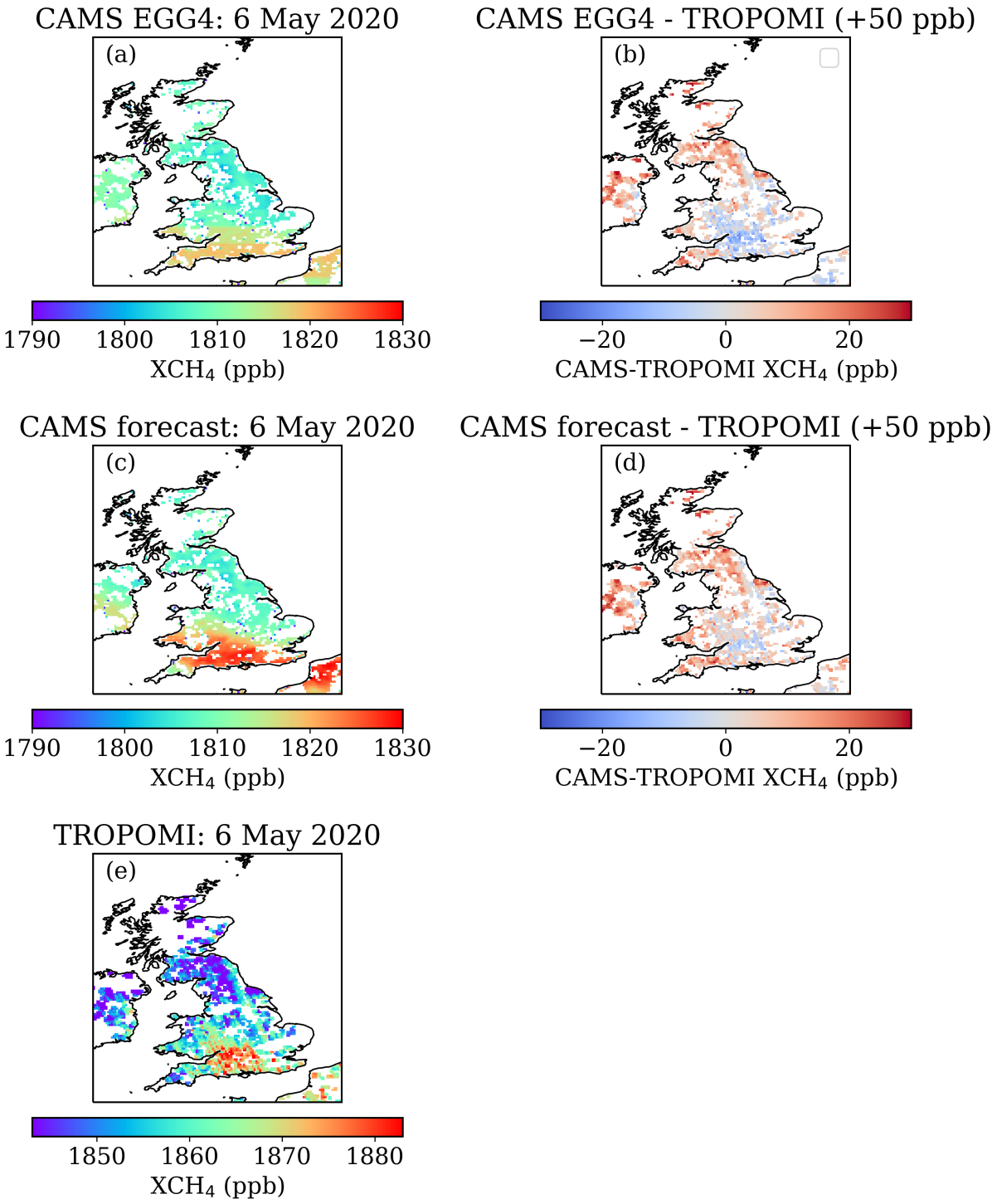


Figure 6.24: (a) CAMS reanalysis (EGG4) XCH_4, (b) CAMS reanalysis - TROPOMI XCH_4, (C) CAMS atmospheric composition forecast XCH_4, (d) CAMS forecast - TROPOMI XCH_4 and (e) TROPOMI XCH_4 for 6 May 2020.

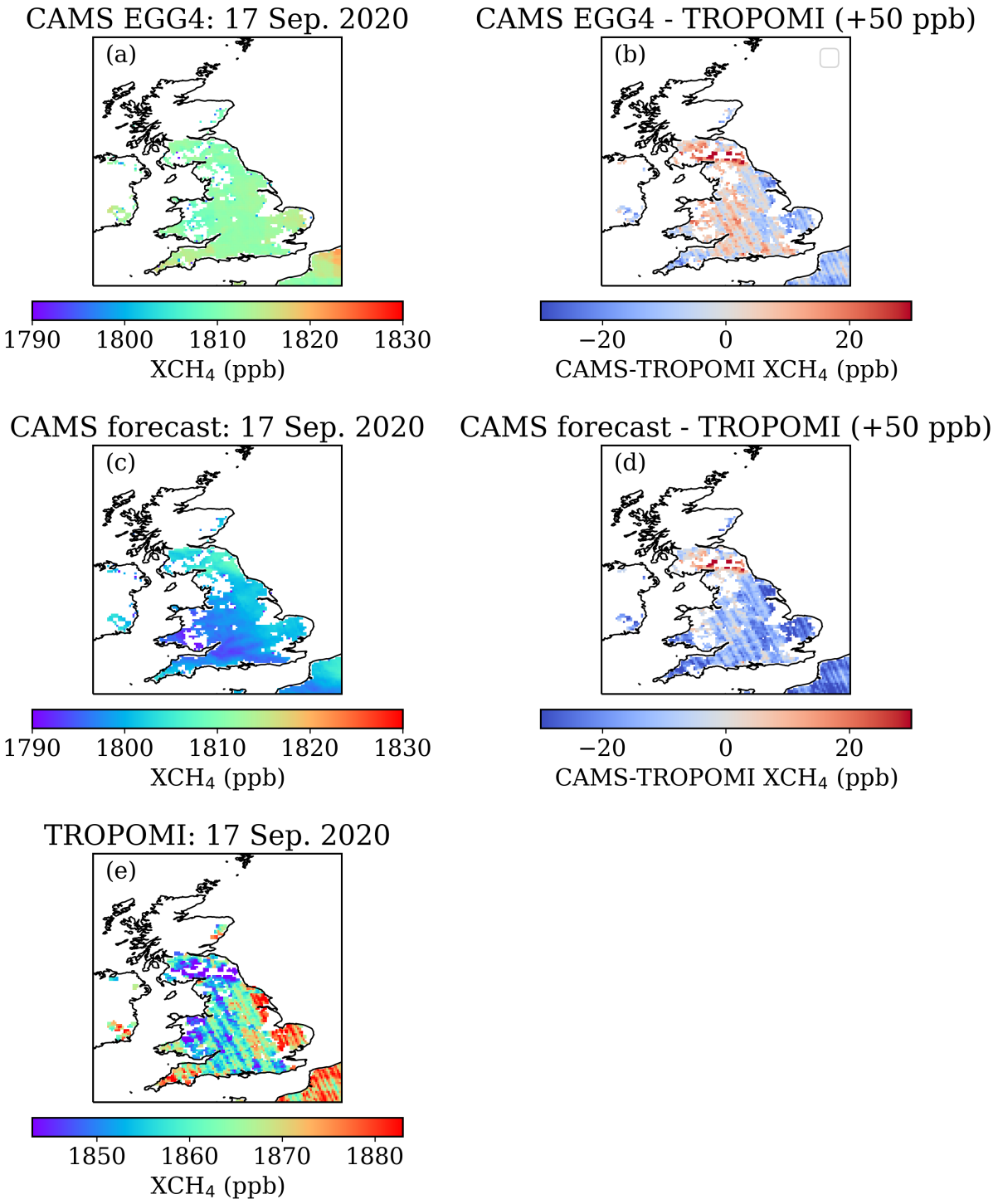


Figure 6.25: (a) CAMS reanalysis (EGG4) XCH_4, (b) CAMS reanalysis - TROPOMI XCH_4, (C) CAMS atmospheric composition forecast XCH_4, (d) CAMS forecast - TROPOMI XCH_4 and (e) TROPOMI XCH_4 for 17 September 2020.

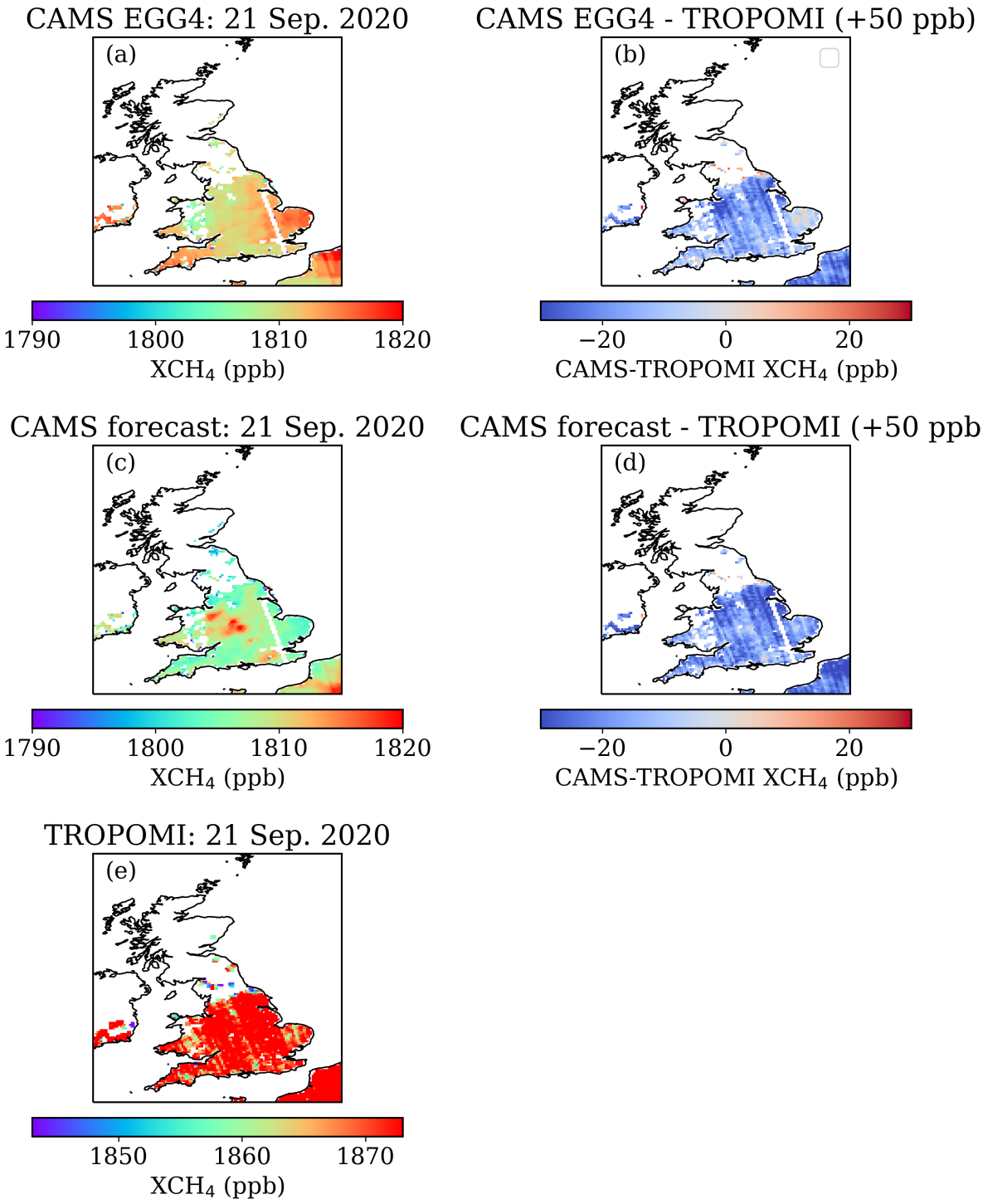


Figure 6.26: (a) CAMS reanalysis (EGG4) XCH_4, (b) CAMS reanalysis - TROPOMI XCH_4, (C) CAMS atmospheric composition forecast XCH_4, (d) CAMS forecast - TROPOMI XCH_4 and (e) TROPOMI XCH_4 for 21 September 2020.

of larger XCH_4 values in the forecasts over smaller areas on 26 February 2019 (Fig. 6.20) and on 21 September 2020 (Fig. 6.26) whereas these larger XCH_4 values are distributed over larger areas in the reanalysis product.

Differences between the CAMS datasets and corresponding TROPOMI XCH_4 values over the UK are also shown in Fig. 6.19–6.26, where a +50 ppb adjustment is applied to account for the underestimation in CAMS XCH_4 since 2019 in the northern hemisphere (Sudarchikova et al. 2021; Ramonet et al. 2021). Adjusted CAMS reanalysis-TROPOMI median differences are between -14.9 ppb to +5.0 ppb (Table 6.3) and CAMS forecast-TROPOMI median differences are between -18.8 ppb and +10.2 ppb (Table 6.3).

Differences between CAMS and TROPOMI XCH_4 vary within certain parts of the UK. Across London, median CAMS-TROPOMI differences are, on average, slightly smaller than the rest of the UK (Table 6.4). Median reanalysis-TROPOMI differences for London on individual days are between -10.9 ppb on 21 September 2020 and +10.9 ppb on 21 April 2019 (Table 6.4). This is similar to the forecast-TROPOMI London median differences, which are between -15.3 ppb on 21 September 2020 and +10.4 ppb on 15 February 2019. CAMS-TROPOMI interquartile ranges across London are $\sim$ 9 ppb for the reanalysis and forecasts, but there are much larger CAMS-TROPOMI interquartile ranges for some days (e.g. 21 April 2019, 17 September 2020; Table 6.4).

Table 6.2: CAMS reanalysis and atmospheric composition forecast XCH_4 median values for the UK. The 25th and 75th percentiles for each day are in the brackets.

Date	CAMS reanalysis median (ppb)	CAMS forecast median (ppb)	reanalysis-forecast (ppb)
15 Feb. 2019	1806.4 (1800.6, 1810.4)	1808.6 (1804.4, 1812.2)	-2.2
26 Feb. 2019	1811.4 (1808.3, 1815.5)	1808.7 (1806.0, 1812.5)	+2.7
27 Jun. 2019	1791.6 (1791.1, 1792.7)	1796.9 (1794.9, 1801.3)	-5.3
20 Apr. 2020	1815.5 (1812.9, 1819.9)	1814.7 (1813.4, 1816.0)	+0.8
21 Apr. 2020	1815.7 (1810.7, 1818.2)	1810.3 (1807.6, 1812.3)	+5.5
6 May 2020	1808.3 (1805.9, 1815.6)	1810.1 (1807.4, 1819.9)	-1.8
17 Sep. 2020	1811.6 (1811.0, 1812.4)	1799.0 (1796.8, 1801.3)	+12.6
21 Sep. 2020	1810.9 (1810.0, 1812.5)	1806.9 (1806.9, 1808.9)	+4.0
Mean	1808.9	1806.9	+1.4

Table 6.3: Median CAMS reanalysis-TROPOMI and CAMS forecast-TROPOMI differences for the UK adjusted by +50 ppb. The 25th and 75th percentiles are in brackets.

Date	CAMS reanalysis-TROPOMI +50 median (ppb)	CAMS forecast-TROPOMI +50 median (ppb)
15 Feb. 2019	-3.9 (-11.0, +3.5)	-1.4 (-8.3, +7.2)
26 Feb. 2019	-6.3 (-11.8, -0.5)	-8.7 (-14.4, -2.3)
27 Jun. 2019	+1.8 (-3.1, +7.3)	+10.2 (+4.8, +15.6)
20 Apr. 2020	-1.3 (-6.9, +5.3)	-2.4 (-8.1, +3.0)
21 Apr. 2020	+5.0 (-2.8, +12.2)	+0.2 (-6.9, +7.1)
6 May 2020	+2.8 (-3.7, +9.0)	+5.9 (+0.9, +11.7)
17 Sep. 2020	+0.2 (-6.6, +6.9)	-12.9 (-19.5, -5.8)
21 Sep. 2020	-14.9 (-20.2, -9.2)	-18.8 (-23.9, -13.6)
Average	-2.1	-3.5
Absolute average	4.5	7.6

Table 6.4: CAMS reanalysis - TROPOMI and CAMS atmospheric composition forecast - TROPOMI XCH_4 median differences for over London. The 25th and 75th percentiles are given in brackets. A +50 ppb adjustment is applied to the values.

Date	CAMS reanalysis-TROPOMI +50 (ppb)	CAMS forecast-TROPOMI +50 (ppb)
15 Feb. 2019	+6.0 (+3.5, +9.2)	+10.4 (+8.5, +12.3)
26 Feb. 2019	-3.2 (-6.5, +3.4)	-3.0 (-9.4, +6.0)
27 Jun. 2019	+5.1 (+0.9, +8.3)	+6.9 (+2.4, +8.6)
20 Apr. 2020	+4.3 (+1.2, +10.5)	+1.1 (-1.6, +4.0)
21 Apr. 2020	+10.9 (+7.9, +19.1)	+6.2 (-0.2, +12.6)
6 May 2020	+2.2 (-1.3, +7.9)	+5.5 (+3.2, +10.4)
17 Sep. 2020	+1.8 (-5.0, +6.7)	-10.4 (-17.8, -6.3)
21 Sep. 2020	-10.9 (-15.6, -7.8)	-15.3 (-19.7, -11.6)
Average	+2.0	+0.2
Absolute average	5.6	7.4

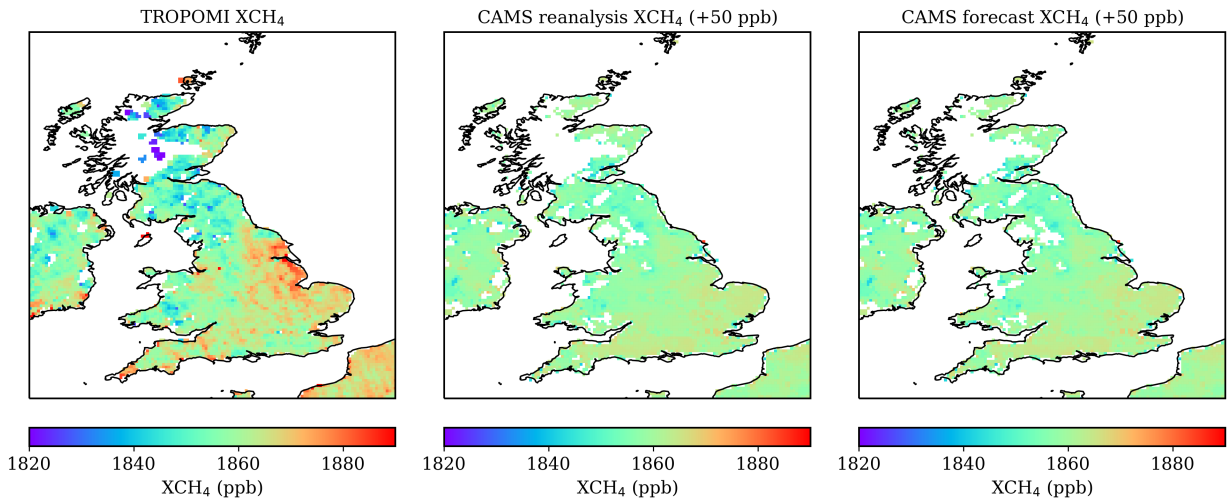


Figure 6.27: Averaged TROPOMI, CAMS reanalysis and CAMS forecast XCH_4 data for the eight days with good UK coverage.

To reduce the influence of the stripes that appear in the individual TROPOMI retrievals the average XCH_4 of the eight days are considered. This is shown in Fig. 6.27 along with the averaged CAMS reanalysis and forecast XCH_4 values. The high XCH_4 feature in the east UK observed in the 2018-2020 averaged TROPOMI XCH_4 is also seen in the averaged eight TROPOMI retrievals but not in the averaged CAMS XCH_4 (Fig. 6.27). The XCH_4 gradient between London and the southeast UK is $\sim$ 5 ppb in the averaged CAMS reanalysis (Fig. 6.27b) and $\sim$ 10 ppb in the averaged CAMS forecasts (Fig. 6.27c). The distinct CH_4 emissions gradient between London and the southeast that is seen in NAEI is diluted by atmospheric transport resulting in average CAMS XCH_4 London-southeast gradients that are smaller than the instrument precision of TROPOMI.

Averaged CAMS forecast-TROPOMI XCH_4 and reanalysis-TROPOMI XCH_4 differences are shown in Fig. 6.28. There are similar CAMS-TROPOMI differences for the CAMS reanalysis and forecasts XCH_4 with most of the differences less than 10 ppb across the UK. However, there are hotspots across the UK with larger discrepancies. For example, there are larger negative differences across the east of the UK and larger positive differences in the Scottish Highlands and near London. Two-dimensional histograms of surface albedo against the CAMS-TROPOMI XCH_4 differences (Fig. 6.29) indicate large negative CAMS-TROPOMI XCH_4 values are linked to higher surface albedo values across the UK. Surface albedo, however, does not explain the lack of observed XCH_4 gradient between London and the southeast, which have positive CAMS-TROPOMI XCH_4

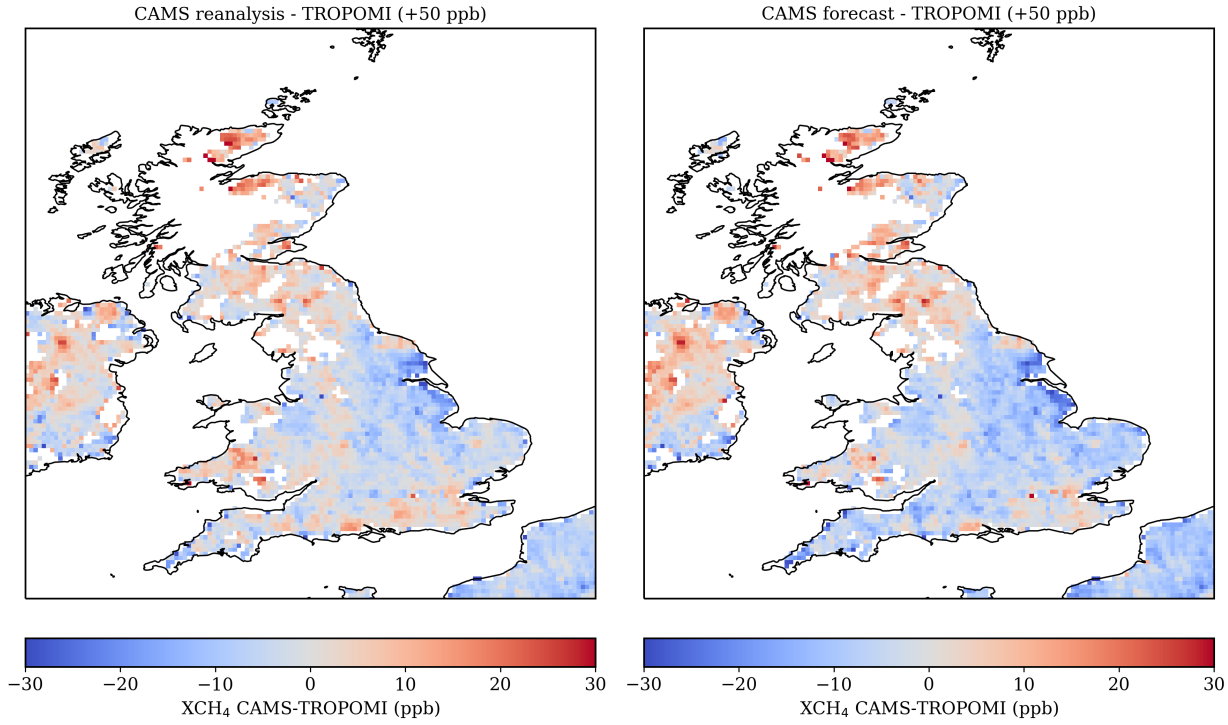


Figure 6.28: Eight-day averaged TROPOMI XCH_4 subtracted from averaged CAMS reanalysis XCH_4 (left panel) and subtracted from CAMS forecast XCH_4 (right panel).

differences (Fig. 6.29).

There are positive correlations in the two-dimensional histograms of AOT against the CAMS-TROPOMI XCH_4 differences (Fig. 6.29). This correlation only occurs for smaller CAMS-TROPOMI XCH_4 differences. For larger CAMS-TROPOMI XCH_4 differences AOT values are more scattered and a correlation is not seen.

The two-dimensional histograms also show most of the CAMS-TROPOMI differences are within ±10 ppb for both the reanalysis and forecast products indicating there is good agreement between the CAMS XCH_4 data products and TROPOMI retrievals across the UK. The larger deviations, as seen, are associated with higher surface albedo values and the AOT also affects CAMS-TROPOMI XCH_4 differences.

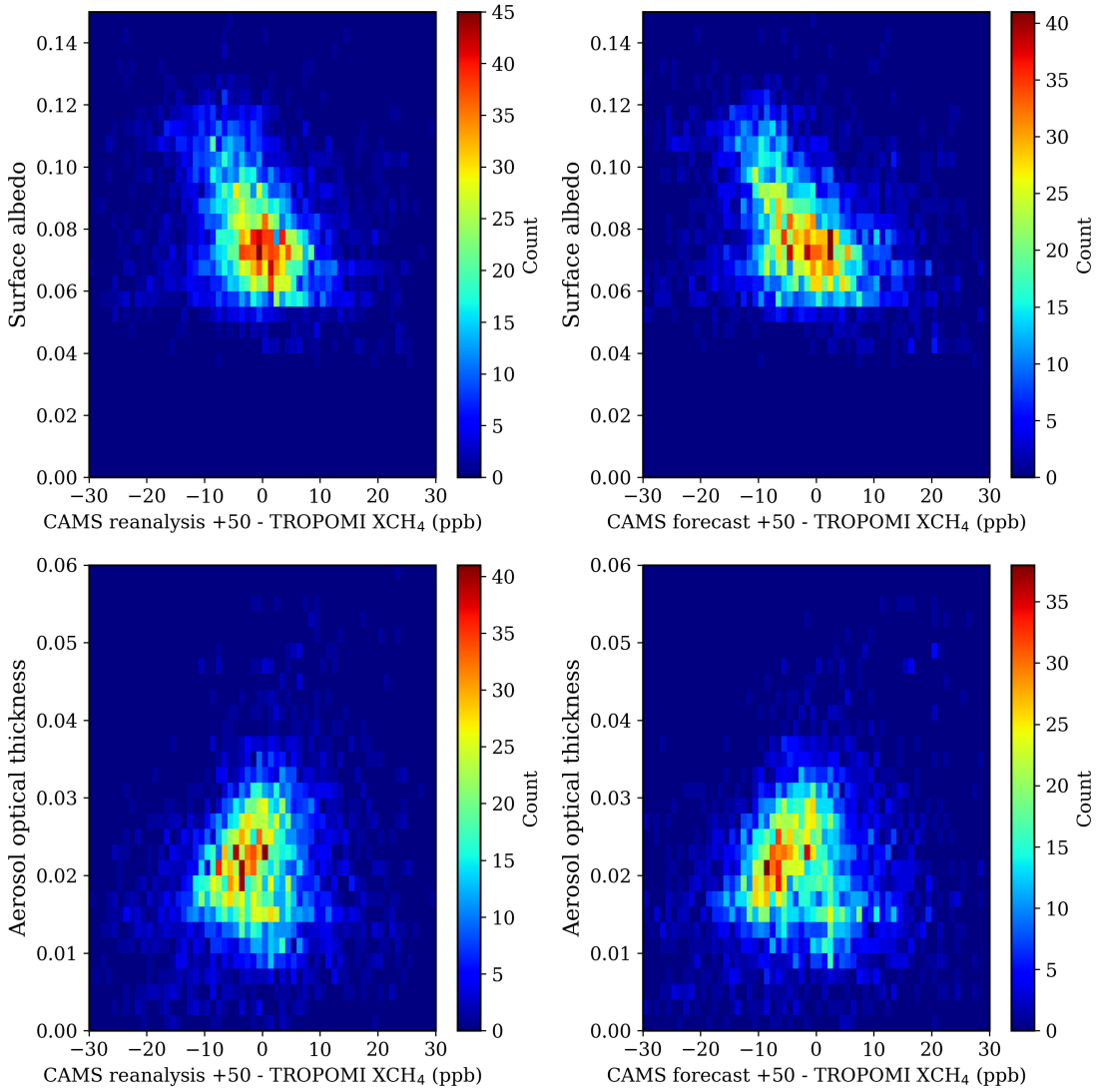


Figure 6.29: Two-dimensional histograms of UK CAMS-TROPOMI XCH_4 differences against surface albedo (top row) and aerosol optical thickness (bottom row). Plots in the first column use CAMS reanalysis data and plots in the second column use CAMS forecast data.

6.3.3 Using TROPOMI measurements to quantify CH_4 emissions from Drax power station

Drax power station is one of the UK's largest CH_4 point source emitters with reported emissions of 3126 t CH_4 yr^{-1}. TROPOMI XCH_4 retrievals from 2019 and 2020 were used to look for distinct plumes coming from Drax power station that could be used to quantify its CH_4 emissions using the CSF approach. Seventeen clear sky TROPOMI retrievals with sufficient pixel coverage to define a local background upwind of the Drax power station were found. Four of these retrievals had higher XCH_4 values in the vicinity of the power station

that could be due to a plume coming from Drax power station. Figure 6.30 shows the XCH_4 retrievals for each of these days with an example of the CSF transects used and the ECMWF ERA5 $0.25^o \times 0.25^o$ wind vectors.

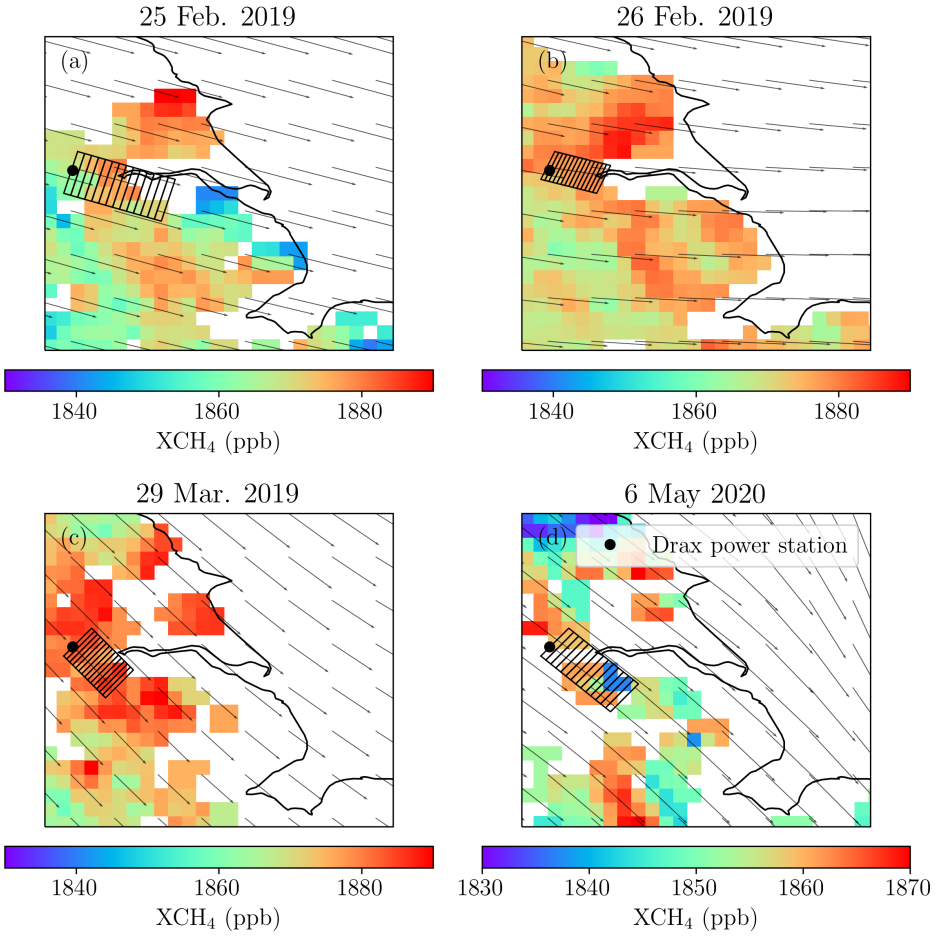


Figure 6.30: TROPOMI XCH_4 retrievals in the vicinity of Drax power station (black marker) with ERA5 wind data and a typical plume transect used for calculating Drax power station emissions.

For each of these days the higher XCH_4 values that were thought to have been plumes coming from Drax power station did not align with the wind vectors. The higher XCH_4 values observed on the 6 May 2020 retrieval were upwind of Drax power station (Fig. 6.30d). Satisfactory plumes coming from Drax power station are therefore not visible in the TROPOMI retrievals and emissions from Drax may be too small to be accurately quantified with TROPOMI XCH_4 observations. This is not unexpected since the reported emissions from Drax power station are lower than the TROPOMI detection threshold (Jacob et al. 2016). Higher XCH_4 values in the retrievals that are in the vicinity of Drax power station could potentially have erroneous pixel

values due to stripes in the flight direction of TROPOMI, which are close to Drax.

6.4 Discussion

TROPOMI XCH_4 measurements that met the data quality standards imposed yielded an average retrieval success rate of 2.98% for the UK and 4.66% for London. Compared to other TROPOMI XCH_4 studies (e.g. Gouw et al. 2020; Plant et al. 2022; Varon et al. 2019), UK data coverage is substantially lower. TROPOMI is therefore currently not that useful for regular monitoring of XCH_4 across the UK but retrievals could be used to complement ground-based measurements from the UK network.

Stripes in the individual retrievals and a strong positive correlation of XCH_4 with surface albedo mean erroneous XCH_4 pixels are still present in the bias-corrected UK TROPOMI XCH_4 retrievals; despite the data quality filtering imposed. There is potential for false interpretations of spatial patterns and magnitudes of UK XCH_4 to be made, with larger XCH_4 values possibly being mistaken for plumes. Other studies that have used TROPOMI to quantify methane emissions from point sources (e.g. Sadavarte et al. 2021; Varon et al. 2019; Pandey et al. 2019) and cities (e.g. Plant et al. 2022) found emissions inferred from TROPOMI were substantially larger than reported in regional emission inventories. Some of the TROPOMI-inferred and emission inventory differences could be due to bias introduced by surface albedo that is not removed in the bias-corrected TROPOMI product.

Individual retrievals also showed a correlation between higher aerosol optical thickness values and lower XCH_4 values in some of the retrievals, but the correlation between aerosol optical thickness and XCH_4 is weaker than between surface albedo and XCH_4.

In general, there is good agreement between the UK TROPOMI XCH_4 and adjusted CAMS reanalysis and forecast XCH_4 with most of the differences within ±10 ppb. Larger CAMS-TROPOMI differences of 10-20 ppb coincided with TROPOMI pixels in regions with higher surface albedo. The modelled XCH_4 in CAMS therefore capture most of the spatial patterns of TROPOMI XCH_4, which have small gradients across the UK.

Averaged CAMS XCH_4 suggest a gradient of 5-10 ppb between London and its surrounding areas, which is smaller than the TROPOMI instrument precision (Hu et al. 2018b). This explains the lack of observed XCH_4 gradient between London and the southeast in the TROPOMI retrievals. London methane emissions

are reported at 0.1 Tg CH_4 yr^{-1} in the 2012 EDGAR v4.3.2 inventory, which when used to simulate CH_4 concentrations are in good agreement with atmospheric CH_4 measurements at ICL (Chapter 4; Saboya et al. 2022).

Methane emission EDGAR v5.0 inventory estimates for eight US cities assessed by Plant et al. (2022) were less than 0.1 Tg CH_4 yr^{-1}, except for New York City which had reported emissions of 0.16 Tg CH_4 yr^{-1}. Plant et al. (2022) used TROPOMI bias-corrected retrievals to quantify CH_4 emissions from these cities, which were found to be on average 0.12 Tg CH_4 yr^{-1} (or $\sim$ 70%) higher than reported in the inventories. Surface albedo bias could, however, lead to higher emissions being quantified at these cities. TROPOMI-inferred methane emissions from Baltimore, Kansas City and Portland were still less than 0.1 Tg CH_4 yr^{-1} and average XCH_4 enhancements of less than 1 ppb were found. These results suggest that either it could be possible to use TROPOMI XCH_4 to quantify London emissions, which has a similar methane emissions rate, or that the signal in the TROPOMI retrievals used to quantify emissions for Baltimore, Kansas City and Portland are too low.

Plumes from Drax power station (one of the highest emitting methane point sources in the UK) were not detected in TROPOMI XCH_4 retrievals. This is not unexpected since the reported emissions rate in NAEI is smaller than the detection threshold of TROPOMI (Hu et al. 2018b). Previous studies that used TROPOMI to quantify emissions using the CSF approach targeted point sources that had higher emission rates than Drax power station. Varon et al. (2019) calculated emissions in the range 9.9 ± 6.8 t CH_4 h^{-1} to 43.3 ± 12.0 t CH_4 h^{-1} from a compressor station in western Turkmenistan using retrievals from both TROPOMI and GHGSat-D. Sadavarte et al. (2021) found emissions from coal mines in Queensland, Australia were nearly seven times larger in TROPOMI than reported in the EDGAR v4.3.2 2012 emission inventory. TROPOMI measurements have not been used to quantify methane emissions from other power stations around the world. It is likely their low emission rates do not make power stations a suitable target for methane emissions quantification using TROPOMI.

The TROPOMI instrument precision of 5 ppb to 10 ppb (Hu et al. 2018a) potentially means smaller sources are missed in the retrievals. Turner et al. (2018) calculated that satellite instruments with a 4 ppb precision are better suited to the magnitude of CH_4 sources, but for instrument precisions larger than 6 ppb the information content is considerably decreased.

6.5 Conclusion

This chapter presents TROPOMI observations of XCH_4 over the UK from between 2018-2020. A success rate of less than 3% is obtained for high-quality, clear-sky TROPOMI retrievals across the UK, which is much lower than the data coverage reported in other TROPOMI studies. A strong negative bias was found between averaged 2018-2020 TROPOMI XCH_4 and surface albedo values for some areas of the UK, suggesting adjustments to the bias-corrected TROPOMI operational product are needed.

Comparison of TROPOMI XCH_4 with the bias-adjusted CAMS reanalysis and forecast products found reasonable agreement in the UK XCH_4 spatial patterns. Most of the CAMS-TROPOMI XCH_4 differences were less than 10 ppb with larger negative CAMS-TROPOMI differences associated with higher surface albedo values. Averaged CAMS forecasts and reanalysis found the XCH_4 gradient between London and the southeast is 5-10 ppb. This is smaller than the instrument precision of TROPOMI which is likely why a strong XCH_4 gradient is not observed in the TROPOMI retrievals.

Low data coverage and the XCH_4 spatial gradients from the CAMS XCH_4 products all together suggest that TROPOMI is not especially useful for quantifying spatial patterns of atmospheric methane across the UK nor for detecting plumes from high-emitting UK point sources. TROPOMI measurements could be used in conjunction with ground-based measurements from the UK's network, but TROPOMI may not be suitable for UK regional inversions since the UK methane spatial gradients are too small.

Chapter 7

Conclusions

"I'm not sure about other climate scientists, but for me being a climate scientist is at once completely heartbreaking, and also the only kind of science I could possibly be doing right now".

— Peter Kalmus, *2022*

7.1 Summary of key findings

The aim of this thesis was to develop different measurement and modelling techniques to evaluate sources of methane emissions in the UK. The work presented in this thesis focused on using ground-based isotopic measurements of ^{13}C and ^{14}C in atmospheric methane, and XCH_4 measurements from TROPOMI to explore different approaches for evaluating regional methane emissions and sources in the UK.

Continuous measurements of atmospheric $\delta^{13}CH_4$ and CH_4 in central London demonstrated methane emissions were underreported by 30% – 35% in the 2017 NAEI. Missing emissions were attributed to natural gas CH_4, which have historically been shown to be underestimated in urban areas. These atmospheric $\delta^{13}CH_4$ measurements represent the longest in situ $\delta^{13}CH_4$ campaign in central London and demonstrated the ability of using a commercially available Picarro isotopic analyser for constraining sector specific methane emissions in an urban setting. The low labour intensity of running the Picarro instrument allows for ongoing monitoring and evaluation of London CH_4 emissions that could be used to inform on city-wide emission mitigation policies. Similar instruments could be deployed to other major cities around the world or UK and used to evaluate city-wide methane emissions.

The utility of additional isotopic measurements for constraining methane sources was presented in Chapter

5. The CH_4-$\delta^{13}CH_4$-$\Delta^{14}CH_4$ isotopic framework provides a method for directly calculating the regional added methane concentrations of different sources from atmospheric measurements of $\delta^{13}CH_4$ and $\Delta^{14}CH_4$. Pseudo-data indicate additional isotopic measurements of $\Delta^{14}CH_4$ could be used to improve the UK methane source apportionment, provided the bias introduced from NPPs can be accounted. Pseudo-data slopes of $\Delta^{14}CH_4$-CH_4 and $\Delta^{14}CH_4$-$\delta^{13}CH_4$ were found to be sufficiently distinct between different sets of simulated data such that atmospheric measurements of $\delta^{13}CH_4$ and $\Delta^{14}CH_4$ could potentially be used in this framework to evaluate different anthropogenic emission inventories for the UK. Areas of the UK where there is a range of collocated sources, such as London, would benefit most from additional isotopic measurements of $\Delta^{14}CH_4$. In particular, as there is a larger proportion of fossil fuel sources. As methane concentrations are higher in London there are smaller ambiguities in the interpretation of methane sources and fossil-fractions from $\Delta^{14}CH_4$-$\delta^{13}CH_4$ and $\Delta^{14}CH_4$-CH_4 slopes.

A first analysis of TROPOMI XCH_4 measurements for the UK was presented in Chapter 6. This analysis revealed that TROPOMI XCH_4 retrievals are not particularly useful for informing on UK methane emissions and regional CH_4 patterns or gradients. The combination of low data availability, surface albedo biases in the bias-corrected retrievals and regional XCH_4 differences smaller than the TROPOMI instrument precision indicate we should not rely solely on satellite-based measurements for informing on UK methane emissions.

The findings in this thesis indicate that ground-based measurements are more powerful for constraining sector specific methane emissions and informing on regional differences than TROPOMI measurements for the UK. Isotopic measurements of $\delta^{13}CH_4$ are found to be valuable for source attribution in urban environments but are limited by spatiotemporal variations and the uncertainties of isotopic signatures used to characterise different methane sources. Pollution events with $\delta^{13}CH_4$ signatures indicating a mixture of biogenic and natural gas methane were found in the London measurements. Additional isotopic tracer measurements are therefore needed to understand the proportion of fossil and non-fossil CH_4 in such events. Simulations indicate that additional isotopic measurements of $\Delta^{14}CH_4$ could be used to augment the methane source constraint, provided the nuclear power plant bias and $\Delta^{14}CH_4$ biogenic signature are quantified.

7.2 Future work

Taking this work forwards, there is potential for ongoing atmospheric methane measurements at Imperial College London to be used for regularly evaluating methane emissions inventories for the London area. To

ensure accurate source apportionments are inferred updated $\delta^{13}CH_4$ source signatures would be needed as it is possible the UK $\delta^{13}CH_4$ signatures used to characterise methane sources have changed since reported in Zazzeri et al. (2017).

Since the onset of CH_4 and $\delta^{13}CH_4$ measurements at ICL there have also been a few atmospheric $\Delta^{14}CH_4$ measurements (Zazzeri et al. 2021). These $\Delta^{14}CH_4$ measurements could be used with concurrent CH_4 and $\delta^{13}CH_4$ measurements in the framework presented in Chapter 5 to infer the source slopes for the London area and added concentrations of different methane sources. However, nuclear power plant $\Delta^{14}CH_4$ influences would need to be accurately simulated at ICL. Quantifying the nuclear power plant influence is key to using $\Delta^{14}CH_4$ measurements for accurately informing on methane sources in the UK. Obtaining further data on when $^{14}CH_4$ is released from NPPs, how long $^{14}CH_4$ is emitted and its magnitude would improve the simulations. Additional source-receptor simulations of different spatial resolutions could be used to assess how changes in model spatial resolution affect the magnitude of NPP $\Delta^{14}CH_4$ across the UK measurement sites. However, without a real-world atmospheric tracer experiment using a different gas of low natural abundance it is challenging to establish an accurate source-receptor relationship between NPPs and the measurement sites.

Although there are few TROPOMI XCH_4 measurements for the UK, retrievals with good coverage of London could be used to quantify total emissions from London and compare with the UK NAEI estimates. In this way, TROPOMI could be used to complement ground-based measurements in London and provide additional constraints on methane emissions.

Bibliography

Abernethy, S. et al. (2021). "Methane removal and the proportional reductions in surface temperature and ozone". In: *Philosophical Transactions of the Royal Society A: Mathematical, Physical and Engineering Sciences* 379.2210. ISSN: 1364503X. DOI: 10.1098/rsta.2021.0104.

Agustí-Panareda, Anna et al. (June 2019). "Modelling CO2 weather – why horizontal resolution matters". In: *Atmospheric Chemistry and Physics* 19.11, pp. 7347–7376. ISSN: 1680-7324. DOI: 10.5194/acp-19-7347-2019. URL: https://acp.copernicus.org/articles/19/7347/2019/.

Allan, D.W. (1966). "Statistics of atomic frequency standards". In: *Proceedings of the IEEE* 54.2, pp. 221–230. ISSN: 0018-9219. DOI: 10.1109/PROC.1966.4634. URL: http://ieeexplore.ieee.org/document/1446564/.

Anderson, G et al. (1986). *AFGL atmospheric constituent profiles (0–120 km)*. Tech. rep. Hanscom Air Force Base, Bedford, Mass.: Air Force Geophys. Lab.

Apituley, A et al. (2021). *Sentinel-5 precursor/TROPOMI Level 2 Product User Manual Methane*. Tech. rep. URL: https://sentinels.copernicus.eu/documents/247904/2474726/Sentinel-5P-Level-2-Product-User-Manual-Methane.pdf/1808f165-0486-4840-ac1d-06194238fa96.

Arnold, Tim et al. (2018). "Inverse modelling of CF4 and NF3 emissions in East Asia". In: *Atmospheric Chemistry and Physics* 18.18, pp. 13305–13320. ISSN: 16807324. DOI: 10.5194/acp-18-13305-2018.

Arora, Naveen Kumar and Isha Mishra (2021). "COP26: more challenges than achievements". In: *Environmental Sustainability* 4.4. DOI: 10.1007/s42398-021-00212-7.

Assan, Sabina et al. (2018). "Can we separate industrial CH4 emission sources from atmospheric observations? - A test case for carbon isotopes, PMF and enhanced APCA". In: *Atmospheric Environment* 187.November 2017, pp. 317–327. ISSN: 18732844. DOI: 10.1016/j.atmosenv.2018.05.004. URL: https://doi.org/10.1016/j.atmosenv.2018.05.004.

Barré, Jérôme et al. (Apr. 2021). "Systematic detection of local CH4 anomalies by combining satellite measurements with high-resolution forecasts". In: *Atmospheric Chemistry and Physics* 21.6, pp. 5117–5136. ISSN: 1680-7324. DOI: 10.5194/acp-21-5117-2021.

Bergamaschi, P. et al. (Sept. 2005). "Inverse modelling of national and European CH4 emissions using the atmospheric zoom model TM5". In: *Atmospheric Chemistry and Physics* 5.9, pp. 2431–2460. ISSN: 1680-7324. DOI: 10.5194/acp-5-2431-2005. URL: https://acp.copernicus.org/articles/5/2431/2005/.

Bergamaschi, P. et al. (2015). "Top-down estimates of European CH4 and N2O emissions based on four different inverse models". In: *Atmospheric Chemistry and Physics* 15.2. ISSN: 16807324. DOI: 10.5194/acp-15-715-2015.

Bergamaschi, Peter et al. (Nov. 2009). "Inverse modeling of global and regional CH4 emissions using SCIAMACHY satellite retrievals". In: *Journal of Geophysical Research* 114.D22, p. D22301. ISSN: 0148-0227. DOI: 10.1029/2009JD012287. URL: http://doi.wiley.com/10.1029/2009JD012287.

Bloom, A. Anthony et al. (June 2017). "A global wetland methane emissions and uncertainty dataset for atmospheric chemical transport models (WetCHARTs version 1.0)". In: *Geoscientific Model Development* 10.6, pp. 2141–2156. ISSN: 1991-9603. DOI: 10.5194/gmd-10-2141-2017. URL: https://gmd.copernicus.org/articles/10/2141/2017/.

Brandt, A. R. et al. (2014). "Methane leaks from North American natural gas systems". In: *Science* 343.6172, pp. 733–735. ISSN: 10959203. DOI: 10.1126/science.1247045.

Brophy, Kieran et al. (2019). "Characterizing uncertainties in atmospheric inversions of fossil fuel CO 2 emissions in California". In: *Atmospheric Chemistry and Physics* 19.5, pp. 2991–3006. ISSN: 16807324. DOI: 10.5194/acp-19-2991-2019.

Butz, A. et al. (July 2011). "Toward accurate CO ₂ and CH ₄ observations from GOSAT". In: *Geophysical Research Letters* 38.14, n/a–n/a. ISSN: 00948276. DOI: 10.1029/2011GL047888.

Butz, A. et al. (2012). "TROPOMI aboard Sentinel-5 Precursor: Prospective performance of CH 4 retrievals for aerosol and cirrus loaded atmospheres". In: *Remote Sensing of Environment* 120. ISSN: 00344257. DOI: 10.1016/j.rse.2011.05.030.

Butz, André et al. (June 2009). "Retrievals of atmospheric CO_2 from simulated space-borne measurements of backscattered near-infrared sunlight: accounting for aerosol effects". In: *Applied Optics* 48.18, p. 3322. ISSN: 0003-6935. DOI: 10.1364/AO.48.003322. URL: https://opg.optica.org/abstract.cfm?URI=ao-48-18-3322.

Chung, Edward and Tim Arnold (2021). "Potential of Clumped Isotopes in Constraining the Global Atmospheric Methane Budget". In: *Global Biogeochemical Cycles* 35.10. ISSN: 19449224. DOI: 10.1029/2020GB006883.

Ciais, P. et al. (2013). *Carbon and Other Biogeochemical Cycles. In: Climate Change 2013: The Physical Science Basis.*

Crippa, M. et al. (2019). *Fossil CO2 and GHG emissions of all world countries - 2019 Report*. Tech. rep. Publications Office of the European Union. DOI: 10.2760/687800.

Crippa, Monica et al. (Oct. 2018). *Gridded emissions of air pollutants for the period 1970-2012 within EDGAR v4.3.2*. DOI: 10.5194/essd-10-1987-2018. URL: https://essd.copernicus.org/articles/10/1987/2018/.

Crutzen, Paul J., Ingo Aselmann, and Wolfgang Seiler (1986). "Methane production by domestic animals, wild ruminants, other herbivorous fauna, and humans". In: *Tellus B: Chemical and Physical Meteorology* 38.3-4. DOI: 10.3402/tellusb.v38i3-4.15135.

Dalsøren, Stig B. and Ivar S.A. Isaksen (2006). "CTM study of changes in tropospheric hydroxyl distribution 1990-2001 and its impact on methane". In: *Geophysical Research Letters* 33.23. ISSN: 00948276. DOI: 10.1029/2006GL027295.

Davis, W (Feb. 1977). *Carbon-14 production in nuclear reactors*. Tech. rep. Oak Ridge, Tennessee: Oak Ridge National Laboratory, pp. 151–191.

DEFRA (2021). *UK Statistics on Waste*. Tech. rep. URL: https://assets.publishing.service.gov.uk/government/uploads/system/uploads/attachment_data/file/918270/UK_Statistics_on_Waste_statistical_notice_March_2020_accessible_FINAL_updated_size_12.pdf.

Dlugokencky, Ed J. (2022). *NOAA/GML*. URL: www.esrl.noaa.gov/gmd/ccgg/trends_ch4/.

drax (2022). *Drax Power Station*. URL: https://www.drax.com/about-us/our-sites-and-businesses/drax-power-station/.

Duren, Riley M. and Charles E. Miller (2012). "Measuring the carbon emissions of megacities". In: *Nature Climate Change* 2.8, pp. 560–562. ISSN: 1758678X. DOI: 10.1038/nclimate1629.

ECMWF (May 2015). *IFS DOCUMENTATION – Cy41r1 Operational implementation PART III: DYNAMICS AND NUMERICAL PROCEDURES*.

— (2021). *CAMS: Reanalysis data documentation*. URL: https://confluence.ecmwf.int/display/CKB/CAMS%3A+Reanalysis+data+documentation.

Eisma, Roos, Alex T. Vermeulen, and Klaas Van Der Borg (July 1995). "14 CH 4 Emissions from Nuclear Power Plants in Northwestern Europe". In: *Radiocarbon* 37.2, pp. 475–483. ISSN: 0033-8222. DOI: 10.

1017/S0033822200030952. URL: https://www.cambridge.org/core/product/identifier/S0033822200030952/type/journal_article.

Engelen, Richard J., Soumia Serrar, and Frédéric Chevallier (Feb. 2009). "Four-dimensional data assimilation of atmospheric CO ₂ using AIRS observations". In: *Journal of Geophysical Research* 114.D3, p. D03303. ISSN: 0148-0227. DOI: 10.1029/2008JD010739.

EPRI (2010). "Estimation of carbon-14 in nuclear power plant gaseous effluents". In: *TR-1021106*.

Feinberg, Aryeh I. et al. (2018). "Isotopic source signatures: Impact of regional variability on the Δ13CH4 trend and spatial distribution". In: *Atmospheric Environment* 174.December 2017, pp. 99–111. ISSN: 18732844. DOI: 10.1016/j.atmosenv.2017.11.037. URL: https://doi.org/10.1016/j.atmosenv.2017.11.037.

Feng, Liang et al. (2017). "Consistent regional fluxes of CH4 and CO2 inferred from GOSAT proxy XCH4:XCO2 retrievals, 2010-2014". In: *Atmospheric Chemistry and Physics* 17.7. ISSN: 16807324. DOI: 10.5194/acp-17-4781-2017.

Fischer, Marc L. et al. (2017). "Simulating estimation of California fossil fuel and biosphere carbon dioxide exchanges combining in situ tower and satellite column observations". In: *Journal of Geophysical Research* 122.6, pp. 3653–3671. ISSN: 21562202. DOI: 10.1002/2016JD025617.

Fisher, Rebecca E. et al. (2017). "Measurement of the 13C isotopic signature of methane emissions from northern European wetlands". In: *Global Biogeochemical Cycles* 31.3, pp. 605–623. ISSN: 19449224. DOI: 10.1002/2016GB005504.

France, J. L. et al. (2016). "Measurements of δ13C in CH4 and using particle dispersion modeling to characterize sources of arctic methane within an air mass". In: *Journal of Geophysical Research* 121.23, pp. 257–14. ISSN: 21562202. DOI: 10.1002/2016JD026006.

Frankenberg, C. et al. (2006). "Satellite chartography of atmospheric methane from SCIAMACHY on board ENVISAT: Analysis of the years 2003 and 2004". In: *Journal of Geophysical Research* 111.D7, p. D07303. ISSN: 0148-0227. DOI: 10.1029/2005JD006235.

Frankenberg, C. et al. (2011). "Global column-averaged methane mixing ratios from 2003 to 2009 as derived from SCIAMACHY: Trends and variability". In: *Journal of Geophysical Research Atmospheres* 116.4. ISSN: 01480227. DOI: 10.1029/2010JD014849.

Fraser, A. et al. (2013). "Estimating regional methane surface fluxes: The relative importance of surface and GOSAT mole fraction measurements". In: *Atmospheric Chemistry and Physics* 13.11. ISSN: 16807324. DOI: 10.5194/acp-13-5697-2013.

Ganesan, A. L. et al. (June 2015). "Quantifying methane and nitrous oxide emissions from the UK and Ireland using a national-scale monitoring network". In: *Atmospheric Chemistry and Physics* 15.11, pp. 6393–6406. ISSN: 1680-7324. DOI: 10.5194/acp-15-6393-2015. URL: https://acp.copernicus.org/articles/15/6393/2015/.

Ganesan, Anita L. et al. (2017). "Atmospheric observations show accurate reporting and little growth in India's methane emissions". In: *Nature Communications* 8.1, pp. 1–7. ISSN: 20411723. DOI: 10.1038/s41467-017-00994-7. URL: http://dx.doi.org/10.1038/s41467-017-00994-7.

Ganesan, Anita L. et al. (2019). "Advancing Scientific Understanding of the Global Methane Budget in Support of the Paris Agreement". In: *Global Biogeochemical Cycles* 33.12, pp. 1475–1512. ISSN: 19449224. DOI: 10.1029/2018GB006065.

Garnett, M. H. et al. (July 2013). "Radiocarbon dating of methane and carbon dioxide evaded from a temperate peatland stream". In: *Biogeochemistry* 114.1-3, pp. 213–223. ISSN: 0168-2563. DOI: 10.1007/s10533-012-9804-2. URL: http://link.springer.com/10.1007/s10533-012-9804-2.

Gidden, Matthew J. et al. (Apr. 2019). "Global emissions pathways under different socioeconomic scenarios for use in CMIP6: a dataset of harmonized emissions trajectories through the end of the century". In: *Geoscientific Model Development* 12.4, pp. 1443–1475. ISSN: 1991-9603. DOI: 10.5194/gmd-12-1443-2019. URL: https://gmd.copernicus.org/articles/12/1443/2019/.

Gonzalez Moguel, Regina et al. (2022). "Using carbon-14 and carbon-13 measurements for source attribution of atmospheric methane in the Athabasca oil sands region". In: *Atmospheric Chemistry and Physics* 22.3. ISSN: 16807324. DOI: 10.5194/acp-22-2121-2022.

Gouw, Joost A. de et al. (2020). "Daily Satellite Observations of Methane from Oil and Gas Production Regions in the United States". In: *Scientific Reports* 10.1, pp. 1–10. ISSN: 20452322. DOI: 10.1038/s41598-020-57678-4. URL: http://dx.doi.org/10.1038/s41598-020-57678-4.

Graven, H D et al. (2012). "Changing controls on oceanic radiocarbon : New insights on shallow-to-deep ocean exchange and anthropogenic CO 2 uptake". In: 117, pp. 1–16. DOI: 10.1029/2012JC008074.

Graven, H., T. Hocking, and G. Zazzeri (2019). "Detection of Fossil and Biogenic Methane at Regional Scales Using Atmospheric Radiocarbon". In: *Earth's Future* 7.3, pp. 283–299. ISSN: 23284277. DOI: 10.1029/2018EF001064.

Graven, H. D. and N. Gruber (2011). "Continental-scale enrichment of atmospheric 14CO 2 from the nuclear power industry: Potential impact on the estimation of fossil fuel-derived CO 2". In: *Atmospheric Chemistry and Physics* 11.23, pp. 12339–12349. ISSN: 16807316. DOI: 10.5194/acp-11-12339-2011.

Graven, Heather, Ralph F. Keeling, and Joeri Rogelj (Nov. 2020). “Changes to Carbon Isotopes in Atmospheric CO 2 Over the Industrial Era and Into the Future”. In: *Global Biogeochemical Cycles* 34.11. ISSN: 0886-6236. DOI: 10.1029/2019GB006170. URL: https://onlinelibrary.wiley.com/doi/10.1029/2019GB006170.

Graven, Heather et al. (2017). “Compiled records of carbon isotopes in atmospheric CO 2 for historical simulations in CMIP6”. In: pp. 4405–4417.

Griffith, David W.T. (2018). “Calibration of isotopologue-specific optical trace gas analysers: A practical guide”. In: *Atmospheric Measurement Techniques* 11.11, pp. 6189–6201. ISSN: 18678548. DOI: 10.5194/amt-11-6189-2018.

Hagenaars, T J et al. (2011). “Estimation of foot and mouth disease transmission parameters, using outbreak data and transmission experiments.” In: *Revue scientifique et technique (International Office of Epizootics)* 30.2, pp. 467–77. ISSN: 0253-1933. URL: http://www.ncbi.nlm.nih.gov/pubmed/21961219.

Hasecamp, O et al. (2019). *Algorithm Theoretical Baseline Docu- ment for Sentinel-5 Precursor methane retrieval*. Tech. rep. URL: https://sentinels.copernicus.eu/documents/247904/2474726/Sentinel-5P-Level-2-Product-User-Manual-Methane.

Hausmann, Petra, Ralf Sussmann, and Dan Smale (2016). “Contribution of oil and natural gas production to renewed increase in atmospheric methane (2007-2014): Top-down estimate from ethane and methane column observations”. In: *Atmospheric Chemistry and Physics* 16.5. ISSN: 16807324. DOI: 10.5194/acp-16-3227-2016.

Helfter, Carole et al. (2016). “Spatial and temporal variability of urban fluxes of methane, carbon monoxide and carbon dioxide above London, UK”. In: *Atmospheric Chemistry and Physics* 16.16, pp. 10543–10557. ISSN: 16807324. DOI: 10.5194/acp-16-10543-2016.

Helmig, Detlev et al. (2016). “Reversal of global atmospheric ethane and propane trends largely due to US oil and natural gas production”. In: *Nature Geoscience* 9.7, pp. 490–495. ISSN: 17520908. DOI: 10.1038/ngeo2721.

Hoesly, Rachel M. et al. (Jan. 2018). “Historical (1750–2014) anthropogenic emissions of reactive gases and aerosols from the Community Emissions Data System (CEDS)”. In: *Geoscientific Model Development* 11.1, pp. 369–408. ISSN: 1991-9603. DOI: 10.5194/gmd-11-369-2018. URL: https://gmd.copernicus.org/articles/11/369/2018/.

Hoheisel, Antje et al. (2019). “An improved method for mobile characterisation of δ 13 CH 4 source signatures and its application in Germany”. In: pp. 1123–1139.

Holloway, A and R Wayne (2010). *Atmospheric Chemistry*. RSC Publishing, pp. 101–105. ISBN: 978-1-84755-807-7.

Hopkins, Francesca M. et al. (2016). "Mitigation of methane emissions in cities: How new measurements and partnerships can contribute to emissions reduction strategies". In: *Earth's Future* 4.9, pp. 408–425. ISSN: 23284277. DOI: 10.1002/2016EF000381.

Hu, Haili et al. (2016). "The operational methane retrieval algorithm for TROPOMI". In: *Atmospheric Measurement Techniques* 9.11, pp. 5423–5440. ISSN: 18678548. DOI: 10.5194/amt-9-5423-2016.

Hu, Haili et al. (2018a). "Toward Global Mapping of Methane With TROPOMI: First Results and Intersatellite Comparison to GOSAT". In: *Geophysical Research Letters* 45.8, pp. 3682–3689. ISSN: 19448007. DOI: 10.1002/2018GL077259. URL: https://doi.org/10.1002/2018GL077259.

Hu, Y. et al. (2018b). "Review of emissions from smouldering peat fires and their contribution to regional haze episodes". In: *International Journal of Wildland Fire* 27.5, pp. 293–312. ISSN: 10498001. DOI: 10.1071/WF17084.

Inness, A et al. (2019). *CAMS global reanalysis (EAC4). Copernicus Atmosphere Monitoring Service (CAMS) Atmosphere Data Store (ADS)*. URL: https://ads.atmosphere.copernicus.eu/cdsapp#!/dataset/cams-global-reanalysis-eac4?tab=overview.

IPCC (2006). *2006 IPCC Guidelines for National Greenhouse Gas Inventories*. URL: https://www.ipcc-nggip.iges.or.jp/public/2006gl/index.html.

— (2014a). "IPCC Fifth Assessment Synthesis Report-Climate Change 2014 Synthesis Report". In: *IPCC Fifth Assessment Synthesis Report-Climate Change 2014 Synthesis Report*.

— (2014b). "IPCC Fifth Assessment Synthesis Report-Climate Change 2014 Synthesis Report". In: *IPCC Fifth Assessment Synthesis Report-Climate Change 2014 Synthesis Report*.

Jackson, Robert B. et al. (2021). "Atmospheric methane removal: A research agenda". In: *Philosophical Transactions of the Royal Society A: Mathematical, Physical and Engineering Sciences* 379.2210. ISSN: 1364503X. DOI: 10.1098/rsta.2020.0454.

Jacob, Daniel J. et al. (2016). "Satellite observations of atmospheric methane and their value for quantifying methane emissions". In: *Atmospheric Chemistry and Physics* 16.22, pp. 14371–14396. ISSN: 16807324. DOI: 10.5194/acp-16-14371-2016.

Janssens-Maenhout, Greet et al. (2012). "EDGAR v4 . 3 . 2 Global Atlas of the three major Greenhouse Gas Emissions for the period 1970-2012 . Supplementary Information". In: *Earth System Science Data* 2010, pp. 1–20. DOI: https://data.europa.eu/doi/10.2904/JRC{_}DATASET{_}EDGAR. URL: http://edgar.jrc.ec.europa.eu/overview.php?v=432&SECURE=123.

Janssens-Maenhout, Greet et al. (July 2019). "EDGAR v4.3.2 Global Atlas of the three major greenhouse gas emissions for the period 1970–2012". In: *Earth System Science Data* 11.3, pp. 959–1002. ISSN: 1866-3516. DOI: 10.5194/essd-11-959-2019. URL: https://essd.copernicus.org/articles/11/959/2019/.

Jeong, Seongeun et al. (2013). "A multitower measurement network estimate of California's methane emissions". In: *Journal of Geophysical Research Atmospheres* 118.19, pp. 11339–11351. ISSN: 21698996. DOI: 10.1002/jgrd.50854.

Jones, Andrew et al. (Apr. 2007). "The U.K. Met Office's Next-Generation Atmospheric Dispersion Model, NAME III". In: *Air Pollution Modeling and Its Application XVII*. Springer US, pp. 580–589. DOI: 10.1007/978-0-387-68854-1{_}62.

Jones, Steve D. et al. (Dec. 2015). "A statistical gap-filling method to interpolate global monthly surface ocean carbon dioxide data". In: *Journal of Advances in Modeling Earth Systems* 7.4, pp. 1554–1575. ISSN: 19422466. DOI: 10.1002/2014MS000416. URL: http://doi.wiley.com/10.1002/2014MS000416.

Keeling, Charles D. (1958). "The concentration and isotopic abundances of atmospheric carbon dioxide in rural areas". In: *Geochimica et Cosmochimica Acta* 13.4, pp. 322–334. ISSN: 00167037. DOI: 10.1016/0016-7037(58)90033-4.

— (July 1961). "The concentration and isotopic abundances of carbon dioxide in rural and marine air". In: *Geochimica et Cosmochimica Acta* 24.3-4, pp. 277–298. ISSN: 00167037. DOI: 10.1016/0016-7037(61)90023-0. URL: https://linkinghub.elsevier.com/retrieve/pii/0016703761900230.

Kessler, J. D. et al. (2008). "A survey of methane isotope abundance (14C, 13C, 2H) from five nearshore marine basins that reveals unusual radiocarbon levels in subsurface waters". In: *Journal of Geophysical Research: Oceans* 113.12, pp. 1–13. ISSN: 21699291. DOI: 10.1029/2008JC004822.

Key, R.M. (2001). "Radiocarbon". In: *Encyclopedia of Ocean Sciences*. Elsevier, pp. 2338–2353. DOI: 10.1006/rwos.2001.0162.

Kirschke, Stefanie et al. (2013). "Three decades of global methane sources and sinks". In: *Nature Geoscience* 6.10, pp. 813–823. ISSN: 17520894. DOI: 10.1038/ngeo1955.

Kort, Eric A. and Christian. Frankenberg (2014). "Anomaly Viewed From Space". In: *Geophysical Research Letters*, pp. 6898–6903. DOI: 10.1002/2014GL061503.Received.

Krings, T. et al. (2011). "MAMAP - A new spectrometer system for column-averaged methane and carbon dioxide observations from aircraft: Retrieval algorithm and first inversions for point source emission rates". In: *Atmospheric Measurement Techniques* 4.9. ISSN: 18671381. DOI: 10.5194/amt-4-1735-2011.

Kunz, C. (1985). “Carbon-14 discharge at three light-water reactors”. In: *Health Physics* 49.1, pp. 25–35. ISSN: 15385159. DOI: 10.1097/00004032-198507000-00002.

Kuze, Akihiko et al. (2009). “Thermal and near infrared sensor for carbon observation Fourier-transform spectrometer on the Greenhouse Gases Observing Satellite for greenhouse gases monitoring”. In: *Applied Optics* 48.35. ISSN: 15394522. DOI: 10.1364/AO.48.006716.

Lan, Xin et al. (2021). *What do we know about the global methane budget? Results from four decades of atmospheric CH 4 observations and the way forward*. DOI: 10.1098/rsta.2020.0440.

Lassey, K. R., D. C. Lowe, and A. M. Smith (2007a). “The atmospheric cycling of radiomethane and the "fossil fraction" of the methane source”. In: *Atmospheric Chemistry and Physics* 7.8, pp. 2141–2149. ISSN: 16807324. DOI: 10.5194/acp-7-2141-2007.

Lassey, K. R. et al. (2007b). “Centennial evolution of the atmospheric methane budget: What do the carbon isotopes tell us?” In: *Atmospheric Chemistry and Physics* 7.8, pp. 2119–2139. ISSN: 16807324. DOI: 10.5194/acp-7-2119-2007.

Lauvaux, Thomas et al. (2021). “Global Assessment of Oil and Gas Methane Ultra-Emitters”. In: 561.February, pp. 557–561. ISSN: 10959203. DOI: 10.1126/science.abj4351. URL: http://arxiv.org/abs/2105.06387.

Levin, Ingeborg et al. (1985). “25 Years of Tropospheric 14 C Observations in Central Europe”. In: *Radiocarbon* 27.1, pp. 1–19. ISSN: 0033-8222. DOI: 10.1017/s0033822200006895.

Levin, Ingeborg et al. (1992). “Levin, Ingeborg, Rainer Bösinger, Georges Bonani, R. Francey, Bernd Kromer, Karl Otto Münnich, Martin Suter, Neil B. A. Trivett and Willy Wolfli. “Radiocarbon in Atmospheric Carbon Dioxide and Methane: Global Distribution and Trends.” (1992).” In.

Levy, Peter (2020). *Greenhouse Gas Fluxes from the UK (ukghg)*. URL: https://github.com/NERC-CEH/ukghg/blob/.

Lorente, Alba et al. (2020). “Methane retrieved from TROPOMI: improvement of the data product and validation of the first two years of measurements”. In: *Atmospheric Measurement Techniques Discussions* August, pp. 1–28. ISSN: 1867-1381. DOI: 10.5194/amt-2020-281.

Lorente, Alba et al. (2021). “Methane retrieved from TROPOMI: Improvement of the data product and validation of the first 2 years of measurements”. In: *Atmospheric Measurement Techniques* 14.1, pp. 665–684. ISSN: 18678548. DOI: 10.5194/amt-14-665-2021.

Lovelock, J. E. (1977). *Methyl chloroform in the troposphere as an indicator of OH radical abundance [3]*. DOI: 10.1038/267032a0.

Lowry, David et al. (2001). “London methane emissions: Use of diurnal changes”. In: *Journal of Geophysical Research* 106.D7, pp. 7427–7448.

Lu, Xiao et al. (2021). *Global methane budget and trend, 2010-2017: Complementarity of inverse analyses using in situ (globalviewplus ch4 obspack) and satellite (gosat) observations*. DOI: 10.5194/acp-21-4637-2021.

Lunt, Mark F. et al. (2016). “Estimation of trace gas fluxes with objectively determined basis functions using reversible-jump Markov chain Monte Carlo”. In: *Geoscientific Model Development* 9.9. ISSN: 19919603. DOI: 10.5194/gmd-9-3213-2016.

Lunt, Mark F. et al. (Nov. 2021a). “Atmospheric observations consistent with reported decline in the UK’s methane emissions (2013–2020)”. In: *Atmospheric Chemistry and Physics* 21.21, pp. 16257–16276. ISSN: 1680-7324. DOI: 10.5194/acp-21-16257-2021. URL: https://acp.copernicus.org/articles/21/16257/2021/.

Lunt, Mark F. et al. (2021b). “Rain-fed pulses of methane from East Africa during 2018-2019 contributed to atmospheric growth rate”. In: *Environmental Research Letters* 16.2. ISSN: 17489326. DOI: 10.1088/1748-9326/abd8fa.

Lunt, Mark M. et al. (2019). “An increase in methane emissions from tropical Africa between 2010 and 2016 inferred from satellite data”. In: *Atmospheric Chemistry and Physics* 19.23. ISSN: 16807324. DOI: 10.5194/acp-19-14721-2019.

Maasakkers, Joannes D. et al. (2019). “Global distribution of methane emissions, emission trends, and OH concentrations and trends inferred from an inversion of GOSAT satellite data for 2010-2015”. In: *Atmospheric Chemistry and Physics* 19.11. ISSN: 16807324. DOI: 10.5194/acp-19-7859-2019.

Manning, A. J. et al. (2011). “Estimating UK methane and nitrous oxide emissions from 1990 to 2007 using an inversion modeling approach”. In: *Journal of Geophysical Research Atmospheres* 116.2, pp. 1–19. ISSN: 01480227. DOI: 10.1029/2010JD014763.

Manning, Alistair J. et al. (2021). “Evidence of a recent decline in UK emissions of hydrofluorocarbons determined by the InTEM inverse model and atmospheric measurements”. In: *Atmospheric Chemistry and Physics* 21.16, pp. 12739–12755. ISSN: 16807324. DOI: 10.5194/acp-21-12739-2021.

Marcotullio, Peter John et al. (2013). “The geography of global urban greenhouse gas emissions: An exploratory analysis”. In: *Climatic Change* 121.4, pp. 621–634. ISSN: 01650009. DOI: 10.1007/s10584-013-0977-z.

Massart, S. et al. (June 2014). “Assimilation of atmospheric methane products into the MACC-II system: from SCIAMACHY to TANSO and IASI”. In: *Atmospheric Chemistry and Physics* 14.12, pp. 6139–6158. ISSN: 1680-7324. DOI: 10.5194/acp-14-6139-2014.

Massart, Sébastien et al. (Feb. 2016). "Ability of the 4-D-Var analysis of the GOSAT BESD XCO2 retrievals to characterise atmospheric CO2 at large and synoptic scales". In: *Atmospheric Chemistry and Physics* 16.3, pp. 1653–1671. ISSN: 1680-7324. DOI: 10.5194/acp-16-1653-2016.

Masson-Delmotte, V. et al. (2021). *IPCC, 2021: Climate Change 2021: The Physical Science Basis*. Tech. rep.

Mays, Kelly L. et al. (2009). "Aircraft-based measurements of the carbon footprint of Indianapolis". In: *Environmental Science and Technology* 43.20. ISSN: 0013936X. DOI: 10.1021/es901326b.

McKain, Kathryn et al. (2015). "Methane emissions from natural gas infrastructure and use in the urban region of Boston, Massachusetts". In: *Proceedings of the National Academy of Sciences* 112.7, pp. 1941–1946. ISSN: 0027-8424. DOI: 10.1073/pnas.1416261112.

Meinshausen, M., S. C. B. Raper, and T. M. L. Wigley (Feb. 2011). "Emulating coupled atmosphere-ocean and carbon cycle models with a simpler model, MAGICC6 – Part 1: Model description and calibration". In: *Atmospheric Chemistry and Physics* 11.4, pp. 1417–1456. ISSN: 1680-7324. DOI: 10.5194/acp-11-1417-2011. URL: https://acp.copernicus.org/articles/11/1417/2011/.

Meinshausen, Malte et al. (Aug. 2020). "The shared socio-economic pathway (SSP) greenhouse gas concentrations and their extensions to 2500". In: *Geoscientific Model Development* 13.8, pp. 3571–3605. ISSN: 1991-9603. DOI: 10.5194/gmd-13-3571-2020. URL: https://gmd.copernicus.org/articles/13/3571/2020/.

Menoud, Malika et al. (2020). "Characterisation of methane sources in Lutjewad, The Netherlands, using quasi-continuous isotopic composition measurements". In: *Tellus, Series B: Chemical and Physical Meteorology* 72.1. ISSN: 16000889. DOI: 10.1080/16000889.2020.1823733.

Miles, Natasha L. et al. (2018). "Calibration and field testing of cavity ring-down laser spectrometers measuring CH4, CO2, and δ13CH4 deployed on towers in the Marcellus Shale region". In: *Atmospheric Measurement Techniques* 11.3, pp. 1273–1295. ISSN: 18678548. DOI: 10.5194/amt-11-1273-2018.

Miller, John et al. (Feb. 2013). "Initial Results of an Intercomparison of AMS-Based Atmospheric 14 CO 2 Measurements". In: *Radiocarbon* 55.3, pp. 1475–1483. ISSN: 0033-8222. DOI: 10.1017/S0033822200048402. URL: https://www.cambridge.org/core/product/identifier/S0033822200048402/type/journal_article.

Miller, John B. and Pieter P. Tans (2003). "Calculating isotopic fractionation from atmospheric measurements at various scales". In: *Tellus, Series B: Chemical and Physical Meteorology* 55.2, pp. 207–214. ISSN: 02806509. DOI: 10.1034/j.1600-0889.2003.00020.x.

Miller, Scot M. et al. (2019). “China’s coal mine methane regulations have not curbed growing emissions”. In: *Nature Communications* 10.1, pp. 1–8. ISSN: 20411723. DOI: 10.1038/s41467-018-07891-7. URL: http://dx.doi.org/10.1038/s41467-018-07891-7.

NAEI (2017). *The UK National Atmospheric Emissions Inventory*. URL: https://naei.beis.gov.uk/.

Nisbet, E. G. et al. (2016). “Rising atmospheric methane: 2007–2014 growth and isotopic shift”. In: *Global Biogeochemical Cycles* 30.9, pp. 1356–1370. ISSN: 19449224. DOI: 10.1002/2016GB005406.

Nisbet, E. G. et al. (2019). “Very Strong Atmospheric Methane Growth in the 4 Years 2014–2017: Implications for the Paris Agreement”. In: *Global Biogeochemical Cycles* 33.3, pp. 318–342. ISSN: 19449224. DOI: 10.1029/2018GB006009.

Nisbet, E. G. et al. (2020). “Methane Mitigation: Methods to Reduce Emissions, on the Path to the Paris Agreement”. In: *Reviews of Geophysics* 58.1, pp. 1–51. ISSN: 8755-1209. DOI: 10.1029/2019rg000675.

Nisbet, Euan and Ray Weiss (2010). “Top-Down Versus Bottom-Up”. In: 328.June, pp. 1241–1244.

Nonbøl, Eric (1996). *Description of the Advanced Gas Cooled Type of Reactor (AGR)*. Tech. rep. Risø National Laboratory.

O’Neill, Brian C. et al. (Feb. 2014). “A new scenario framework for climate change research: the concept of shared socioeconomic pathways”. In: *Climatic Change* 122.3, pp. 387–400. ISSN: 0165-0009. DOI: 10.1007/s10584-013-0905-2. URL: http://link.springer.com/10.1007/s10584-013-0905-2.

Palmer, Paul I. et al. (Aug. 2018). “A measurement-based verification framework for UK greenhouse gas emissions: an overview of the Greenhouse gAs Uk and Global Emissions (GAUGE) project”. In: *Atmospheric Chemistry and Physics* 18.16, pp. 11753–11777. ISSN: 1680-7324. DOI: 10.5194/acp-18-11753-2018. URL: https://acp.copernicus.org/articles/18/11753/2018/.

Palmer, Paul I. et al. (2021). “The added value of satellite observations of methane forunderstanding the contemporary methane budget”. In: *Philosophical Transactions of the Royal Society A: Mathematical, Physical and Engineering Sciences* 379.2210. ISSN: 1364503X. DOI: 10.1098/rsta.2021.0106.

Pandey, Sudhanshu et al. (2016). “Inverse modeling of GOSAT-retrieved ratios of total column CH4 and CO2 for 2009 and 2010”. In: *Atmospheric Chemistry and Physics* 16.8. ISSN: 16807324. DOI: 10.5194/acp-16-5043-2016.

Pandey, Sudhanshu et al. (Dec. 2019). “Satellite observations reveal extreme methane leakage from a natural gas well blowout”. In: *Proceedings of the National Academy of Sciences* 116.52, pp. 26376–26381. ISSN: 0027-8424. DOI: 10.1073/pnas.1908712116. URL: https://pnas.org/doi/full/10.1073/pnas.1908712116.

Pataki, D. E. et al. (2003). “The application and interpretation of Keeling plots in terrestrial carbon cycle research”. In: *Global Biogeochemical Cycles* 17.1. ISSN: 08866236. DOI: 10.1029/2001GB001850.

Pitt, Joseph R. et al. (2019). “Assessing London CO2, CH4 and CO emissions using aircraft measurements and dispersion modelling”. In: *Atmospheric Chemistry and Physics* 19.13, pp. 8931–8945. ISSN: 16807324. DOI: 10.5194/acp-19-8931-2019.

Plant, Genevieve et al. (2022). “Evaluating urban methane emissions from space using TROPOMI methane and carbon monoxide observations”. In: *Remote Sensing of Environment* 268. ISSN: 00344257. DOI: 10.1016/j.rse.2021.112756.

Prather, Michael J., Christopher D. Holmes, and Juno Hsu (2012). “Reactive greenhouse gas scenarios: Systematic exploration of uncertainties and the role of atmospheric chemistry”. In: *Geophysical Research Letters* 39.9. ISSN: 00948276. DOI: 10.1029/2012GL051440.

Prinn, R. G. et al. (2001). “Evidence for substantial variations of atmospheric hydroxyl radicals in the past two decades”. In: *Science* 292.5523. ISSN: 00368075. DOI: 10.1126/science.1058673.

Prinn, R. G. et al. (2005). “Evidence for variability of atmospheric hydroxyl radicals over the past quarter century”. In: *Geophysical Research Letters* 32.7. ISSN: 00948276. DOI: 10.1029/2004GL022228.

Qu, Zhen et al. (2021). “Global distribution of methane emissions: A comparative inverse analysis of observations from the TROPOMI and GOSAT satellite instruments”. In: *Atmospheric Chemistry and Physics* 21.18. ISSN: 16807324. DOI: 10.5194/acp-21-14159-2021.

Quay, P. D. et al. (1991). “Carbon isotopic composition of atmospheric CH4: Fossil and biomass burning source strengths”. In: *Global Biogeochemical Cycles* 5.1. ISSN: 19449224. DOI: 10.1029/91GB00003.

Quay, Paul et al. (1999). “The isotopic composition of atmospheric methane”. In: *Global Biogeochemical Cycles* 13.2, pp. 445–461.

RADD (2017). *RADD Database*. URL: http://europa.eu/radd/nuclideDischargeOverview.dox?pageID=NuclideDischargeOverview.

Ramonet, M et al. (2021). *Validation report for the CAMS greenhouse gas global reanalysis, years 2003-2020*. Tech. rep. Copernicus Atmospheric Monitoring Service. URL: https://atmosphere.copernicus.eu/sites/default/files/2021-04/CAMS84_2018SC3_D5.1.2-2020.pdf.

Ramsden, Alice E. et al. (2022). “Quantifying fossil fuel methane emissions using observations of atmospheric ethane and an uncertain emission ratio”. In: *Atmospheric Chemistry and Physics* 22.6. ISSN: 16807324. DOI: 10.5194/acp-22-3911-2022.

Randerson, J. T. et al. (2012). “Global burned area and biomass burning emissions from small fires”. In: *Journal of Geophysical Research G: Biogeosciences* 117.4. ISSN: 01480227. DOI: 10.1029/2012JG002128.

Rella, C. W. et al. (2015). "Local- and regional-scale measurements of CH4, Δ13CH4, and C2H6 in the Uintah Basin using a mobile stable isotope analyzer". In: *Atmospheric Measurement Techniques* 8.10, pp. 4539–4559. ISSN: 18678548. DOI: 10.5194/amt-8-4539-2015.

Rennick, Chris et al. (July 2021). "Boreas: A Sample Preparation-Coupled Laser Spectrometer System for Simultaneous High-Precision In Situ Analysis of δ 13 C and δ 2 H from Ambient Air Methane". In: *Analytical Chemistry* 93.29, pp. 10141–10151. ISSN: 0003-2700. DOI: 10.1021/acs.analchem.1c01103. URL: https://pubs.acs.org/doi/10.1021/acs.analchem.1c01103.

Ricardo Energy & Environment (2019). "UK Emission Mapping Methodology 2017". In: 1, p. 49.

Richmond, B et al. (2019). "UK Informative Inventory Report (1990 to 2019)". In: April, p. 210. URL: https://uk-air.defra.gov.uk/assets/documents/reports/cat09/1904121008_GB_IIR_2019_v2.0.pdf.

Riddick, S. N. et al. (2018). "Development of a low-maintenance measurement approach to continuously estimate methane emissions: A case study". In: *Waste Management* 73, pp. 210–219. ISSN: 18792456. DOI: 10.1016/j.wasman.2016.12.006. URL: https://doi.org/10.1016/j.wasman.2016.12.006.

Rigby, M., A. J. Manning, and R. G. Prinn (2012). "The value of high-frequency, high-precision methane isotopologue measurements for source and sink estimation". In: *Journal of Geophysical Research Atmospheres* 117.12, pp. 1–14. ISSN: 01480227. DOI: 10.1029/2011JD017384.

Rigby, Matt et al. (2018). *Report to BEIS: Long-term atmospheric measurement and interpretation (of radiatively active trace gases) BEIS contract number : GA0201 Annual Report (Sept 2017 - Sept 2018)*. Tech. rep. University if Bristol, Met. Office.

Rigby, Matthew et al. (2017). "Role of atmospheric oxidation in recent methane growth". In: *Proceedings of the National Academy of Sciences* 114.21, pp. 5373–5377. ISSN: 0027-8424. DOI: 10.1073/pnas.1616426114.

Roberts, M. L. and J. R. Southon (2007). "A preliminary determination of the absolute 14C12C ratio of OX-I". In: *Radiocarbon* 49.2. ISSN: 00338222. DOI: 10.1017/S0033822200042363.

Röckmann, Thomas et al. (2016). "In situ observations of the isotopic composition of methane at the Cabauw tall tower site". In: pp. 10469–10487. DOI: 10.5194/acp-16-10469-2016.

Rosentreter, Judith A. et al. (2021). "Half of global methane emissions come from highly variable aquatic ecosystem sources". In: *Nature Geoscience* 14.4, pp. 225–230. ISSN: 17520908. DOI: 10.1038/s41561-021-00715-2. URL: http://dx.doi.org/10.1038/s41561-021-00715-2.

Roy-Barman, Matthieu and Catherine Jeandel (2016). “Marine Geochemistry”. In: *Marine Geochemistry*. 1st ed. Oxford University Press. Chap. 3. ISBN: 978-0-19-878750-1. DOI: 10.1093/acprof:oso/9780198787495.001.0001.

Saboya, Eric et al. (Mar. 2022). “Continuous CH4 and d13CH4 measurements in London demonstrate under-reported natural gas leakage”. In: *Atmospheric Chemistry and Physics* 22.5, pp. 3595–3613. ISSN: 1680-7324. DOI: 10.5194/acp-22-3595-2022. URL: https://acp.copernicus.org/articles/22/3595/2022/.

Sadavarte, Pankaj et al. (2021). “Methane Emissions from Superemitting Coal Mines in Australia Quantified Using TROPOMI Satellite Observations”. In: *Environmental Science and Technology* 55.24. ISSN: 15205851. DOI: 10.1021/acs.est.1c03976.

Sargent, Maryann R. et al. (2021). “Majority of US urban natural gas emissions unaccounted for in inventories”. In: *Proceedings of the National Academy of Sciences* 118.44, e2105804118. ISSN: 0027-8424. DOI: 10.1073/pnas.2105804118/-/DCSupplemental.Published. URL: https://www.pnas.org/content/118/44/e2105804118%0Ahttps://www.pnas.org/content/118/44/e2105804118.abstract.

Saunois, Marielle et al. (2016). “The global methane budget 2000-2012”. In: *Earth System Science Data* 8.2, pp. 697–751. ISSN: 18663516. DOI: 10.5194/essd-8-697-2016.

Saunois, Marielle et al. (2020). “The Global Methane Budget 2000 – 2017”. In: pp. 1561–1623.

Schuur, E. A. G, E.R.M Druffel, and S. E Trumbore (2016). *Radiocarbon and Climate Change: Mechanisms, Applications and Laboratory Techniques*. Ed. by Edward A.G. Schuur, Ellen Druffel, and Susan E. Trumbore. 1st ed. Cham: Springer International Publishing. ISBN: 978-3-319-25641-2. DOI: 10.1007/978-3-319-25643-6. URL: http://link.springer.com/10.1007/978-3-319-25643-6.

Shallcross, Dudley E., M. Aslam K. Khalil, and Christopher L. Butenhoff (2007). “The atmospheric methane sink”. In: *Greenhouse Gas Sinks*. DOI: 10.1079/9781845931896.0171.

Shepheard, Marcus (2020). *Institute for Government: UK Net zero target*. URL: https://www.instituteforgovernment.org.uk/explainers/net-zero-target.

Sherwood, Owen A. et al. (2017). “Global inventory of gas geochemistry data from fossil fuel, microbial and burning sources, version 2017”. In: *Earth System Science Data* 9.2, pp. 639–656. ISSN: 18663516. DOI: 10.5194/essd-9-639-2017.

Solazzo, Efisio et al. (Apr. 2021). “Uncertainties in the Emissions Database for Global Atmospheric Research (EDGAR) emission inventory of greenhouse gases”. In: *Atmospheric Chemistry and Physics* 21.7, pp. 5655–

5683. ISSN: 1680-7324. DOI: 10.5194/acp-21-5655-2021. URL: https://acp.copernicus.org/articles/21/5655/2021/.

Spahni, R. et al. (June 2011). "Constraining global methane emissions and uptake by ecosystems". In: *Biogeosciences* 8.6, pp. 1643–1665. ISSN: 1726-4189. DOI: 10.5194/bg-8-1643-2011. URL: https://bg.copernicus.org/articles/8/1643/2011/.

Sparks, Nathan and Ralf Toumi (2010). "Remote sampling of a CO2 point source in an urban setting". In: *Atmospheric Environment* 44.39, pp. 5287–5294. ISSN: 13522310. DOI: 10.1016/j.atmosenv.2010.07.048. URL: http://dx.doi.org/10.1016/j.atmosenv.2010.07.048.

Stanley, Kieran M. et al. (2018). "Greenhouse gas measurements from a UK network of tall towers: Technical description and first results". In: *Atmospheric Measurement Techniques* 11.3, pp. 1437–1458. ISSN: 18678548. DOI: 10.5194/amt-11-1437-2018.

Stavert, Ann R. et al. (2022). "Regional trends and drivers of the global methane budget". In: *Global Change Biology* 28.1. ISSN: 13652486. DOI: 10.1111/gcb.15901.

Streets, David G. et al. (2013). *Emissions estimation from satellite retrievals: A review of current capability*. DOI: 10.1016/j.atmosenv.2013.05.051.

Stuiver, M. and P. D. Quay (1981). "Atmospheric 14C changes resulting from fossil fuel CO2 release and cosmic ray flux variability". In: *Earth and Planetary Science Letters* 53.3. ISSN: 0012821X. DOI: 10.1016/0012-821X(81)90040-6.

Stuiver, Minze (1983). "International Agreements and the Use of the New Oxalic Acid Standard". In: *Radiocarbon* 25.2. ISSN: 0033-8222. DOI: 10.1017/s0033822200006159.

Stuiver, Minze and Henry A Polach (July 1977). "Discussion Reporting of 14C Data". In: *Radiocarbon* 19.03, pp. 355–363. ISSN: 0033-8222. DOI: 10.1017/S0033822200003672. URL: https://www.cambridge.org/core/product/identifier/S0033822200003672/type/journal_article.

Sudarchikova, N. et al. (Mar. 2021). *Validation report of the CAMS near-real-time global atmospheric composition service: Period September-November 2020*. Tech. rep. opernicus Atmosphere Monitoring Service (CAMS) report,

Suess, HE (1955). "Radiocarbon concentration in modern wood". In: *Science* 122.I, pp. 415–417. URL: http://www.bcin.ca/Interface/openbcin.cgi?submit=submit&Chinkey=65360.

Tans, Pieter P. (Mar. 1997). "A note on isotopic ratios and the global atmospheric methane budget". In: *Global Biogeochemical Cycles* 11.1, pp. 77–81. ISSN: 08866236. DOI: 10.1029/96GB03940. URL: http://doi.wiley.com/10.1029/96GB03940.

Thompson, D. R. et al. (2016). “Space-based remote imaging spectroscopy of the Aliso Canyon CH4 superemitter”. In: *Geophysical Research Letters* 43.12, pp. 6571–6578. ISSN: 19448007. DOI: 10.1002/2016GL069079.

Townsend-Small, Amy et al. (2012). “Isotopic measurements of atmospheric methane in Los Angeles, California, USA: Influence of "fugitive" fossil fuel emissions”. In: *Journal of Geophysical Research Atmospheres* 117.7, pp. 1–11. ISSN: 01480227. DOI: 10.1029/2011JD016826.

Tratt, David M. et al. (2014). “Airborne visualization and quantification of discrete methane sources in the environment”. In: *Remote Sensing of Environment* 154.1. ISSN: 00344257. DOI: 10.1016/j.rse.2014.08.011.

Turner, A. J. et al. (2015). “Estimating global and North American methane emissions with high spatial resolution using GOSAT satellite data”. In: *Atmospheric Chemistry and Physics* 15.12. ISSN: 16807324. DOI: 10.5194/acp-15-7049-2015.

Turner, A. J. et al. (2016). “A large increase in U.S. methane emissions over the past decade inferred from satellite data and surface observations”. In: *Geophysical Research Letters* 43.5. ISSN: 19448007. DOI: 10.1002/2016GL067987.

Turner, Alexander J. et al. (2017). “Ambiguity in the causes for decadal trends in atmospheric methane and hydroxyl”. In: *Proceedings of the National Academy of Sciences of the United States of America* 114.21. ISSN: 10916490. DOI: 10.1073/pnas.1616020114.

Turner, Alexander J. et al. (2018). “Assessing the capability of different satellite observing configurations to resolve the distribution of methane emissions at kilometer scales”. In: *Atmospheric Chemistry and Physics* 18.11, pp. 8265–8278. ISSN: 16807324. DOI: 10.5194/acp-18-8265-2018.

UK Environment Agency (Sept. 2019). *D7 waste exemption: burning waste*.

UK Government (2008). *Climate Change Act 2008: Elizabeth II. Chapter 27*.

Umezawa, Taku et al. (2017). “Intercomparisons of δ¹³C and δD measurements of atmospheric CH₄ for combined use of datasets from different laboratories”. In: *Atmospheric Measurement Techniques Discussions*, pp. 1–44. DOI: 10.5194/amt-2017-281.

Valley, John W. and David R. Cole (2019). *Stable isotope geochemistry*. Vol. 43. DOI: 10.1016/s0037-0738(97)00056-0.

Van der Stricht, S and A Janssens (2005). “Radioactive Effluents from Nuclear Power Stations and Nuclear Fuel Reprocessing Sites in the European Union”. In: *Radiation Protection, European Commission*.

Van Der Werf, Guido R. et al. (2017). “Global fire emissions estimates during 1997-2016”. In: *Earth System Science Data* 9.2, pp. 697–720. ISSN: 18663516. DOI: 10.5194/essd-9-697-2017.

Varon, D. J. et al. (2019). “Satellite Discovery of Anomalously Large Methane Point Sources From Oil/Gas Production”. In: *Geophysical Research Letters* 46.22. ISSN: 19448007. DOI: 10.1029/2019GL083798.

Veefkind, J. P. et al. (2012). “TROPOMI on the ESA Sentinel-5 Precursor: A GMES mission for global observations of the atmospheric composition for climate, air quality and ozone layer applications”. In: *Remote Sensing of Environment* 120.2012, pp. 70–83. ISSN: 00344257. DOI: 10.1016/j.rse.2011.09.027. URL: http://dx.doi.org/10.1016/j.rse.2011.09.027.

Venturi, S. et al. (2020). “Seasonal and diurnal variations of greenhouse gases in Florence (Italy): Inferring sources and sinks from carbon isotopic ratios”. In: *Science of the Total Environment* 698, p. 134245. ISSN: 18791026. DOI: 10.1016/j.scitotenv.2019.134245. URL: https://doi.org/10.1016/j.scitotenv.2019.134245.

Verhulst, Kristal R. et al. (2017). “Carbon dioxide and methane measurements from the Los Angeles Megacity Carbon Project – Part 1: calibration, urban enhancements, and uncertainty estimates”. In: *Atmospheric Chemistry and Physics* 17.13, pp. 8313–8341. ISSN: 1680-7324. DOI: 10.5194/acp-17-8313-2017. URL: https://www.atmos-chem-phys.net/17/8313/2017/.

Voulgarakis, A. et al. (2013). “Analysis of present day and future OH and methane lifetime in the ACCMIP simulations”. In: *Atmospheric Chemistry and Physics* 13.5, pp. 2563–2587. ISSN: 16807316. DOI: 10.5194/acp-13-2563-2013.

Wahlen, M et al. (1989). “Carbon-14 in Methane Sources and in Atmospheric Methane: The Contribution from Fossil Carbon”. In: *Science* 245.in Articles, p. 286. URL: /archive/#classic.

Wang, Yilong et al. (2017). “Estimation of observation errors for large-scale atmospheric inversion of CO2 emissions from fossil fuel combustion”. In: *Tellus, Series B: Chemical and Physical Meteorology* 69.1, pp. 1–26. ISSN: 16000889. DOI: 10.1080/16000889.2017.1325723. URL: http://doi.org/10.1080/16000889.2017.1325723.

Warwick, Nicola J. et al. (2016). “Using δ13C-CH4 and δD-CH4 to constrain Arctic methane emissions”. In: *Atmospheric Chemistry and Physics* 16.23, pp. 14891–14908. ISSN: 16807324. DOI: 10.5194/acp-16-14891-2016.

Webster, H. N. et al. (2012). “Operational prediction of ash concentrations in the distal volcanic cloud from the 2010 Eyjafjallajkull eruption”. In: *Journal of Geophysical Research Atmospheres* 117.2, pp. 1–17. ISSN: 01480227. DOI: 10.1029/2011JD016790.

Wecht, Kevin J. et al. (2014). “Mapping of North American methane emissions with high spatial resolution by inversion of SCIAMACHY satellite data”. In: *Journal of Geophysical Research* 119.12. ISSN: 21562202. DOI: 10.1002/2014JD021551.

Wenger, Angelina et al. (Nov. 2019). "Atmospheric radiocarbon measurements to quantify CO2 emissions in the UK from 2014 to 2015". In: *Atmospheric Chemistry and Physics* 19.22, pp. 14057–14070. ISSN: 1680-7324. DOI: 10.5194/acp-19-14057-2019. URL: https://acp.copernicus.org/articles/19/14057/2019/.

White, W. H. et al. (1976). "Formation and transport of secondary air pollutants: Ozone and aerosols in the St. Louis urban plume". In: *Science* 194.4261. ISSN: 00368075. DOI: 10.1126/science.959846.

Wunch, Debra et al. (May 2011). "The Total Carbon Column Observing Network". In: *Philosophical Transactions of the Royal Society A: Mathematical, Physical and Engineering Sciences* 369.1943, pp. 2087–2112. ISSN: 1364-503X. DOI: 10.1098/rsta.2010.0240. URL: https://royalsocietypublishing.org/doi/10.1098/rsta.2010.0240.

Xueref-Remy, I. et al. (2020). "Anthropogenic methane plume detection from point sources in the Paris megacity area and characterization of their δ13C signature". In: *Atmospheric Environment* 222.February 2019. ISSN: 18732844. DOI: 10.1016/j.atmosenv.2019.117055.

Yver Kwok, C. et al. (2015). "Comprehensive laboratory and field testing of cavity ring-down spectroscopy analyzers measuring H2O, CO2, CH4 and CO". In: *Atmospheric Measurement Techniques* 8.9, pp. 3867–3892. ISSN: 18678548. DOI: 10.5194/amt-8-3867-2015.

Zazzeri, G., E. Acuña Yeomans, and H. D. Graven (2018). "Global and regional emissions of radiocarbon from nuclear power plants from 1972 to 2016". In: *Radiocarbon* 60.4, pp. 1068–1081. ISSN: 00338222. DOI: 10.1017/RDC.2018.42.

Zazzeri, G. et al. (2015). "Plume mapping and isotopic characterisation of anthropogenic methane sources". In: *Atmospheric Environment* 110, pp. 151–162. ISSN: 18732844. DOI: 10.1016/j.atmosenv.2015.03.029.

Zazzeri, G. et al. (2017). "Evaluating methane inventories by isotopic analysis in the London region". In: *Scientific Reports* 7.1, pp. 1–13. ISSN: 20452322. DOI: 10.1038/s41598-017-04802-6.

Zazzeri, Giulia (2016). "Methane Emissions in UK: Deciphering Regional Sources with Mobile Measurements and Isotopic Characterisation". PhD thesis, p. 264.

Zazzeri, Giulia, Xiaomei Xu, and Heather Graven (July 2021). "Efficient Sampling of Atmospheric Methane for Radiocarbon Analysis and Quantification of Fossil Methane". In: *Environmental Science & Technology* 55.13, pp. 8535–8541. ISSN: 0013-936X. DOI: 10.1021/acs.est.0c03300. URL: https://pubs.acs.org/doi/10.1021/acs.est.0c03300.

Appendices

Appendix A

Derivation of Chapter 5 CH_4-$\delta^{13}CH_4$-$\Delta^{14}CH_4$ equations

Equation 5.5

From Eq. 5.4, added fossil CH_4 concentrations, C_f, can be expressed as

$$C_f = F(C_a - C_{bg}), \tag{A.1}$$

and added CH_4 concentrations from non-fossil sources, C_b, can be expressed as

$$C_b = (1 - F)(C_a - C_{bg}). \tag{A.2}$$

Substituting Eq. A.1 and A.2 into Eq. 5.3 (the $^{14}CH_4$ mass balance) yields

$$\Delta_a C_a = \Delta_{bg} C_{bg} + \Delta_f F(C_a - C_{bg}) + \Delta_b (C_a - C_{bg} - FC_a + FC_{bg}) + A_{nuc},$$

$$\Delta_a C_a = C_a(F(\Delta_f - \Delta_b) + \Delta_b) - C_{bg}(F(\Delta_f - \Delta_b) + \Delta_b - \Delta_{bg}) + A_{nuc}.$$

Hence,

$$\Delta_a = -\frac{1}{C_a}(F(\Delta_f - \Delta_b) + \Delta_b - \Delta_{bg})C_{bg} + (F(\Delta_f - \Delta_b) + \Delta_b + A_{nuc}).$$

Equation 5.6

Consider added CH_4 sources split between fossil and non-fossil sources such that $N = 2$. Therefore, $C_s = C_f + C_b$. Then,

$$C_a = C_{bg} + C_f + C_b,$$

which can be used to express C_b as

$$C_b = C_a - C_{bg} - C_f. \tag{A.3}$$

Substituting Eq. A.3 into Eq. 5.3 gives:

$$\Delta_a C_a = \Delta_{bg} C_{bg} + \Delta_f C_f + \Delta_b (C_a - C_{bg} - C_f) + A_{nuc},$$

$$C_f(\Delta_f - \Delta_b) = C_a(\Delta_a - \Delta_b) - C_{bg}(\Delta_{bg} - \Delta_b) - A_{nuc}.$$

Therefore,

$$C_f = C_a \left(\frac{\Delta_a - \Delta_b}{\Delta_f - \Delta_b} \right) - C_{bg} \left(\frac{\Delta_{bg} - \Delta_b}{\Delta_f - \Delta_b} \right) - \frac{A_{nuc}}{\Delta_f - \Delta_b}.$$

Dividing each term in Eq. A by $(C_a - C_{bg})$ gives

$$F = \frac{1}{C_a - C_{bg}} \left(C_a \left(\frac{\Delta_a - \Delta_b}{\Delta_f - \Delta_b} \right) - C_{bg} \left(\frac{\Delta_{bg} - \Delta_b}{\Delta_f - \Delta_b} \right) - \frac{A_{nuc}}{\Delta_f - \Delta_b} \right).$$

Equation 5.7

Substituting Eq. A.3 into Eq. 5.2 gives:

$$\delta_a C_a = \delta_{bg} C_{bg} + \delta_f C_f + \delta_b (C_a - C_{bg} - C_f),$$

$$(\delta_a - \delta_{bg}) C_a = (\delta_{bg} - \delta_b) C_{bg} + (\delta_f - \delta_b) C_f.$$

Hence,

$$C_f = C_a \left(\frac{\delta_a - \delta_b}{\delta_f - \delta_b} \right) - C_{bg} \left(\frac{\delta_{bg} - \delta_b}{\delta_f - \delta_b} \right).$$

Dividing by $(C_a - C_{bg})$ gives

$$F = \frac{1}{C_a - C_{bg}} \left(C_a \left(\frac{\delta_a - \delta_b}{\delta_f - \delta_b} \right) - C_{bg} \left(\frac{\delta_{bg} - \delta_b}{\delta_f - \delta_b} \right) \right).$$

Equations 5.9 and 5.10

Although Gaussian elimination can be used to solve the set of linear equations in Eq. 5.8, they can also be solved through substitution. Let,

$$C_3 = C_a - C_{bg} - C_1 - C_2.$$

Therefore,

$$\delta_a C_a = \delta_{bg} C_{bg} + \delta_1 C_1 + \delta_2 C_2 + \delta_3 (C_a - C_{bg} - C_1 - C_2). \tag{A.4}$$

Hence,

$$(\delta_a - \delta_3)C_a = (\delta_{bg} - \delta_3)C_{bg} + (\delta_1 - \delta_3)C_1 + (\delta_2 - \delta_3)C_2. \tag{A.5}$$

Similarly,

$$(\Delta_a - \Delta_3)C_a = (\Delta_{bg} - \Delta_3)C_{bg} + (\Delta_1 - \Delta_3)C_1 + (\Delta_2 - \Delta_3)C_2 + A_{nuc}. \tag{A.6}$$

Substituting Eq. A.5 into Eq. A.6:

$$(\Delta_a - \Delta_3)C_a = (\Delta_{bg} - \Delta_3)C_{bg} + (\Delta_1 - \Delta_3)C_1 + (\Delta_2 - \Delta_3)\left(\left(\frac{\delta_a - \delta_3}{\delta_2 - \delta_3}\right)C_a - \left(\frac{\delta_{bg} - \delta_3}{\delta_2 - \delta_3}\right)C_{bg} - \left(\frac{\delta_1 - \delta_3}{\delta_2 - \delta_3}\right)C_1\right) + A_{nuc},$$

$$C_a\left(\frac{\Delta_a - \Delta_3}{\Delta_2 - \Delta_3} - \frac{\delta_a - \delta_3}{\delta_2 - \delta_3}\right) = C_{bg}\left(\frac{\Delta_{bg} - \Delta_3}{\Delta_2 - \Delta_3} - \frac{\delta_{bg} - \delta_3}{\delta_2 - \delta_3}\right) + C_1\left(\frac{\Delta_1 - \Delta_3}{\Delta_2 - \Delta_3} - \frac{\delta_1 - \delta_3}{\delta_2 - \delta_3}\right) + \frac{A_{nuc}}{\Delta_2 - \Delta_3}.$$

Hence,

$$C_1 = \left(\frac{\Delta_1 - \Delta_3}{\Delta_2 - \Delta_3} - \frac{\delta_1 - \delta_3}{\delta_2 - \delta_3}\right)^{-1}\left(C_a\left(\frac{\Delta_a - \Delta_3}{\Delta_2 - \Delta_3} - \frac{\delta_a - \delta_3}{\delta_2 - \delta_3}\right) - C_{bg}\left(\frac{\Delta_{bg} - \Delta_3}{\Delta_2 - \Delta_3} - \frac{\delta_{bg} - \delta_3}{\delta_2 - \delta_3}\right) - \frac{A_{nuc}}{\Delta_2 - \Delta_3}\right).$$

The same approach is used to derive Eq. 5.10.

Equations 5.13 and 5.14

Since,

$$\Delta_a - \Delta_{bg} = \frac{1}{C_a}(\Delta_{bg}C_{bg} + \sum_i^N \Delta_i C_i) - \Delta_{bg}$$

$$\Delta_a - \Delta_{bg} = \frac{\Delta_{bg}}{C_a}(C_{bg} - C_a) + \frac{1}{C_a}\sum_i^N \Delta_i C_i.$$

Then,

$$\Delta_a - \Delta_{bg} = \frac{1}{C_a}(-\Delta_{bg}\sum_i^N C_i + \sum_i^N \Delta_i C_i),$$

$$\Delta_a - \Delta_{bg} = \frac{1}{C_a}\sum_i^N C_i(\Delta_i - \Delta_{bg}).$$

Equation 5.13 is similarly derived.

Equation 5.15

Starting from Eq. 5.14 and dividing by $\delta_a - \delta_{bg}$ gives,

$$\frac{\Delta_a - \Delta_{bg}}{\delta_a - \delta_{bg}} = \frac{\sum_i^N C_i(\Delta_i - \Delta_{bg})}{\sum_i^N C_i(\delta_i - \delta_{bg})}.$$

Appendix B

Calculating uncertainties of $\Delta^{14}CH_4$-$\delta^{13}CH_4$ slopes

Slopes of $\Delta^{14}CH_4$-$\delta^{13}CH_4$ in chapter 5 are calculated following a pragmatic approach. As slopes are calculated from Eq. 5.15, uncertainties are propagated following the terms in Eq. 5.15. Uncertainties of $\delta^{13}CH_4$ signatures - $\sigma_{13C,sig}$ -(±3‰; Zazzeri et al. 2017) are combined with the background $\delta^{13}CH_4$ uncertainty - $\sigma_{13C,bg}$- (0.1‰) and $\delta^{13}CH_4$ measurement uncertainty - $\sigma_{13C,a}$ - (0.2‰) by

$$\sigma_{13C} = \sqrt{\sigma^2_{13C,sig} + \sigma^2_{13C,bg} + \sigma^2_{13C,a}} = \sqrt{3^2 + 0.1^2 + 0.2^2},$$

to give the uncertainty of $\delta_i - \delta_{bg}$.

The uncertainty of the fossil $\Delta^{14}CH_4$ signature is 0‰. The biospheric $\Delta^{14}CH_4$ signature is the combination of $\Delta^{14}CO_2$ uncertainty (±3‰) and turnover time uncertainty (30‰; based on the difference in $\Delta^{14}CO_2$ from a 0 year and 6 year turnover time for the year 2018). The uncertainty in background $\Delta^{14}CH_4$ is the combination of 11‰ measurement uncertainty (Townsend-Small et al. 2012). The background $\Delta^{14}CH_4$ uncertainty is combined with the $\Delta^{14}CH_4$ signature uncertainty using:

$$\sigma_{14C} = \sqrt{\sigma^2_{14C,sig} + \sigma^2_{14C,bg}}.$$

For fossil CH_4, σ_{14C} = 11.4‰ and for biospheric CH_4 σ_{14C} = 32.1‰. σ_{14C} and σ_{13C} are combined as follows to give an overall uncertainty for each of the $\Delta^{14}CH_4$-$\delta^{13}CH_4$ slopes:

$$\sigma = \text{slope} \times \sqrt{\left(\frac{\sigma_{13C}}{\delta_i - \delta_{bg}}\right)^2 + \left(\frac{\sigma_{14C}}{\Delta_i - \Delta_{bg}}\right)^2}. \tag{B.1}$$